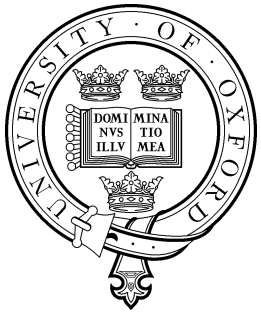
Vertex model approaches to epithelial tissues in developmental systems



Aaron Smith

Hertford College

University of Oxford

A thesis submitted for the degree of

Doctor of Philosophy

Michaelmas 2011

Acknowledgements

I would like to thank my supervisors, Professor Philip Maini, Dr Ruth Baker and Dr David Kay for their fantastic support and advice over the last three years. They have shown a great deal of patience and understanding, while always responding quickly to my questions and requests for help. They have guided and encouraged me throughout this project and I am very grateful for their kindness.

I would like to thank Dr Shankar Srinivas, whose fascinating investigations into cell migration in the mouse embryo are where all this work began. His experimental insights have provided the basis for many simulations during this project, and I am delighted that together we have been able to understand the role of rosettes. I hope that the model built up in this thesis will continue to be used and prove useful to Dr Srinivas and his group.

Many thanks must also go to all the staff at the Life Sciences Interface Doctoral Training Centre. This thesis would not have been possible without all their hard work. I extend my gratitude to the Engineering and Physical Sciences Research Council for funding this study.

I am also indebted to staff and colleagues at the Centre for Mathematical Biology. I would particularly like to thank my office-mates, Kit and Thomas, for sharing in the highs and lows and helping me out along the way. Kit also read through a complete draft of this thesis, I am very grateful for his insightful suggestions.

Finally I would like to thank my parents for their love. Dad, I know you'll enjoy reading this thesis, even if you don't understand it all. Mum, I know you would have been proud.

Contents

1 Introduction **3**

1.1 Use of computational models 4

1.2 Computational models in developmental biology 6

1.3 Epithelia in developmental systems 14

1.3.1 Mouse VE 14

1.3.2 *Drosophila* wing imaginal disc 16

1.4 Thesis outline 18

2 Two-dimensional model **21**

2.1 Initial configurations 22

2.2 Force laws 24

2.2.1 Tension forces 25

2.2.2 Pressure forces 26

2.2.3 Boundary forces 27

2.3 Equations of motion 28

2.4 Junctional rearrangements 29

2.5 Growth and proliferation 31

2.6 Cell death 33

2.7 Summary of model equations 34

2.8 Numerical solutions 35

2.8.1 Explicit numerical methods 35

2.8.2 Implicit numerical methods 39

2.9 Simulations of one force 41

2.10 Simulations of all forces 44

2.11 Simulations with cell growth 47

2.12 Simulations with cell proliferation 51

2.13 Simulations with cell death 53

2.14 Summary 57

3 Modelling diffusing growth factors **59**
3.1 Diffusion equation . . . 62
3.1.1 Boundary condition derivation . . . 63
3.2 Weak form derivation . . . 65
3.2.1 ALE reference frame . . . 66
3.3 Discrete approximation . . . 69
3.4 FE implementation . . . 72
3.5 Convergence properties of solution . . . 76
3.6 Simulation run time . . . 81
3.7 Effects of cellular rearrangements . . . 83
3.7.1 Proliferation . . . 83
3.7.2 T1 transitions . . . 85
3.7.3 Cell death . . . 86
3.8 Morphogen-dependent growth . . . 86
3.8.1 Radial Dpp gradient . . . 88
3.9 Summary . . . 93

4 Chemical production and ingestion **96**
4.1 Production . . . 98
4.2 Ingestion . . . 100
4.3 Internal chemical concentration . . . 103
4.4 Simulations of chemical ingestion . . . 106
4.5 Effects of cellular rearrangements . . . 110
4.5.1 T1 transitions . . . 110
4.5.2 Proliferation . . . 110
4.5.3 Cell death . . . 111
4.6 Simulations with cellular rearrangements . . . 111
4.7 *Drosophila* epidermis . . . 113
4.8 Summary . . . 119

5 Modelling AVE migration in the mouse embryo **123**
5.1 AVE migration in the mouse embryo . . . 125
5.1.1 Onset of migration . . . 125
5.1.2 Discovery of rosettes . . . 127
5.2 Extensions to the 2D model . . . 129
5.2.1 Vertex joining and splitting . . . 129
5.2.2 Periodic boundary conditions . . . 130

5.2.3 Mapping from the 2D plane to a cylinder . . . 132
5.2.4 Inducing migration of a single cell . . . 135
5.2.5 Summary of the cylindrical model . . . 137
5.3 Ellipsoid model . . . 138
5.3.1 Creating an initial cellular mesh . . . 138
5.3.2 Forces on the ellipsoid surface . . . 140
5.3.3 Mapping vertices to the ellipsoid surface . . . 142
5.3.4 Relaxing to mechanical equilibrium . . . 143
5.3.5 Force validation . . . 146
5.3.6 Growth and proliferation . . . 149
5.3.7 Modelling the barrier to migration . . . 152
5.4 Summary . . . 154

6 Simulations of AVE migration **156**
6.1 Migration of a single cell . . . 157
6.1.1 Migration force . . . 157
6.1.2 Incorporating the barrier to migration . . . 159
6.1.3 More protruding vertices . . . 161
6.2 Migration of multiple cells . . . 165
6.2.1 Experimental data . . . 166
6.2.2 Simulations with rosettes . . . 168
6.3 PCP-signalling mutants . . . 174
6.4 Summary . . . 175

7 Discussion **180**
7.1 Results . . . 180
7.2 Further work . . . 182
7.2.1 Theoretical . . . 182
7.2.2 Applications . . . 184
7.3 Summary . . . 186

Bibliography **188**

Abstract

The purpose of this thesis is to develop a vertex model framework that can be used to perform computational experiments related to the dynamics of epithelial tissues in developmental systems. We focus on three example systems: the *Drosophila* wing imaginal disc, the *Drosophila* epidermis and the visceral endoderm of the mouse embryo. Within these systems, key questions pertaining to size-control mechanisms and coordination of cell migration remain unanswered and are amenable to computational testing.

The vertex model presented here builds upon existing frameworks in three key ways. Firstly, we include novel force terms, representing, for example, the reaction of a cell to being compressed and its shape becoming distorted during a highly dynamic process such as cell migration. Secondly, we incorporate a model of diffusing morphogenetic growth factors within the vertex framework, using an arbitrary Lagrangian-Eulerian formulation of the diffusion equation and solving with the finite-element method (FEM). Finally, we implement the vertex model on the surface of an ellipsoid, in order to simulate cell migration in the mouse embryo.

Throughout this thesis, we validate our model by running simple simulations. We demonstrate convergence properties of the FEM scheme and discuss how the time taken to solve the system scales with tissue size. The model is applied to biological systems and its utility demonstrated in several contexts. We show that when growth is dependent on morphogen concentration in the *Drosophila* wing disc, proliferation occurs preferentially in regions of high concentration. In the *Drosophila* epidermis, we show that a recently proposed mechanism of compartment size-control, in which a growth-factor is released in limited amounts, is viable. Finally, we examine the phenomenon of rosettes in the mouse embryo, which occur when five or more cells meet at a common vertex. We show, by running simulations both with and without rosettes, that they are crucial facilitators of ordered migration, and are thus critical in the patterning of the early embryo.

Nomenclature

a.u.	Arbitrary units
ALE	Arbitrary Lagrangian-Eulerian
AVE	Anterior visceral endoderm
Brk	Brinker
cAMP	Cyclic adenosine monophosphate
CDT	Cell doubling time
cycE	cyclin E
Dpp	Decapentaplegic
EGFR	Epidermal growth factor receptor
ExE	Extra-embryonic ectoderm
FEM	Finite-element method
GFP	Green fluorescent protein
Hh	Hedgehog
ICM	Inner cell mass
ODE	Ordinary differential equation
PDE	Partial differential equation
RK	Runge-Kutta
Spi	Spitz
VE	Visceral endoderm

Chapter 1

Introduction

Mathematical and computational models of multi-cellular systems have become extremely useful tools in a variety of areas, including tumour angiogenesis (Chaplain, 2000), slime mould development (Maree et al., 1999), cell sorting (Graner and Glazier, 1992), and embryogenesis (Painter et al., 2000). These models exhibit various levels of detail, ranging from coarse-grained approximations (Chaplain, 2000, Keller and Segel, 1970), to complex sub-cellular biomechanical dynamics (Gracheva and Othmer, 2004). In developmental biology, we are often interested in processes on a spatial scale that require modelling at a level between these two extremes, where each cell is treated as a discrete entity and assigned a limited set of properties. The cell numbers present in the systems of interest often render this kind of model appropriate, both biologically and computationally.

Epithelium is a type of animal tissue which lines the surfaces and cavities of structures in the body (Walbot and Holder, 1987). Epithelial cells have roles ranging from secretion and selective absorption to protection, transcellular transport and detection of sensation. Epithelial tissues consist of tightly packed groups of cells, with few spaces between them. Cells are attached to each other by junctional protein complexes known as tight junctions and desmosomes (Walbot and Holder, 1987).

Epithelia are divided into two categories, the simple epithelium and the stratified epithelium. Simple epithelium is a mono-layer, with every cell in contact with the underlying scaffolding, known as the basement membrane. As epithelia are avascular, the tissue obtains its nutrients from substances diffusing from the blood vessels in the basement membrane, which is selectively permeable. Stratified epithelium, meanwhile, consists of more than one layer, and is thus found in regions where the tissue has to withstand harmful chemicals or great mechanical stresses. The outer layer of skin of the human body, for example, is a stratified epithelium.

In this thesis we will focus on the use of cell-based models of epithelial tissues in developmental biology. We will begin in Section 1.1 by explaining why computational models are useful in biological systems, and why epithelia are particularly amenable to computational modelling. In Section 1.2 we will describe various types of cell-based model that are currently available. We will give examples of systems of interest in Section 1.3 that we will revisit later in the thesis. Finally, in Section 1.4 we will detail the structure of the rest of the thesis.

1.1 Use of computational models

As computational power increases, complex mathematical models have become ever more viable tools in the study of biological systems. Once created, they can be simulated multiple times, from a wide range of initial conditions, with a huge variety of parameter combinations. Biological systems, with their inherent stochasticity, require repeated experiments, as a single observation of the system behaviour is insufficient to draw reliable conclusions. These types of experiments are often not viable in a biological laboratory, where the problems of obtaining relevant data *in vivo*, as well as the costs and technical difficulties associated with creating realistic *in vitro* environments, are often prohibitive.

Computational models facilitate immediate access to all system variables, something lacking in experimental data. Models can be used to examine the effects of altering a single state variable. To run such an experiment *in vivo* is almost impossible, as all other variables must be kept constant. We will see an example of this kind of computational experiment in Chapter 5 of this thesis, where we change a single parameter in our model of cell migration in the mouse embryo, and observe a stark contrast in the system behaviour that yields a key insight into the process.

Epithelial tissues often consist of cells with similar properties, making them highly amenable to computational modelling using cell-based models. In these models, each cell is a discrete entity that follows a set of simple rules. The behaviour of the system can be elicited by solving the governing equations. By making adjustments to the program, we can then perform computational experiments and infer the importance of each system input. Simple epithelia are particularly useful model systems, as they can often be represented as junctional networks in two dimensions (2D). Compared to a three-dimensional (3D) representation, this simplifies the model and crucially reduces the computational power required.

In many cases cell-based models are not appropriate for the biology of a given system, and in these instances often a continuum model is required. In continuum models, tissues are not broken up into individual cells and instead are represented by a set of differential equations (see e.g. Chaplain (2000)). This is often true when the number of cells in a system is large and the computational complexity of a cell-based model would be prohibitive. Continuum models have successfully been used to simulate epithelial tissues, such as Aegerter-Wilmsen et al. (2007). In this thesis we choose to focus on developing cell-based approaches to modelling epithelia. We are not dismissing continuum models, and it should always be remembered that before choosing between cell-based approaches, the question of whether to use a cell-based or continuum model should first be addressed.

In Section 1.2 we will discuss the various types of cell-based model currently available. There are several approaches that can successfully be used in the modelling of simple epithelia. We will see later, in Section 1.3, that vertex models have certain properties that make them ideal in systems of interest such as the *Drosophila* wing imaginal disc and the visceral endoderm (VE) of the mouse embryo.

1.2 Computational models in developmental biology

The vertex model, first developed by Weliky and Oster (1990) and Weliky et al. (1991), is an off-lattice cell-based model. It was initially designed to simulate the basic features of cell rearrangement during a process known as epiboly in the teleost fish *Fundulus heteroclitus*, and later applied to convergent extension in the African frog *Xenopus laevis*. In this section we will give a brief outline of the development of the vertex model. Later, in Chapter 2, we will explain the rationale and justification for the assumptions underlying the model in more detail.

In the vertex model, a tissue mono-layer is described by a 2D pattern of polygons, representing the junctions between cells (Fig. 1.1). Two-dimensional cellular patterns

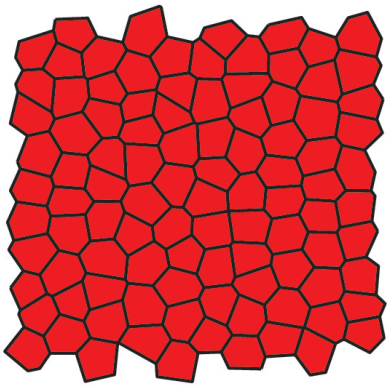


Figure 1.1: *A polygonal tessellation representing an epithelial tissue of 100 cells.*

were first described as Dirichlet domains, also known as Voronoi polygons, by Honda

(1978). Equations of motion are formulated for each vertex and solved to elucidate the behaviour of the system over time.

In Weliky and Oster (1990), the authors implement two types of force, an elastic tension force and a force due to internal pressure (henceforth referred to as a 'pressure force'), which act in the directions shown in Fig. 1.2. The elastic tension forces at a

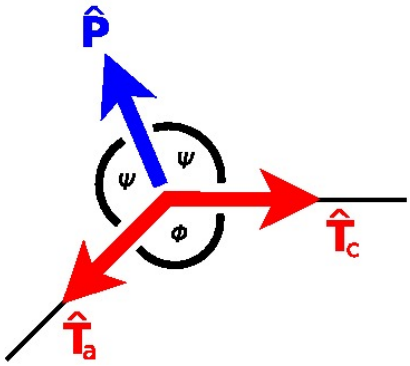


Figure 1.2: *Direction of tension ($\hat{\boldsymbol{T}}$) and pressure ($\hat{\boldsymbol{P}}$) forces acting on vertices in the vertex model. Tension forces act along cell edges in clockwise ($\hat{\boldsymbol{T}}_c$) and anti-clockwise ($\hat{\boldsymbol{T}}_a$) directions. Pressure bisect the angle ϕ between two edges. Reprinted with permission from Smith et al. (2011).*

vertex in a given cell are

$$\mathbf{T}_a = \hat{\mathbf{T}}_a \times k_{elas} \times P,$$
$$\mathbf{T}_c = \hat{\mathbf{T}}_c \times k_{elas} \times P,$$

where $\mathbf{T}_a$ is the tension force in the direction of the anti-clockwise vertex, $\mathbf{T}_c$ is the tension force in the direction of the clockwise vertex, $\hat{\mathbf{T}}_a$ and $\hat{\mathbf{T}}_c$ are unit direction vectors in the direction of the respective forces, k_{elas} is the elastic modulus of the cell cortex and P is the cell perimeter. The pressure force at a vertex, meanwhile, is given by

$$\mathbf{P} = C \times \frac{\hat{\mathbf{P}}}{cell\ area},$$

where C is a constant and $\hat{\mathbf{P}}$ is a unit vector in the direction of the pressure force, which bisects the angle between the two edges joined at the vertex.

The net force acting on a vertex i in this cell is given by

$$\mathbf{F}_i = \mathbf{P} + \mathbf{T}_a + \mathbf{T}_c,$$

while the total force on vertex i, which includes the sum of the forces due to each of the cells to which i belongs, as well as any external forces, is

$$\bar{\mathbf{F}}_i = \sum_{\alpha=1}^{N_i} \mathbf{F}_i + \mathbf{F}_{\text{ext}},$$

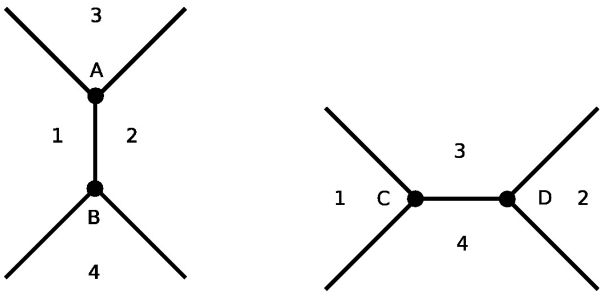
where N_i is the number of cells sharing vertex i and $\mathbf{F}_{\text{ext}}$ represents any external forces. Making the biologically realistic assumption that inertial forces are negligible (see Chapter 2), the equations of motion take the form

$$\mu \frac{\mathrm{d}\mathbf{x}_i}{\mathrm{d}t} = \bar{\mathbf{F}}_i(\mathbf{x}_i), \tag{1.1}$$

where μ is a viscous coefficient and $\mathbf{x}_i$ describes the position of vertex i. Equation (1.1) is solved via an iterative method, and the behaviour of the tissue over time can thus be observed. Solutions of equations of motion of this form will be discussed in Chapter 2.

The authors also included a switching process, known as a T1 transition, which allows cells connected by very short edges to change their connections with neighbours. Fig. 1.3 shows a T1 transition. Weliky and Oster (1990) used their model to show that force considerations alone could explain cell rearrangement within the epidermal enveloping layer of *Fundulus heteroclitus*. They also determined that a certain combination of cell motility rules, including refractory boundaries, contact inhibition and polarized protrusive activity are able to reproduce normal notochord development in *Xenopus laevis* (Weliky et al., 1991).

Nagai and Honda (2001) proposed a dynamic vertex model that could successfully



(a) (b)

Figure 1.3: *A T1 transition for two close vertices. (a) Initially cells 1 and 2 share edge AB, which separates cells 3 and 4. (b) After the rearrangement cells 3 and 4 share edge CD, separating cells 1 and 2. Reprinted with permission from Smith et al. (2011).*

reproduce realistic epithelial cellular topology. They considered two types of forces; a tension of the cell boundary, U_l, and a resistance force against large changes in cell area, U_D. They derived equations of motion of the form

$$\mu \frac{\mathrm{d}\mathbf{x}_i}{\mathrm{d}t} = -\nabla_i (U_l + U_D), \tag{1.2}$$

where μ is a coefficient of friction. They also included T1 transitions, and showed that the characteristic properties of epithelial tissues could arise spontaneously from a range of starting conditions under simple assumptions regarding cellular dynamics.

Hufnagel et al. (2007) implemented a vertex model to show that growth of the *Drosophila* wing imaginal disc can be regulated by a combination of morphogen gradients and mechanical feedback. Stationary cellular configurations satisfy a mechanical force balance, which can also be described as the local minima of an energy function, given by

$$E(\mathbf{x}_i, \xi_\alpha) = \sum_\alpha \left[P_\alpha + a(v_\alpha - V_0)^2 + b \sum_{\beta=\nu(\alpha)} (\xi_\alpha - \xi_\beta)^2 + c(\xi_\alpha - 1)^2 \right], \tag{1.3}$$

where $\mathbf{x}_i$ is the position of vertex i, P_α, v_α, and ξ_α represent the perimeter, volume and height of cell α, respectively, V_0 is the target volume and a, b, and c are parameters

controlling the strength of the various terms. The function $\nu(\alpha)$ returns cell α's neighbouring cells, so the second summation in (1.3) is over α's neighbours. Note that $\nu(\alpha)$ is unrelated to v_α, the cell's volume. The energy function (1.3) penalises neighbouring cells with differing heights, while keeping cells close to their target volume, V_0, and unstressed height, which is set to unity. The function also works to minimise cell perimeters. The authors make cell growth rate dependent on height, which acts as an indicator of the stress the cell is under.

Farhadifar et al. (2007) studied the effects of cell proliferation on the packing geometry of an epithelial tissue. They also minimised an energy function, in this case given by

$$E(\mathbf{x}_i) = \sum_\alpha \frac{K_\alpha}{2}\left(A_\alpha - A_\alpha^{(0)}\right)^2 + \sum_{<i,j>} \Lambda_{ij} l_{ij} + \sum_\alpha \frac{\Gamma_\alpha}{2} P_\alpha^2. \tag{1.4}$$

The first term is similar to U_D in the Nagai and Honda model, acting to prevent cells areas, A_α, from deviating far from their preferred area, $A_\alpha^{(0)}$. The K_α are the elastic coefficients. The second term is analogous to U_l in the Nagai and Honda model, describing line tensions, Λ_{ij}, at junctions of length l_{ij}. The final term represents the contractility of the cell perimeters, P_α, with coefficient Γ_α. The force on each vertex, i, is related to the energy function by

$$F_i = -\frac{\partial E}{\partial \mathbf{x}_i}.$$

To implement cell proliferation, a cell is chosen at random and its preferred area is doubled. The network is then relaxed, before a new cell boundary is introduced at a random orientation. The daughter cells are assigned new preferred areas, and the network is once again relaxed. The authors were able to find regions of parameter space where the model recapitulates the correct cellular topology of the tissue.

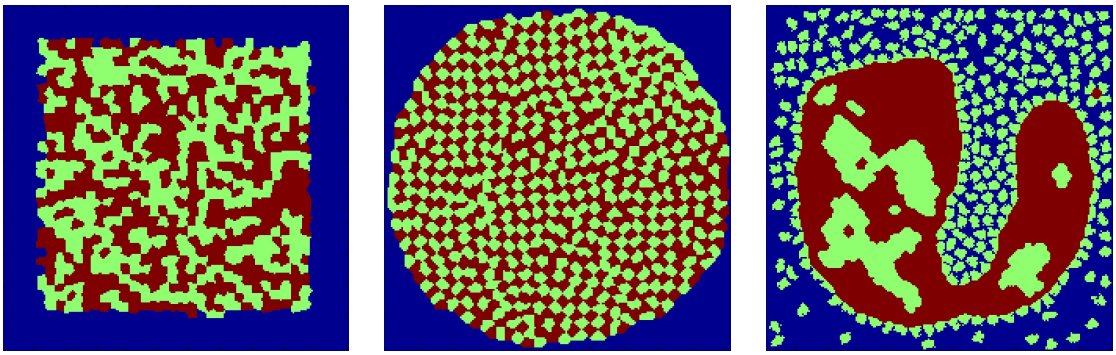
Subsequent vertex models have often been based upon the energy formulation (1.4) of Farhadifar et al. These include the models of Aegerter-Wilmsen et al. (2010),

Landsberg et al. (2009), Rauzi et al. (2008) and Wartlick et al. (2011), which will be described in more detail later in Chapter 3. Force frameworks, such as those of Weliky and Oster (1990), are appropriate for dynamic regimes far from equilibrium, whereas minimising an energy function makes more sense for a system relaxing towards mechanical equilibrium. The difference is however conceptual, and the two frameworks are equivalent.

Several other classes of cell-level models are available for studying the dynamics of developmental systems. One such example is the Potts model, first used in cell modelling by Graner and Glazier (1992), in which the domain is discretised into lattice points, with 'clumps' of lattice points forming cells. Each lattice point is given a value representing the cell to which it belongs, and each cell is assigned a 'type'. Most of these kinds of model aim to simulate two or three different cell types, and/or a medium such as extracellular matrix. Where two cells come into contact with each other (i.e. where adjacent lattice points belong to different cells), there is a surface contact energy which depends on the respective cell types. Cell motion then occurs to reduce the total energy of the system. Lattice points are chosen at random, and switched to belong to neighbouring cells with a probability that depends on the total change in energy that would result from the switch. Typically, energetically favourable events occur with probability one and unfavourable events with probability $e^{-\Delta H/\beta}$, where ΔH is the change in energy and β is a parameter representing the 'temperature' of the system. The Potts model can be extended to include a volume constraint, preventing cells from disappearing altogether or from becoming too large.

The Potts model has been used to study a range of biological phenomena. Glazier and Graner (1993) examined cell sorting, dispersal and 'chess-board' pattern formation (see Fig. 1.4). Mombach and Glazier (1996) modelled the motion of single cells in aggregates of embryonic cells. Savill and Hogeweg (1997), meanwhile, modelled mound formation, cell sorting and slug migration in the cellular slime mould *Dic-*

tyostelium discoideum. They added dynamics of the chemoattractant cyclic adenosine monophosphate (cAMP) to the model by solving the governing partial differential equations (PDEs) for cAMP concentration at all lattice points and subsequently modifying the energy equations appropriately. They found their relatively simple model capable of simulating *D. discoideum* at all stages; from 'single cells to crawling slug'. Other authors have included thermotaxis, phototaxis and haptotaxis into Potts models in a similar manner (Maree et al., 1999, Merks and Glazier, 2006, Turner and Sherratt, 2002).



(a) (b) (c)

Figure 1.4: *Results of two Potts model simulations with two cell types and a medium. (a) The initial configuration used in both simulations. The two cell types, l and d, are represented by light (green) and dark (red) shading, respectively. The medium, M, is in blue. In (b), the contact energy between cells of the same type is higher than the contact energy between cells of different types. This causes cells to preferentially form edges with cells of the opposite type, leading to the observed chess-board pattern. The contact energy of both cells with the medium is higher again, ensuring the cells stay clumped together and form a circular boundary. The contact energy values used are $J_{ll} = 10$, $J_{dd} = 8$, $J_{ld} = 6$ and $J_{lM} = J_{dM} = 12$. Lattice size is 201 $\times$ 201, and the simulation is run for 50 Monte Carlo (MC) iterations, where one MC is defined as 16 $\times$ number of lattice points. A volume constraint of the form $\sum_\sigma \lambda(v_\sigma - V)^2$ is added to the energy of the system, where $\sum_\sigma$ represents the sum over each cell, v_σ is the volume of a particular cell (the number of lattice points that make up the cell), V is the target volume, defined as the average initial cell volume, and $\lambda = 1$ is a parameter corresponding to the strength of the volume constraint. The temperature of the system, β, is 10. (c) The contact energies have been changed to $J_{ll} = 14$, $J_{dd} = 4$, $J_{ld} = 11$, $J_{lM} = 2$ and $J_{dM} = 16$. In this case light cells preferentially form edges with the medium, whereas dark cells stay clumped together, giving the cell dispersal pattern. All other parameters are unchanged.*

Another cell-based model is the cell-centre framework developed by Meineke et al.

(2001) to simulate 2D cell movement and arrangement in the intestinal crypt. Like the vertex model, but in contrast to the Potts model, the Meineke model is off-lattice. Previous models of the 2D cell layer in the crypt were also lattice-based (Finney et al., 1989, Loeffler et al., 1986, Paulus et al., 1993). In the Meineke model, the centre of each cell is connected to each of its nearest neighbours by a spring. Forces are induced whenever a spring is longer or shorter than a given rest length, and the sum of forces on a cell centre leads to cell movement. A Voronoi tessellation is performed to approximate the actual shape of each cell. Cell division can be included in this model by creating a new cell with its centre initially very close to the parent. The rest length of the spring connecting the two daughter cells grows over time from an initial small value (0.1 of the rest length between mature cells), ensuring that the cells do not immediately jump apart. Meineke et al. (2001) found that, by assuming stem cells divide rapidly at the base of the crypt, their model could accurately recreate the dynamic cell behaviour higher up the crypt. Experiments by Kaur and Potten (1986), however, showed that mitotic pressure is unlikely to be the only driving force behind cell migration in the crypt, implying a role for active migration.

Two further cell-based models are worthy of mention here; over-lapping sphere models, such as that of Drasdo and Höhme (2005) and the sub-cellular element model (SCEM) of Newman (2005). In the SCEM, intra- and inter- cellular interactions between the elements are encoded into phenomenological potentials, which determine the equations of motion for each element. The use of sub-cellular elements allows complex cell shapes to emerge naturally from cellular interactions, rather than from complicated geometrical constructions.

Epithelia are ubiquitous in adult animal bodies, lining everything from the mouth and the insides of the lungs to the cornea. They also make up the exocrine and endocrine glands. In Section 1.3 we will give examples of two epithelial tissues with key roles in development. These are the mouse VE and the *Drosophila* wing imaginal disc. We

will explain why the vertex model is an ideal framework to simulate these systems, and the kinds of questions we can ask about them.

1.3 Epithelia in developmental systems

1.3.1 Mouse VE

The mouse embryo implants in the uterine lining approximately 4.5 days after fertilization (embryonic day 4.5 or E4.5) (Srinivas, 2006). At this stage, the blastocyst possesses an inner cell mass (ICM) and a fluid-filled cavity, surrounded by an outer layer of cells known as the trophectoderm. The ICM differentiates into two tissues, the epiblast, which gives rise to the foetus and extra-embryonic mesoderm, and the primitive endoderm, which gives rise to the epithelial VE and the parietal endoderm (Srinivas, 2006).

Rapid proliferation of the trophectoderm leads to the formation of the extra-embryonic ectoderm (ExE) and the ectoplacental cone (Tanaka et al., 1998), pushing the epiblast into the fluid-filled cavity. By E5.5, the epiblast and ExE together form an arrangement of tissues known as the 'egg-cylinder', with the VE overlying both tissues. Although this arrangement is peculiar to rodents, the topological relationship between component tissues and gene expression patterns are similar to other species (Srinivas, 2006).

Around E5.5, a subset of VE cells differentiate into the anterior visceral endoderm (AVE). The AVE migrates from the distal tip of the embryo to the future anterior, defined as the region of the embryo that gives rise to the rostral neural tissue (Fig. 1.5). By this process, the AVE imparts information concerning the anterior-posterior axis. In mutant embryos in which migration fails to occur, the embryo is patterned incorrectly (Ding et al., 1998, Kimura et al., 2000).

Recent experiments have revealed the presence of multi-cellular rosettes during

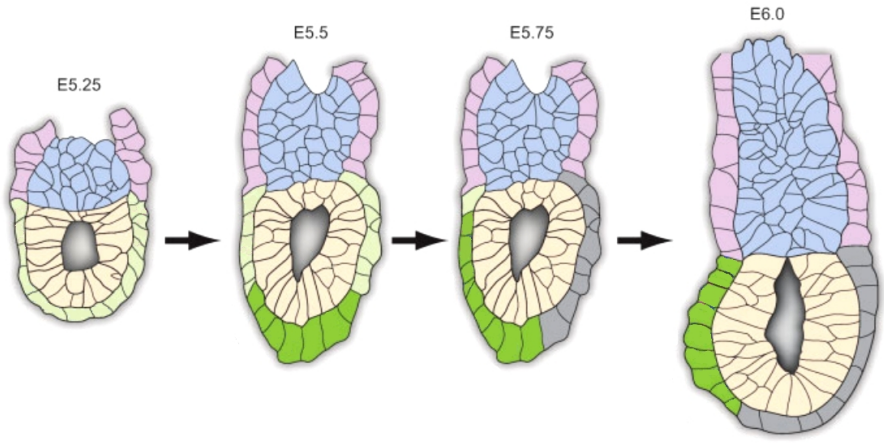


Figure 1.5: *Overview of AVE induction and migration. The 'egg-cylinder' stage embryo consists of three tissues, the epiblast in the distal region (bottom section), the ExE in the proximal region (top section) and the VE, a simple epithelium surrounding both tissues. The AVE is induced around E5.5, when a subset of cells (dark green) at the distal tip of the embryo differentiate and migrate to the future anterior at the boundary between the epiblast and the ExE. Reprinted with permission from Srinivas (2006).*

AVE migration (Trichas et al., 2012). These occur when five or more cells meet at a common vertex. This deviates from standard packing of epithelia, with primarily hexagonal cells meeting at junctions of three vertices (Gibson et al., 2006).

The vertex model is ideal for simulating AVE migration. The VE remains a continuous sheet of cells, without gaps, throughout the process. The AVE migrates via junctional rearrangements, including T1 transitions and rosette formation. The vertex model represents the tissue as a 2D network of junctions between cells and, unlike the other models detailed in Section 1.2, permits the explicit modelling of junctional rearrangements.

AVE migration will be discussed in further detail in Chapters 5 and 6. We will implement the vertex model on the surface of an ellipsoid in order to represent a realistic geometry for the mouse embryo. We will include a migration force, a barrier to migration to represent the mechanism by which migration stops and rosette formation. By adjusting the number of rosettes that form in simulations, we will show that they are crucial facilitators of ordered migration.

1.3.2 *Drosophila* wing imaginal disc

The *Drosophila* wing imaginal disc is an epithelial tissue which grows from an embryonic primordium of about 55 cells, which each undergo an average of 9.1 divisions, giving a final tissue size of roughly 30,500 cells (Martín et al., 2009). The disc is patterned into various compartments, notably the anterior and posterior compartments, which act as separate developmental units, capable of autonomous regulation of growth (Martín and Morata, 2006). Cell division in the disc often occurs in small synchronized clusters (Milàn et al., 1996), though the amount of clustering has recently been disputed (Aegerter-Wilmsen et al., 2010). Growth is sigmoidal, with an average cell doubling time (CDT) of $\sim 10 - 12$ hours (Garcia-Bellido and Merriam, 1971). Martín et al. (2009) have recently shown that the CDT varies dramatically during development, from $5.5 - 5.7$ hours initially, up to 30 hours at the last division. The majority of divisions therefore take place towards the start of disc development. The adult wing is produced by eversion (turning inside-out) of the wing disc, with size and shape predetermined by the patterns of cell growth, division and a small amount of programmed cell death, or apoptosis, in the disc.

The *Drosophila* wing imaginal disc has often been used as a model system in which to study the problem of size determination. Tissue size in many developmental systems has been shown to be largely independent of total cell number (Conlon and Raff, 1999). In the *Drosophila* epidermis, experiments where rates of cell proliferation and cell death are perturbed show that when the number of cells is much larger or smaller than normal, cell size compensates to leave a tissue of similar dimensions (Parker, 2006). This implies that tissue dimensions are regulated directly, rather than through cell number.

Tissue size depends on regulators acting at both the tissue level and organism level, as well as environmental factors such as climate and availability of nutrients. Chemical signalling molecules that regulate cell growth and proliferation locally (tissue-

level) are growth factors, whereas those that regulate systemically (organism-level) are growth hormones. Tissue-level size control mechanisms are the most important in the majority of organs (Bryant and Simpson, 1984). Morphogenetic growth factors, such as Decapentaplegic (Dpp) in the *Drosophila* wing disc, form gradients in many developmental systems in order to coordinate tissue patterning and stimulate growth. In many such systems, however, growth is uniform despite the presence of a morphogen gradient.

Several models of size control exist to explain the mechanisms by which growth factors control tissue growth, and most of these studies focus on the *Drosophila* wing disc. One of the simplest was proposed by Day and Lawrence (2000), which states that cells monitor the local steepness of the gradient, and grow when it is sufficiently large. Although this attractively explains why growth comes to a stop as the tissue grows and the gradient stretches, it fails to explain the observed growth at the source of the morphogen and in tissues in which the growth-factor is over-expressed. A modified version of this theory was proposed by Rogulja and Irvine (2005). Their idea was that for some cells growth depends on the slope of the gradient, whereas for others it depends on the slope and the absolute value of signalling. This model suffers from the same flaws as its predecessor.

Another type of model was proposed by Serrano and O'Farrell (1997), who predicted a parallel inhibitory gradient, balancing the growth-factor gradient and producing net uniform growth and proliferation. Under this model a uniform gradient should lead to homogeneous growth, however this is not observed for Dpp in the wing disc (Affolter and Basler, 2007, Rogulja and Irvine, 2005). More recent models include feedback between growth-factor gradients and mechanical properties of the tissue such as stress (Aegerter-Wilmsen et al., 2007, Hufnagel et al., 2007, Shraiman, 2005). These models will be discussed in more detail in Chapter 3.

Vertex models are an ideal computational tool for testing hypotheses concerning

the *Drosophila* wing disc. They have been used by several authors (Aegerter-Wilmsen et al., 2010, Hufnagel et al., 2007, Landsberg et al., 2009) to provide insights into the regulation of growth in the wing disc. The disc is a tightly packed mono-layer of cells, without gaps between neighbours. Contacts between neighbouring cells can change via T1 transitions and apoptosis, both of which can be modelled naturally in the vertex framework. Recent studies have begun to incorporate a model of growth factors into the vertex model (Schilling et al., 2011, Wartlick et al., 2011). In Chapter 3 we will show how the vertex model provides a natural mesh for the finite-element (FE) method (FEM), allowing us to solve the diffusion equation across the domain for morphogen concentration.

In this section we have seen that the mouse VE and *Drosophila* wing disc are epithelia with important roles in development that can be modelled using the vertex framework. The broad remit of this thesis is to develop and extend vertex-based approaches to modelling epithelial tissues, with a particular focus on the problems of size determination in *Drosophila* and AVE migration in the mouse embryo. In Section 1.4 we outline the structure of the rest of this thesis.

1.4 Thesis outline

We begin in Chapter 2 by introducing our formulation of the vertex model. Based on previous frameworks such as those of Weliky and Oster (1990) and Farhadifar et al. (2007), we will explain how and why our model differs from its predecessors. We will detail how initial configurations are created and the force laws underlying the model, as well as the equations of motion and junctional rearrangements. We will also include cell growth, proliferation and death. The model will then be comprehensively tested computationally. We will show that our numerical approximation to the solution of the equations of motion converges towards a more accurate solution as the time-step

tends to zero. Simulations will be run showing the evolution of a tissue under various conditions, demonstrating the validity of the numerical implementation. To complete the chapter we will demonstrate the effects of cell proliferation and cell death on a growing tissue.

In Chapter 3 we will incorporate a description of morphogen concentration into the vertex framework. The method will account for the movement of the domain as the tissue evolves as well as key cellular processes such as junctional rearrangements, proliferation and death. The method has applications in biological systems in which a chemical spreading across an epithelium controls mechanical properties of a cell. We use an arbitrary Lagrangian-Eulerian (ALE) reference frame to derive a weak form of the governing diffusion equation. We then implement the FEM, using the vertex model to create a suitable FE mesh. We will show that our FE approximation converges towards a more accurate solution as space- and time-steps decrease, and prove that simulation time scales well with tissue size. As the FE mesh is based on vertex positions, when cellular rearrangements occur the FE mesh changes. We will demonstrate how this can be dealt with in our framework, and run simulations of chemical-dependent growth.

Chapter 4 will examine how chemical production and ingestion can be included in the morphogen model. *In vivo*, growth factors are produced by chemical reactions within cells. We will show how each cell can be assigned a production rate that feeds into the concentration diffusing through the domain. We will also allow cells to ingest the diffusing chemical, thus building up an internal concentration that can affect mechanical properties of the cell. The internal chemical will not be able to diffuse between cells, and a separate equation for internal chemical concentration will therefore be solved. We will round off this chapter with simulations of the *Drosophila* epidermis, showing how our vertex framework of cellular mechanical properties in conjunction with the morphogen model can be used to model a real biological system.

In Chapter 5 we will look in more detail at the biology behind AVE migration, before describing some preliminary extensions to the 2D model such as periodic boundary conditions. Crucially, we will allow vertices to join together, permitting the formation of rosettes. We will motivate the need for a more realistic ellipsoid-based model, and describe how initial configurations are created, how force directions are calculated, and how vertices are mapped back to the ellipsoid surface after each iteration of the approximation to the solution of the equations of motion. We again verify the numerical implementation by running simulations of individual force terms, and finally show how a barrier to migration can be implemented.

In Chapter 6 we will use the model developed in Chapter 5 to run simulations of AVE migration. We will begin by simulating migration of a single cell, testing different methods of applying a migration force. We will then move on to discuss migration of multiple cells. We will introduce biological data from our experimental collaborators, and use it to validate our simulations. We will run two types of simulations, those in which rosettes form and those in which they do not. A single parameter change will effect these two cases. Using a combination of simulation and experimental results, we will demonstrate that rosettes are crucial facilitators of ordered AVE migration.

In Chapter 7 we conclude this work with a short discussion. We review the techniques developed in the thesis and summarise the key results. We consider possible extensions to the work presented and future directions that might be taken.

Chapter 2

Two-dimensional model

In the previous chapter we saw that simple epithelia are mono-layers of cells that line various internal and external surfaces of the body and play crucial roles in developmental biology. We reviewed the strengths and weaknesses of various types of cell-based model, and saw examples of their application.

In this chapter we will describe the 2D vertex model that has been developed in order to study some of the systems detailed in the first chapter. Beginning with how initial configurations are created (Section 2.1), we will go on to describe how we include force laws (Section 2.2), equations of motion (Section 2.3) and junctional rearrangements (Section 2.4) underlying the model, plus descriptions of cell growth, proliferation (Section 2.5) and death (Section 2.6). Along the way we will explain how and why this model differs from previous vertex formulations. We will summarise the model equations in Section 2.7, before discussing numerical solutions to the equations of motion in Section 2.8.

We will then display the results of simulations, and show the evolution of a tissue over time under various conditions. In Sections 2.9 and 2.10, we will see a tissue relaxing to mechanical equilibrium under the force laws, demonstrating the validity of our numerical implementation. Section 2.11 will show a growing tissue, while cell

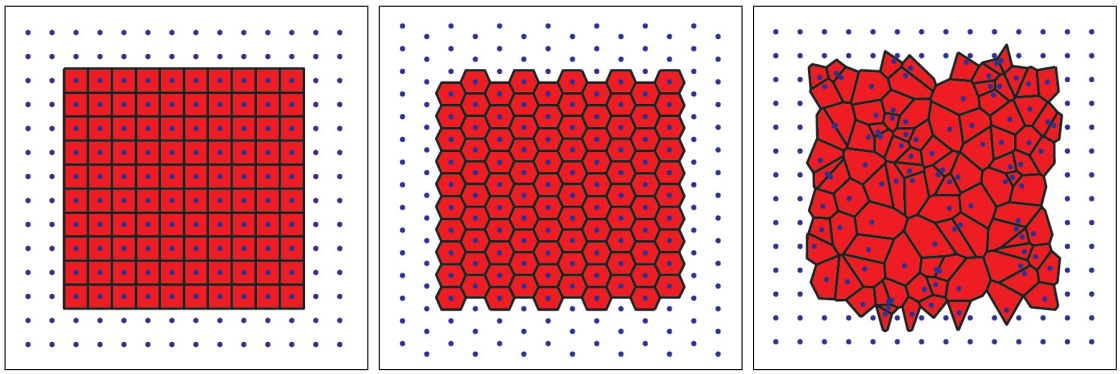
proliferation will be introduced into simulations in Section 2.12. Finally, we will see the effect of cell death in Section 2.13.

2.1 Initial configurations

In order to implement a vertex-based model, we first require the tessellation of a 2D domain into non-overlapping polygonal cells. Honda (1978) showed that cellular patterns are well described by Dirichlet domains, also known as Voronoi cells, which cover a plane without leaving any gaps. For a set of points, P, the Voronoi cell associated with a given point, $p \in P$, is the open domain, Ω_p, such that for any point, $x \in \Omega_p$, $|x - p| = \min|x - P_i|$ for all i. In other words, all points within the Voronoi cell are closer to the point p than to any other point in P.

We choose points such that the initial width of the tissue is approximately unity. In this thesis all variables are dimensionless, and quoted in arbitrary units (a.u.) throughout, unless stated otherwise. Thus, assuming a roughly square configuration, the initial average area of each cell is given by $\sim 1/N_c$, where N_c is the total number of cells, and the initial average cell width is $\sim 1/\sqrt{N_c}$. Points can be spaced regularly throughout the domain, creating regular polygons such as squares (Fig. 2.1(a)) and hexagons (Fig. 2.1(b)), or completely at random (Fig. 2.1(c)). In all three cases layers of 'ghost' Voronoi points are placed around the domain. Once the initial configuration has been created, these ghost points disappear and play no further part in simulations. The outermost cells in a Voronoi tessellation contain all points on the domain to infinity, hence the ghost points are necessary to ensure that all cells have finite size.

The type of tessellation used to create an initial configuration will depend on the system in question. Often, a biologically realistic configuration will be more regular than the completely random configuration of Fig. 2.1(c), but less regular



(a) (b) (c)

Figure 2.1: *Regular tessellations of a unit domain using Voronoi cells (red). The Voronoi points are indicated by blue dots. (a) Square tessellation, (b) hexagonal tessellation and (c) random tessellation.*

than the perfect hexagonal tessellation of Fig. 2.1(b). This kind of configuration can be obtained by adding a small amount of random noise to each Voronoi point in a hexagonal tessellation. Fig. 2.2 shows a tessellation of this kind.

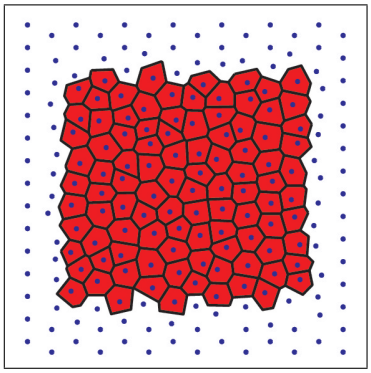


Figure 2.2: *Random tessellation, based on hexagonal packing, with noise added to obtain less regular configuration.*

In Section 2.2 we will detail the force laws that act on vertices in the model. We will explain the meaning and biological justification for each term. Previous vertex models have formulated equations of motion in terms of either forces or energy. The earlier models of Weliky and Oster (1990) and Weliky et al. (1991) used force considerations, whereas more recent works, since that of Nagai and Honda (2001), have tended to use energy formulations. The two representations are equivalent and equally valid,

however, it makes sense conceptually to think in terms of minimizing energy when a system is relaxing towards mechanical equilibrium, whereas in dynamic regimes far from equilibrium a formulation based on force considerations is more appropriate. Here we choose a force-based description, as the systems we will be examining involve highly dynamic processes far from equilibrium.

2.2 Force laws

In the vertex model, the shape, size, and movement of cells emerge from the application of forces to polygon vertices (Nagai and Honda, 2001, Weliky and Oster, 1990). Typically, forces represent cell-cell adhesion, actin-myosin contractility, elasticity, pressure, and protrusion. These depend on basic properties of the cell such as perimeter, height, area and edge lengths. The model is quasi-2D, in the sense that we assume that the apical surfaces of cells form a 2D mono-layer. However, each cell is assigned a volume and height and can be represented in three dimensions (3D) (Fig. 2.3).

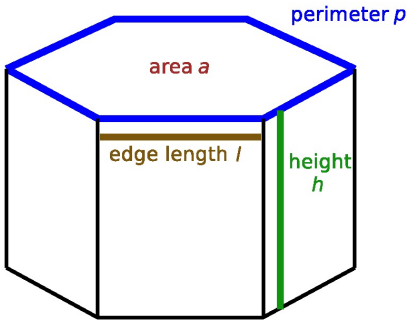


Figure 2.3: *Three-dimensional schematic of an epithelial cell, showing four key quantities used in the model; perimeter, p, area, a, height, h, and edge length, l. Reprinted with permission from Smith et al. (2011).*

The model described here consists of two types of forces, which act in the directions shown earlier in Fig. 1.2.

2.2.1 Tension forces

In our model, stress on each cell edge manifests as a tension force on the vertices at the ends of the edge. The first component of this force is a line tension, dependent on the length of the edge, which represents effects of cell-cell adhesion and actin-myosin contractility. Previous vertex models, including those of Farhadifar et al. (2007) and Rauzi et al. (2008), have included these effects. Stronger adhesion or reduced contractility leads to reduced stress on the edge, and thus lower tension and larger edge lengths. The second component, meanwhile, depends on the cell perimeter and represents contractility of the actin-myosin ring.

Within a given cell, each vertex belongs to two edges and experiences forces in the direction of the two tension unit vectors shown in Fig. 1.2. The contribution from a cell to the tension on a vertex is given by

$$\mathbf{T} = C_L \left(l_c \hat{\mathbf{T}}_c + l_a \hat{\mathbf{T}}_a \right) + C_P \left(\hat{\mathbf{T}}_c + \hat{\mathbf{T}}_a \right) p, \tag{2.1}$$

where C_L and C_P are constants related to the line tension and perimeter force, respectively, l_c and l_a are the lengths of the clockwise and anti-clockwise edges, $\hat{\mathbf{T}}_c$ and $\hat{\mathbf{T}}_a$ are unit vectors in the direction of the clockwise and anti-clockwise vertices (see Fig. 1.2) and p is the length of cell perimeter (see Fig. 2.3). The tension force acts to decrease the length of edges and perimeters. Larger edge lengths and perimeters generate larger tension forces, which act to move neighbouring vertices closer to each other, thus shrinking local edge lengths.

2.2.2 Pressure forces

The pressure force, meanwhile, is dependent on cell area, height-to-area ratio, and local deformation. It is given by

$$\mathbf{P} = \left[C_A \frac{|a_t - a|^{n_1+1}}{(a_t - a)} + C_H H + C_D \frac{|\phi - \theta|^{n_2+1}}{(\phi - \theta)} \right] \hat{\mathbf{P}}, \tag{2.2}$$

where C_A, C_H, and C_D are constants associated with the three components, a is the cell area, a_t is a 'target' area, H is the height-to-area ratio, θ is the target angle, equal to average internal angle of the cell ($\theta = \pi(s-2)/s$ for an s-sided polygon), ϕ is the internal angle at the current vertex (see Fig. 1.2), n_1 and n_2 are positive integer values and $\hat{\mathbf{P}}$ is the unit vector in the direction of the pressure force (see Fig. 1.2). The first and third terms are written in this way to ensure that the sign of the force is correct regardless of whether n_1 and n_2 are even or odd.

The first term represents the elasticity of the cell and C_A is the elastic coefficient. The second term represents the effect of a cell opposing being squashed and elongating in the direction normal to the surface. When this occurs, the height-to-area ratio, H, increases, leading to an increase in pressure that acts to increase the cell area, thus reducing H. Each cell is assigned a volume, $v_k(t)$, which is a function of time (see Section 2.5). Knowing the volume and area of every cell, heights can then be calculated.

The third term in (2.2) represents the reaction of the internal components of the cell, such as the cytoskeleton, to being subjected to a large external force. Unlike the first two terms, this type of force has not been included in previous vertex model formulations. In the processes in which we are interested, such as AVE migration in the mouse embryo, concave cells arise occasionally *in vivo* when they are subjected to significant forces, but cells will not stay in this configuration for very long. We therefore include a force in the model designed to keep cell shapes close to regular.

In systems where cells are naturally elongated, the target angle, θ, can be altered accordingly.

2.2.3 Boundary forces

An extra force is implemented to ensure integrity of the tissue is maintained and edges of non-adjacent cells are unable to overlap on the boundary. Previous studies have dealt with the tissue boundary in one of two ways. The first of these is to use periodic boundary conditions, which simplify the problem and require no further consideration of boundary effects (Farhadifar et al., 2007, Hufnagel et al., 2007, Rauzi et al., 2008). However, this method requires growth of the tissue to be imposed on the system, rather than it emerging as a property of cellular growth. We choose to implement a more realistic free boundary on the tissue, similar to that used in Canela-Xandri et al. (2011). They adapt the energy formulation of the vertex model to include an external line tension that ensures the tissue stays sufficiently compact and round.

The boundary force in our formulation only applies to vertices on the boundary, which can be identified by the fact that they belong to a maximum of two cells, and takes the form

$$\mathbf{B} = C_{B1}\frac{|\phi_B - \theta_B|^{n_3+1}}{(\phi_B - \theta_B)}\hat{\mathbf{P}}_B + C_{B2}\left(\frac{|l_{Bc} - L|^{n_4+1}}{(l_{Bc} - L)}\hat{\mathbf{T}}_{Bc} + \frac{|l_{Ba} - L|^{n_4+1}}{(l_{Ba} - L)}\hat{\mathbf{T}}_{Ba}\right), \quad (2.3)$$

where C_{B1} and C_{B2} are the boundary force constants, ϕ_B is the internal angle at the boundary vertex, θ_B is the average internal angle, given by $\theta_B = \pi(N_B - 2)/N_B$ for N_B boundary nodes, $\hat{\mathbf{P}}_B$, $\hat{\mathbf{T}}_{Bc}$ and $\hat{\mathbf{T}}_{Ba}$ are unit vectors in the direction of the pressure- and tension-like forces, l_{Bc} and l_{Ba} are the lengths of the clockwise and anti-clockwise edges, respectively, L is the mean edge length, and n_3 and n_4 are positive integers.

This force tends to make the boundary smooth and circular, and keep boundary edges from shrinking. Junctional rearrangements (Section 2.4) are unable to occur on

the boundary, so it is important that edges do not become very small, hence there is a difference between the edge-dependent force here and that in the tension equation (2.1). The angle-dependent force is similar to that in the pressure-force equation (2.2), which keeps cells as close to regular as possible.

In Section 2.3 we will show how the force laws we have just described are translated into equations of motion, by considering Newton's second law and making the assumption that inertial terms are negligible.

2.3 Equations of motion

According to Newton's laws, total force equals mass times acceleration, i.e.

$$\mathbf{F} - \mu \frac{\mathrm{d}\mathbf{x}}{\mathrm{d}t} = m \frac{\mathrm{d}^2\mathbf{x}}{\mathrm{d}t^2}, \tag{2.4}$$

where $\mathbf{F}(\mathbf{x}, t)$ is a vector of the sum of the forces, described in Section 2.2, acting on the vertices, t is time, $\mathbf{x}(t)$ is the position vector of the vertices, μ is the viscous coefficient, and m is mass. The initial conditions are denoted $\mathbf{x}(0) = \mathbf{x}^0$ and $\mathbf{v}(0) = \mathbf{v}^0$, where $\mathbf{v} = \mathrm{d}\mathbf{x}/\mathrm{d}t$.

Odell et al. (1981) have shown that in the blastula, a spherical layer of cells that forms during the early stages of embryo development, the ratio of the magnitude of the acceleration term to the viscous term is less than 10^{-5}, and thus the Reynolds number Re $<<$ 1. They conclude that for nearly all embryological processes, inertial forces may be neglected. Equation (2.4) can therefore be re-written

$$\mathbf{F} \approx \mu \frac{\mathrm{d}\mathbf{x}}{\mathrm{d}t}. \tag{2.5}$$

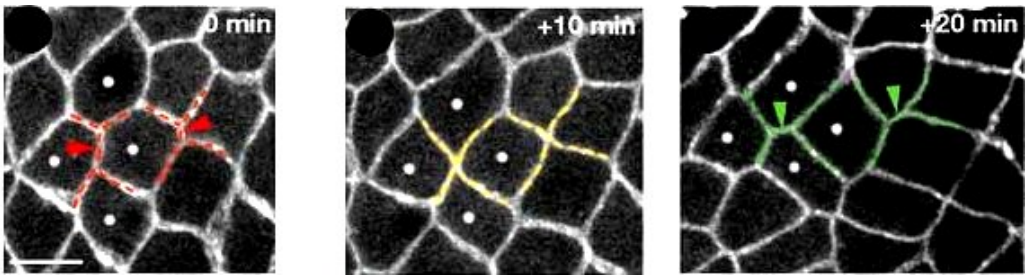
The lack of an inertial term in (2.5) implies that the dynamics at a given moment are completely described by the forces acting at that moment, and are independent of past forces. This is a characteristic property of life at low Reynolds number (Purcell, 1977), and this assumption has been made in previous vertex models (Weliky and Oster, 1990).

An analytic solution to the nonlinear system of equations (2.5) is not generally possible, so a numerical approximation is instead found. Numerical solutions to (2.5) will be discussed in Section 2.8. Meanwhile, in Section 2.4 we will introduce a common type of junctional rearrangement called a T1 transition, which occurs in many developmental systems including the *Drosophila* wing disc and the visceral endoderm of the mouse embryo.

2.4 Junctional rearrangements

In addition to the force laws described above, an elementary rearrangement of vertices known as a T1 transition is included in the model. Junctional rearrangements occur between neighbouring vertices that fall below a certain threshold distance, expressed as a fraction T_{T1} of the mean edge length. This type of transition has been used by other authors in previous vertex models (Farhadifar et al., 2007, Weliky and Oster, 1990).

A diagrammatic representation of a T1 transition was shown earlier in Fig. 1.3. In this figure, vertices A and B have moved closer together than the threshold distance, and rearrangement begins (Fig. 1.3(a)). Vertices C and D are created on a line that bisects the line AB perpendicularly. Cell 1 then reconnects to vertex C, cell 2 to vertex D, and cells 3 and 4 share both vertices C and D (Fig. 1.3(b)). Fig. 2.4, taken from Bertet et al. (2004), shows two T1 transitions occurring during elongation of the *Drosophila* germ-band.



(a) (b) (c)

Figure 2.4: *T1 transitions in the Drosophila germ-band. Cell contacts switch from the red dashed lines in (a), through the yellow lines in (b), to the green lines in (c). Reprinted with permission from Macmillan Publishers Ltd: Letters to Nature (Bertet et al., 2004).*

T1 transitions allow the system to escape from local energy minima, and prevent cells overlapping each other. They allow cell intercalation, and thus facilitate large scale tissue rearrangements, such as elongation of the *Drosophila* germ-band (Rauzi et al., 2008). If vertex A were to pass vertex B in Fig. 1.3(a), cell 3 would essentially be lying on top of cell 4. The rearrangement ensures that the tissue remains a monolayer, in line with the systems we are modelling.

This type of rearrangement cannot occur on boundary edges, which belong to only one cell. They can occur next to the boundary, and can lead to the creation of a new boundary edge. For example, if cell 3 in Fig. 1.3(a) did not exist, the transition could go ahead as shown and the new edge CD in Fig. 1.3(b) would now be a boundary edge, on which no further transitions could then occur. This highlights the need for a boundary line force in equation (2.3); to ensure that this edge does not become very short.

An important additional point to note is that T1 transitions cannot occur on 3-sided cells, as the resultant 'cell' would be a straight line. Triangular cells can instead undergo cell death (Section 2.6), where all three edges disappear and the triangle shrinks to a single point.

So far we have seen how cells can relax to a mechanical equilibrium, and how T1 transitions can prevent the system being trapped in local energy minima. In Section

2.5 we will look at a process that pushes the system away from equilibrium; cell growth. As a cell grows, its perimeter, area and volume are constantly changing, preventing forces from finding a natural balance. The tissue is further disrupted by proliferation events, which can have dramatic effects on the local surrounding tissue. Many systems of interest involve large amounts of growth. As we saw in Chapter 1, the *Drosophila* wing disc grows over several orders of magnitude during the larval stages of development. It is therefore crucial to include growth and division in the model.

2.5 Growth and proliferation

When we first introduced cell volume, $v_k(t)$, in Section 2.2, we saw that it is a time-dependent function. We can thus define a rate of change of volume, and, given an initial value $v_k(0) = v_k^0$, solve the resulting differential equation to find the volume at any time-point. To accommodate a simple method allowing cells to grow and subsequently divide, each cell k can be given a growth speed, g_k. Growth is then implemented logistically over time according to

$$\frac{\mathrm{d}v_k}{\mathrm{d}t} = g_k v_k \left(1 - \frac{v_k}{V_k}\right), \tag{2.6}$$

where v_k is the volume of cell k and V_k is the target volume, which is constant in time. Equation (2.6) implies that when $v_k \ll V_k$, we have $dv_k/dt \approx g_k v_k$. Solving and applying the initial condition yields $v_k \approx v_k^0 e^{g_k t}$. In other words, growth is exponential, with rate constant g_k. As $v_k \to V_k$, $dv_k/dt \to 0$, so the volume of the cell approaches its target volume at a decreasing rate. Equation (2.6) can be solved analytically, yielding

$$v_k = \frac{v_k^0 V_k}{v_k^0 + (V_k - v_k^0)e^{-g_k t}}. \tag{2.7}$$

It will be important to consider the time-scale of growth, relative to that of mechanical rearrangements. If a cell grows very fast, it will push the system far away from equilibrium. Slow growth, meanwhile, will mean that the system remains in a quasi-steady state, ensuring that cell shapes do not become highly irregular. Accurate biological data on the relative times is often unavailable, though recent studies have begun to probe the time-scales of mechanical rearrangements using laser ablation experiments (Landsberg et al., 2009).

Both *in vivo* and in our model, the likelihood of a cell dividing correlates with cell size. We will discuss possible ways to link the two processes in Section 2.11. To implement cell division, firstly an angle of proliferation is chosen. This can simply be drawn from a uniform distribution, or biased in a certain direction, if desired, to investigate directed proliferation. A straight line is then drawn, passing through the centroid of the cell at the prescribed angle. Two new vertices are created at the points where the line intercepts cell edges. Fig. 2.5 demonstrates this process.

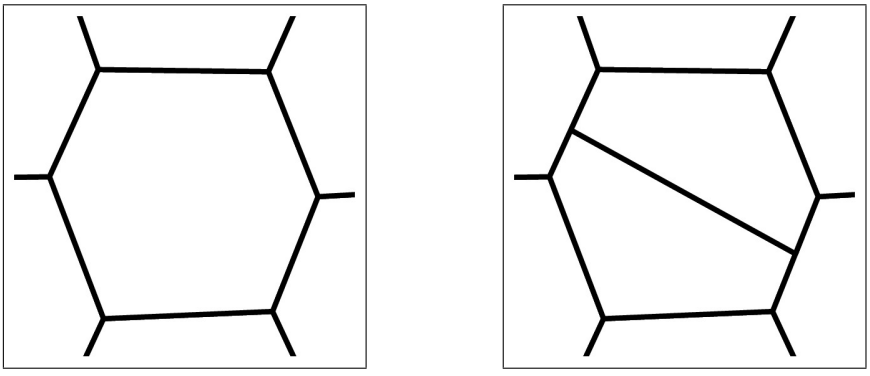


Figure 2.5: *Cell division in the vertex model. (a) The initial cell, which has been chosen to divide. (b) A straight line is added, passing through the cell centroid at an angle drawn from a uniform distribution. Two new vertices are formed where the line meets cell edges.*

The volume of the dividing cell is split between the daughter cells, in the same ratio as their areas. As a result, the heights of the daughter cells are equal after division. Upon division, a cell's target area is set to increase linearly from its current area to the overall target area, a_t, over a certain time period. This ensures that there

is no sudden spike in the area force term (2.2).

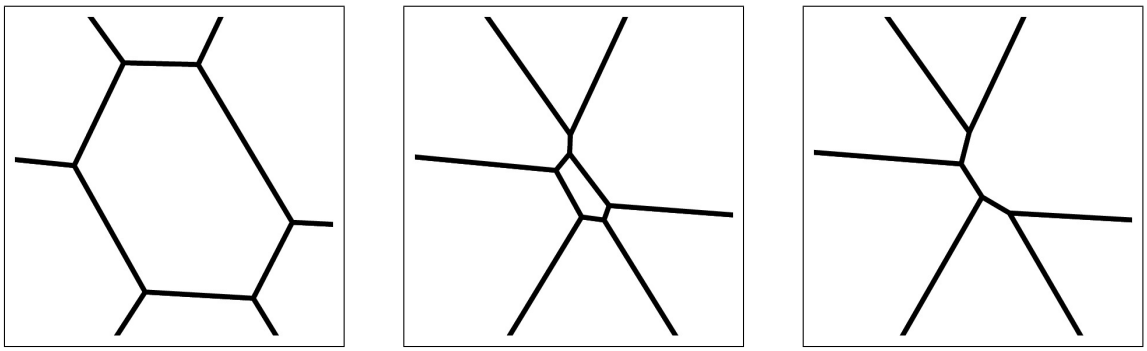
As well as growth and proliferation, cell death is a crucial process in many developmental systems. For example, in posterior compartments of the *Drosophila* epidermis, about half the excess cells produced by over-expressing the gene cyclin E die due to apoptosis (Parker, 2006). In Section 2.6, we explain how apoptosis is incorporated into the model.

2.6 Cell death

Each cell in our vertex model is assigned a state variable, which represents whether the cell is normal or dying. When a normal cell becomes apoptotic, its state variable changes and subsequently the forces acting on it change. The internal pressure forces gradually vanish as the cell loses its elasticity, and the tension forces increase, causing the cell to constrict, its area to shrink and edge lengths to shorten. As the cell becomes very small, T1 transitions occur on the edges, and soon the cell consists of only three vertices. At this point, T1 transitions can no longer occur and instead the cell contracts to a single point when its area falls below a certain threshold. The three neighbouring cells then all share a new vertex which is created at the centre of the dying cell. Fig. 2.6 shows the death of a cell.

We noted in Section 2.4 that T1 transitions cannot occur on certain boundary edges. For this reason cells on the boundary cannot die in the same way as other cells. We therefore do not allow boundary cells to become apoptotic, and the consequences of this will be discussed later (Section 2.13).

In this chapter thus far we have introduced a number of equations governing the vertex model. In Section 2.7 we briefly reproduce them for the benefit of the reader.



(a) (b) (c)

Figure 2.6: *Cell death. (a) The dying cell shrinks as its pressure forces vanish and tension increases. (b) T1 transitions occur and the number of cell edges reduces as the cell becomes very small. (c) The cell is killed off and reduced to a single vertex, with all neighbouring cells reconnected to this point.*

2.7 Summary of model equations

We began with three force equations, governing tension, pressure and boundary forces. They are given, respectively, by

$$\begin{aligned}
\mathbf{T} &= C_L\left(l_c\hat{\mathbf{T}}_c + l_a\hat{\mathbf{T}}_a\right) + C_P\left(\hat{\mathbf{T}}_c + \hat{\mathbf{T}}_a\right)p,\\
\mathbf{P} &= \left[C_A\frac{|a_t - a|^{n_1+1}}{(a_t - a)} + C_H H + C_D\frac{|\phi - \theta|^{n_2+1}}{(\phi - \theta)}\right]\hat{\mathbf{P}},\\
\mathbf{B} &= C_{B1}\frac{|\phi_B - \theta_B|^{n_3+1}}{(\phi_B - \theta_B)}\hat{\mathbf{P}}_B + C_{B2}\left(\frac{|l_{Bc} - L|^{n_4+1}}{(l_{Bc} - L)}\hat{\mathbf{T}}_{Bc} + \frac{|l_{Ba} - L|^{n_4+1}}{(l_{Ba} - L)}\hat{\mathbf{T}}_{Ba}\right).
\end{aligned}$$

The equations of motion are then given by

$$\mathbf{F} = \mu\frac{\mathrm{d}\mathbf{x}}{\mathrm{d}t},$$

with initial conditions $\mathbf{x}(0) = \mathbf{x}^0$, where $\mathbf{F} = \mathbf{T} + \mathbf{P} + \mathbf{B}$. Initial configurations were discussed in Section 2.1. Cell growth, meanwhile, is governed by

$$\frac{\mathrm{d}v_k}{\mathrm{d}t} = g_k v_k\left(1 - \frac{v_k}{V_k}\right),$$

which can be solved given appropriate initial conditions. We have also introduced T1 transitions (Section 2.4), cell proliferation (Section 2.5) and cell death (Section 2.6).

We have now covered most of the cellular and junctional processes that will be needed in the vertex model. In Section 2.8, we will examine different ways to solve the system of equations of motion (2.5). By the end of this section we will be able to run simple test simulations, beginning from the initial configurations described in Section 2.1 and evolving according to the force laws in Section 2.2. We will begin to observe the behaviour of tissues over time, and show that the method we use converges towards an accurate numerical solution.

2.8 Numerical solutions

2.8.1 Explicit numerical methods

Consider the system of equations of motion (2.5). Taking the Taylor expansion of $\mathbf{x}$, the position vector of vertex positions, around an arbitrary point, t', we obtain

$$\begin{aligned}\mathbf{x}(t'+\Delta t) &= \mathbf{x}(t') + \Delta t \left.\frac{\mathrm{d}\mathbf{x}}{\mathrm{d}t}\right|_{t'} + ..., \\ &\approx \mathbf{x}(t') + \Delta t\, \mathbf{f}(\mathbf{x}, t'),\end{aligned} \tag{2.8}$$

where $\mathbf{f}(\mathbf{x}, t) = \mathrm{d}\mathbf{x}/\mathrm{d}t = \mathbf{F}(\mathbf{x}, t)/\mu$. We define a discretisation in time over the range $(0, T]$, given by $\cup_{n=1}^{n=N_T}(t^{n-1}, t^n]$, where T is the final time, N_T is the number of time-intervals, and $t^n - t^{n-1} = \Delta t$ for all n. The total number of time-points, including t^0, is $N_T + 1$. The system can be solved iteratively, based on (2.8), as follows:

$$\mathbf{x}^{n+1} = \mathbf{x}^n + \Delta t\, \mathbf{f}^n, \tag{2.9}$$

where the superscript represents the time-point (e.g. $\mathbf{x}^n = \mathbf{x}(t^n)$). This is the forward Euler method. It is a first-order numerical method for solving ordinary differential equations (ODEs), with errors of order Δt as $\Delta t \to 0$ (Ascher and Petzold, 1998). It is also a fully explicit method, as the solution at t^{n+1} is defined purely in terms of values obtained at t^n.

More accurate explicit methods include the higher-order Adams-Bashforth methods, for example the second-order version (Hairer et al., 1993):

$$\mathbf{x}^{n+1} = \mathbf{x}^n + \frac{\Delta t}{2}(3\mathbf{f}^n - \mathbf{f}^{n-1}).$$

These methods suffer from the disadvantage of needing information from two previous time-steps, rather than just one in the case of the forward Euler method. There is therefore a problem finding an approximation at t^1, where only one previous time-point exists. This issue can be overcome by running a few steps of the forward Euler method, with smaller time-steps, to get started, then switching to a higher order Adams-Bashforth method.

Another group of ODE methods are Runge-Kutta (RK) methods. These take intermediate time-steps to obtain a higher-order method. They include the fourth-order version (Ascher and Petzold, 1998), given by

$$\begin{aligned}
a &= \Delta t\, \mathbf{f}(\mathbf{x}^n, t^n), \\
b &= \Delta t\, \mathbf{f}(\mathbf{x}^n + \frac{a}{2}, t^n + \frac{\Delta t}{2}), \\
c &= \Delta t\, \mathbf{f}(\mathbf{x}^n + \frac{b}{2}, t^n + \frac{\Delta t}{2}), \\
d &= \Delta t\, \mathbf{f}(\mathbf{x}^n + c, t^n + \Delta t), \\
\mathbf{x}^{n+1} &= \mathbf{x}^n + \frac{1}{6}(a + 2b + 2c + d).
\end{aligned}$$

This more accurate RK method, with errors of order $(\Delta t)^4$, can be used in conjunction

with a small time-step to obtain a highly accurate solution for a system of cells relaxing to mechanical equilibrium. This then allows us to examine the convergence properties of the forward Euler scheme by calculating an error function between the forward Euler approximation and the more accurate RK approximation.

We create an initial configuration of 100 cells and allow the system to relax for $t \in [0, 1]$. In these simulations there is no cell growth, proliferation, nor death, and T1 transitions do not occur. Each cell is assigned an initial volume, v_0, which in this case does not change during the simulation as there is no cell growth. To assign cell volumes, we first determine a mean volume by taking *mean(cell area)*$^{3/2}$, then draw volumes from a normal distribution centred around this value. A minimum value of 20% of the mean volume is also implemented to ensure cells have a non-negative volume of reasonable magnitude.

For the accurate solution we take a Δt of 1/16,000 in the RK method. Other parameter values can be found in Table 2.1. The relative values of the force constants

Parameter	C_L	C_P	C_A	C_H	C_D	C_{B1}	C_{B2}	$n_1 - n_4$	μ
Value	0.1	0.05	2000	0.001	0.1	0.1	50	2	1

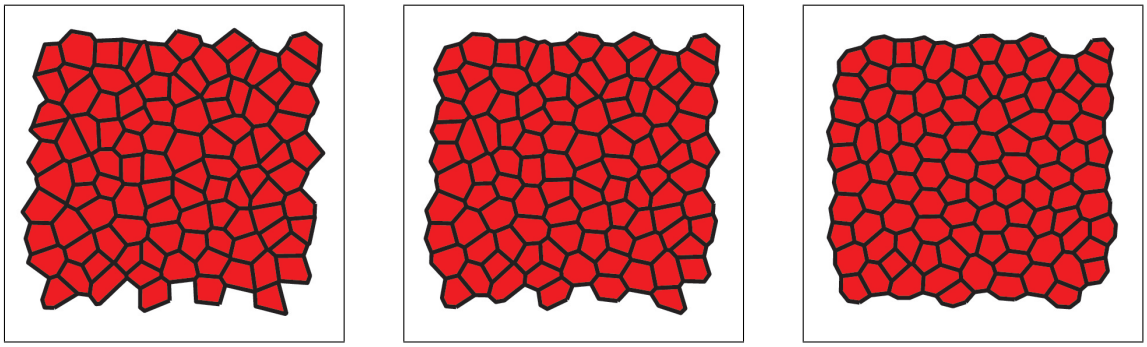
Table 2.1: *Parameter values used in simulation of cells relaxing to mechanical equilibrium, comparing the forward Euler method to a more accurate RK approximation.*

C_L, C_P, C_A, C_H and C_D are chosen such that each component has an approximately equal effect on each vertex. We saw in Section 2.1 that average cell area is roughly equal to $1/N_c$, where N_c is the number of cells. In this simulation the average cell area is therefore approximately 1/100. As the area force constant C_A is multiplied by area squared ($\sim 1/10,000$) in equation (2.2), this explains why its value is several orders of magnitude greater than the other constants. The constant C_H, meanwhile, is multiplied by height-to-area ratio, which has a mean around 10, and this constant thus takes a smaller value than the others. The boundary forces, with constants C_{B1} and C_{B2}, are chosen to have a stronger effect than the other forces on boundary vertices (see Section 2.10 for more details).

Time-step	Value of error function
1/500	$1.8\text{x}10^{-4}$
1/1000	$8.8\text{x}10^{-5}$
1/2000	$4.3\text{x}10^{-5}$
1/4000	$2.1\text{x}10^{-5}$

Table 2.2: *Value of the error function* (2.10) *for a system of 100 cells relaxing to equilibrium using the forward Euler method with* $\Delta t = 1/500,\ 1/1000,\ 1/2000$ *and* $1/4000$.

Fig. 2.7 shows the evolution of the tissue during this RK simulation. Further



(a) (b) (c)

Figure 2.7: *Simulation of 100 cells relaxing from a random initial configuration to mechanical equilibrium using a 4th-order RK method. Parameter values given in Table 2.1. (a)* $t = 0$*, (b)* $t = 0.1$*, (c)* $t = 1$.

simulations are run, beginning from the same initial configuration, using the forward Euler method with Δt values of 1/500, 1/1000, 1/2000, and 1/4000, respectively. The error function is defined to be

$$\epsilon = \text{mean}_i \left(||\mathbf{x}_i^{\text{E}} - \mathbf{x}_i^{\text{RK}}|| \right), \tag{2.10}$$

where $\mathbf{x}^{\text{E}}$ is the vector of vertex positions from the forward Euler approximation, $\mathbf{x}^{\text{RK}}$ is the vector of vertex positions from the RK solution, and $||\cdot||$ represents the Euclidean norm. In other words, we find the distance between each vertex and its 'true' position, and take the mean over all vertices to find the error ϵ. Table 2.2 shows the value of the error function for the various values of Δt. We observe that the forward Euler method converges with Δt as expected. As the time-step halves,

so approximately does the value of the error function.

In the simulations presented thus far, the time-step, Δt, was kept constant throughout each simulation. An alternative approach would be to allow Δt to vary, depending on the state of the simulation. In a near-equilibrium situation, with all cells close to their target area and no short edges in the system, the time-step could be large, allowing vertices to move a larger distance during each iteration. However, when there are small edges, or cells close to division or death, the time-step could be shortened to ensure that the dynamics of junctional rearrangements, proliferation, and apoptosis are captured. The adaptive time-step could be applied globally to the whole system, or could work on a specific region where an event of interest is likely to occur in the near future.

A potential problem with the explicit methods described thus far is that they can be numerically unstable for large values of Δt, resulting in the amplification of errors. In Section 2.8.2, we will discuss how the equations of motion (2.5) could be approximated using implicit methods, which are inherently more stable. At the end of the section we will compare explicit and implicit methods, and conclude that for our purposes, the forward Euler approximation is the optimal numerical scheme.

2.8.2 Implicit numerical methods

Implicit ODE methods use information about the derivative at t^{n+1} in order to compute the solution x^{n+1}. A fully-implicit version of (2.9), known as the backward Euler method (Ascher and Petzold, 1998), can be written

$$\mathbf{x}^{n+1} = \mathbf{x}^n + \Delta t \mathbf{f}^{n+1}. \tag{2.11}$$

As $\mathbf{x}^{n+1}$ is defined implicitly in (2.11), an iterative method such as Jacobi, Newton, or Gauss-Seidel must be used to find the solution (Ascher and Petzold, 1998). The

scheme can be set up as follows,

$$\begin{aligned}
\mathbf{x}_1^{n+1,k} &= \mathbf{x}_1^n + \Delta t\ f_1(t^{n+1}, \mathbf{x}_1^{n+1,k-1}, \mathbf{x}_2^{n+1,k-1}, \mathbf{x}_3^{n+1,k-1}, ...), \\
\mathbf{x}_2^{n+1,k} &= \mathbf{x}_2^n + \Delta t\ f_2(t^{n+1}, \mathbf{x}_1^{n+1,k}, \mathbf{x}_2^{n+1,k-1}, \mathbf{x}_3^{n+1,k-1}, ...), \\
\mathbf{x}_3^{n+1,k} &= \mathbf{x}_3^n + \Delta t\ f_3(t^{n+1}, \mathbf{x}_1^{n+1,k}, \mathbf{x}_2^{n+1,k}, \mathbf{x}_3^{n,k-1}, ...), \\
&\ ...
\end{aligned} \tag{2.12}$$

where the subscript indicates the vertex. This is known as Picard's method. We iterate over the dummy variable, k, until the solution converges to some desired tolerance level.

This iterative scheme is significantly more computationally expensive than the forward Euler method. Each time a vertex moves, variables such as cell areas, cell perimeters and angles between edges must be re-calculated for all cells to which the vertex belongs. In the explicit method, each of these variables must only be calculated once during an update, with the vertices moved simultaneously once all forces have been calculated. Each iteration within an update of the implicit approximation is therefore more expensive than a complete update of the explicit method, and many iterations may be required to ensure convergence of the scheme.

One advantage of the implicit scheme is that larger time-steps can be taken, without introducing instabilities into the numerical approximation. However, large time-steps require more iterations for the solution to converge, reducing the advantage of an implicit scheme over an explicit method with smaller time-steps. There is a further consideration that tips the balance in favour of an explicit method. The time-steps in our simulations are constrained by the need to capture the dynamics of various rearrangements processes, such as T1 transitions and cell proliferation. The advantage of being able to take large time-steps in the backward Euler method is therefore largely negated.

Stability issues do not arise in the forward Euler method, as long as the time-steps are sufficiently small. We therefore proceed in the remainder of this thesis with the forward Euler method, as described in Section 2.8.1. Where simulation results are presented, we will show the time-step used. In all cases, simulations have also been run with smaller time-steps to ensure stability issues do not arise.

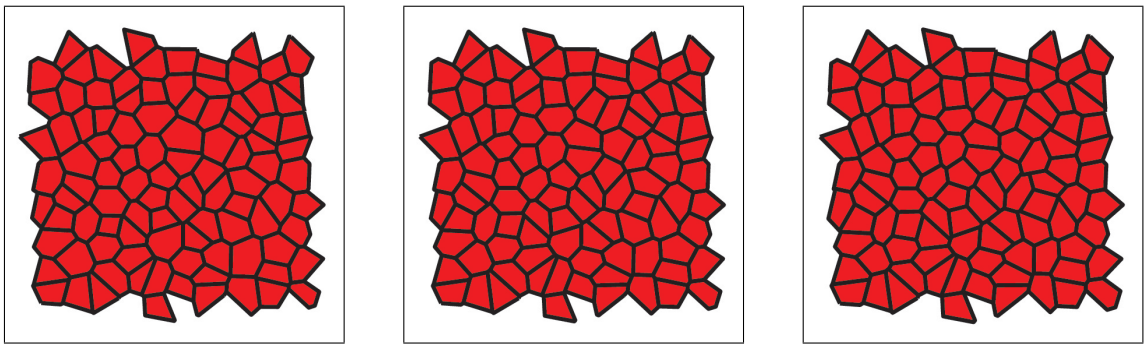
We are now able to approximate our system of equations (2.5) using the forward Euler method. Over the next few sections we will run simulations, initially showing that the force laws produce the desired effect (Section 2.9 and Section 2.10), then bringing in growth (Section 2.11), proliferation (Section 2.12), and finally death (Section 2.13).

2.9 Simulations of one force

One way of testing whether the model is behaving as expected is to allow cells to relax from an initial configuration under the influence of just one of the force terms detailed in Section 2.2. In other words, we can set any six of the seven constants (C_L, C_P, C_A, C_H, C_D, C_{B1} and C_{B2}) to zero, and examine the effect of a single term from the force equations. For example, consider the area force term (equation (2.2)), given by

$$\mathbf{A} = \left[C_A \frac{|a_t - a|^{n_1+1}}{(a_t - a)} \right] \hat{\mathbf{P}}. \tag{2.13}$$

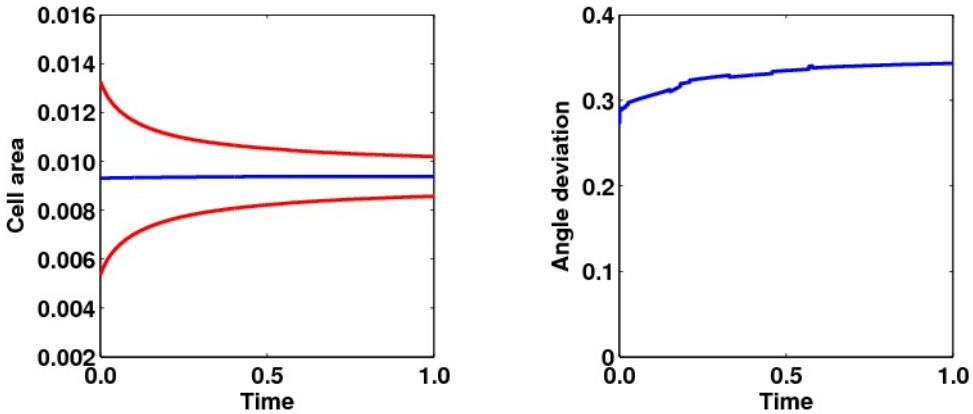
We expect that, in the absence of cell growth, proliferation, and death, cell areas should converge to the target area, a_t, which is defined to be the initial mean cell area. In this simulation $a_t = 9.3 \times 10^{-3}$. Note that this number is approximately equal to $1/N_c = 10^{-2}$, which, as we saw in Section 2.1, is an estimate of the initial average cell area. T1 transitions are allowed to occur on edges that fall below 5% of the mean edge length (i.e. $T_{\mathrm{T1}} = 0.05$). Fig. 2.8 shows the evolution of a tissue of 100 cells over the time range $t \in [0, 1]$, with $C_A = 100$ and $\Delta t = 10^{-3}$.



(a) (b) (c)

Figure 2.8: *Simulation of cells relaxing under the influence of area force term* (2.13) *only. See text for parameter values. (a)* $t = 0$*, (b)* $t = 0.1$*, (c)* $t = 1$*.*

It is not immediately clear from looking at Fig. 2.8 whether the area force term (2.13) is having the expected effect. Therefore, we examine the distribution of cell areas over time during the simulation. Fig. 2.9(a) shows the mean area over time, as well as the mean +/- two standard deviations. 95% of cell areas lie within this range for normally distributed cell areas. This figure demonstrates that while the mean area stays constant, the standard deviation clearly decreases significantly, demonstrating that areas do converge as expected.



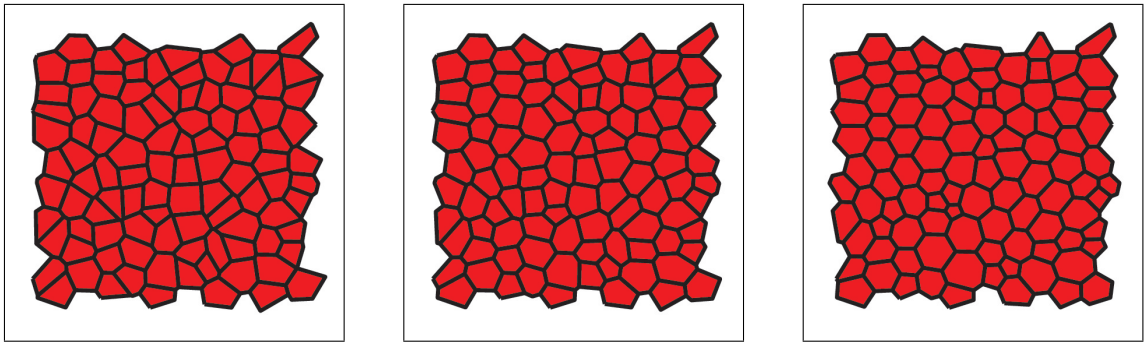
(a) (b)

Figure 2.9: *Cell shape statistics for simulation shown in Fig. 2.8. (a) Mean cell area (blue) and mean +/- 2 standard deviations (red). The target area is equal to the initial mean cell area, and the distribution of areas therefore converges towards this value. (b) Mean deviation from ideal internal angle,* θ *(see Section 2.2.2). As there is no force term encouraging cell shapes to be regular, the mean angle deviation does not decrease, and in fact increases slightly over the simulation.*

Fig. 2.9(b) shows the mean deviation from internal angle during the simulation. This is included for comparison with the following simulation, in which we perform the same statistical analysis with the deformation force term (equation (2.2)) given by

$$\mathbf{D} = \left[C_D \frac{|\phi - \theta|^{n_2+1}}{(\phi - \theta)} \right] \hat{\mathbf{P}}, \tag{2.14}$$

which works to keep cells as regular in shape as possible. In this case we set the area constant C_A to 0, and the deformation constant C_D to 5×10^{-3}. All other parameters are the same as in the previous simulation. The evolution of the tissue can be observed in Fig. 2.10.

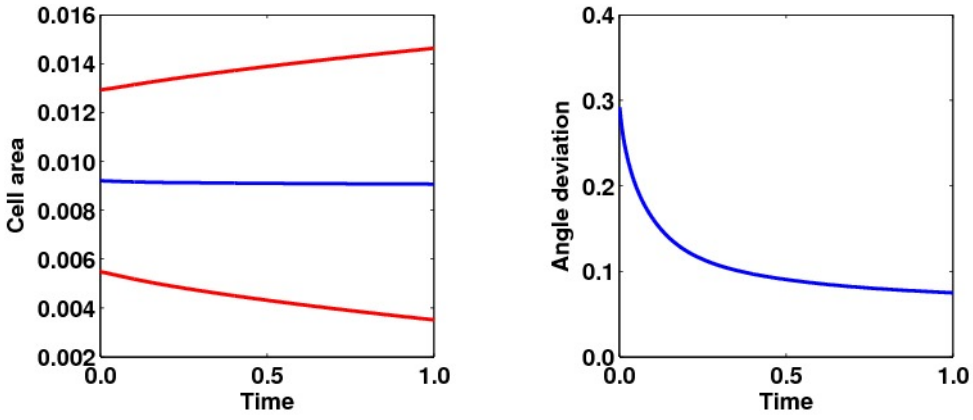


(a) (b) (c)

Figure 2.10: *Simulation of cells relaxing under the influence of deformation force* (2.14) *only. See text for parameter values. (a)* $t = 0$*, (b)* $t = 0.1$*, (c)* $t = 1$*.*

We see a marked difference in the behaviour of the tissue under the action of the deformation force in contrast to the area force. As there is no restriction on cell area, we observe both very small and very large cells. Fig. 2.11(a) shows the distribution of cell areas in this case. Without the presence of the area force, cell areas do not converge towards the mean, as was observed in Fig. 2.9(a). However, examining the mean deviation from average internal angle, θ, over all vertices, we observe that it decreases over time (Fig. 2.11(b)). This is expected as deformation force causes angles to tend towards the average value in each cell, so the deviation, $|\phi - \theta|$, tends to zero. It is not possible, however, for every angle to reach its ideal value, as the effect of

neighbouring cells with potentially different internal angles must be considered. For this reason, the mean angle deviation in Fig. 2.11(b) tends to a non-zero value. Fig. 2.11(b) can be contrasted with Fig. 2.9(b), which shows the deviation from ideal angle in the area force simulation. There, no decrease in the mean is observed, and in fact there is a slight increase as cells jostle to reach the target area.



(a) (b)

Figure 2.11: *Cell shape statistics for simulation shown in Fig. 2.10. (a) Mean cell area (blue) and mean +/- 2 standard deviations (red). As there is no force encouraging cells towards the target area, the distribution of cell areas increases during the simulation. (b) Mean deviation from ideal internal angle, θ. The mean angle deviation decreases as the deformation force encourages angles to tend to θ.*

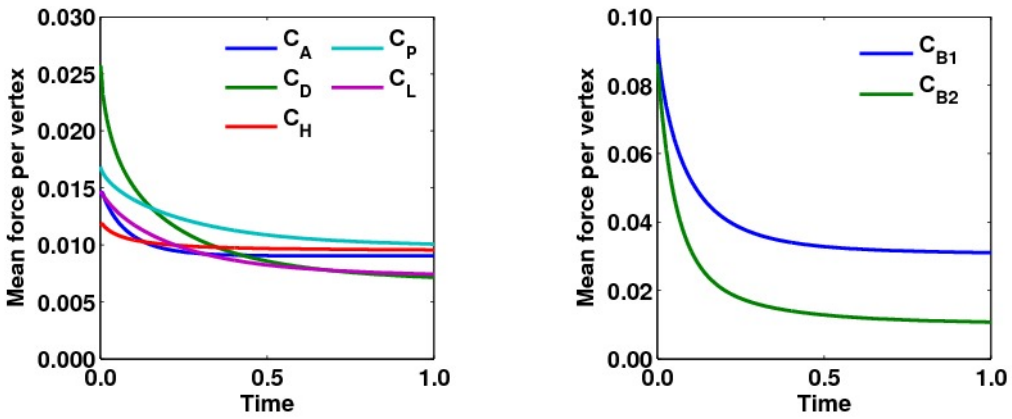
In Section 2.10 we will run a simulation with all the force terms, and show that each term contributes to the dynamics of the tissue.

2.10 Simulations of all forces

In Section 2.8 we stated that the force constants are chosen such that each force term has a roughly equal effect on each vertex. This can be demonstrated in two ways, firstly by finding the average magnitude per vertex of each force term, and secondly by showing the convergence of an appropriate statistic during simulations. Using the parameters from Table 2.1, we run another simulation of 100 cells relaxing to

equilibrium. In this case, $\Delta t = 1/1000$, and again we allow T1 transitions on edges that are shorter than 5% of the mean.

Fig. 2.12(a) demonstrates that each force term from the tension and pressure equations (2.1) and (2.2) has an approximately equal mean effect per vertex. The randomness of the initial configuration results in some variation between forces at the start of a simulation. Fig. 2.12(b) demonstrates that the magnitudes of the boundary forces are higher than the other forces. This is necessary in order to keep the boundary smooth. It should be noted that mean force per vertex in this context implies mean boundary force per *boundary* vertex, not the mean over all vertices.



(a) (b)

Figure 2.12: *Graphs of mean force per vertex for each of the force terms described in Section 2.2 during a simulation of 100 cells relaxing to mechanical equilibrium. Parameter values are as in Table 2.1. The legend identifies the force term by the constant associated with it. The plots are not of these constants, but of the mean magnitude per vertex of the force term associated with the constant. (a) Tension and pressure force terms. (b) Boundary force terms.*

Statistics similar to those used in Section 2.9 can be examined to show the behaviour of the tissue. For example, the distribution of cell areas is expected to converge towards the target value. Fig. 2.13(a) shows the mean cell area, and the mean +/- 2 standard deviations. As expected, the distribution of cell areas narrows, though there is a clear difference from the case of cell areas only. Due to the presence of other competing forces in the current simulation, cell areas do not converge as strongly.

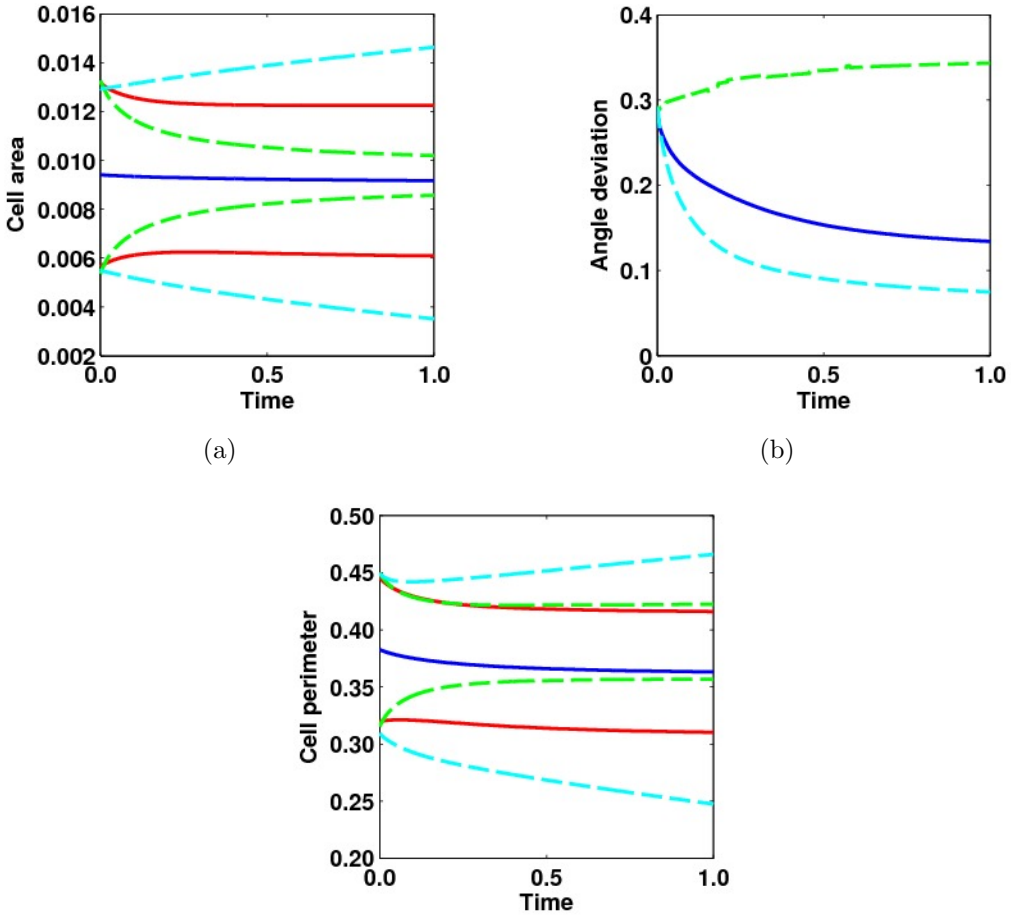


Figure 2.13: *Cell shape statistics for simulation shown in Fig. 2.12. The equivalent statistics for the case of area force only (green) and deformation force only (cyan) are superimposed on each plot as dotted lines for the sake of comparison. (a) Mean cell area (blue) and mean +/- 2 standard deviations (red). (b) Mean deviation from ideal internal angle. (c) Mean cell perimeter (blue) and mean +/- 2 standard deviations (red). As all force terms are acting in this simulation, each of the plots shows either a decreasing mean or a convergence of the distribution.*

The mean deviation from ideal internal angle (Fig. 2.13(b)) decreases, as in Section 2.9. The decrease is not as dramatic as the case when only the deformation force was acting, but is a clear trend. There is also convergence in the distribution of cell perimeters, as demonstrated in Fig. 2.13(c), which shows that the force term associated with constant C_P in (2.1) is acting on the tissue. Similar trends are found for the effect of the remaining tension and pressure force terms, as well as the boundary terms, on the tissue. We choose not to show all results here for the sake of

brevity.

In Section 2.11 we will incorporate cell growth into our simulations, and examine the effect on cell volume and area distributions, as well as height-to-area ratios.

2.11 Simulations with cell growth

We run a simulation with growth implemented according to equation (2.7) for each cell. Initial cell volumes are assigned as described in Section 2.8, and the target volume is set to 110% of the maximum initial volume, ensuring that all cells are growing at the start of the simulation. In this simulation the maximum initial volume was 1.95×10^{-3}, so $V_k = 2.15 \times 10^{-3}$. The growth speeds, g_k, are set to unity for each cell. We run the simulation over $t \in [0, 100]$, with a Δt of 1/1000. Other parameters are as in Table 2.1.

Fig. 2.14(a) shows the mean cell volume over time during the course of the simulation, as well as the mean +/- two standard deviations. The figure demonstrates that the mean cell volume initially increases, while the distribution of volumes narrows. The cells whose initial volumes were largest approach the target volume first, and the distribution continues to narrow as more and more cells reach the target. Eventually all cells are at the target volume, at which point the standard deviation falls to zero and we observe a straight line in Fig. 2.14(a). It should be noted that under the logistic growth model (Section 2.5) cells never actually reach the target volume, they tend to it as time tends to infinity. However, we can see that in reasonable time frames, cell volumes approximate the target volume to a high level of accuracy. The inset shows a close up of the mean volume and distribution over the first 10 time-units of the simulation.

Fig. 2.14(b) shows the mean cell area during these simulations. It increases initially, and there is a narrowing of the distribution of areas. This increase in mean

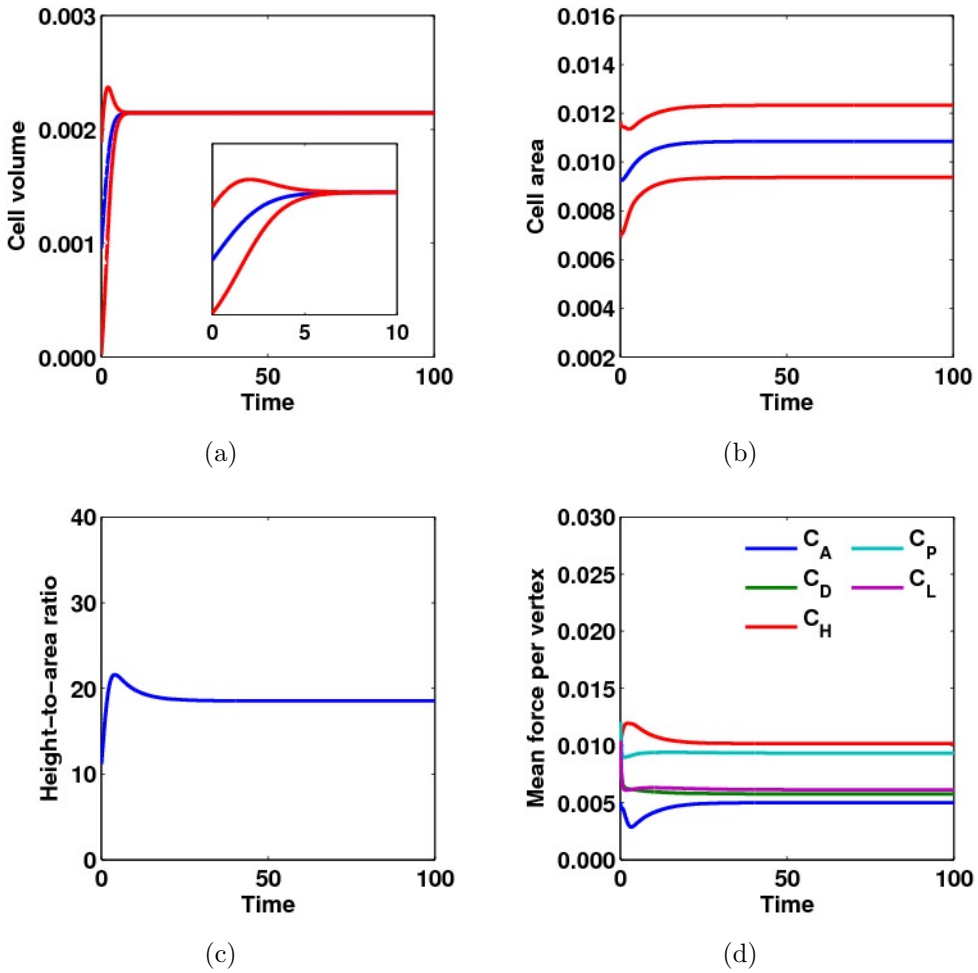


Figure 2.14: *Statistics for simulation of 100 growing cells with growth speed, g_k, equal to unity for each cell. See text and Table 2.1 for parameters. (a) Mean cell volume (blue) and mean +/- 2 standard deviations (red). The target volume is 2.15×10^{-3} for each cell. The inset shows a detailed view of the first 10 time-units. (b) Mean cell area (blue) and mean +/- 2 standard deviations (red). (c) Mean height-to-area ratio. (d) Mean force per vertex for various force terms.*

cell area is a consequence of the second term in (2.2), which produces a pressure force proportional to the height-to-area ratio. As cell volumes grow, the mean height-to-area ratio increases, leading to an increased pressure and subsequent enlarging of the cell area. This then reduces the height-to-area ratio, as demonstrated in Fig. 2.14(c). Clearly, there is a trade-off here between the area force term, which strives to keep cells as near to the target area as possible, and the height-to-area force term, which acts to increase cell areas as the cell becomes elongated vertically. As a result of

this trade-off, the mean cell area at the end of the simulation is slightly above the target area, while the mean height-to-area ratio is also slightly above what it would be without the presence of the area force.

As cell height is equal to volume over area, the height-to-area ratio for each cell is equal to the volume over the square of the area. The order of magnitude of the height-to-area ratio thus depends on the orders of magnitude of volume and area. Looking at the data in Fig. 2.14, a rough calculation shows that $\textit{volume/area}^2 \approx 0.002/0.01^2 = 20$, which is why the height-to-area ratio is around this value.

Fig. 2.14(d) shows the mean force per vertex during this simulation for each of the tension and pressure force terms described in Section 2.2. The forces are identified in the legend by the constant associated with them. The height-to-area force, represented by C_H, is the only one of the five that is increasing at $t = 0$. The other four forces all show an initial decrease as the system relaxes, followed by an increase as the effects of growth become apparent, and a levelling out as growth stops and the system reaches a new mechanical equilibrium. The height-to-area force increases from the start because it is directly related to cell volumes, which themselves increase from the beginning of the simulation.

Fig. 2.14 also demonstrates the time-scale over which the system reaches equilibrium after the growth phase. The inset of Fig. 2.14(a) shows that growth had finished by $t = 10$, whereas the effect on cell area and height-to-area ratio continues until at least $t = 20$ (Fig. 2.14(b) and Fig. 2.14(c)), and the forces (Fig. 2.14(d)) take a similar length of time to respond. These facts show that in this simulation, growth occurred on a fast time-scale in comparison to mechanical relaxation. If growth were slow, we would expect to see the system relaxing at the same time as growth occurred, rather than growth being a 'shock' that the system catches up with afterwards.

In order to test this we run another simulation, beginning from an identical initial configuration, in which the cell growth speed, g_k, is reduced by an order of magnitude

to 0.1. All other parameters are the same as before. In this case, as expected, the mean volume increases at a slower rate (Fig. 2.15(a)). The mean cell area (Fig. 2.15(b)) and mean height-to-area ratio (Fig. 2.15(c)), meanwhile, increase on a comparable time-scale to the volume, unlike in the previous simulation. The mean height-to-area ratio, in particular, shows very different behaviour in this simulation compared to the last. There is no spike at the start of the simulation, as the cell areas have time to respond to the increased height-to-area force term as the cell grows. Fig. 2.15(d) shows the mean magnitude of the various force terms per vertex for this simulation.

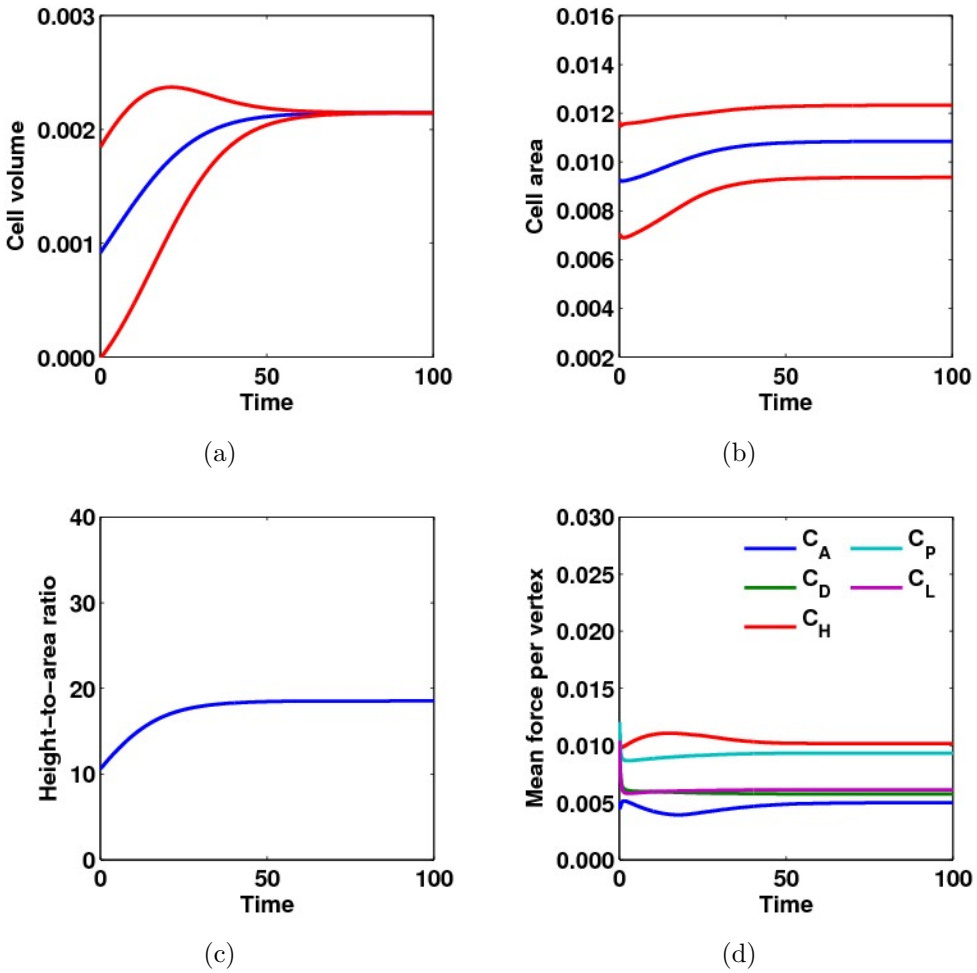


Figure 2.15: *Statistics for simulation of 100 growing cells with growth speed, g_k, equal to 0.1 for each cell. See text and Table 2.1 for parameters. (a) Mean cell volume (blue) and mean +/- 2 standard deviations (red). The target volume is 2.15×10^{-3}. (b) Mean cell area (blue) and mean +/- 2 standard deviations (red). (c) Mean height-to-area ratio. (d) Mean force per vertex for various force terms.*

In this section cells simply grew to their target volume, and the system was subsequently able to relax to mechanical equilibrium. In Section 2.12, we will see what happens when cell proliferation is implemented.

2.12 Simulations with cell proliferation

Cell proliferation can be implemented in one of two ways. In the first method, division occurs at regular intervals, f_p, and the largest cell in the tissue is chosen to divide. In the second method, cells are allowed to divide with increasing probability based on the ratio of their current volume to the target volume. This ensures that cells close to the target volume are likely to divide, whereas those which are much smaller have very little chance of undergoing mitosis. Under this method, as the cell numbers increase, proliferation events occur more and more frequently. This is in contrast to the first method, in which the frequency of proliferation events is independent of the number of cells. Under the first method, for a given cell, the average time between divisions increases as the tissue size gets larger, because the cell's probability of being chosen to divide is smaller. Interestingly, it has been observed biologically that the average cell doubling time increases during the development of the *Drosophila* wing disc, from 5.5-5.7 hours initially up to 30 hours at the last division (Martín et al., 2009). Thus the first method, which may at first seem biologically unrealistic, may in fact be useful in some systems.

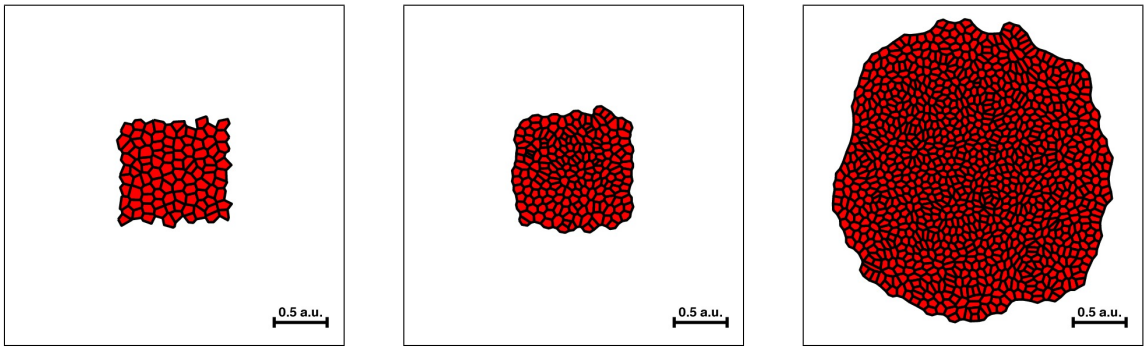
We implement a simulation over $t \in (0, 100]$, in which a proliferation event occurs every 0.1 time-units. Over the course of the simulation, the tissue grows from 100 to 1100 cells. In this simulation, all cells start with the same initial volume, equal to the mean initial volume described in Section 2.8. The target volume is also set to this value. In other words, there is no growth in the system until cell division occurs. This should ensure that mean cell volume remains approximately constant during

simulations, unlike the simulations in Section 2.11, where we examined the effects of growth without proliferation. Upon division, the target area of each daughter cell grows linearly from its initial area to the overall target area in one time-unit. A summary of other parameters can be found in Table 2.3. The evolution of the tissue

Parameter	C_L	C_P	C_A	C_H	C_D	C_{B1}
Value	0.1	0.05	2000	0.001	0.1	0.1
Parameter	C_{B2}	$n_1 - n_4$	μ	g_k	T_{T1}	f_p
Value	50	2	1	0.1	0.05	0.1

Table 2.3: *Parameter values used in simulation of tissue growing from 100 to 1100 cells with proliferation at regular intervals.*

can be observed in Fig. 2.16 (see also Thesis Movie 1 at http://aaronmsmith.co.uk/movies).



(a) (b) (c)

Figure 2.16: *Simulation of tissue growing from 100 to 1100 cells with regular proliferation events. See Table 2.3 for parameter values. (a) $t = 0$, (b) $t = 10$, (c) $t = 100$.*

We observe that the tissue boundary stays relatively smooth and round as the tissue grows, due to the boundary forces described in Section 2.2.3. This seems to cause a squashing of cells in the centre of the tissue, leading to a build up of forces in these regions. These kinds of stresses have been postulated by previous authors to provide a mechanical feedback into growth regulation (Aegerter-Wilmsen et al., 2007, Shraiman, 2005).

The mean cell volume (Fig. 2.17(a)) initially decreases, due to the relatively fast rate of cell division, then gradually increases back towards the target volume as the

simulation progresses. It seems apparent from Fig. 2.16 that cell areas become smaller as the tissue grows. By examining the mean cell area over time (Fig. 2.17(b)), this can be established quantitatively. The mean cell area decreases, particularly during the first part of the simulation, before levelling out. This leads to a spike in the area force term (Fig. 2.17(d)), as cells grow back towards their target area. The roughness of the curves is caused by proliferation events and an increase in the number of T1 transitions, which cause mini-spikes in the force terms. There is a concurrent increase in the mean height-to-area ratio (Fig. 2.17(c)), which is expected given the decrease in mean area without such a significant decrease in mean volume. One way in which to prevent these phenomena occurring, if they prove to be biologically unrealistic, would be to increase the strength of the second term in equation (2.2) by increasing the value of the constant C_H. This term controls the feedback between height and area, and increasing its strength would cause cell areas to increase and lead to a subsequent decrease in height-to-area ratios.

In Section 2.13 we will implement cell death, as described in Section 2.6. We will show how this process acts to relieve the build-up of forces in the centre of the tissue seen in this section, and discuss issues that arise on the boundary during simulations.

2.13 Simulations with cell death

We run a simulation with parameters from Table 2.3, this time allowing cells to die as well as proliferate. We choose an apoptosis period that is double the proliferation period. In this way, for every two proliferation events, a single cell becomes apoptotic and eventually dies. Note that there is a delay between a cell becoming apoptotic and its death, during which it shrinks as the forces acting on it change (Section 2.6). We expect roughly half the cells created by proliferation in Section 2.12 to be killed off.

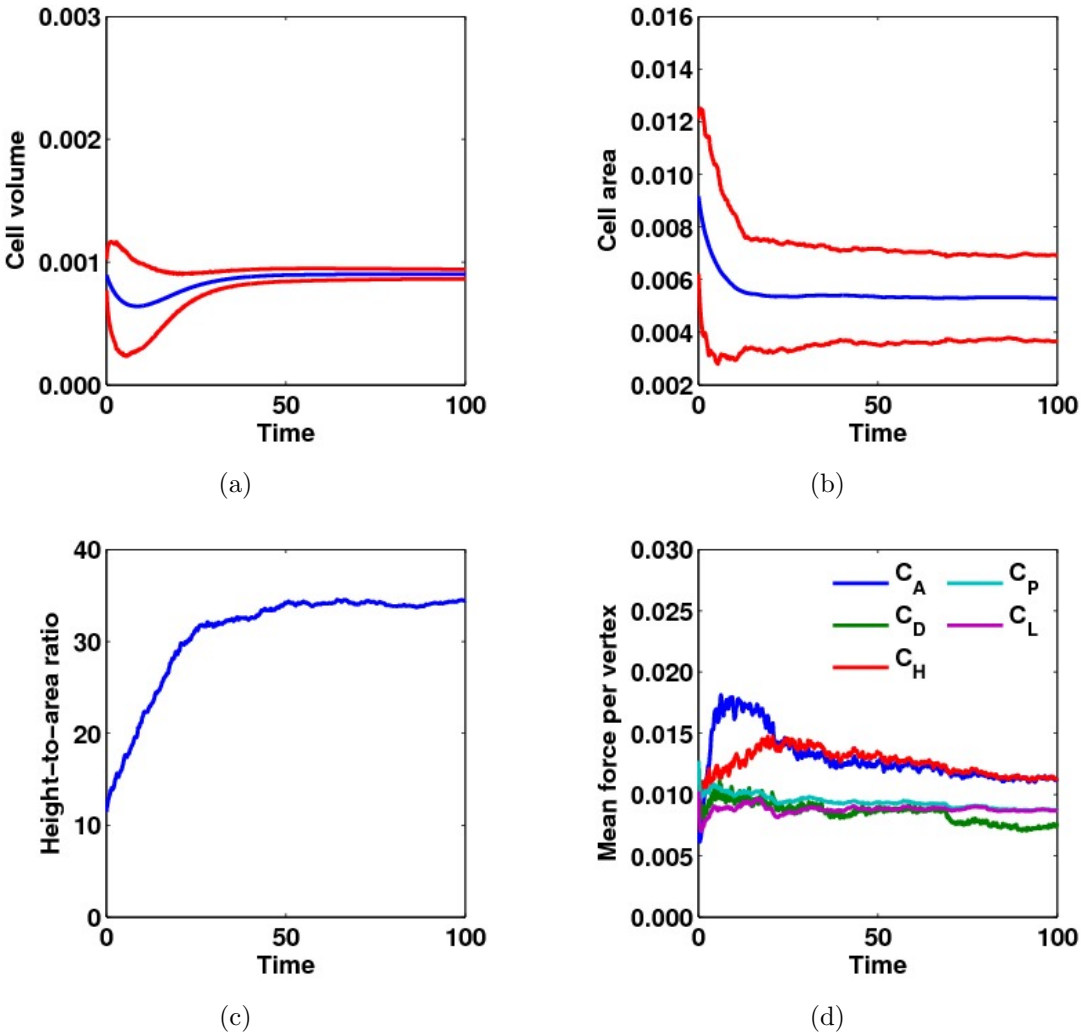
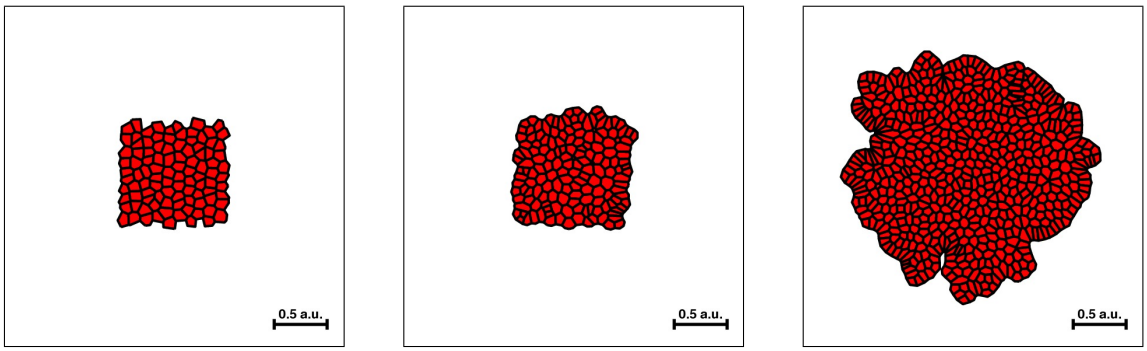


Figure 2.17: *Statistics for simulation shown in Fig. 2.16. (a) Mean cell volume (blue) and mean +/- 2 standard deviations (red). (b) Mean cell area (blue) and mean +/- 2 standard deviations (red). (c) Mean height-to-area ratio. (d) Mean force per vertex for various force terms.*

Fig. 2.18 shows the evolution of the tissue over the time range $t \in [0, 100]$ (see also Thesis Movie 2 at http://aaronmsmith.co.uk/movies). We can draw contrasts with Fig. 2.16, in particular noting the smaller total number of cells. The final number of cells in this simulation is 610, with ten of these cells in an apoptotic state. Not all of these apoptotic cells can be seen, though one or two are clear as they are very small and on the verge of death.

We also observe a squashing of cells on the boundary. This could to be due to



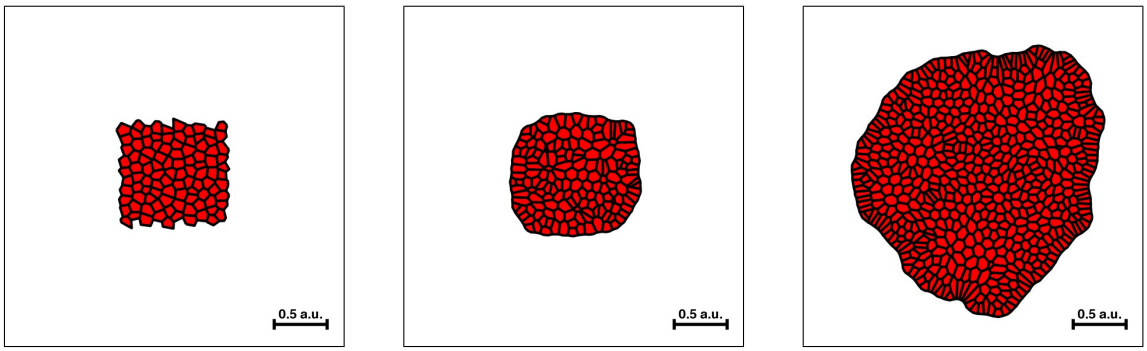
(a) (b) (c)

Figure 2.18: *Simulation of tissue growing from 100 to 610 cells with regular proliferation and apoptosis. See Table 2.3 for parameters. (a)* $t = 0$*, (b)* $t = 10$*, (c)* $t = 100$*.*

the fact that boundary cells cannot become apoptotic (Section 2.6), so there is a relatively higher number of cells on the boundary compared to the rest of the tissue. As a result of this, the boundary seems less able to maintain its smooth, circular shape, and distinct bulges can be seen. This is clearer in the movie, which also shows that separate bulges start overlapping each other, which is biologically unrealistic for a two-dimensional epithelial tissue. One way round this issue is to make the boundary force stronger, for example by multiplying the constant C_{B1} in equation (2.3) by a factor of 10 (Fig. 2.19).

An alternative is to implement a method for junctional rearrangements on the boundary, which would then allow boundary cells to die. One possibility for achieving this would be to allow boundary edges that fall below the rearrangement threshold to contract to a single point. In other words, the two vertices that make up the edge will join together to become a single vertex. This process will be discussed and implemented later in Chapter 5, in the context of cell migration in the mouse embryo.

Fig. 2.19 shows the evolution of the tissue with the boundary force increased by a factor of 10. Although the shape of the boundary is more regular, we still observe a squashing of cells, with the long axes of the cells aligned in a parallel manner. Whilst this appears initially to be a limitation of the model, this phenomenon is similar to what is actually observed in some epithelia (S. Srinivas, *pers. comm.*).



(a) (b) (c)

Figure 2.19: *Simulation of tissue growing from 100 to 610 cells with regular proliferation and apoptosis. In this simulation the boundary force constant C_{B1} has been increased by a factor of 10 to ensure the boundary stays smooth. See Table 2.3 for other parameters. (a) $t = 0$, (b) $t = 10$, (c) $t = 100$.*

There is currently no direct experimental evidence that forces are greater on the boundary. Laser ablation experiments (Farhadifar et al., 2007, Rauzi et al., 2008) could in theory be performed *in vivo* to justify the assumption. However, it is known that in the *Drosophila* wing disc, for example, the surrounding tissue exerts pressure, which can be represented by increased tension. The boundary is also circular, again suggesting that an increased boundary force is realistic.

Examining the mean cell volume, cell area, height-to-area ratio and force terms per vertex for the simulation shown in Fig. 2.18, we observe similar trends to the simulation with cell proliferation only. As Fig. 2.20 shows, however, in this case the decrease in mean cell area, and the increase in mean height-to-area ratio, are not as great. This shows that the cells that have died create room within the tissue for the remaining cells, and thus relieve the build-up of forces in the tissue. This is confirmed by Fig. 2.17(d), which shows that the spike in the area force term from the previous simulation is no longer observed.

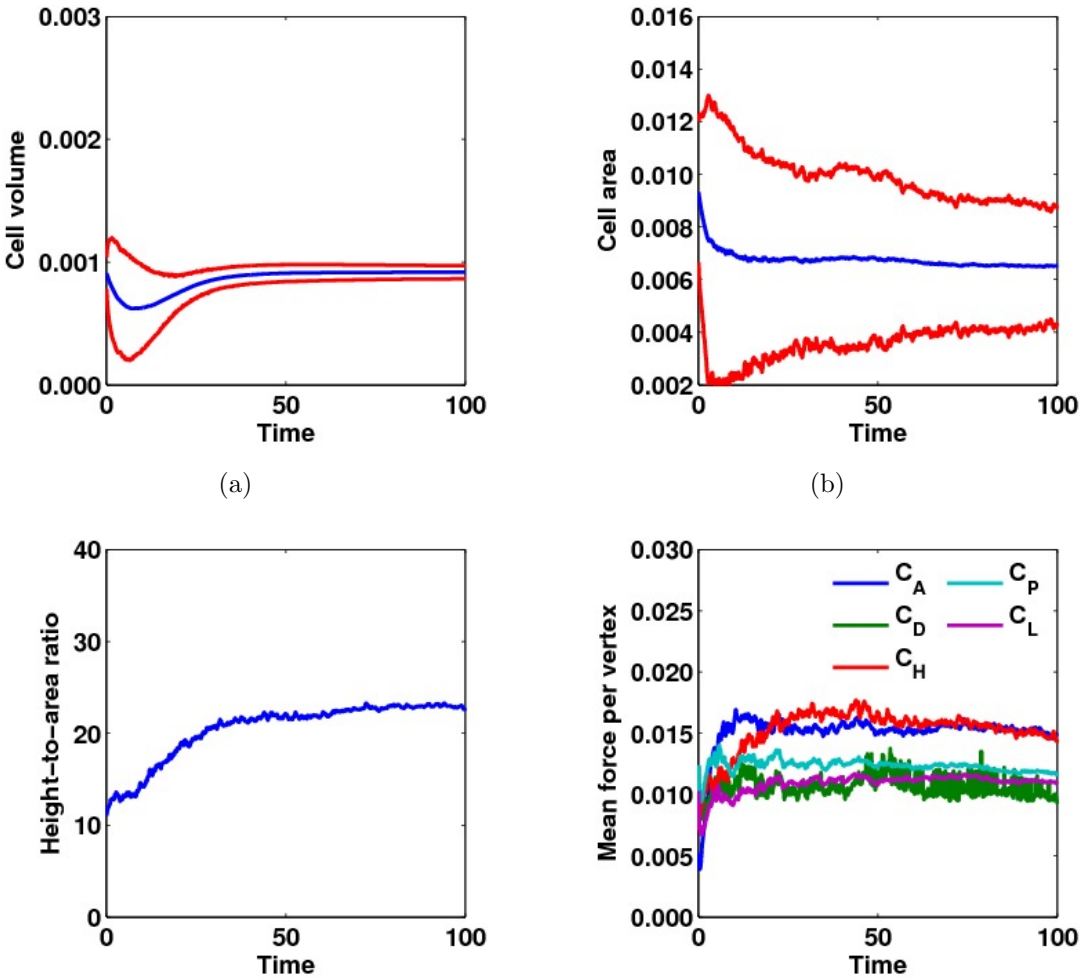


Figure 2.20: *Statistics for simulation shown in Fig. 2.18. (a) Mean cell volume (blue) and mean +/- 2 standard deviations (red). (b) Mean cell area (blue) and mean +/- 2 standard deviations (red). (c) Mean height-to-area ratio. (d) Mean force per vertex for various force terms.*

2.14 Summary

In this chapter we have built up a 2D vertex model description of epithelial tissues. We began by showing how Voronoi tessellations are used to create initial configurations, which can either be regular or have a degree of randomness (Section 2.1). We described the force laws that are applied to cell vertices, representing cell-cell adhesion, actin-myosin contractility, cell elasticity and boundary effects (Section 2.2). By ignoring inertial terms we were able to derive equations of motion. We then went on

to describe junctional rearrangements (Section 2.4) as well as cell growth and proliferation (Section 2.5), and cell death (Section 2.6). Solutions were approximated with the forward Euler method. It was shown that the Euler approximations converge towards an accurate solution obtained using the 4th order RK method (Section 2.8).

Beginning in Section 2.9, we ran simulations and examined the tissue-level effects of our force laws and rearrangement processes. We began by allowing the tissue to relax to mechanical equilibrium under just one of the force terms from Section 2.2, and showed that it behaves as expected by examining an appropriate statistic over the course of a simulation. We then included all the force terms (Section 2.10), and showed that each term contributes to the evolution of the tissue. In Section 2.11 we incorporated growth into the simulations, showing how an increase in mean cell volume eventually leads to an increase in both mean cell area and height-to-area ratio. Section 2.12 introduced cell proliferation in simulations, demonstrated by a tissue growing over an order of magnitude from 100 to 1100 cells. Finally, in Section 2.13 we included cell death, observing how it leads to a reduction in stress in the tissue, and also noting issues associated with the boundary.

We now have a complete physical model of cell behaviour in a simple epithelium. We have seen how to create initial configurations and have described the basic force laws, junctional rearrangements, as well as cell growth, proliferation, and death. To examine the relationship between tissue growth and chemical signalling factors, in Chapter 3 we will explore how to model diffusion within the vertex model framework. This will allow morphogen concentrations to feed back into the physical properties of cells discussed in this chapter, and simulations of the interplay between mechanics and growth factors to be examined.

Chapter 3

Modelling diffusing growth factors

In the previous chapter we built up a physical two-dimensional cellular model. This vertex-based approach included force laws, junctional rearrangements, cell growth, proliferation, and death. As well as the mechanical properties of cells, many developmental processes are believed to rely on morphogenetic chemical signalling factors known as growth factors. Although the definition of a morphogen is somewhat ambiguous, here we use the terms 'morphogen' and 'growth-factor' interchangeably.

Several studies have examined the effects of cell proliferation, rearrangements and mechanical forces on tissue growth and epithelial packing (Aegerter-Wilmsen et al., 2010, Bittig et al., 2008, Farhadifar et al., 2007, Rauzi et al., 2008). Concurrently, there has been much interest in the role played by morphogens (Affolter and Basler, 2007). To date, however, there have been few attempts to combine these strands into a single coherent modelling framework. Multi-scale models such as CHASTE (Cancer, Heart and Soft Tissue Environment) have recently begun to address these issues (Fletcher et al., 2012, van Leeuwen et al., 2009).

In this chapter we present a novel comprehensive computational framework within which the effects of growth factors on epithelial tissues can be studied. The method incorporates the vertex model developed in Chapter 2, in conjunction with a solver

for the governing chemical equations. The vertex model provides a natural mesh for the FEM, with node movements determined by force laws. The arbitrary Lagrangian-Eulerian (ALE) reference frame is adopted to account for movement of the domain.

Farhadifar et al. (2007), in their seminal work, developed a vertex model and examined the effects of proliferation upon cellular topology, finding regions of parameter space where their vertex model accurately represents the packing geometry of the growing *Drosophila* wing imaginal disc. Rauzi et al. (2008), meanwhile, showed that anisotropy of cortical tension can drive tissue elongation. This was achieved by including an angle dependence in their tension force.

Aegerter-Wilmsen et al. (2007) used a tissue-level model to postulate that net growth of the *Drosophila* wing disc can be regulated by a combination of morphogen gradients and mechanical forces. In their model, growth factors initially stimulate growth in the middle of the wing disc, leading to a stretching of the lateral regions. This, in turn, induces growth in those areas via mechanical feedback, which eventually causes compression back at the centre of the disc, inhibiting growth. Their model crucially accounts for the termination of growth when the wing disc reaches a certain size. More recently, the same authors (Aegerter-Wilmsen et al., 2010) used a vertex model and showed that, by including mechanical feedback as a regulator for cellular growth, they could faithfully reproduce the experimentally observed polygon distribution of the wing disc tissue. Hufnagel et al. (2007) also use mechanical feedback within a vertex model. They made the cell-growth rate dependent on the height of each cell, which acts as an indicator of the stress it is under. Growth can only occur, however, when a minimum threshold of the morphogen *Decapentaplegic* (Dpp) is exceeded. The Dpp gradient is imposed as a simple radial function, exponentially decaying with a constant characteristic length.

Landsberg et al. (2009) used a vertex model to show that the antero-posterior compartment boundary of the *Drosophila* wing disc can be maintained by a 2.5-fold

increase in tension at cell edges near the boundary. They were also able to verify the existence of this increased tension experimentally. Schilling et al. (2011) attempted to explain the biochemical signalling pathways behind this phenomenon. They implemented a system of ODEs and PDEs to describe the diffusion and downstream signalling of the morphogen Hedgehog (Hh). They observed experimentally that the Hh signalling pathway affects the maintenance of the anterior-posterior boundary, and then showed with their vertex-based model that this can be explained by assuming that the pathway re-distributes tension forces within cells.

Wartlick et al. (2011) implemented morphogen dynamics in a vertex model by assigning molecule numbers for two morphogens to each cell and solving a system of coupled PDEs representing production, degradation, and transport. They showed experimentally that the concentration and signalling gradients of Dpp in the *Drosophila* wing disc scale with tissue size during development, and that an increase in signalling levels of 50% induces cell division. By implementing these observations in the vertex model they showed that temporal changes in Dpp levels could be an important mechanism in regulating growth.

Some of the models described above include basic representations of morphogen gradients, particularly the recent works of Schilling et al. (2011) and Wartlick et al. (2011). The method described in this chapter is a novel framework that models the mechanical properties of cells along with a dynamic representation of morphogen distribution. It also exhibits key physical properties such as conservation of mass, and is able to account for the movement and growth of the domain as well as important cellular processes such as proliferation and junctional rearrangements. The method has applications in many biological systems as it can be adapted to any process in which a chemical spreading across an epithelium interacts with the mechanical properties of a cell.

Beginning with the diffusion equation in Section 3.1 and boundary condition in

Section 3.1.1, we derive a weak form of the governing chemical equations in Section 3.2, utilising an ALE reference frame. In Section 3.3 we explain how the vertex model is used to create a suitable FE mesh, while Section 3.4 deals with the details of implementation of the FEM. In Section 3.5 we show that our FE approximation converges towards a more accurate solution as space- and time-steps decrease, and in Section 3.6 we show how the time taken to run simulations scales with tissue size. Section 3.7 demonstrates the effects of cellular rearrangements such as T1 transitions, proliferation, and death on the FE mesh. To complete the chapter we show some simulation results in Section 3.8.

The majority of work in this chapter appears in the paper: A. M. Smith, R. E. Baker, D. Kay & P. K. Maini. Incorporating chemical signalling factors into vertex-based models of epithelial tissues. *J. Math. Bio.*, 2011. doi: 10.1007/s00285-011-0464-y.

3.1 Diffusion equation

The distribution of morphogen across a 2D cellular domain, $\Omega(t)$, can be described by a diffusion equation with source term, of the form

$$\frac{\partial c}{\partial t} - \nabla \cdot (\nu \nabla c) = f, \tag{3.1}$$

where $c(\mathbf{x}, t)$ is the amount of chemical at point $\mathbf{x} = (x, y)$ on the domain at time t, $\nu(\mathbf{x}, t)$ is the diffusion coefficient and $f(c, \mathbf{x}, t)$ is a function containing an arbitrary number of source and sink functions representing chemical reaction kinetics. Note that we do not include the dependencies of each function when we write out the equation. For the sake of clarity we continue with this convention throughout this thesis. Functions are written with their dependencies the first time they are mentioned in the text. The reader should thus take care when looking at equations to determine

which variables are, for example, time- and space- dependent.

Equation (3.1) does not contain an advection term, so in this case the chemical is not transported with the moving domain. The chemical thus diffuses through the domain externally to the cells. We will see examples later in Chapter 4 where cells are able to ingest the chemical which then becomes internalised and moves with them, represented by an advection term in the governing equation.

The initial condition is denoted $c(\mathbf{x}, 0) = c^0(\mathbf{x})$, whilst the zero-flux boundary condition is given by

$$\frac{\partial c}{\partial \mathbf{n}} = -\frac{c\mathbf{v} \cdot \mathbf{n}}{\nu} \text{ on } \partial\Omega(t), \tag{3.2}$$

where $\mathbf{v}(\mathbf{x}, t)$ is the velocity of the domain, and $\mathbf{n}$ is the unit outward normal vector.

3.1.1 Boundary condition derivation

Consider the diffusion equation (3.1). For conservation of mass, we require

$$\int_{\Omega(t)} c \, \mathrm{d}\mathbf{x} = \bar{c_0} + \int_{\hat{t}=0}^{t} \int_{\Omega(\hat{t})} f \, \mathrm{d}\mathbf{x} \, \mathrm{d}\hat{t} \tag{3.3}$$

where $\bar{c_0}$ is the initial amount of morphogen in the domain, given by

$$\bar{c_0} = \int_{\Omega(0)} c^0 \, \mathrm{d}\mathbf{x},$$

and $\hat{t}$ is a dummy variable. In other words, the total morphogen in the domain at time t is equal to the initial amount plus the amounts released and degraded since time 0. Taking the derviative of (3.3) with respect to time yields

$$\frac{\mathrm{d}}{\mathrm{d}t} \int_{\Omega(t)} c \, \mathrm{d}\mathbf{x} = \int_{\Omega(t)} f \, \mathrm{d}\mathbf{x},$$

as $\bar{c_0}$ is a constant. Applying Reynolds' Transport Theorem to the left hand side,

$$\begin{aligned}\frac{\mathrm{d}}{\mathrm{d}t}\int_{\Omega(t)} c\,\mathrm{d}\mathbf{x} &= \int_{\Omega(t)}\left(\frac{Dc}{Dt} + c\nabla\cdot\mathbf{v}\right)\,\mathrm{d}\mathbf{x},\\ &= \int_{\Omega(t)}\left(\frac{\partial c}{\partial t} + \mathbf{v}\cdot\nabla c + c\nabla\cdot\mathbf{v}\right)\,\mathrm{d}\mathbf{x},\\ &= \int_{\Omega(t)}\left(\frac{\partial c}{\partial t} + \nabla\cdot(c\mathbf{v})\right)\,\mathrm{d}\mathbf{x},\end{aligned}$$

where D/Dt represents the material derivative. So we have

$$\int_{\Omega(t)}\left(\frac{\partial c}{\partial t} + \nabla\cdot(c\mathbf{v})\right)\,\mathrm{d}\mathbf{x} = \int_{\Omega(t)} f\,\mathrm{d}\mathbf{x}. \tag{3.4}$$

Now, substituting (3.1) into (3.4):

$$\int_{\Omega(t)}\left(f + \nabla\cdot(\nu\nabla c) + \nabla\cdot(c\mathbf{v})\right)\,\mathrm{d}\mathbf{x} = \int_{\Omega(t)} f\,\mathrm{d}\mathbf{x}.$$

Cancelling the f terms and applying the Divergence Theorem gives

$$\int_{\partial\Omega(t)}\left(\nu\nabla c\cdot\mathbf{n} + c\mathbf{v}\cdot\mathbf{n}\right)\,\mathrm{d}S = 0. \tag{3.5}$$

Note that the boundary condition (3.2) is consistent with this equation. A further constraint can be imposed in (3.5); not only must the integral be zero, the flux density, given by the integrand, must be equal to zero at all points on the boundary. This ensures that no chemical flows into or out of the domain. Thus we obtain

$$\nu\nabla c\cdot\mathbf{n} + c\mathbf{v}\cdot\mathbf{n} = 0,$$

and finally, the boundary condition

$$\frac{\partial c}{\partial\mathbf{n}} = -\frac{c\mathbf{v}\cdot\mathbf{n}}{\nu}.$$

In Section 3.2 we derive a weak form of the diffusion equation (3.1). This is the first stage towards implementing the FEM to solve (3.1). The FEM is a natural choice for solving this type of equation on a moving domain, and the vertex model provides us with a convenient FE mesh. Note, of course, that this mesh changes dynamically, driven by the force laws described in Chapter 2. We therefore consider an ALE reference frame in order to deal with the mesh movement relative to the movement of the domain.

3.2 Weak form derivation

Equation (3.1) can be converted into a corresponding weak form, which will ultimately enable us to implement the FEM and find approximations to the solution (see Section 3.3). The weak form is stated as follows: find $c(\mathbf{x}, t) \in H^1(\Omega(t)) := \{y : \int_{\Omega(t)}(|\nabla y|^2 + y^2)\, \mathrm{d}\mathbf{x} < \infty\}$ such that, for any test function $v(\mathbf{x}, t) \in H^1(\Omega(t))$, we have

$$\int_{\Omega(t)} v\frac{\partial c}{\partial t}\, \mathrm{d}\mathbf{x} - \int_{\Omega(t)} v\nabla \cdot (\nu \nabla c)\, \mathrm{d}\mathbf{x} = \int_{\Omega(t)} vf\, \mathrm{d}\mathbf{x}. \tag{3.6}$$

Note that v, representing the test function, differs from ν, representing the diffusion coefficient. Equation (3.6) can be rearranged, in order to implement the boundary condition (3.2). By standard vector identities it can be shown that

$$v\nabla \cdot (\nu \nabla c) = \nabla \cdot (v\nu \nabla c) - \nabla v \cdot (\nu \nabla c). \tag{3.7}$$

Substituting (3.7) into (3.6), we obtain

$$\int_{\Omega(t)} v\frac{\partial c}{\partial t}\, \mathrm{d}\mathbf{x} - \int_{\Omega(t)} \nabla \cdot (v\nu \nabla c)\, \mathrm{d}\mathbf{x} + \int_{\Omega(t)} \nabla v \cdot (\nu \nabla c)\, \mathrm{d}\mathbf{x} = \int_{\Omega(t)} vf\, \mathrm{d}\mathbf{x}.$$

Applying the Divergence Theorem to the second term yields

$$\int_{\Omega(t)} v\frac{\partial c}{\partial t}\,\mathrm{d}\mathbf{x} - \int_{\partial\Omega(t)} v\nu\nabla c\cdot\mathbf{n}\,\mathrm{d}S + \int_{\Omega(t)} \nabla v\cdot(\nu\nabla c)\,\mathrm{d}\mathbf{x} = \int_{\Omega(t)} vf\,\mathrm{d}\mathbf{x},$$

and implementing the boundary condition (3.2) on c gives

$$\int_{\Omega(t)} v\frac{\partial c}{\partial t}\,\mathrm{d}\mathbf{x} + \int_{\partial\Omega(t)} vc\mathbf{v}\cdot\mathbf{n}\,\mathrm{d}S + \int_{\Omega(t)} \nabla v\cdot(\nu\nabla c)\,\mathrm{d}\mathbf{x} = \int_{\Omega(t)} vf\,\mathrm{d}\mathbf{x}. \tag{3.8}$$

3.2.1 ALE reference frame

The ALE is a reference frame that combines features of both the traditional Lagrangian and Eulerian frames. The Lagrangian frame, often used in solid-structure problems, corresponds directly to points within the structure and deforms with it. The Eulerian frame, meanwhile, is fixed in space, and allows average values of fluid passing a given region to be easily calculated. The ALE frame is an arbitrary reference frame, able to move in space whilst permitting the flow of particles through the mesh (Belytschko and Kennedy, 1978, Donea et al., 1982, Hughes et al., 1981, Nobile, 2001).

We define an arbitrary mapping from $\Omega(t)$ to a static reference frame $\hat{\Omega}$. The inverse of this mapping defines the ALE reference frame, which moves with velocity $\mathbf{w}(\mathbf{x},t)$. The chemical distribution in the static frame is denoted $\hat{c}(\hat{\mathbf{x}},t)$, where $\hat{\mathbf{x}} = (\hat{x},\hat{y})$ is a point on the static domain, and the test functions are labelled $\hat{v}(\hat{\mathbf{x}})$. Considering the total derivative of $\hat{c}$ with respect to time gives

$$\frac{\mathrm{d}\hat{c}}{\mathrm{d}t} = \frac{\partial\hat{c}}{\partial t} + \hat{\nabla}\hat{c}\cdot\hat{\mathbf{w}}, \tag{3.9}$$

where $\hat{\nabla}$ represents the grad operator in the static frame, and $\hat{\mathbf{w}}(\hat{\mathbf{x}},t)$ is the velocity of the movement of the ALE frame in the static frame. Considering the first term of

(3.8), if the Jacobian of the mapping from $\Omega(t)$ to $\hat{\Omega}$ is denoted by J_t, we can write

$$\int_{\Omega(t)} v\frac{\partial c}{\partial t}\,\mathrm{d}\mathbf{x} = \int_{\hat{\Omega}} \hat{v}\frac{\partial \hat{c}}{\partial t}|J_t|\,\mathrm{d}\hat{\mathbf{x}}. \tag{3.10}$$

Substituting (3.9) into (3.10) yields

$$\begin{aligned}\int_{\Omega(t)} v\frac{\partial c}{\partial t}\,\mathrm{d}\mathbf{x} &= \int_{\hat{\Omega}} \hat{v}\left(\frac{\mathrm{d}\hat{c}}{\mathrm{d}t} - \hat{\nabla}\hat{c}\cdot\hat{\mathbf{w}}\right)|J_t|\,\mathrm{d}\hat{\mathbf{x}},\\ &= \int_{\hat{\Omega}} \hat{v}\frac{\mathrm{d}\hat{c}}{\mathrm{d}t}|J_t|\,\mathrm{d}\hat{\mathbf{x}} - \int_{\hat{\Omega}} \hat{v}\hat{\nabla}\hat{c}\cdot\hat{\mathbf{w}}|J_t|\,\mathrm{d}\hat{\mathbf{x}}.\end{aligned} \tag{3.11}$$

Considering the first term on the right-hand side and applying the product rule we have

$$\int_{\hat{\Omega}} \hat{v}\frac{\mathrm{d}\hat{c}}{\mathrm{d}t}|J_t|\,\mathrm{d}\hat{\mathbf{x}} = \int_{\hat{\Omega}} \frac{\mathrm{d}}{\mathrm{d}t}\left(\hat{v}\hat{c}|J_t|\right)\,\mathrm{d}\hat{\mathbf{x}} - \int_{\hat{\Omega}} \hat{v}\hat{c}\frac{\mathrm{d}}{\mathrm{d}t}|J_t|\,\mathrm{d}\hat{\mathbf{x}}, \tag{3.12}$$

which holds as $\hat{v}$ is independent of time.

We now use the relationship

$$\frac{\mathrm{d}}{\mathrm{d}t}|J_t| = |J_t|\hat{\nabla}\cdot\hat{\mathbf{w}}, \tag{3.13}$$

which can be proved as follows:

$$\begin{aligned}\frac{\mathrm{d}}{\mathrm{d}t}|J_t| &= \frac{\mathrm{d}}{\mathrm{d}t}\left(\frac{\partial\hat{x}}{\partial x}\frac{\partial\hat{y}}{\partial y} - \frac{\partial\hat{x}}{\partial y}\frac{\partial\hat{y}}{\partial x}\right),\\ &= \frac{\partial\hat{x}}{\partial x}\frac{\partial}{\partial y}\left(\frac{\mathrm{d}\hat{y}}{\mathrm{d}t}\right) + \frac{\partial\hat{y}}{\partial y}\frac{\partial}{\partial x}\left(\frac{\mathrm{d}\hat{x}}{\mathrm{d}t}\right) - \frac{\partial\hat{x}}{\partial y}\frac{\partial}{\partial x}\left(\frac{\mathrm{d}\hat{y}}{\mathrm{d}t}\right) - \frac{\partial\hat{y}}{\partial x}\frac{\partial}{\partial y}\left(\frac{\mathrm{d}\hat{x}}{\mathrm{d}t}\right),\\ &= \frac{\partial\hat{x}}{\partial x}\frac{\partial\hat{w}_y}{\partial y} + \frac{\partial\hat{y}}{\partial y}\frac{\partial\hat{w}_x}{\partial x} - \frac{\partial\hat{x}}{\partial y}\frac{\partial\hat{w}_y}{\partial x} - \frac{\partial\hat{y}}{\partial x}\frac{\partial\hat{w}_x}{\partial y},\\ &= \left(\frac{\partial\hat{x}}{\partial x}\frac{\partial\hat{y}}{\partial y} - \frac{\partial\hat{x}}{\partial y}\frac{\partial\hat{y}}{\partial x}\right)\left(\frac{\partial\hat{w}_x}{\partial\hat{x}} + \frac{\partial\hat{w}_y}{\partial\hat{y}}\right),\\ &= |J_t|\hat{\nabla}\cdot\hat{\mathbf{w}},\end{aligned}$$

where $\hat{w}_x$ and $\hat{w}_y$ are the components of the velocity, $\hat{\mathbf{w}}$, in the $\hat{x}$ and $\hat{y}$ directions,

respectively. Substituting (3.13) into (3.12) we obtain

$$\int_{\hat{\Omega}} \hat{v}\frac{\mathrm{d}\hat{c}}{\mathrm{d}t}|J_t| \,\mathrm{d}\hat{\mathbf{x}} = \int_{\hat{\Omega}} \frac{\mathrm{d}}{\mathrm{d}t}\left(\hat{v}\hat{c}|J_t|\right) \,\mathrm{d}\hat{\mathbf{x}} - \int_{\hat{\Omega}} \hat{v}\hat{c}|J_t|\hat{\nabla}\cdot\hat{\mathbf{w}} \,\mathrm{d}\hat{\mathbf{x}}. \tag{3.14}$$

Now substituting (3.11) and (3.14) back into (3.8) yields

$$\begin{aligned}\int_{\hat{\Omega}} \frac{\mathrm{d}}{\mathrm{d}t}\left(\hat{v}\hat{c}|J_t|\right) \,\mathrm{d}\hat{\mathbf{x}} - \int_{\hat{\Omega}} \hat{v}\hat{c}|J_t|\hat{\nabla}\cdot\hat{\mathbf{w}} \,\mathrm{d}\hat{\mathbf{x}} - \int_{\hat{\Omega}} \hat{v}\left(\hat{\nabla}\hat{c}\cdot\hat{\mathbf{w}}\right)|J_t| \,\mathrm{d}\hat{\mathbf{x}} \\ + \int_{\partial\Omega(t)} vc\mathbf{v}\cdot\mathbf{n} \,\mathrm{d}S + \int_{\Omega(t)} \nabla v\cdot(\nu\nabla c) \,\mathrm{d}\mathbf{x} = \int_{\Omega(t)} vf \,\mathrm{d}\mathbf{x}.\end{aligned}$$

The second and third terms on the left-hand side can be transformed back to integrals over $\Omega(t)$ and combined into a single term. The time derivative can now be taken outside the integral in the first term, giving

$$\begin{aligned}\frac{\mathrm{d}}{\mathrm{d}t}\int_{\hat{\Omega}} \hat{v}\hat{c}|J_t| \,\mathrm{d}\hat{\mathbf{x}} - \int_{\Omega(t)} v\nabla\cdot(c\mathbf{w}) \,\mathrm{d}\mathbf{x} + \int_{\partial\Omega(t)} vc\mathbf{v}\cdot\mathbf{n} \,\mathrm{d}S \\ + \int_{\Omega(t)} \nabla v\cdot(\nu\nabla c) \,\mathrm{d}\mathbf{x} = \int_{\Omega(t)} vf \,\mathrm{d}\mathbf{x}.\end{aligned}$$

Noting that

$$v\nabla\cdot(c\mathbf{w}) = \nabla\cdot(vc\mathbf{w}) - \nabla v\cdot(c\mathbf{w}),$$

and applying the Divergence Theorem we have

$$\begin{aligned}\frac{\mathrm{d}}{\mathrm{d}t}\int_{\hat{\Omega}} \hat{v}\hat{c}|J_t| \,\mathrm{d}\hat{\mathbf{x}} - \int_{\partial\Omega(t)} vc\mathbf{w}\cdot\mathbf{n} \,\mathrm{d}S + \int_{\Omega(t)} \nabla v\cdot(c\mathbf{w}) \,\mathrm{d}\mathbf{x} \\ + \int_{\partial\Omega(t)} vc\mathbf{v}\cdot\mathbf{n} \,\mathrm{d}S + \int_{\Omega(t)} \nabla v\cdot(\nu\nabla c) \,\mathrm{d}\mathbf{x} = \int_{\Omega(t)} vf \,\mathrm{d}\mathbf{x}.\end{aligned} \tag{3.15}$$

Recall that the mapping which defined the ALE frame was completely arbitrary, and thus any velocity function $\mathbf{w}$ can be used. We choose $\mathbf{w}$ to equal the velocity of the cells, and thus allow the cell movements to define the ALE frame. In this way we are modelling movement of the cells as different from the movement of the material

domain, with $\mathbf{w} \neq \mathbf{v}$. If a single cell grows whilst its neighbour shrinks, for example, there may be little change in the material domain but a large distortion of the ALE domain.

Although $\mathbf{w} \neq \mathbf{v}$ generally, there is one place where the two velocities are equal, on the boundary of the domain. Here the domain movement and the cell movement coincide, causing the frames to overlap spatially. Thus the boundary terms in (3.15) cancel out, leaving the final weak form:

$$\frac{\mathrm{d}}{\mathrm{d}t}\int_{\hat{\Omega}} \hat{v}\hat{c}|J_t| \,\mathrm{d}\hat{\mathbf{x}} + \int_{\Omega(t)} \nabla v \cdot (c\mathbf{w}) \,\mathrm{d}\mathbf{x} + \int_{\Omega(t)} \nabla v \cdot (\nu \nabla c) \,\mathrm{d}\mathbf{x} = \int_{\Omega(t)} vf \,\mathrm{d}\mathbf{x}. \qquad (3.16)$$

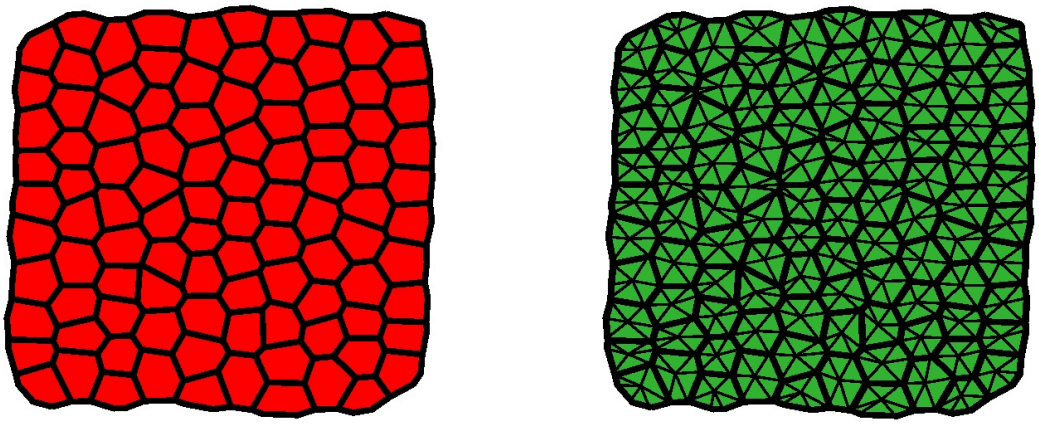
In Section 3.3 we will begin to show how equation (3.16) can be solved numerically. We will first discretise the problem and integrate in time, before taking the cell configuration and using it to create a triangular mesh of the domain for the FEM. Approximating the solution as linear on each triangle we will create a system of matrix equations, using a series of functions as the test function v in (3.16).

3.3 Discrete approximation

We replace the continuous infinite-dimensional problem (3.16) with a discrete finite-dimensional approximation. A set of $N(t)$ node-points $\{\mathbf{y}_i(t)\}_{i=1}^{N}$ in $\Omega(t)$ are connected to form a mesh of the domain consisting of $M(t)$ triangular elements $\{\tau_i(t)\}_{i=1}^{M}$. The triangles are such that $\mathrm{int}(\cup_i \overline{\tau}_i) = \Omega(t)$ and $\overline{\tau}_i \cap \overline{\tau}_j$ for $i \neq j$ is either a node, an edge, or is empty, where $\overline{\tau}_i$ represents the closure of the triangle τ_i. We define $V_h(\Omega(t))$ to be a finite-dimensional subspace of $H^1(\Omega(t))$, consisting of continuous functions that are linear within each element τ_i, and look for approximations to c in this space.

A basis of V_h is given by the functions $\{\phi_i(\mathbf{x}, t)\}_{i=1}^{N}$, where, for each i, ϕ_i is

a continuous piecewise linear function such that $\phi_i(\mathbf{y}_j, t) = \delta_{ij}$ (the Kronecker delta function). To create the triangular FE mesh, we take the pre-existing cell vertices, and use the centre of each cell as an additional node-point. This is demonstrated in Fig. 3.1, which shows an original cellular configuration and its corresponding triangular FE mesh.



(a) (b)

Figure 3.1: *Creating an FE mesh from a cell configuration. (a) Cell configuration. (b) Counterpart FE mesh. The centre of each cell is used as an additional node-point along with the cell vertices to create a triangular tessellation of the domain.*

The FE approximation to c, denoted $c_h(\mathbf{x}, t)$, is defined by

$$c_h = \sum_{i=1}^{N} \alpha_i \phi_i,$$

where $c_h \in V_h$, and $\alpha_i(t)$ is a real number that weights each basis function within the approximation. α_i is also the value of c_h at node i, as $\phi_i = 1$ at this node and all other basis functions equal zero.

We now define a discretisation in time over the range $(0, T]$ to match that of the vertex model (Section 2.3), given by $\cup_{n=1}^{n=N_T}(t^{n-1}, t^n]$, where T is the final time, N_T is the number of time-points, $t^n - t^{n-1} = \Delta t$ for all n, and $t^0 = 0$. The time-discrete

FE approximation to c is given by

$$c_h^n = \sum_{i=1}^{N^n} \alpha_i^n \phi_i^n.$$

Note that a superscript n on any function of time indicates that the function is evaluated at $t = t^n$, on domain $\Omega(t^n)$. Integrating the first term of (3.16) in time between t^{n-1} and t^n yields

$$\int_{t^{n-1}}^{t^n} \left(\frac{\mathrm{d}}{\mathrm{d}t} \int_{\hat{\Omega}} \hat{v}\hat{c}|J_t| \, \mathrm{d}\hat{\mathbf{x}} \right) \, \mathrm{d}t = \int_{\Omega^n} v^n c^n \, \mathrm{d}\mathbf{x} - \int_{\Omega^{n-1}} v^{n-1} c^{n-1} \, \mathrm{d}\mathbf{x}.$$

Approximating the remaining terms in (3.16) as piecewise constant in time in each interval $(t^{n-1}, t^n]$ and integrating over this time range, we obtain

$$\int_{t^{n-1}}^{t^n} \left(\int_{\Omega(t)} \nabla v \cdot (\nu \nabla c) \, \mathrm{d}\mathbf{x} \right) \, \mathrm{d}t = \Delta t \int_{\Omega^n} \nabla v^n \cdot (\nu^n \nabla c^n) \, \mathrm{d}\mathbf{x},$$
$$\int_{t^{n-1}}^{t^n} \left(\int_{\Omega(t)} \nabla v \cdot (c\mathbf{w}) \, \mathrm{d}\mathbf{x} \right) \, \mathrm{d}t = \Delta t \int_{\Omega^n} \nabla v^n \cdot (c^n \mathbf{w}^n) \, \mathrm{d}\mathbf{x},$$
$$\int_{t^{n-1}}^{t^n} \left(\int_{\Omega(t)} v f \, \mathrm{d}\mathbf{x} \right) \, \mathrm{d}t = \Delta t \int_{\Omega^n} v^n f^n \, \mathrm{d}\mathbf{x}.$$

We thus obtain the fully discrete form of (3.16), given by

$$\sum_{i=1}^{N^n} \alpha_i^n \Bigg(\int_{\Omega^n} v^n \phi_i^n \, \mathrm{d}\mathbf{x} + \Delta t \int_{\Omega^n} \nabla v^n \cdot (\nu^n \nabla \phi_i^n) \, \mathrm{d}\mathbf{x} + \Delta t \int_{\Omega^n} \nabla v^n \cdot (\phi_i^n \mathbf{w}^n) \, \mathrm{d}\mathbf{x} \Bigg) =$$
$$\Delta t \int_{\Omega^n} v^n f^n \, \mathrm{d}\mathbf{x} + \sum_{i=1}^{N^{n-1}} \alpha_i^{n-1} \int_{\Omega^{n-1}} v^{n-1} \phi_i^{n-1} \, \mathrm{d}\mathbf{x}. \tag{3.17}$$

If we can find the set of α_i values at each time-point, n, we will have the desired approximation to c. The left-hand side of (3.17) can be written as a row vector, containing the term within the outer brackets for each ϕ_i, multiplied by a column of the α_i values. The right-hand side is a single number. To solve this problem at each time point n for N^n unknown α_i^n values, we must substitute in N^n test functions, v^n.

The most obvious choice is to use the basis functions $\{\phi_j^n\}_{j=1}^{N^n}$. We therefore have a series of rows, each using a different ϕ_j, multiplied by the column vector of α_i values. The system can thus be re-written as a matrix equation of the form

$$(L^n + W^n)\alpha^n = R^n, \tag{3.18}$$

where L^n and W^n are $N^n \times N^n$ matrices, while α^n and R^n are $N^n \times 1$ column vectors. The elements in each matrix are given by

$$\begin{aligned} L_{ji} &= \int_{\Omega^n} \left(\phi_j^n \phi_i^n + \Delta t \nabla \phi_j^n \cdot (\nu^n \nabla \phi_i^n) \right) \mathrm{d}\mathbf{x}, \\ W_{ji} &= \Delta t \int_{\Omega^n} \nabla \phi_j^n \cdot (\phi_i^n \mathbf{w}^n) \, \mathrm{d}\mathbf{x}, \\ R_j &= \Delta t \int_{\Omega^n} \phi_j^n f^n \, \mathrm{d}\mathbf{x} + \sum_{i=1}^{N^{n-1}} \alpha_i^{n-1} \int_{\Omega^{n-1}} \phi_j^{n-1} \phi_i^{n-1} \, \mathrm{d}\mathbf{x}. \end{aligned} \tag{3.19}$$

Section 3.4 will describe how the system of matrix equations (3.19) is formed by mapping each triangular element in turn to a canonical triangle, and integrating the basis functions on this triangle.

3.4 FE implementation

In the matrix equations for L and W (3.19), we see terms relating to one basis function, ϕ_i, being multiplied by terms relating to another, ϕ_j. Two basis functions only produce non-zero products if they are non-zero in a common triangle. Most matrix entries are therefore zero, and the matrices can be created as sparse structures, increasing the efficiency of the algorithm.

The most efficient way to construct the matrices is not sequentially, i.e. looping over every basis function, and performing the integrals of (3.19) by multiplying with every other basis function, as we know this will mainly produce entries that are zero.

Instead, each triangle of the mesh is looped over, and entries in the matrices that relate to the basis functions in the current triangle are updated.

For each triangular element, $\mathbf{e}$, of the mesh, with vertices at $\mathbf{P}_1$, $\mathbf{P}_2$, and $\mathbf{P}_3$, we can define a linear mapping $\mathbf{F}(\tilde{x}, \tilde{y})$ from the canonical triangle, $\tilde{\mathbf{e}}$, which has vertices at (0,0), (0,1), and (1,0), as in Fig. 3.2. This mapping takes the form

$$\begin{aligned} x &= a_{11}\tilde{x} + a_{12}\tilde{y} + c_1, \\ y &= a_{21}\tilde{x} + a_{22}\tilde{y} + c_2. \end{aligned} \tag{3.20}$$

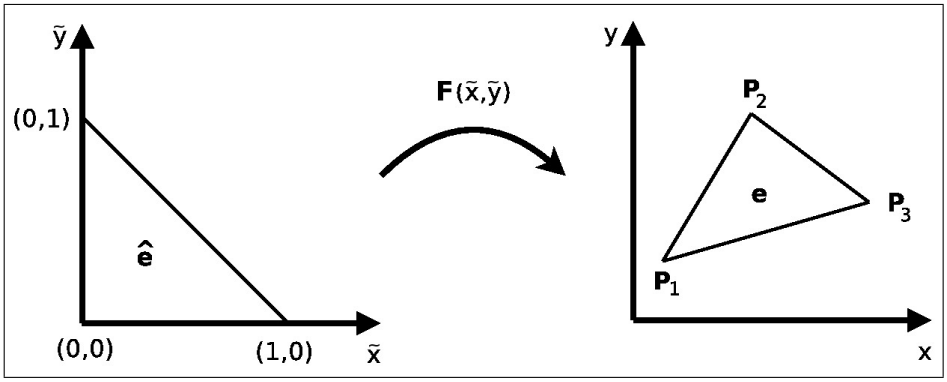


Figure 3.2: *Mapping from the canonical triangle, with vertices at (0,0), (0,1) and (1,0), to an arbitrary triangular element of the FE mesh.*

On the canonical triangle the three basis functions associated with the element are given by

$$\begin{aligned} \tilde{\phi}_1(\tilde{x}, \tilde{y}) &= 1 - \tilde{x} - \tilde{y}, \\ \tilde{\phi}_2(\tilde{x}, \tilde{y}) &= \tilde{y}, \\ \tilde{\phi}_3(\tilde{x}, \tilde{y}) &= \tilde{x}. \end{aligned}$$

Now, as we loop over elements of the mesh, the first type of integral we encounter in

system (3.19) is of the form

$$\int_{\mathbf{e}} \phi_i \phi_j \, \mathrm{d}\mathbf{x} = \int_{\tilde{\mathbf{e}}} \tilde{\phi}_i \tilde{\phi}_j |J_{\tilde{\mathbf{e}}}| \, \mathrm{d}\tilde{\mathbf{x}}, \tag{3.21}$$

where $J_{\tilde{\mathbf{e}}}$ is the Jacobian of the mapping $\mathbf{F}$, given by

$$J_{\tilde{\mathbf{e}}} = \begin{bmatrix} \dfrac{\partial x}{\partial \tilde{x}} & \dfrac{\partial x}{\partial \tilde{y}} \\ \dfrac{\partial y}{\partial \tilde{x}} & \dfrac{\partial y}{\partial \tilde{y}} \end{bmatrix} = \begin{bmatrix} a_{11} & a_{12} \\ a_{21} & a_{22} \end{bmatrix}.$$

By substituting the known points into (3.20), it can be shown that

$$J_{\tilde{\mathbf{e}}} = \begin{bmatrix} P_{3x} - P_{1x} & P_{2x} - P_{1x} \\ P_{3y} - P_{1y} & P_{2y} - P_{1y} \end{bmatrix}.$$

Thus the integrals (3.21) can be performed analytically in the form

$$|J_{\tilde{\mathbf{e}}}| \int_0^1 \int_0^{1-x} \tilde{\phi}_i \tilde{\phi}_j \, \mathrm{d}\tilde{y} \, \mathrm{d}\tilde{x},$$

and it is found that

$$\int_{\mathbf{e}} \phi_i \phi_j \, \mathrm{d}\mathbf{x} = \begin{cases} \frac{1}{12} \, |J_{\tilde{\mathbf{e}}}| \text{ if } i = j, \\ \frac{1}{24} \, |J_{\tilde{\mathbf{e}}}| \text{ if } i \neq j. \end{cases} \tag{3.22}$$

Now consider a second type of integral from the system (3.19), of the form

$$\int_{\mathbf{e}} \nabla \phi_j \cdot (\nu \nabla \phi_i) \, \mathrm{d}\mathbf{x}. \tag{3.23}$$

In the simplest case, ν is a constant and can be taken outside the integral. We have

$$\nabla\phi_i = \begin{pmatrix} \dfrac{\partial\phi_i}{\partial x} \\ \\ \dfrac{\partial\phi_i}{\partial y} \end{pmatrix} = \begin{pmatrix} \dfrac{\partial\phi_i}{\partial\tilde{x}}\dfrac{\partial\tilde{x}}{\partial x} + \dfrac{\partial\phi_i}{\partial\tilde{y}}\dfrac{\partial\tilde{y}}{\partial x} \\ \\ \dfrac{\partial\phi_i}{\partial\tilde{x}}\dfrac{\partial\tilde{x}}{\partial y} + \dfrac{\partial\phi_i}{\partial\tilde{y}}\dfrac{\partial\tilde{y}}{\partial y} \end{pmatrix}.$$

The integrals (3.23) can therefore be written

$$\begin{aligned}\nu\int_{\mathbf{e}} \nabla\phi_j\cdot\nabla\phi_i \,\mathrm{d}\mathbf{x} = \nu\int_{\tilde{\mathbf{e}}} &\left(\frac{\partial\tilde{\phi}_i}{\partial\tilde{x}}\frac{\partial\tilde{x}}{\partial x} + \frac{\partial\tilde{\phi}_i}{\partial\tilde{y}}\frac{\partial\tilde{y}}{\partial x}\right)\left(\frac{\partial\tilde{\phi}_j}{\partial\tilde{x}}\frac{\partial\tilde{x}}{\partial x} + \frac{\partial\tilde{\phi}_j}{\partial\tilde{y}}\frac{\partial\tilde{y}}{\partial x}\right) \\ &+ \left(\frac{\partial\tilde{\phi}_i}{\partial\tilde{x}}\frac{\partial\tilde{x}}{\partial y} + \frac{\partial\tilde{\phi}_i}{\partial\tilde{y}}\frac{\partial\tilde{y}}{\partial y}\right)\left(\frac{\partial\tilde{\phi}_j}{\partial\tilde{x}}\frac{\partial\tilde{x}}{\partial y} + \frac{\partial\tilde{\phi}_j}{\partial\tilde{y}}\frac{\partial\tilde{y}}{\partial y}\right)|J_{\tilde{\mathbf{e}}}|\,\mathrm{d}\mathbf{x}. \end{aligned} \tag{3.24}$$

The terms $\partial\tilde{x}/\partial x$, $\partial\tilde{y}/\partial x$, $\partial\tilde{x}/\partial y$, and $\partial\tilde{y}/\partial y$ can be computed by calculating the inverse transpose of the Jacobian, given by

$$(J_{\tilde{\mathbf{e}}}^{-1})^T = \begin{bmatrix} \dfrac{\partial\tilde{x}}{\partial x} & \dfrac{\partial\tilde{x}}{\partial y} \\ \\ \dfrac{\partial\tilde{y}}{\partial x} & \dfrac{\partial\tilde{y}}{\partial y} \end{bmatrix} = \frac{1}{\det(J_{\tilde{\mathbf{e}}})}\begin{bmatrix} a_{22} & -a_{21} \\ \\ -a_{12} & a_{11} \end{bmatrix}.$$

The integrand of (3.24) is thus simply a number that we can calculate and take outside the integral, leaving us to integrate

$$\int_0^1\int_0^{1-x} 1\,\mathrm{d}\tilde{y}\,\mathrm{d}\tilde{x} = \frac{1}{2}.$$

Therefore, the final expression is

$$\begin{aligned}\nu\int_{\mathbf{e}} \nabla\phi_j\cdot\nabla\phi_i \,\mathrm{d}\mathbf{x} = \frac{|J_{\tilde{\mathbf{e}}}|}{2}\nu &\left(\frac{\partial\tilde{\phi}_i}{\partial\tilde{x}}\frac{\partial\tilde{x}}{\partial x} + \frac{\partial\tilde{\phi}_i}{\partial\tilde{y}}\frac{\partial\tilde{y}}{\partial x}\right)\left(\frac{\partial\tilde{\phi}_j}{\partial\tilde{x}}\frac{\partial\tilde{x}}{\partial x} + \frac{\partial\tilde{\phi}_j}{\partial\tilde{y}}\frac{\partial\tilde{y}}{\partial x}\right) \\ &+ \left(\frac{\partial\tilde{\phi}_i}{\partial\tilde{x}}\frac{\partial\tilde{x}}{\partial y} + \frac{\partial\tilde{\phi}_i}{\partial\tilde{y}}\frac{\partial\tilde{y}}{\partial y}\right)\left(\frac{\partial\tilde{\phi}_j}{\partial\tilde{x}}\frac{\partial\tilde{x}}{\partial y} + \frac{\partial\tilde{\phi}_j}{\partial\tilde{y}}\frac{\partial\tilde{y}}{\partial y}\right).\end{aligned}$$

The final type of integral amongst the matrix equations (3.19) is

$$\int_{\mathbf{e}} \nabla\phi_j \cdot (\phi_i \mathbf{w})\, \mathrm{d}\mathbf{x},$$

where the domain velocity for the triangle is given by

$$\mathbf{w}^n = \frac{\phi_1}{\Delta t}\left(\mathbf{P}_1^n - \mathbf{P}_1^{n-1}\right) + \frac{\phi_2}{\Delta t}\left(\mathbf{P}_2^n - \mathbf{P}_2^{n-1}\right) + \frac{\phi_3}{\Delta t}\left(\mathbf{P}_3^n - \mathbf{P}_3^{n-1}\right).$$

We therefore have

$$\int_{\mathbf{e}} \nabla\phi_j \cdot (\phi_i \mathbf{w})\, \mathrm{d}\mathbf{x} = \frac{|J_{\tilde{\mathbf{e}}}|}{\Delta t}(\nabla\tilde{\phi}_j) \cdot \Bigg((\mathbf{P}_1^n - \mathbf{P}_1^{n-1}) \int_{\tilde{\mathbf{e}}} \tilde{\phi}_i\tilde{\phi}_1\, \mathrm{d}\mathbf{x} + (\mathbf{P}_2^n - \mathbf{P}_2^{n-1}) \int_{\tilde{\mathbf{e}}} \tilde{\phi}_i\tilde{\phi}_2\, \mathrm{d}\mathbf{x} + (\mathbf{P}_3^n - \mathbf{P}_3^{n-1}) \int_{\tilde{\mathbf{e}}} \tilde{\phi}_i\tilde{\phi}_3\, \mathrm{d}\mathbf{x} \Bigg).$$

Using (3.22), we obtain

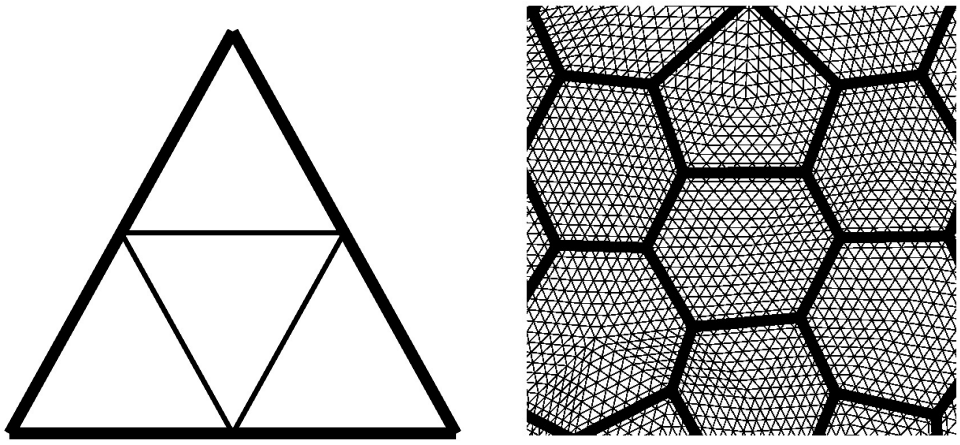
$$\int_{\mathbf{e}} \nabla\phi_j \cdot (\phi_i \mathbf{w})\, \mathrm{d}\mathbf{x} = \frac{|J_{\tilde{\mathbf{e}}}|}{24\Delta t}(\nabla\tilde{\phi}_j) \cdot (\mathbf{P}_1^n - \mathbf{P}_1^{n-1} + \mathbf{P}_2^n - \mathbf{P}_2^{n-1} + \mathbf{P}_3^n - \mathbf{P}_3^{n-1} + \mathbf{P}_i^n - \mathbf{P}_i^{n-1}).$$

Simulations of the morphogen spreading model can now be run on an evolving cellular domain, given an initial condition c_h^0 and source function f. We have not yet discussed the effect on the FE solution of T1 transitions or proliferation, and this will be dealt with in Section 3.7. Before moving on, however, we test the convergence properties of the FE approximation.

3.5 Convergence properties of solution

Since it is not possible to obtain analytical solutions for a diffusing chemical on a cellular domain moving according to our force laws, we choose to compare the coarse mesh approximation to a highly refined (in time and space) reference solution. The

FE mesh shown in Fig. 3.1 can be refined by sub-partitioning each triangle. New nodes are added at the mid-point of each triangle edge and joined to construct four smaller triangles (Fig. 3.3(a)). This process can be repeated *ad infinitum*, creating a highly refined mesh (Fig. 3.3(b)). By also using a small value of the time-step, Δt, we can find an accurate numerical solution with which other approximations can be compared.



(a) (b)

Figure 3.3: *(a) A triangle of the FE mesh (thick line) is sub-divided into four smaller elements (thin lines), by connecting together new nodes placed at the centre of its edges. (b) Part of an FE mesh after 3 iterations of mesh refinement, with each original triangle sub-divided into 64 smaller elements.*

In these simulations a random initial cellular configuration of 100 cells relaxes to mechanical equilibrium. The cell movements are identical in each simulation, with various FE solutions superimposed. Simulations are kept as simple as possible at the cellular level, with no junctional rearrangements, cell growth, or proliferation events. Cell volumes are drawn from a normal distribution, as described in Section 2.8.

Setting $f = 0$ in (3.1) yields the standard diffusion equation, given by

$$\frac{\partial c}{\partial t} = \nabla \cdot (\nu \nabla c) = \nu \nabla^2 c, \tag{3.25}$$

if the diffusion coefficient, ν, is a constant. In each simulation the chemical profile

begins with a step function that takes a value of 0.1 in a small strip, 0.15 units wide, at one edge of the tissue, and zero everywhere else. Other simulation parameters are given in Table 3.1.

Parameter	C_L	C_P	C_A	C_H	C_D
Value	0.1	0.05	2000	0.001	0.1
Parameter	C_{B1}	C_{B2}	$n_1 - n_4$	μ	ν
Value	0.1	50	2	1	0.1

Table 3.1: *Parameter values used in simulations in this section. All parameters, other than space- and time-steps for the FE solver, are the same in all simulations.*

An accurate numerical solution is first established, using four iterations of mesh refinement. Each triangle of the original mesh now contains 256 smaller elements. For this accurate solution, Δt is 1/8000. The evolution of the cellular domain from this simulation is then used in the subsequent test simulations. We implement four of these test simulations, corresponding to four separate levels of refinement, with the space- and time-steps each halving as the level number increases. The first level corresponds to no refinement of the mesh, i.e. the standard mesh shown in Fig. 3.1, and a Δt of 1/500. The next levels correspond to one, two, and three mesh refinements, with time-steps of 1/1000, 1/2000 and 1/4000, respectively. Each simulation is run over $t \in [0, 1]$. The evolution of the tissue over time is shown in Fig. 3.4. We also show the profile of the diffusing chemical during the second test simulation, with one iteration of mesh refinement and $\Delta t = 1/1000$.

A simple check that simulations behave as expected is to calculate the total chemical in the system, $\bar{c}(t)$, at each time-point. This is approximated by

$$\bar{c} = \int_{\Omega(t)} c_h \, \mathrm{d}\mathbf{x} = \int_{\Omega(t)} \sum_{i=1}^{N(t)} \alpha_i \phi_i \, \mathrm{d}\mathbf{x} = \sum_{i=1}^{N(t)} \alpha_i \int_{\Omega(t)} \phi_i \, \mathrm{d}\mathbf{x}. \tag{3.26}$$

With no source or sink terms, we expect $\bar{c}$ to remain constant, and that is indeed what is found (results not shown).

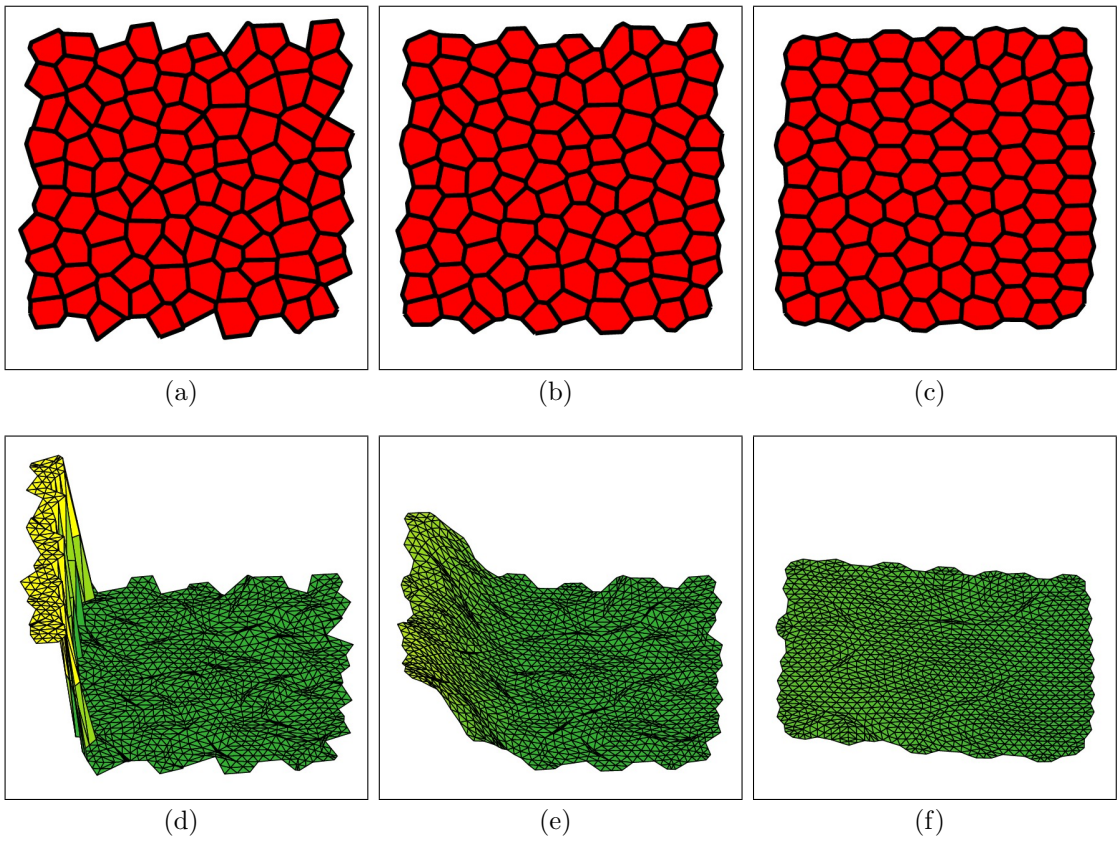


Figure 3.4: *Solution of equation* (3.25) *on a cellular domain. Parameter values can be found in Table 3.1. (a)-(c): Initial random cellular configuration of 100 cells (a) relaxing to mechanical equilibrium (c). (d)-(f): Chemical distribution, represented by height of the plot, diffusing on the same domain from an initial step function (d) which takes a value of 0.1 in a thin strip at the left-hand edge of the tissue. In this simulation two levels of mesh refinement are implemented. The limits of the z-axis in (d-f) are [0,0.1]. (a,d)* $t = 0$*, (b,e)* $t = 0.1$*, (c,f)* $t = 1$*.*

To compare our coarse approximations with the accurate numerical solution, an error function is defined as

$$\left(\int_0^T \int_{\Omega(t)} |c_h - \tilde{c}_h|^2 \, \mathrm{d}\mathbf{x} \, \mathrm{d}t \right)^{1/2},$$

where $c_h(\mathbf{x}, t)$ is the approximate and $\tilde{c}_h(\mathbf{x}, t)$ the accurate numerical solution. Recall

that we can write

$$c_h = \sum_{j=1}^{N} \alpha_j \phi_j,$$
$$\tilde{c}_h = \sum_{i=1}^{\tilde{N}} \tilde{\alpha}_i \tilde{\phi}_i,$$

where N and $\tilde{N}$ are the number of nodes in the accurate solution and approximate solution, respectively. To calculate the solution error, we interpolate the α_j values to find values at all the nodes that are part of the accurate solution. As the approximation is piecewise linear, by using linear interpolation no further error is introduced. We then define the vector, d, where $d_i = \tilde{\alpha}_i - \alpha_i$, for all i. Thus we can write

$$\begin{aligned}
E &= \int_0^T \int_{\Omega(t)} \left(\sum_{i=1}^{N'} \left| \left(\tilde{\alpha}_i - \alpha_i \right) \phi_i \right| \right)^2 \, \mathrm{d}\mathbf{x} \, \mathrm{d}t, \\
&= \int_0^T \int_{\Omega(t)} \left[d_1\phi_1 + d_2\phi_2 + ... + d_{\tilde{N}}\phi_{\tilde{N}} \right] \left[d_1\phi_1 + d_2\phi_2 + ... + d_{\tilde{N}}\phi_{\tilde{N}} \right] \, \mathrm{d}\mathbf{x} \, \mathrm{d}t, \\
&= \int_0^T \int_{\Omega(t)} \left[d_1^2\phi_1^2 + d_1 d_2 \phi_1 \phi_2 + ... + d_2 d_1 \phi_2 \phi_1 + d_2^2 \phi_2^2 + ... + d_{\tilde{N}}^2 \phi_{\tilde{N}}^2 \right] \, \mathrm{d}\mathbf{x} \, \mathrm{d}t, \\
&= \int_0^T d^T M d \, \mathrm{d}t,
\end{aligned}$$

where M is a matrix given by

$$M_{ij} = \int_{\Omega(t)} \phi_i \phi_j \, \mathrm{d}\mathbf{x}.$$

Approximating the error as piecewise constant in time we obtain

$$E = \sum_{k=1}^{N'_T} \Delta t' \left(d^n \right)^T M^n d^n,$$

where N'_T and $\Delta t'$ refer to the number of time-points and the time-step, respectively, in the accurate solution. Clearly, the approximate solution does not update for ev-

ery value of k as Δt is larger in the test solution. The α_i values therefore update periodically with k, and are constant between updates.

The value of the error function for each simulation is shown in Table 3.2. We

Refinement level	Value of error function
1	2.2×10^{-4}
2	8.0×10^{-5}
3	3.2×10^{-5}
4	1.2×10^{-5}

Table 3.2: *Value of error function for each level of refinement. Space- and time-steps each halve as the refinement level increases. See text for details.*

observe a clear convergence as the size of the space- and time-steps decrease. For each increase in refinement level, the solution error decreases by a factor of between 2.5 and 2.75.

In Section 3.6 we examine how the time taken to form and solve the system of matrix equations (3.19) scales with the number of cells in the tissue. This is an important consideration, as epithelial tissues grow over several orders of magnitude during development. The *Drosophila* wing disc, for example, grows from around 50 cells to over 30,000 over the course of a few days (Martín et al., 2009). It is therefore important that our scheme be robust enough to deal with tissues with these numbers of cells in reasonable computational time-frames.

3.6 Simulation run time

To get an idea of how simulation time of the numerical scheme scales with tissue size, we run three test simulations with tissues of 100 cells, 1000 cells, and 10,000 cells, respectively. The initial condition and parameter values are the same as in Section 3.5, and each simulation is run for 1000 iterations, corresponding to a Δt of 1/1000, with no refinement of the FE mesh. At each iteration, the time taken to form and

solve the matrix equations is recorded, and we subsequently take the average time over the 1000 iterations.

Simulations are performed in `Matlab`, with matrices formed in `C++`-based `mex` functions. The matrix system (3.18) is solved using the `Matlab` backslash operator. Simulations are performed on a 'no name' brand machine with 4 AMD (Advanced Micro Devices) Phenom(tm) II 945 processors (3GHz clock speed, 2MB L2 cache, 6MB L3 cache), 64-bit kernel running Ubuntu Linux 10.04 LTS.

Number of cells	100	1000	10,000
Number of nodes	340	3130	30,400
Number of elements	600	6000	60,000
Mean time per iteration (s)	5.7×10^{-3}	6.7×10^{-2}	1.0

Table 3.3: *Average time taken to form and solve the system of matrix equations for chemical distribution for tissues of 100, 1000, and 10,000 cells.*

We observe from Table 3.3 that as the number of cells increases by a factor of 10, the mean time taken per iteration increases by a factor between 12 and 15. For tissues with up to tens of thousands of cells it is therefore possible to accurately simulate in reasonable time-frames. These cell numbers are representative of most systems of biological interest. We have not tested the scheme for much larger tissue sizes, of the orders of hundreds of thousands or millions of cells, which may show much larger increases in time as the cell number increases. These orders of magnitude may be relevant in some application areas, and, in these examples, more efficient methods may need to be considered, including whether aspects of the system could be parallelised. In these cases, however, it could be argued that continuum models might be more appropriate than the cell-based approach we take to modelling.

We have now seen how the FE mesh is created from the positions of the cell vertices, and shown that the solution converges in a diffusion example without any junctional rearrangements or proliferation at the cell level. For more realistic examples we must reincorporate these processes, and the next section will focus on what happens to the

mesh in such cases.

3.7 Effects of cellular rearrangements

3.7.1 Proliferation

As cell vertex positions are used to create the FE mesh, when a cell divides the mesh necessarily changes. The amount of morphogen at the new nodes created by the division must be found. Fig. 3.5 shows the effect of mitosis on the mesh within a dividing cell. The original mesh in the cell (a), consisting of six elements, changes to that shown in (b), with ten elements.

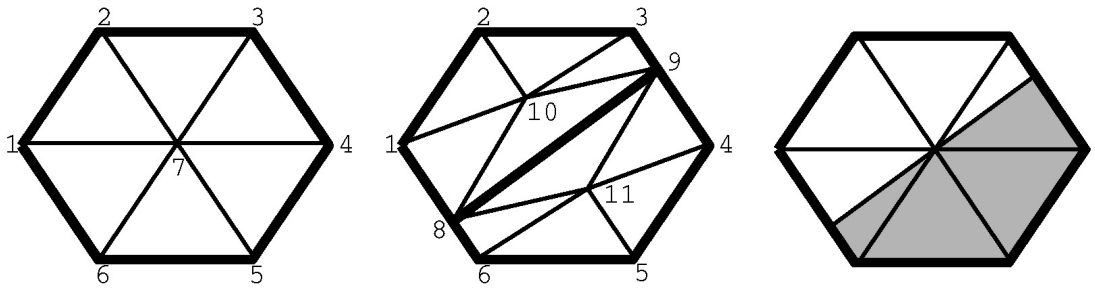


Figure 3.5: *Finite elements corresponding to an hexagonal cell before and after mitosis. The cell in (a) contains six triangular elements, whilst the two daughter cells in (b) each contain five, for a total of ten. The values at the four new nodes (8-11) must be calculated. (c) Temporary FE mesh used during mitosis. This mesh contains the two new nodes that correspond to the two new cell vertices, but still has a node at the centre of the mother cell, rather than the two new nodes at the centres of the two daughter cells.*

Since the FEM provides a continuous approximation in the spatial domain to the chemical distribution, $c(\mathbf{x}, t)$, we may interpolate to find the value at the two new nodes that are also cell vertices. For example, the value at node 9 can be calculated from the known values at nodes 3 and 4. If d_{ij} represents the distance between nodes

i and j, then the value at node 9, c_9, is approximated by

$$c_9 = c_4 \left(\frac{d_{39}}{d_{34}} \right) + c_3 \left(\frac{d_{49}}{d_{34}} \right).$$

These new vertices also affect the FE mesh within cells adjacent to the dividing cell that share the edges on which the new vertices have been created. For example, in this case, the cells that share edges 1-6 and 3-4 will each gain an extra element. There are also two extra new nodes in the FE mesh at the centres of the new cells (10 and 11 in this example), while the node at the centre of the previous cell (node 7), no longer exists.

The total amount of chemical, $C_k(t)$, in a cell k is estimated by integrating the FE approximation to c over the cell, i.e.

$$C_k = \int_{\Omega_k} c_h \, \mathrm{d}\mathbf{x} = \int_{\Omega_k} \sum_{l=1}^{L_k} \alpha_l \phi_l \, \mathrm{d}\mathbf{x} = \sum_{l=1}^{L_k} \alpha_l \int_{\Omega_k} \phi_l \, \mathrm{d}\mathbf{x}, \tag{3.27}$$

where Ω_k is the area of the domain occupied by cell k, l is a local node index and $L_k(t)$ is the number of nodes in the cell. Now, suppose at a given time-point $t = t^n$ the total amount of chemical, C_k^n, in a cell is known, along with the values at all nodes apart from one. Assume without loss of generality that this is node L_k^n. The total amount of chemical in cell k at this time can be written

$$C_k^n = \sum_{l=1}^{L_k^n - 1} \alpha_l^n \int_{\Omega_k} \phi_l^n \, \mathrm{d}\mathbf{x} + \alpha_{L_k^n} \int_{\Omega_k} \phi_{L_k^n} \, \mathrm{d}\mathbf{x},$$

and thus an expression for the value at node L_k^n is obtained:

$$\alpha_{L_k^n} = \frac{C_k^n - \sum_{l=1}^{L_k^n - 1} \alpha_l^n \int_{\Omega_k} \phi_l^n \, \mathrm{d}\mathbf{x}}{\int_{\Omega_k} \phi_{L_k^n} \, \mathrm{d}\mathbf{x}}. \tag{3.28}$$

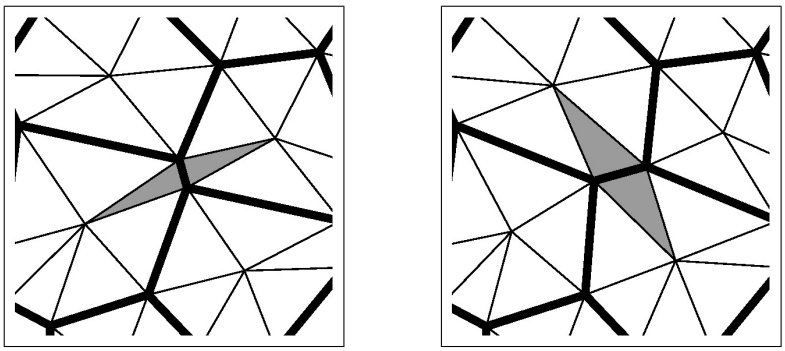
Note that $\alpha_{L_k^n}$ will be positive, as $C_k^n > \sum_{l=1}^{L_k^n - 1} \alpha_l^n \int_{\Omega_k} \phi_l^n \, \mathrm{d}\mathbf{x}$ and $\int_{\Omega_k} \phi_{L_k^n} \, \mathrm{d}\mathbf{x} > 0$.

After division, if the total amount of chemical in each of the new cells is known, the value at the new central node can be found using (3.28). The only remaining question is what the total amount of chemical in each cell should be. The simplest method would be to find the total amount in the mother cell and divide it equally between the two daughter cells. However, this neglects two important considerations. The first is that the areas of the daughter cells are not necessarily equal, and a larger cell is more likely to have a greater total amount of morphogen. The second is that the cell could be sitting on a sharp gradient of morphogen, in which case the amount in one section of the mother cell could be significantly greater than that in the rest of the cell, and this should be reflected in the daughter cells.

In order to solve this problem a temporary mesh for each of the new cells is adopted, as shown in Fig. 3.5(c), in order to calculate an approximation to the previous total amount of chemical in the section of the mother cell now taken up by each daughter cell. This temporary mesh includes the two new cell vertices created during mitosis, but not the two new central nodes. The values at all nodes are known, so (3.27) can be used to find the total amounts in each shaded region. Finally, we can apply (3.28) to find the values at the central nodes of the new cells.

3.7.2 T1 transitions

T1 transitions also alter the FE mesh, though not as dramatically as a proliferation event. In the example shown earlier in Fig. 1.3, cells 1 and 2 each lose an element, whereas cells 3 and 4 gain an extra element each. As this type of rearrangement only occurs on very short edges, the values at nodes C and D are taken to be equal to the average of those at A and B. Fig. 3.6 demonstrates the effect on the FE mesh of a T1 swap.



(a) (b)

Figure 3.6: *The effect of a T1 transition on the FE mesh. (a) The two cells that share the edge that is about to undergo the transition each contain one element (shaded) that the edge is part of. (b) After the transition, the two elements have disappeared, and two new elements (shaded) have formed in the cells that share the new edge. The values at the new nodes are both given the average of the value at the old nodes, as this is a good approximation over the small distances that the transition occurs.*

3.7.3 Cell death

As a dying cell shrinks, T1 transitions occur on the short edges. These are dealt with, from the FE mesh point of view, as described in Section 3.7.2. When the final triangular cell dies off, the three elements in the dying cell are removed from the FE system. The three cells neighbouring the apoptotic cell will also each lose an element. Adjacent elements are reconnected to the node at the centre of the old cell. The value at this node is known, as the centres of cells are already mesh nodes.

We are now able to run a full simulation, with all the cellular processes described earlier, including T1 transitions, cell growth, proliferation and death, and the morphogen spreading model all in place. In Section 3.8 we will demonstrate the model in action.

3.8 Morphogen-dependent growth

In simulations to this point, the diffusing chemical has been de-coupled from the mechanical properties of cells. By making cell growth explicitly dependent on mor-

phogen distribution, we can begin to probe the role of the Dpp in the *Drosophila* wing imaginal disc, which has often been used as a model system for the study of morphogens. As described in Chapter 1, the disc grows from an embryonic primordium consisting of about 55 cells to reach a final size of roughly 30,500 cells (Martín et al., 2009). Growth is sigmoidal, with an average cell doubling time (CDT) of roughly 10-12 hours (Garcia-Bellido and Merriam, 1971), and is uniform across the disc.

Dpp is a morphogen that acts as an important growth-promoting factor in the wing disc. When Dpp expression is reduced, smaller wings are observed (Spencer et al., 1982), and large discs occur when Dpp is over-expressed (Burke and Basler, 1996). The exact mechanism by which Dpp controls growth is unknown. One particular mystery is how a morphogen that forms a gradient can lead to uniform growth in the wing disc. Many theories have been postulated, none of which fully explain the observed phenomena (Aegerter-Wilmsen et al., 2007, Day and Lawrence, 2000, Hufnagel et al., 2007, Rogulja and Irvine, 2005, Schwank and Basler, 2010, Serrano and O'Farrell, 1997, Wartlick et al., 2011).

The framework developed in this chapter can be used to test some of the hypotheses regarding the mechanisms by which Dpp controls growth. The first step towards this goal is to set up a steady gradient of Dpp across the cellular domain and allow the growth rate of cells to be dependent on the value of Dpp at the centre of the cell. We expect proliferation to occur preferentially in regions of high Dpp. In order to examine growth regulation, changes to the model can be made, and those that elicit the desired uniform growth isolated.

Equation (2.6) can be modified to be dependent on Dpp as follows:

$$\frac{\mathrm{d}v_k}{\mathrm{d}t} = (1 + \lambda c_k) g_k v_k \left(1 - \frac{v_k}{V_k}\right), \tag{3.29}$$

where g_k is the growth speed of cell k, $v_k(t)$ is the volume, V_k is the target volume, $c_k(t)$

is the value of Dpp at the central node of the cell and λ is a parameter representing the strength of the effect of morphogen signalling on the growth rate. Equation (3.29) can no longer be solved analytically, due to the inclusion of a dependence on c_k, which itself is a complex time-dependent function. Therefore we solve numerically using the forward Euler method as follows:

$$v_k^{n+1} = v_k^n \left(1 + g_k(1 + \lambda c_k)\Delta t \left(1 - \frac{v_k^n}{V_k}\right)\right).$$

3.8.1 Radial Dpp gradient

A steady radial Dpp gradient can be set up in our system by including both source and degradation terms in the function f on the right-hand side of (3.1). Representing the source term as piecewise linear on the finite elements, we define the function $f_1(c, \mathbf{x}, t)$ by

$$f_1 = \sum_{i=1}^{N} s_i \phi_i,$$

where $s_i(t)$ is a weighting given to each basis function, ϕ_i, within the source term. The s_i values are set as follows

$$s_i = \begin{cases} S & |\mathbf{x}_i| < r \\ 0 & |\mathbf{x}_i| > r \end{cases},$$

where S is a constant and $|\mathbf{x}_i|$ is the distance from node i to the centre of the tissue. A subset of basis functions within a radius r of the centre of the tissue are thus designated to be source-producing.

Degradation of Dpp, meanwhile, is implemented by adding a term, $f_2(c, \mathbf{x}, t)$, of the form

$$f_2 = -dc,$$

where d is a constant, representing the rate of degradation. Incorporating $f = f_1 + f_2$

into the matrix equations (3.19), the equation for the vector R becomes

$$R_j = \Delta t \sum_{i=1}^{N^n} s_i^n \int_{\Omega^n} \phi_i^n \phi_j^n \ \mathrm{d}\mathbf{x} + (1 - d\,\Delta t) \sum_{i=1}^{N^{n-1}} \alpha_i^{n-1} \int_{\Omega^{n-1}} \phi_j^{n-1} \phi_i^{n-1} \ \mathrm{d}\mathbf{x}.$$

The governing equation we are now solving is given by

$$\frac{\partial c}{\partial t} - \nabla \cdot (\nu \nabla c) = -dc + \sum_{i=1}^{N} s_i \phi_i. \tag{3.30}$$

Fig. 3.7 shows a sequence of images from a simulation run over $t \in [0, 100]$, with $\Delta t = 1/1000$ (see also Thesis Movie 3 at http://aaronmsmith.co.uk/movies). Other parameter values are given in Table 3.4. This simulation includes junctional

Parameter	C_L	C_P	C_A	C_H	C_D	C_{B1}	C_{B2}	$n_1 - n_4$	f_p
Value	0.1	0.05	2000	0.001	0.1	0.1	50	2	15
Parameter	μ	g_k	T_{T1}	ν	S	r	d	λ	
Value	1	0.1	0.05	0.01	0.1	0.2	1	100	

Table 3.4: *Parameter values used in simulations of Drosophila wing disc.*

rearrangements, cell growth and mitosis, but not cell death. To demonstrate the effect of the new term in equation (3.29), we make proliferation a stochastic process, dependent on cell volume, and we observe proliferation rates at different locations in the tissue. The probability of proliferation for cell k at each iteration is given by

$$p_m = \begin{cases} \Delta t \, (v_k / V_k) \, / f_p & v_k \geq 0.85 V_k \\ 0 & v_k < 0.85 V_k \end{cases}. \tag{3.31}$$

In other words, above a cut-off point at 85% of the target volume, the probability of division is proportional to the ratio between cell volume and the target volume. This ensures that larger cells are more likely to divide and therefore there should be more proliferation events in regions of the tissue that are growing faster. The factor f_p ensures that, on average, a cell at the target volume will divide once in every f_p

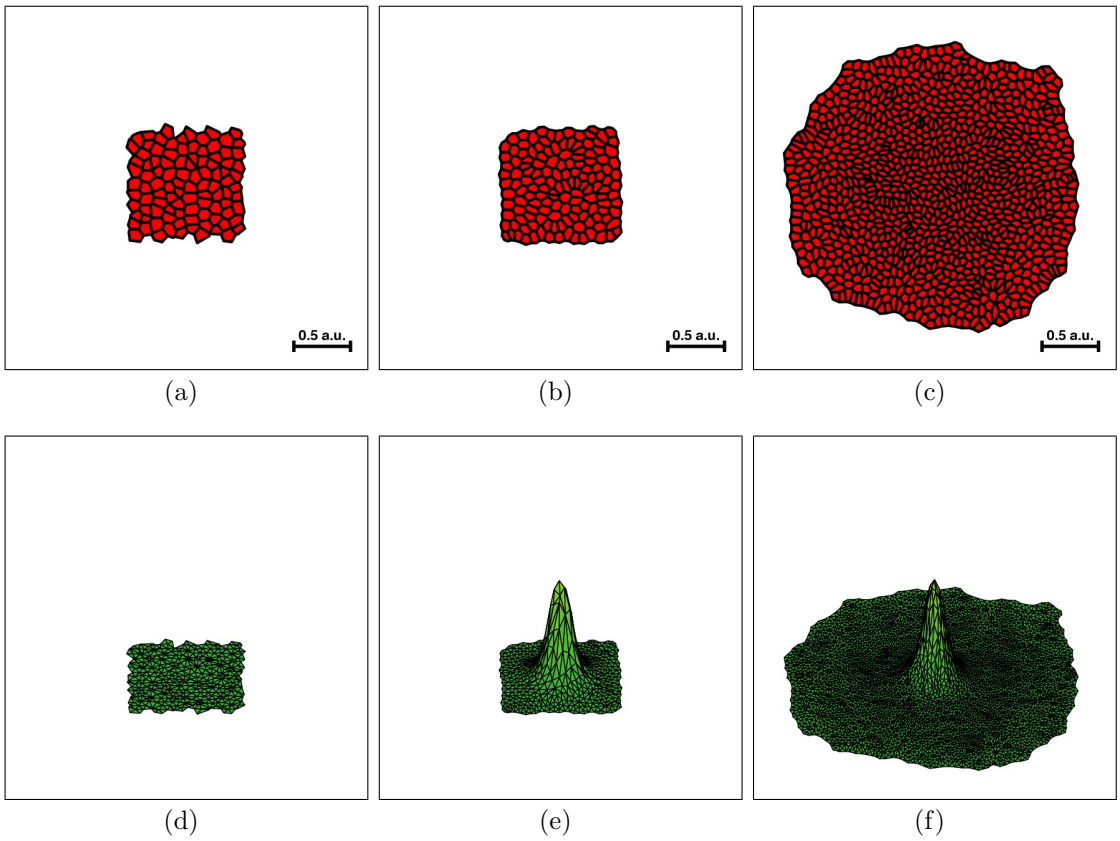


Figure 3.7: *Simulation of tissue growth with radial Dpp gradient. Parameter values can be found in Table 3.4. (a-c) The tissue evolves according to force and growth laws, along with junctional rearrangements and proliferation. Cell growth is accelerated by the amount of Dpp in the cell. Scale bars show 0.5 arbitrary units (a.u.) (d-f) Solution of equation* (3.30)*. The Dpp distribution, represented by the height of the plot, is initially zero everywhere, before source is produced in a small radius around the centre of the disc and diffuses throughout the domain. The limits of the z-axis in (d-f) are [0,0.05]. (a,d)* $t = 0$*, (b,e)* $t = 1$*, (c,f)* $t = 100$*.*

time-units. Each cell is initially at the target volume, as described in Section 2.12.

As growth has been made dependent on Dpp quantity, it is expected that cells in central regions will grow faster than those on the outside, and subsequently proliferate more frequently. However, a correction must be made for the fact that the total number of cells in a region between radii r and $r + dr$ for small dr is approximately proportional to r. As there are more cells at larger radii, there will be extra proliferation events, so a direct comparison is misleading. The histogram data are therefore divided by the radius at the centre of each bin. As the tissue is growing,

only cell divisions that occur within its original radius are considered. The relative number of divisions at greater radii will be small as cells only exist in these regions for part of the simulations. Fig. 3.8 shows the corrected histogram. The distribution

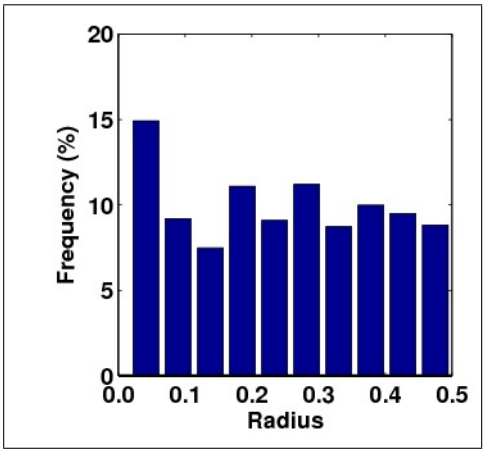


Figure 3.8: *Histogram of the radii at which mitosis events occur for simulation shown in Fig. 3.7.*

is more or less uniform, as would be expected if growth were uniform throughout the disc. However, the peak of the distribution is at the centre of the tissue, with 15% of proliferation events occurring in the first bin of the histogram. This shows that morphogen-dependent growth has driven extra proliferation events at the centre of the tissue.

In vivo, growth across the *Drosophila* wing imaginal disc, measured via proliferation rates, is uniform. Fig. 3.9, taken from Schwank et al. (2008), demonstrates levels of Dpp signalling across the wing disc and rates of proliferation. More complex simulations are therefore required to shed insight into mechanisms that control growth. These could take the form of suggested hypotheses such as gradient models, where cells respond to the local steepness of the Dpp gradient (Day and Lawrence, 2000, Lawrence and Struhl, 1996); hybrid models, where cells in some regions of the tissue respond to the gradient and cells in other regions to the absolute value (Rogulja and Irvine, 2005); inhibitor models, where a parallel inhibitory gradient exists (Serrano and O'Farrell, 1997); and mechanical feedback models, where stress and stretching

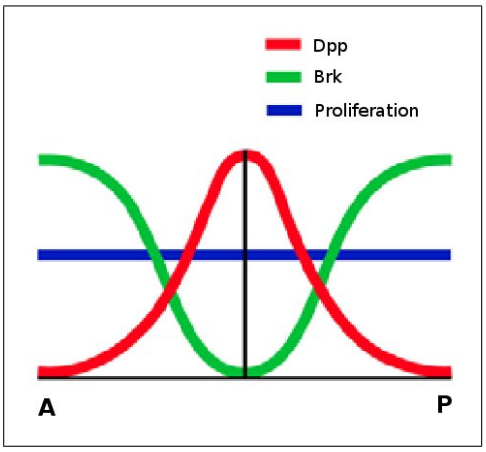


Figure 3.9: *Illustration of Dpp level, Brk level and cell proliferation in wild-type disc. A - anterior, P - posterior. Reprinted with permission from Schwank et al. (2008).*

as well as morphogen distributions feed back into growth (Hufnagel et al., 2007, Shraiman, 2005). These models are reviewed in Schwank and Basler (2010).

Two recent studies claim to have finally solved the riddle of how uniform growth in the wing disc is achieved, despite the presence of a Dpp gradient. Schwank et al. (2011) built on their previous work, which had shown that Dpp acts to repress growth in lateral regions of the wing disc by repressing the growth inhibitor Brinker (Brk) (Schwank et al., 2008). They over-expressed Dpp throughout the wing disc, thus down-regulating Brk, and showed that excess proliferation occurred in lateral regions only. In this earlier study they postulated a second gradient, parallel to Dpp, that inhibits growth in medial regions. In the 2011 publication, they showed that the Fat tumour-suppressor pathway is not reliant on Dpp activity, as had previously been supposed. They went on to show that Fat represses growth in medial regions of the disc, and thus fulfils the role of a complementary growth regulation system that they had hypothesised.

Wartlick et al. (2011), meanwhile, claimed that it is not Dpp signalling levels, *per se*, that induce growth, but temporal changes in those levels. They showed that in cells of the wing disc, a change in signalling levels of 50% induces cell division. This could explain how uniform growth is achieved, if the relative change in Dpp levels

were uniform across cells, despite the fact that the absolute values of Dpp would be far greater in certain regions of the disc.

Clearly, there is still no definitive answer to the question of how uniform growth is achieved in the presence of a morphogen gradient. Different biological systems may use different means to achieve the same end, drawing on one or more of the models suggested above. Our simulations have demonstrated that tissue-level effects can be elucidated by enabling a feedback between morphogen distribution and growth. Future work could focus on resolving which types of model faithfully replicate the observed phenomena.

3.9 Summary

In this chapter, we began to incorporate a model for chemical signalling factors, known as morphogens, into our framework. We derived a weak form based on the ALE reference frame, and implemented the diffusion equation on a moving domain. This was solved using the FEM by taking a triangular mesh of the domain based on the positions of cell vertices and cell centres. We showed how the integrals are performed by mapping to a canonical triangle. We then looked at the convergence properties of the numerical solution by computing an error function to estimate the deviation from a very accurate numerical solution, obtained using a highly refined mesh and small time-steps. We examined the time taken to run simulations, before examining the effects of junctional rearrangements on the FE mesh.

This new framework enables the diffusing chemical to feed back into the vertex model and influence variables such as the growth rate of cells or the mechanical forces. We showed an example in which the growth rate of cells was made dependent on the distribution of a chemical representing Dpp in the *Drosophila* wing imaginal disc. It was shown that this led to a higher rate of proliferation in areas of the disc where

the amount of Dpp was greatest. This example demonstrates a potential utility of the system, where simple hypotheses regarding the nature of growth factors can be tested to check if the results are consistent with what is known about growth of the tissue. Further work is required to decipher how uniform growth can result, despite the presence of a morphogen gradient. Our model allows this kind of question to be examined systematically.

The model has the potential to be adapted to other systems. Morphogens have been shown to play crucial roles in growth and patterning in other organisms, including Sonic hedgehog in mouse and chick limb development (Bénazet and Zeller, 2009). Morphogens in *Xenopus* were among the first to be shown to belong to known families of growth factors, such as fibroblast growth-factor and the transforming growth-factor-beta families (Kimelman and Kirschner, 1987). Returning to the *Drosophila* wing disc, the morphogen Wingless forms a gradient that establishes the dorso-ventral axis and drives growth, however as we have seen in this chapter growth is uniform across the disc (Milàn et al., 1996, Schwank and Basler, 2010).

As simulations become more sophisticated, the potential for them to be adapted to solve problems in other areas will increase. It will also be possible to adjust the model to work with other types of cell representations. As long as the cell-domain can be broken up into elements for the FE mesh, and the movement of the domain is prescribed by rules between iterations, the formulation we propose can be implemented.

In Chapter 4 we will implement an extension to this work. In the current chapter we made growth dependent on the amount of morphogen at the centre of each cell, which is not biologically realistic. *In vivo*, cell surfaces contain receptors that bind with the diffusing chemical and lead to cellular ingestion. This process can be modelled, allowing cells to have an internal chemical quantity that moves with the cell and affects its growth. This will require a system of two coupled equations, for the

diffusing and internal chemicals.

Chapter 4

Chemical production and ingestion

In Chapter 3, we developed a representation of diffusing growth factors that can be naturally incorporated within the vertex model framework. Using an ALE reference frame and the FEM, we showed how the diffusion equation can be solved on the moving cellular domain. We ran simulations in which the growth rate of cells was made dependent on the local chemical concentration. Simple source and degradation functions were implemented, enabling chemical to be added or removed from the system.

In vivo, morphogens are produced by biochemical reactions within each cell. Our source term in Section 3.8.1 was defined to be piecewise linear on the finite elements, which, in most cases, overlap several cells. A more realistic approach would be to have the source functions defined on cells, so that rates of production could be adjusted on a cell-by-cell basis.

In our previous simulations, the cellular growth rate was dependent on the concentration of chemical at the centre of the cell, and this concentration was not affected by the growth-promoting process. *In vivo*, the surface of each cell contains receptor molecules, which bind with the diffusing chemical, eventually leading to cellular ingestion of the chemical (endocytosis). We desire a more realistic way to repre-

sent this process, in which cells ingest the diffusing chemical and have an internal concentration, which can then influence the cellular growth rate.

We begin this chapter in Section 4.1 by defining a source function, $S(\mathbf{x}, t)$, that is piecewise constant on cells. We show how this term feeds into the system of matrix equations (3.19) and how the vector on the right-hand side of the system can be created efficiently. In Section 4.2 we define an internal chemical concentration, $C(\mathbf{x}, t)$, and an endocytotic rate, $E(\mathbf{x}, t, c, C)$. We show how endocytosis affects the external, diffusing chemical and leads to another term in the system of matrix equations. We examine how E can be chosen to simplify calculations. Section 4.3 introduces the governing equation for C, with an advection term for cell movement. We explain how the internal concentration is updated in simulations as cells ingest chemical and the domain moves.

In this framework the internal chemical concentration, C, is a spatially-dependent function defined over the whole domain. An alternative approach would be to have a value of internal chemical for each cell, with a set of ODEs representing the change in each over time as more chemical is ingested. This method is used by Schilling et al. (2011) and Wartlick et al. (2011). In our scheme a single PDE with an advection term represents the same process. In the simplest case, the approach suggested here reduces to the alternative framework, as we will show in Section 4.3. The advantage of our technique is that the value of internal chemical is known at each point on the domain. This allows the effect of the internal chemical on forces and physical properties of the cell to be resolved at a finer scale. Extensions to this work may include diffusion processes on a cellular level, to model phenomena such as planar cell polarity (Aigouy et al., 2010).

In Section 4.4 we run simulations of cells relaxing to mechanical equilibrium, with chemical production, ingestion and diffusion. We show that the total amount of chemical diffusing in the system is equal to the amount produced less the amount ingested,

validating our model implementation, and that internal chemical concentrations follow the expected concentration gradient. In Section 4.5, we describe the effects of cellular rearrangements on the internal chemical concentration, before running simulations with rearrangements in Section 4.6. Finally, in Section 4.7, we will describe recent experiments on the *Drosophila* epidermis, and suggest how our new modelling framework can be used to probe questions of interest, such as whether secretion of a limited quantity of a growth factor is a viable mechanism of size control.

4.1 Production

We denote the chemical production rate of cell k by $\hat{\beta}_k(t)$. A source function, $S(\mathbf{x}, t)$, is defined as

$$S = \sum_{k=1}^{N_c} \frac{\hat{\beta}_k}{a_k} \Psi_k, \tag{4.1}$$

where $N_c(t)$ is the number of cells, $a_k(t)$ is the area of cell k, and $\Psi_k(\mathbf{x}, t)$ is a piecewise constant function, equal to one in cell k and zero elsewhere. The production rate at a point on the surface of the cell, $\beta_k(t)$, is given by $\beta_k = \hat{\beta}_k / a_k$. The discrete-time approximation to (4.1) is given by

$$S^n = \sum_{k=1}^{N_c^n} \beta_k^n \Psi_k^n,$$

where the superscript n indicates that the function is evaluated at time $t = t^n$ (see Section 2.8 and Section 3.3).

In Chapter 3 we defined our approximation, c_h^n, to the diffusing chemical, c, by

$$c_h^n = \sum_{i=1}^{N^n} \alpha_i^n \phi_i^n,$$

where N^n is the number of basis functions at time $t = t^n$ and α_i^n are the coefficients

of the basis functions, $\phi_i^n(\mathbf{x})$. The α_i^n values are calculated by solving the matrix system $(L^n + W^n)\alpha^n = R^n$, where the matrices are given by the system (3.19), which we reproduce here for the benefit of the reader:

$$
\begin{aligned}
L_{ji} &= \int_{\Omega^n} \left(\phi_j^n \phi_i^n + \Delta t \nabla \phi_j^n \cdot (\nu^n \nabla \phi_i^n) \right) \mathrm{d}\mathbf{x}, \\
W_{ji} &= \Delta t \int_{\Omega^n} \nabla \phi_j^n \cdot (\phi_i^n \mathbf{w}^n) \, \mathrm{d}\mathbf{x}, \\
R_j &= \Delta t \int_{\Omega^n} \phi_j^n f^n \, \mathrm{d}\mathbf{x} + \sum_{i=1}^{N^{n-1}} \alpha_i^{n-1} \int_{\Omega^{n-1}} \phi_j^{n-1} \phi_i^{n-1} \, \mathrm{d}\mathbf{x}.
\end{aligned}
$$

Replacing the function $f(\mathbf{x}, t)$ on the right-hand side of (3.19) with the source term (4.1), we obtain

$$
R_j = \underbrace{\Delta t \sum_{k=1}^{N_c^n} \beta_k^n \int_{\Omega^n} \phi_j^n \Psi_k^n \, \mathrm{d}\mathbf{x}}_{R'} + \sum_{i=1}^{N^{n-1}} \alpha_i^{n-1} \int_{\Omega^{n-1}} \phi_j^{n-1} \phi_i^{n-1} \, \mathrm{d}\mathbf{x}.
$$

We desire an efficient way to generate the vector R'. One method would be to loop over the test functions, ϕ_j^n, and for each j sum the integrals of the products of the basis function with each Ψ_k^n. However, this is inefficient as ϕ_j^n and Ψ_k^n are zero in most places, and the product $\phi_j^n \Psi_k^n$ is therefore often zero. In fact, some of the basis functions are only non-zero in one cell (those whose nodes take a value of one at the centre of a cell), and the majority are only non-zero in two or three cells. The Ψ_k^n functions, meanwhile, are only non-zero in one cell, so integrating $\phi_j^n \Psi_k^n$ for every j, k combination is wasteful. Instead, we begin by setting the vector $R' = 0$. We then loop over each cell k, and for each k we loop over the triangular elements within that cell. Each triangle is non-zero for three basis functions, namely the three basis functions that peak at its three nodes. We also know that only one Ψ^n is non-zero in the current cell, namely Ψ_k^n, and is equal to one. Therefore, within each element, $\mathbf{e}^n$,

three integrals of the form

$$\beta_k^n \int_{\mathbf{e}^n} \phi_j^n \, \mathrm{d}\mathbf{x}, \tag{4.2}$$

must be performed, corresponding to the three non-zero basis functions. For each of these three j values, the result must be added to the jth entry in R'. At the end of the loops, each entry in R' will contain the complete sum $\Delta t \sum_{k=1}^{N_c^n} \beta_k^n \int_{\Omega^n} \phi_j^n \Psi_k^n \, \mathrm{d}\mathbf{x}$. Note that this procedure could be parallelised in order to attain a computational speed-up. The integral (4.2) is performed by mapping to the canonical triangle, as described in Section 3.4. We find that

$$\beta_k^n \int_{\mathbf{e}^n} \phi_j^n \, \mathrm{d}\mathbf{x} = \beta_k^n |J_{\hat{\mathbf{e}}}| \int_{\hat{\mathbf{e}}} \hat{\phi}_j \, \mathrm{d}\hat{\mathbf{x}} = \frac{1}{6} \beta_k^n |J_{\hat{\mathbf{e}}}|,$$

where $J_{\hat{\mathbf{e}}}$ is the Jacobian of the mapping from $\mathbf{e}^n$ to $\hat{\mathbf{e}}$.

Given a production rate, $\hat{\beta}_k$, for each cell, we can now simulate the morphogen spreading model with the source function (4.1) implemented. In Section 4.2 we will define an internal chemical concentration for each cell, and allow cells to ingest the diffusing chemical. This represents cell surface receptor molecules *in vivo* binding with the diffusing growth factors and inducing endocytosis. Ultimately this will allow us to make properties of the cell, such as the growth rate, dependent on the internal concentration.

4.2 Ingestion

We denote the endocytotic rate at a point on the domain by $E(\mathbf{x}, t, c, C)$, where $C(\mathbf{x}, t)$ is the amount of ingested chemical at each point in the tissue. The rate of endocytosis incorporates the binding of the chemical to surface receptors and its subsequent ingestion into the cell. A more realistic model would have separate quantities for bound chemical and intracellular chemical. This would allow us to account for

differences in binding and ingestion rates and for more complex effects such as reversible binding. For the sake of simplicity we wrap these effects together in a single process which occurs at rate E.

We define $C = \sum_{k=1}^{N_c} \gamma_k \Psi_k$, where $\gamma_k(t)$ is spatially constant. C is thus a spatially piecewise constant function, taking a value of γ_k in cell k. The total ingested chemical, $\hat{\gamma}_k(t)$, in a cell is given by $\hat{\gamma}_k = \gamma_k a_k$.

The function E is continuous in each cell, k, but may be discontinuous across cell boundaries if there is a dependence on C. In each cell, the dependence of E on C is actually a dependence on $\hat{\gamma}_k$, that is to say the endocytotic rate is not affected by the internal concentrations in neighbouring cells. We can thus break E down into a sum of functions for each cell denoted $E_k(\mathbf{x}, t, c, \hat{\gamma}_k)$. An expression for E is then given by

$$E = \sum_{k=1}^{N_c} E_k \Psi_k. \tag{4.3}$$

Note that the functions E_k are in some ways analogous to the rate of production at a point on the cell surface, β_k, though E_k is not necessarily constant across each cell.

A discrete-time approximation to (4.3) is given by

$$E^n = \sum_{k=1}^{N_c^n} E_k^n \Psi_k^n.$$

Equation (4.3) can be incorporated into the matrix system of equations (3.19) by adding a new term to its right-hand side, so that R_j becomes

$$\begin{aligned} R_j = &\underbrace{-\Delta t \sum_{k=1}^{N_c^{n-1}} \int_{\Omega^{n-1}} \phi_j^{n-1} E_k^{n-1} \Psi_k^{n-1} \, \mathrm{d}\mathbf{x}}_{R''} + \Delta t \sum_{k=1}^{N_c^n} \beta_k^n \int_{\Omega^n} \phi_j^n \Psi_k^n \, \mathrm{d}\mathbf{x} \\ &+ \sum_{i=1}^{N^{n-1}} \alpha_i^{n-1} \int_{\Omega^{n-1}} \phi_j^{n-1} \phi_i^{n-1} \, \mathrm{d}\mathbf{x}. \end{aligned} \tag{4.4}$$

The E_k terms cannot be taken outside the integral, as E_k is not spatially constant. Note that in the new term we take values at time $n-1$, as the values of c and C at time t^n are not yet known. We will discuss how the value of C is updated in Section 4.3.

A simple example for E_k is $E_k = b_k c$, where b_k is a parameter proportional to the density of receptor molecules on the cell surface, which is assumed in this case to be constant across the cell. A cell with a greater density of receptors is therefore able to ingest a greater proportion of the chemical in its surroundings. In this case the endocytotic rate is independent of the total internal chemical currently in the cell, denoted $\hat{\gamma}_k$. We might instead assume that there exists a maximum 'carrying capacity', $\hat{\gamma}_k^{\max}$, for the internal chemical, in which case an expression for the endocytotic rate would be of the form $E_k = b_k c\,(1 - \hat{\gamma}_k/\hat{\gamma}_k^{\max})$. Here the endocytotic rate is proportional to c when $\hat{\gamma}_k$ is small, but tends to zero as $\hat{\gamma}_k$ tends to $\hat{\gamma}_k^{\max}$. We can imagine a class of E_k functions of the form $E_k = g(\hat{\gamma}_k)c$, where there is no explicit dependence on $\mathbf{x}$ or t, and a linear dependence on c. For these types of function R'' becomes

$$R''_j = -\Delta t \sum_{k=1}^{N_c^{n-1}} g(\hat{\gamma}_k^{n-1}) \sum_{i=1}^{N^{n-1}} \alpha_i^{n-1} \int_{\Omega_k} \phi_j^{n-1} \phi_i^{n-1}\, \mathrm{d}\mathbf{x}.$$

We can create this vector in a manner similar to that described in Section 4.1. Firstly, the vector R'' is initialised to zero. We loop over the cells k, and compute the function $g(\hat{\gamma}_k^{n-1})$ for the current cell. Within each cell, we loop over the elements and perform the integrals, updating the appropriate entries in R''_j each time.

We are now able to update the concentration of the external chemical, c, as our cells ingest chemical. In the next section we will look at the behaviour of the internal chemical, C, during this process.

4.3 Internal chemical concentration

We define the PDE (4.5) to represent the behaviour of the internal chemical, $C(\mathbf{x}, t)$.

$$\frac{\partial C}{\partial t} = E + \nabla \cdot (C\mathbf{w}), \tag{4.5}$$

where $\mathbf{w}(\mathbf{x}, t)$ is the speed of the cell movements. In other words, the rate of change of C at any point on the domain is equal to the endocytotic rate at that point, plus an advection term due to the cell movement. In this case, in contrast to Section 3.1, we are modelling the chemical as being internal to cells, and moving with them. The boundary condition is no flux between cells, or in/out of the tissue. The only way a cell can gain extra internal chemical is through endocytosis of the diffusing chemical.

As C is piecewise constant on cells, we multiply by a test function, $u(\mathbf{x}, t)$, from the space of all piecewise constant functions on cells. Integrating over the moving domain, $\Omega(t)$, we find

$$\int_{\Omega(t)} u\frac{\partial C}{\partial t}\,\mathrm{d}\mathbf{x} = \int_{\Omega(t)} uE\,\mathrm{d}\mathbf{x} + \int_{\Omega(t)} u\nabla \cdot (C\mathbf{w})\,\mathrm{d}\mathbf{x}.$$

Mapping to a static reference frame as before (see Section 3.1), we obtain

$$\frac{\mathrm{d}}{\mathrm{d}t}\int_{\hat{\Omega}} \hat{u}\hat{C}|J_t|\,\mathrm{d}\hat{\mathbf{x}} + \int_{\Omega(t)} u\nabla \cdot (C\mathbf{w})\,\mathrm{d}\mathbf{x} = \int_{\Omega(t)} uE\,\mathrm{d}\mathbf{x} + \int_{\Omega(t)} u\nabla \cdot (C\mathbf{w})\,\mathrm{d}\mathbf{x}. \tag{4.6}$$

The second terms on the left and right of (4.6) cancel, leaving

$$\frac{\mathrm{d}}{\mathrm{d}t}\int_{\hat{\Omega}} \hat{u}\hat{C}|J_t|\,\mathrm{d}\hat{\mathbf{x}} = \int_{\Omega(t)} uE\,\mathrm{d}\mathbf{x}. \tag{4.7}$$

Integrating (4.7) in time and transforming back to the moving domain yields

$$\int_{\Omega^n} u^n C^n\,\mathrm{d}\mathbf{x} = \Delta t\int_{\Omega^{n-1}} u^{n-1}E^{n-1}\,\mathrm{d}\mathbf{x} + \int_{\Omega^{n-1}} u^{n-1}C^{n-1}\,\mathrm{d}\mathbf{x},$$

where we are approximating the right-hand side of (4.7) as piecewise constant in time. Now substituting in full expressions for C and E (see Section 4.2), we find

$$\sum_{k=1}^{N_c^n} \gamma_k^n \int_{\Omega_k^n} u^n \Psi_k^n \, \mathrm{d}\mathbf{x} = \Delta t \sum_{k=1}^{N_c^{n-1}} \int_{\Omega_k^{n-1}} u^{n-1} E_k^{n-1} \Psi_k^{n-1} \, \mathrm{d}\mathbf{x} + \sum_{k=1}^{N_c^{n-1}} \gamma_k^{n-1} \int_{\Omega_k^{n-1}} u^{n-1} \Psi_k^{n-1} \, \mathrm{d}\mathbf{x}.$$

We now substitute in each of the functions $\{\Psi_l\}_{l=1}^{N_c}$ as a test function, u, creating a system of N_c^n equations for the N_c^n unknown γ_k values. This gives rise to a matrix equation of the form

$$L^n \gamma^n = R^n, \tag{4.8}$$

where L^n is an $N_c^n \times N_c^n$ matrix, γ^n is a $N_c^n \times 1$ column vector containing the unknown γ_k values, and R^n is an N_c^n x 1 column vector containing known terms. The matrices are given by

$$L_{lk} = \int_{\Omega_k^n} \Psi_l^n \Psi_k^n \, \mathrm{d}\mathbf{x},$$

$$R_l = \underbrace{\Delta t \sum_{k=1}^{N_c^{n-1}} \int_{\Omega^{n-1}} \Psi_l^{n-1} E_k^{n-1} \Psi_k^{n-1} \, \mathrm{d}\mathbf{x}}_{R'} + \sum_{k=1}^{N_c^{n-1}} \gamma_k^{n-1} \int_{\Omega^{n-1}} \Psi_l^{n-1} \Psi_k^{n-1} \, \mathrm{d}\mathbf{x}.$$

Considering the matrix L, we note that the product $\Psi_k^n \Psi_l^n$ is equal to zero everywhere if $l \neq k$. If $l = k$, the product is one in cell l and zero everywhere else. Therefore, L is a diagonal matrix, with the diagonal elements given by

$$L_l = \int_{\Omega_l} 1 \, \mathrm{d}\mathbf{x} = a_l^n,$$

where a_l^n is the area of the cell. We saw in Section 4.2 that the product $\gamma_l a_l$ is equal to the total ingested chemical in a cell, $\hat{\gamma}_l$. $L^n \gamma^n$ is therefore equal to $\hat{\gamma}^n$, a column vector

containing the total chemical in each cell. The second term in the expression for R can similarly be found by multiplying the area of each cell at the previous time-step by the concentration value in that cell (i.e. $\hat{\gamma}^{n-1} = \gamma_l^{n-1} a_l^{n-1}$).

By considering where the product $\Psi_l^{n-1}\Psi_k^{n-1}$ is non-zero, the first term in the expression for R can be simplified to

$$R_l' = \Delta t \int_{\Omega_l} E_l^{n-1} \, \mathrm{d}\mathbf{x}.$$

Thus our matrix equation (4.8) can be re-written in the form

$$\hat{\gamma}^n = \hat{\gamma}^{n-1} + \Delta t \int_{\Omega_l} E_l^{n-1} \, \mathrm{d}\mathbf{x}.$$

That is to say, the total internal chemical in a cell at time t^n equals the total in that cell at t^{n-1}, plus the amount ingested during the previous time-step. This is exactly what we set out to describe when we began this section with the governing differential equation (4.5).

Making the simplifying assumption that E_k^n can be represented in the form $g(\hat{\gamma}_k^n)c^n$ (see Section 4.2), the term R' can be written

$$R_l' = \Delta t \; g(\hat{\gamma}_l^n) \int_{\Omega_l} c^n \, \mathrm{d}\mathbf{x} = \Delta t \; g(\hat{\gamma}_l^n) \sum_{i=1}^{N^n} \alpha_i^n \int_{\Omega_l} \phi_i^n \, \mathrm{d}\mathbf{x}.$$

We are thus able to solve the matrix system of equations (4.8) for the unknown γ values.

We are now able to update the functions representing the diffusing chemical, c, and the internal chemical, C, when cells ingest chemical. In Section 4.4 we will show that total mass of chemical is conserved in the system when we run a basic simulation of cells relaxing to mechanical equilibrium.

4.4 Simulations of chemical ingestion

To verify that our model works as expected, we run a simulation where chemical is produced by cells whose centres lie in a thin strip of width 0.2 at the left-hand side of a domain of 100 cells. This set-up is a basic representation of a chemical produced in one 'compartment' diffusing into its neighbouring compartment (see Section 4.7). The production rate within the source-producing cells is $\hat{\beta}_k = 0.1$, and zero everywhere else. The endocytotic rate function, E_k, is given by $E_k = b_k c$ in each cell, with $b_k = 1$. Source-producing cells are also able to ingest the morphogen.

In this simulation the cells relax over $t \in [0, 1]$ from their random initial configuration to mechanical equilibrium. Cell volumes are all initially the same, and equal to the target volume, so there is no cell growth in the system. A summary of other parameters can be found in Table 4.1. Fig. 4.1 shows the evolution of the tissue and

Parameter	C_L	C_P	C_A	C_H	C_D	C_{B1}
Value	0.1	0.05	2000	0.001	0.1	0.1
Parameter	C_{B2}	$n_1 - n_4$	μ	T_{T1}	ν	$\hat{\beta}_k$
Value	50	2	1	0.05	0.01	0.1

Table 4.1: *Parameter values used in simulation with chemical production and ingestion.*

morphogen concentration over time.

We record the total amount of chemical released into the tissue, $\bar{S}(t)$, by integrating the source function S over space and time as follows

$$\begin{aligned} \bar{S} &= \int_{\hat{t}=0}^{t} \int_{\Omega(\hat{t})} S \, \mathrm{d}\mathbf{x} \, \mathrm{d}\hat{t} = \Delta t \sum_{n=0}^{n} \sum_{k=1}^{N_c^n} \beta_k^n \int_{\Omega^n} \Psi_k^n \, \mathrm{d}\mathbf{x}, \\ &= \Delta t \sum_{n=0}^{n} \sum_{k=1}^{N_c^n} \beta_k^n a_k^n = \Delta t \sum_{n=0}^{n} \sum_{k=1}^{N_c^n} \hat{\beta}_k^n, \end{aligned} \tag{4.9}$$

assuming the source functions are constant in time between time-points. The variable $\hat{t}$ is a dummy variable. The total internal chemical, $\bar{C}(t)$, can be found at any moment

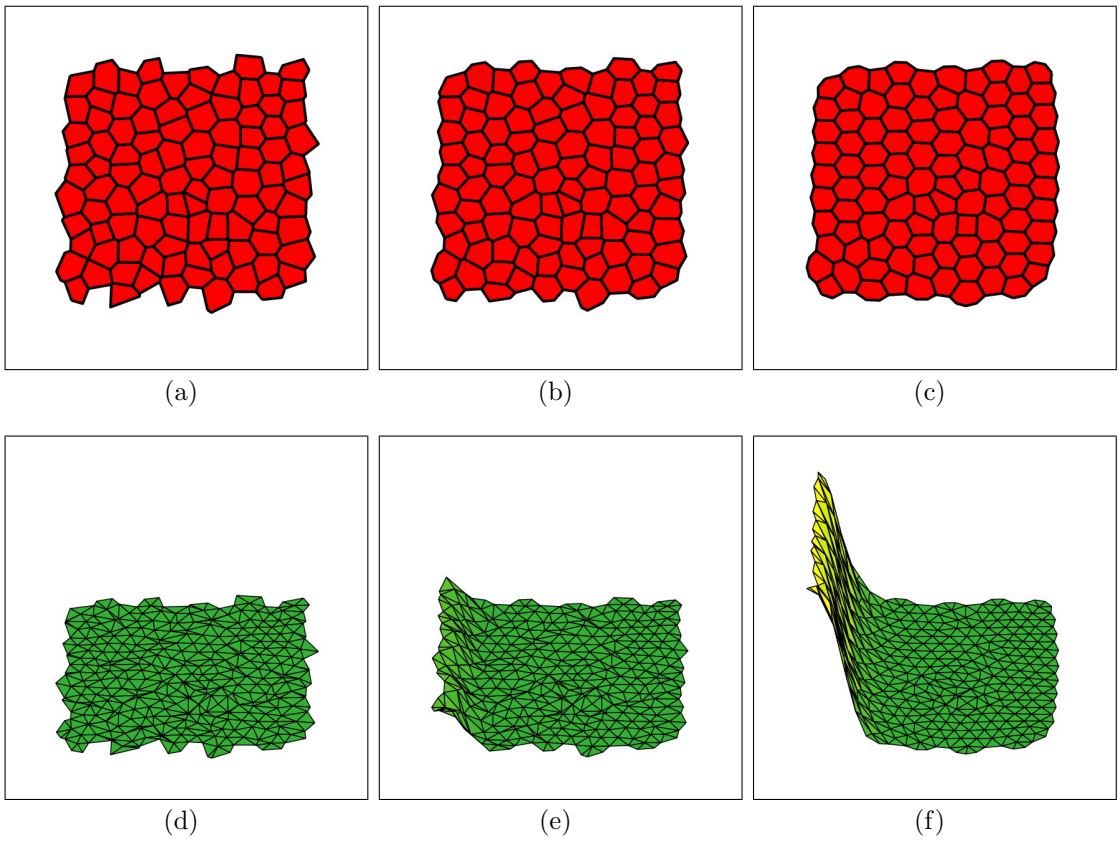


Figure 4.1: *Simulation of cells relaxing to mechanical equilibrium with cellular chemical production and ingestion. Parameter values can be found in Table 4.1. (a-c) The tissue evolves according to the force laws detailed in Chapter 2. (d-f) Concentration of morphogen. The chemical distribution, represented by the height of the plot, is initially zero everywhere, before source is produced in a strip of width 0.2 at the left-hand side and diffuses throughout the domain. The chemical is ingested by cells. See text for details. The limits of the z-axis in (d-f) are [0,5]. (a,d)* $t = 0$*, (b,e)* $t = 0.1$*, (c,f)* $t = 1$*.*

by integrating C over the domain:

$$\bar{C} = \int_{\Omega(t)} C(\mathbf{x}, t)\, \mathrm{d}\mathbf{x} = \sum_{k=1}^{N_c^n} \gamma_k^n \int_{\Omega^n} \Psi_k(\mathbf{x}, t)\, \mathrm{d}\mathbf{x} = \sum_{k=1}^{N_c^n} \hat{\gamma}_k^n.$$

Subtracting $\bar{C}$ from $\bar{S}$ to obtain the net quantity of chemical released, we should be left with the total amount of the external, diffusing chemical in the system, c, denoted $\bar{c}(t)$, which can be calculated using equation (3.26).

Fig. 4.2 shows the amount of chemical released over time, as well as the internal chemical quantity and the net quantity released, which should be equal to the

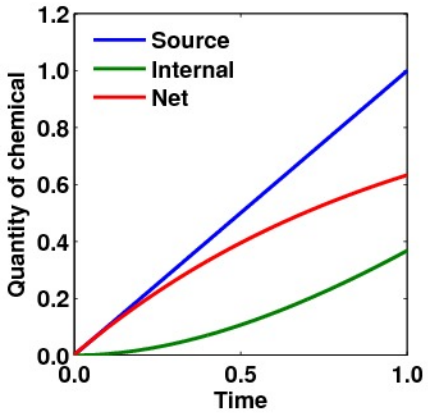


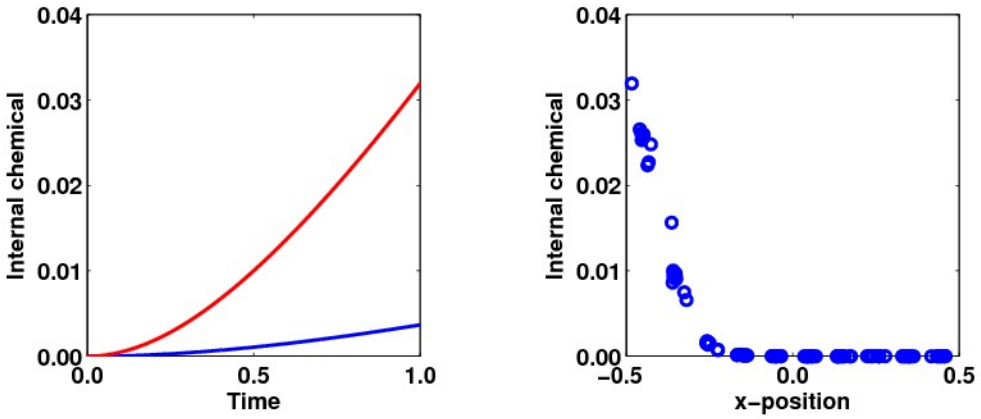
Figure 4.2: *Quantity of chemical released as source into tissue, amount found within cells and difference between the two for simulation of cells relaxing to mechanical equilibrium, with cellular chemical production and ingestion. The total diffusing chemical, when plotted on the same graph, is indistinguishable from the net chemical. Parameter values are given in Table 4.1. See text for details.*

amount left diffusing in the system. Plotted on the same figure, the actual quantity of diffusing chemical overlies the net chemical and cannot be seen. A quantitative error measurement can be obtained by taking

$$\epsilon = \left(\frac{1}{T} \int_0^T \left| \frac{\bar{c} - (\bar{S} - \bar{C})}{\bar{c}} \right|^2 \, \mathrm{d}t \right)^{1/2} \approx \left(\frac{\Delta t}{T} \sum_{n=0}^{n=N_T} \left| 1 - \frac{(\bar{S}^n - \bar{C}^n)}{\bar{c}^n} \right|^2 \right)^{1/2}. \qquad (4.10)$$

In other words, we take the difference between the quantity of diffusing chemical and net chemical source, and find the square of the ratio of this difference to the quantity of diffusing chemical. Integrating over time, dividing by the total time and taking the square root gives us our error. In dividing by the quantity of diffusing chemical, we ensure that the magnitude of the error measurement is independent of the magnitude of chemical quantity, which will help when comparing error measurements between different simulations. Dividing by the total time, T, ensures that the magnitude of the error measurement is independent of the length of the simulation, which will again help to compare different sets of data. In this case, applying (4.10) yields a value of 1.2×10^{-4}, proving that the difference between the quantity of diffusing chemical and net chemical is small relative to the amount of diffusing chemical.

Fig. 4.3(a) shows the mean and maximum internal chemical in each cell over the course of the simulation. As would be expected, these increase over time as the diffusing chemical is ingested by cells. Fig. 4.3(b), meanwhile, shows the chemical inside each cell as a function of its position along the x-axis at the end of the simulation. Cells nearer the source ingest more chemical and therefore have higher internal chemical values.



(a) (b)

Figure 4.3: *Internal chemical statistics for simulation shown in Fig. 4.2. (a) Mean (blue) and maximum (red) internal chemical in cells over time. (b) Distribution of internal chemical quantities at the end of the simulation.*

In this section we ran a simulation to show some basic properties of the model are working as we would expect. We showed that mass is conserved when chemical is ingested, and that cells in regions of greater concentration ingest more chemical. In Section 4.5 we will describe the effects of cellular rearrangements on the internal chemical function C.

4.5 Effects of cellular rearrangements

4.5.1 T1 transitions

When a T1 transition occurs, cell areas change. If the internal chemical value, γ_k, remains constant for cells affected by the transition, then the total chemical in each cell, given by

$$\hat{\gamma}_k = \int_{\Omega_k} C \, \mathrm{d}\mathbf{x} = \gamma_k a_k,$$

will appear to change, contradicting our assumption that internalised chemical cannot pass between cells. If T1 transitions only occur over small edge lengths, however, the changes in area, and thus internal chemical, will be small, so the effects of this problem may be considered negligible.

A simple alternative is to adjust γ_k to ensure that the total concentration, $\hat{\gamma}_k$, in each cell is the same after a T1 transition as it was before. This is achieved by taking

$$\gamma_k' = \gamma_k \frac{a_k}{a_k'}, \tag{4.11}$$

where γ_k' represents the adjusted value of γ_k, and a_k' is the cell area after the rearrangement.

4.5.2 Proliferation

When cell proliferation occurs, the internal chemical is divided between the daughter cells relative to the ratio of their volumes. As the ratio of the volumes is equal to the ratio of the areas, in practice the γ values for the daughter cells are simply equal to the value, γ_k, in the mother cell. This ensures that total concentration remains constant, as $\gamma_k a_l + \gamma_k a_m = \gamma_k(a_l + a_m) = \gamma_k a_k$, where a_l and a_k represent the areas of the two daughter cells.

4.5.3 Cell death

As is the case in a T1 transition, cell areas change during a cell death event. Assuming the dying cell is triangular, it will have three neighbours, which will all experience a slight increase in cell area, as they are connected to the new vertex at the centre of the dead cell. In order to keep the quantity of chemical in each of these cells constant, we must change the concentration value, γ_k, for each of them. This is achieved using equation (4.11).

If $\hat{\gamma}_k$ remains constant, as the dying cell shrinks its γ_k value will become quite large as the area becomes small. The chemical inside the dying cell can either be degraded and removed from the system, or released as a point source for the diffusing chemical (Section 4.1), depending on the appropriate biology of the system.

In this section we have described what happens to the internal chemical function, C, during T1 transitions, cell proliferation and cell death. In Section 4.6, we will run a simulation with the various cellular rearrangements and show, as before, that the net chemical source is equal to the amount of chemical diffusing through the domain.

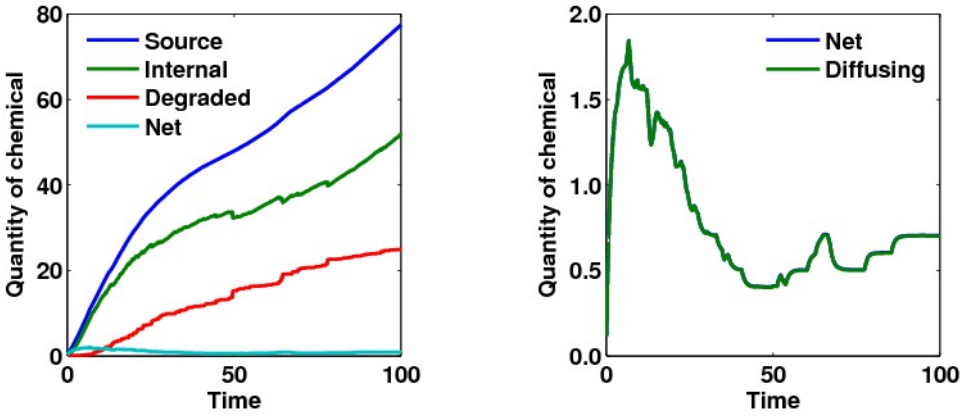
4.6 Simulations with cellular rearrangements

We can now run a simulation of cellular chemical ingestion with the various rearrangements, including T1 transitions, proliferation, and cell death. At the cellular level, this simulation is similar to that in Section 2.13. It is run over $t \in [0, 100]$, with a proliferation event every 0.1 time-units. A new cell becomes apoptotic every 0.2 time-units. When a cell becomes apoptotic, we assume that its internal chemical degrades. We keep a record of the total amount of degraded chemical, in order to show that mass is conserved during the simulation. Cell volumes are all initially at the target volume, so growth begins once a proliferation event occurs. Cell growth

speeds, g_k, are equal to one for each cell.

The chemical concentration is initially zero across the domain, for both the diffusing chemical, c, and the internal chemical, C. We designate a subset of cells in a strip of width 0.2 at the left-hand edge of the domain to be source-producing, and allow this chemical to diffuse and be ingested by all cells. The production rate is $\hat{\beta}_k = 0.1$ in the source-producing cells, and zero in the rest of the domain. The endocytotic rate function, E_k, as before, is given by $E_k = b_k c$, with $b_k = 1$. Other parameters are as in Table 4.1.

Fig. 4.4(a) shows the total chemical released over time, $\bar{S}$, as well as the total internal chemical, $\bar{C}$, and the total degraded chemical, $\bar{D}$, throughout the simulation. Subtracting the degraded chemical and the internal chemical from the source, we expect to find the quantity of diffusing chemical in the domain. In Fig. 4.4(b) we plot the diffusing chemical quantity and the net chemical from (a). The two lines overlap, such that it is impossible to see that there are two separate lines.



(a) (b)

Figure 4.4: *Chemical quantity statistics for simulation of growing tissue with regular proliferation and apoptosis events and cellular chemical production and ingestion. See text for parameter values. (a) Quantity of chemical released as source into tissue, amount found within cells, amount degraded and net value. (b) Total diffusing chemical in the system and net value from (a). The two lines overlap, such that only one line can be seen. Note that the scale on the y-axis differs between (a) and (b).*

The error measurement (4.10) can be adjusted to include the degraded chemical

as follows

$$\epsilon = \left(\frac{1}{T} \int_0^T \left| \frac{\bar{c} - (\bar{S} - \bar{C} - \bar{D})}{\bar{c}} \right|^2 \, \mathrm{d}t \right)^{1/2} \approx \left(\frac{\Delta t}{T} \sum_{n=0}^{n=N_T} \left| 1 - \frac{(\bar{S}^n - \bar{C}^n - \bar{D}^n)}{\bar{c}^n} \right|^2 \right)^{1/2}.$$

For this simulation we obtain $\epsilon = 5.4 \times 10^{-4}$. This error is of the same order of magnitude as the simulations without regular proliferation and death, showing that these processes have not significantly altered the accuracy of our solutions. The small magnitude of the error shows that the difference between the net chemical quantity and the amount of diffusing chemical is small relative to the quantity of diffusing chemical.

We have shown that simulations of ingestion are robust to cellular rearrangements, and the model behaves as expected during a simulation of cells proliferating and dying. In Section 4.7 we will describe a potential application area of the model, namely the *Drosophila* epidermis.

4.7 *Drosophila* epidermis

Insect bodies are broken up into fundamental building blocks, known as compartments, which are classified as anterior (A) or posterior (P). Cells from different compartments rarely intermingle, and are often separated by so-called organizers (Canela-Xandri et al., 2011, Landsberg et al., 2009, Rauzi et al., 2008). Compartment size appears to be tightly controlled, and is robust to substantial changes in cell number (Neufeld et al., 1998, Weigmann et al., 1997). In fact, cases have been been observed in many animal species of organs or whole organisms reaching normal sizes despite huge variations in cell proliferation and *Drosophila* compartments are one example of this dimension-sensing phenomenon. Another example comes from tetraploid salamanders (*Amblystoma mexicanum*), which have half the number of cells

of their diploid counterparts, but grow to the same size (Day and Lawrence, 2000). Interestingly, when finding their way around a maze, the tetraploid salamanders take twice as many attempts, due to having fewer neurones in the brain (Vernon and Butsch, 1957).

Parker (2006) set about investigating how size is regulated in *Drosophila* dorsal abdominal larval epidermis P compartments. These particular compartments have the advantage of a relatively small number of cells and well-understood patterns of cell proliferation. Parker began by showing that compartment size is not determined by cell number. This was achieved in two ways. Firstly he expressed *cyclin E (cycE)*, which forced cells to divide. The average number of cells in the P compartment grew from 44 to 59, however, compartment size did not vary from wild-type. Secondly, he expressed *p27Dacapo (dap)*, which blocked proliferation and caused the average cell number to reduce to 33. Again, compartment size was essentially unchanged. In both cases the size of cells simply adjusted to compensate for the altered cell number. In the case of increased *cycE* expression, mean cell size decreased, whereas for *dap* it increased.

Further experiments showed that about half of the excess cells created when *cycE* is expressed are killed off by apoptosis. Apoptosis is rare in the wild-type, with about one cell death per compartment on average (J. Zartmann, *pers. comm.*). When apoptosis is blocked and *cycE* is expressed, the resultant compartment has 74 cells. These compartments still maintain normal size.

Taken together, these results indicate that the size of individual cells is regulated to ensure the overall compartment reaches a certain size, and that cells have a probability of survival that is dependent on the number of cells in the compartment. This indicates a role for extracellular signals in the growth of the compartment. An interesting pattern of apoptosis also emerges in the case of *cycE* expression, with a clear anterior bias for cell death.

Parker was able to show that compartment dimensions are dependent on epidermal growth factor (EGFR) signalling, and that the primary activating ligand is Spitz (Spi). This is released by neighbouring A compartment cells, diffusing into the P compartment before activating the EGFR signalling pathway. Cells grow based on the amount of Spi available, which also determines their probability of undergoing apoptosis. Spi is secreted in limited amounts, so when a cell divides the per-cell level of Spi drops, decreasing cell size and reducing cell survival. Fig. 4.5 summarizes the key experiments that the author presents, and how they fit in with the model of growth control.

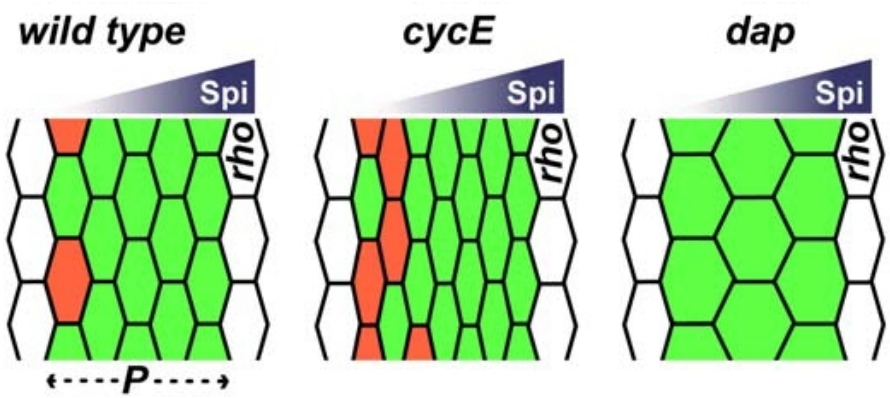


Figure 4.5: *Model of size control in Drosophila epidermis P compartments. Spi is released in limited quantities by cells expressing the gene rhomboid (rho) in the adjacent A compartment. Spi promotes both growth and survival. Cells far from the source of Spi die (red). CycE over-expression causes excess proliferation, resulting in a drop in per-cell Spi availability. This reduces cell size and causes more cells to die off, particularly those furthest from the source. Dap expression blocks proliferation, leading to a higher per-cell availability of Spi, and thus increased cell size and survival. Reprinted with permission from Parker (2006).*

To demonstrate the significance of Spi secretion occurring in limited amounts, we can run two simulations, one with an constant growth factor supply and one in which the amount of chemical released is capped. We start both simulations with 100 cells and run them over $t \in [0, 50]$. Each cell begins at the assigned target volume, V_k. Cell growth speeds, g_k, are equal to one for each cell. We make growth dependent on

the internal concentration of each cell, modifying the growth equation (2.6) to

$$\frac{\mathrm{d}v_k}{\mathrm{d}t} = (1 + \lambda\hat{\gamma}_k)g_k v_k \left(1 - \frac{v_k}{V_k}\right),$$

where v_k is the volume of cell k, λ is a parameter representing the strength of the effect of the internal chemical on growth and $\hat{\gamma}_k$ is the total internal chemical in a cell. Thus cells with a large internal chemical quantity should grow faster than those with smaller values. Proliferation is implemented according to equation (3.31).

As before, the chemical concentration is initially zero, for both c and C, across the domain. A subset of cells at the left-hand edge are designated to be source-producing, with production rate $\hat{\beta}_k = 0.1$. On this occasion the endocytotic rate function, E_k, is given by $E_k = b_k c(1 - \hat{\gamma}_k/\hat{\gamma}_k^{\max})$, with $b_k = 1$ and $\hat{\gamma}_k^{\max} = 0.1$. Cells thus ingest chemical up to a maximum amount of 0.1. Other parameters are as in Table 4.1. Apoptosis is not included in these simulations.

In the first simulation, Spi secretion is limited to 20 a.u. Fig. 4.6 shows the evolution of the diffusing chemical, c, during the simulation. We observe that, from initially taking a value of zero everywhere, chemical starts being produced at the left-hand edge of the domain. This chemical diffuses, and is ingested by cells. At a certain point during the simulation, chemical stops being produced, and the distribution falls back to zero across the domain. We can also observe the distribution of internal chemical quantities across the domain in Fig. 4.7. We find that, early on in the simulation, cells near the chemical source ingest the diffusing morphogen up to the maximum amount. As these cells grow faster than those with lower internal concentrations, we begin to see proliferation events in this region, with the internal chemical shared between the daughter cells in the same ratio as their volumes. As the simulation progresses, more and more cells fill up their quota of internal chemical, causing more and more cell divisions. Crucially, as the Spi source is limited, after division there is not enough

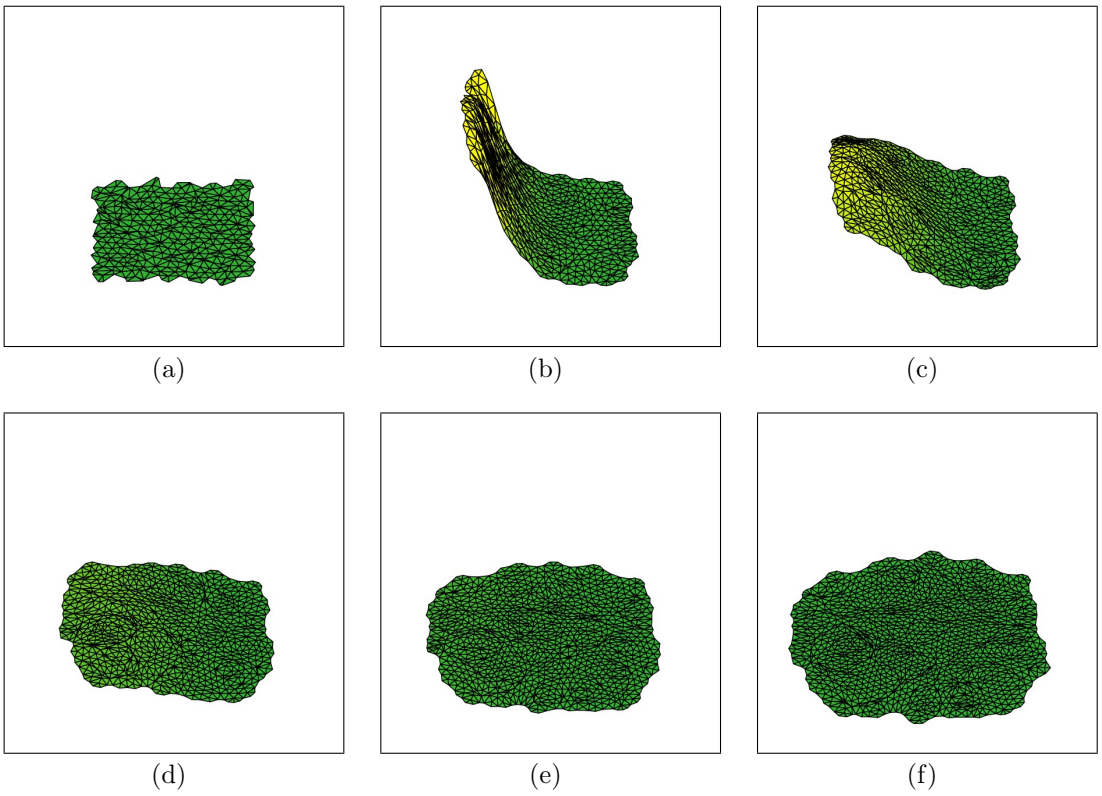


Figure 4.6: *Simulation of morphogen released in limited amount. See text for parameter values. Initially chemical is produced at the left-hand edge (a), and a gradient forms across the domain as the chemical diffuses (b). Once the source is switched off (c), the gradient shrinks and eventually the chemical concentration is zero across the domain (f). The limits of the z-axis in all panels are [0,30]. (a) t=0, (b) t=10, (c) t=20, (d) t=30, (e) t=40, (f) t=50.*

diffusing chemical for many daughter cells to ingest to maximum capacity, so they remain without a full quota of internal chemical and grow more slowly.

In the following simulation we allow Spi to be unlimited, rather than turning off the source at a certain value. All other parameters are the same as in the previous simulation. Fig. 4.8 shows the evolution of the diffusing chemical, c, over the course of the simulation. The morphogen gradient grows over time, and unlike the previous simulation (Fig. 4.6), does not flatten out and return to zero at the end of the simulation. Fig. 4.9 shows the distribution of internal chemical quantity at several time-points during the simulation. As before, cells at the left-hand side initially ingest chemical and reach the maximum internal value quickly. They then grow faster and

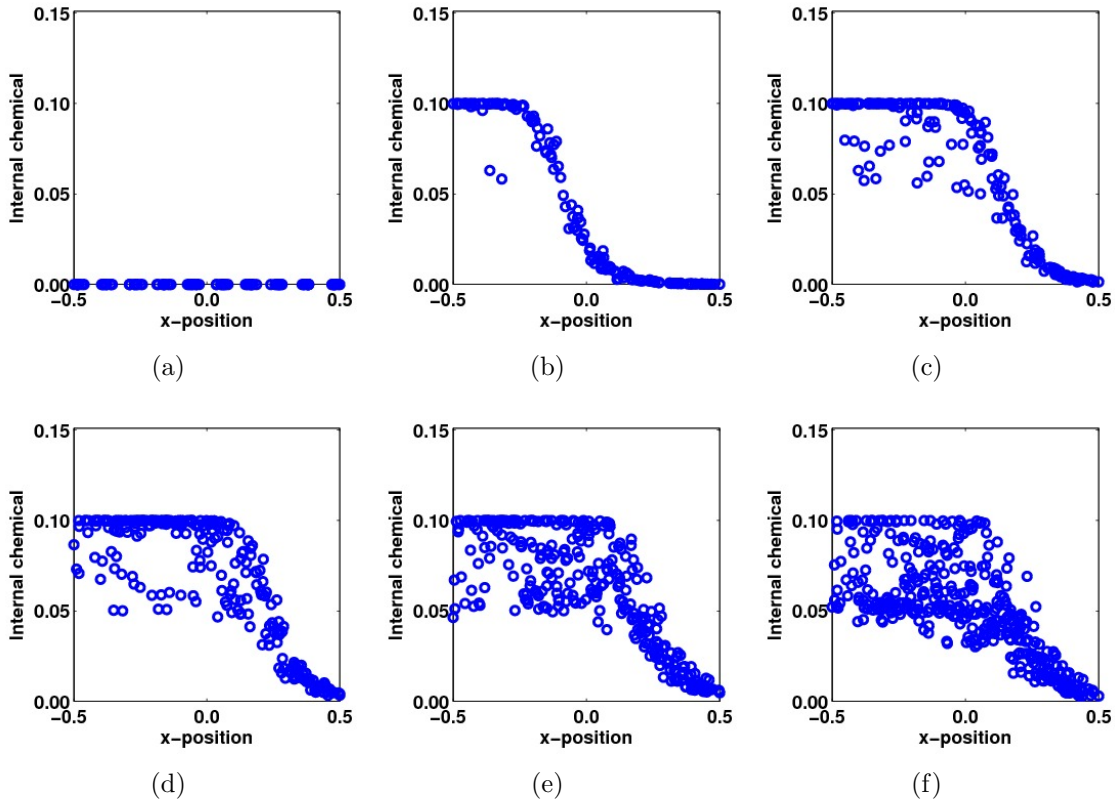


Figure 4.7: *Distribution of internal chemical quantity as a function of position along the x-axis for simulation shown in Fig. 4.6. Positions are normalised to lie between -0.5 and 0.5. Initially zero everywhere, cells on the left-hand side quickly ingest chemical up to the maximum amount (0.1). These cells grow faster than cells with lower values of internal chemical. As time progresses, cells further across to the right of the domain have the maximum amount of chemical, and cells on the left begin to divide, with the internal chemical shared between the daughter cells. As the quantity of Spi is limited, the internal chemical in the daughter cells is unable to build back up to the maximum value, and by the end of the simulation we observe a spread of concentrations. All circles are 'open', and only appear closed where several circles lie over one another. (a) t=0, (b) t=10, (c) t=20, (d) t=30, (e) t=40, (f) t=50.*

divide more than other cells in the tissue. As the simulation progresses, cells further to the right of the domain fill up with chemical. As the Spi source is constant in this simulation, once a cell divides and its internal chemical is split between the daughter cells, the amount in the daughter cells can grow back to the maximum as they each ingest further chemical. For this reason, the distribution is very different in the later stages of the simulation from that seen in Fig. 4.7. Most cells are at the maximum internal value, while those that have recently divided are growing back towards it.

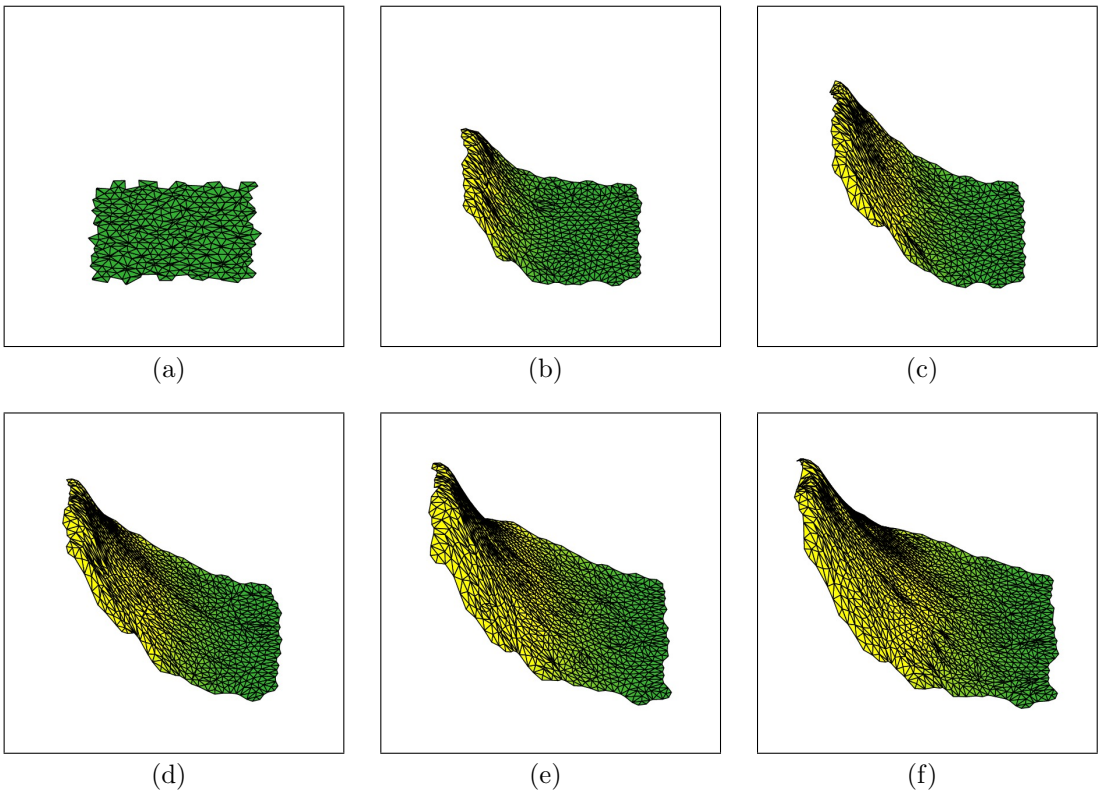


Figure 4.8: *Simulation with constant source of morphogen. See text for parameter values. Initially chemical is produced at the left-hand edge, and a gradient forms across the domain as the chemical diffuses. The limits of the z-axis in all panels is [0,50]. (a) t=0, (b) t=10, (c) t=20, (d) t=30, (e) t=40, (f) t=50.*

As well as the differences between internal chemical quantity within cells, the two simulations also lead to differing tissue-level properties. In the first simulation, with a limited supply of Spi, the total area of all the cells at the end of the simulation was 2.18, while with constant Spi signalling it was 2.32. The total volume of all cells in the first case, meanwhile, was 0.27, while it was 0.30 in the second case. This demonstrates how, by secreting Spi in limited amounts, the size of the tissue can be regulated.

4.8 Summary

In this chapter we incorporated more realistic source and ingestion terms into the morphogen model built up in Chapter 3. We began by defining a source function

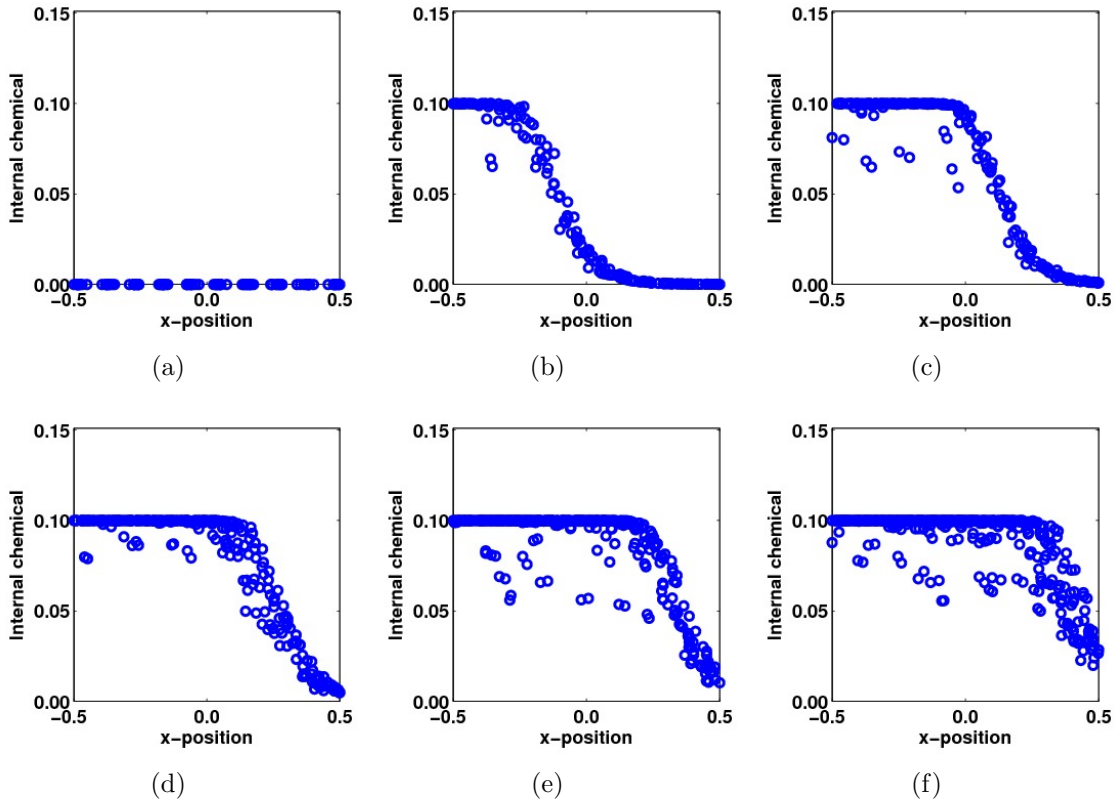


Figure 4.9: *Distribution of internal chemical quantity as a function of position along the x-axis for simulation shown in Fig. 4.8. Positions are normalised to lie between -0.5 and 0.5. Initially zero everywhere, cells on the left-hand side quickly ingest chemical up to the maximum amount (0.1). These cells grow faster than cells with lower values of internal chemical. As time progresses, cells further across to the right of the domain have the maximum amount of chemical, and cells on the left begin to divide, with the internal chemical shared between the daughter cells. In this simulation the source of Spi is constant, so once a cell divides the internal chemical in the two daughter cells can build back towards the maximum. (a) t=0, (b) t=10, (c) t=20, (d) t=30, (e) t=40, (f) t=50.*

that is piecewise constant on cells, and showing how this feeds into the system of matrix equations for the distribution of our diffusing chemical. We then looked for a better way to represent morphogen ingestion, where cell receptor molecules bind with the diffusing chemical and effect a process known as endocytosis. We defined an endocytotic rate function and an internal chemical concentration across the domain, and again fed these terms back into the governing system of equations for the diffusing chemical. Next, we defined a new equation for the evolution of internal chemical concentration, based on an advection term. In this way, the internal chemical moves

with cells and does not diffuse between them. We showed how this equation can be solved in an iterative manner so that at any point during our simulations we can find approximations to both the diffusing and internal chemicals.

We ran simulations with the new methods of production and ingestion, and validated the model by showing consistency between the amount of chemical released, the amount diffusing, and the amount inside cells. We looked at the effects of cellular rearrangements on the internal chemical concentration and ran further simulations with these processes included. Finally, we looked at experimental data from the *Drosophila* epidermis, which suggested that compartment size could be regulated by secretion of a limited amount of the growth factor Spi. We ran two simulations of a chemical produced in a strip at the left-hand side of the domain, one with constant and one with limited source. We showed that in the case of constant morphogen production, the domain grew larger in terms of both area and volume than in the case of limited production. This suggests that the production of morphogen in limited amounts is a viable method of size control. A more comprehensive parameter sensitivity analysis would be required out to verify this result.

The model developed in this chapter and Chapter 3 represents a novel description of morphogen dynamics within a 2D tissue. This is the first time an ALE reference frame has been implemented in this context, allowing the diffusion of the morphogen to be independent of cell movements. By including the ability for cells to ingest chemical and build up an internal concentration, we mimic the key process of endocytosis.

The simulations in this chapter of the growth of *Drosophila* epidermis compartments and those at the end of Chapter 3 concerning the wing imaginal disc have shown how our model can begin to address some of the controversies surrounding tissue-size control. As we have seen, various mechanisms have been proposed, based on chemical signalling factors, mechanical feedback or a combination of the two. To further elucidate the correct processes, simulations must be more rigorously compared

with experimental data. It may be possible to recapitulate the wild-type behaviour using more than one of the proposed models, in which case it will be necessary to compare the behaviour of mutant embryos in computational experiments and *in vivo*.

In Chapter 5 we will look at a new biological problem, that of AVE migration in the mouse embryo. We will explain why this process is crucial in the patterning of the embryo, and what questions remain unanswered despite experimental investigation. We will then use the vertex model framework to address these questions. We will describe initial extensions that can be made to the vertex model in order to adapt it to the geometry of the mouse embryo, ultimately leading to an ellipsoid-based model. We will explain how forces are applied in 3D, and how vertices are mapped to the ellipsoid surface. We will validate the new model by showing that the forces behave as they should, and discuss how processes such as growth, proliferation, and rearrangements translate to the new model.

Chapter 5

Modelling AVE migration in the mouse embryo

In the previous chapter we completed our 2D vertex-based framework by incorporating chemical production and ingestion into the model of chemical signalling factors. Throughout this thesis, we have suggested possible application areas for our models, and in many cases have run sample simulations to demonstrate proof-of-concept. In the next two chapters we will look at a specific application, and use the model to understand real biological data concerning the mouse visceral endoderm (VE). This simple epithelium plays a crucial role in patterning the 'egg-cylinder'-stage mouse embryo, and thus has a critical function in embryo development. In this chapter we will extend the 2D model to a 3D surface, in order to represent a realistic geometry for the mouse embryo.

This work has been carried out in collaboration with Dr. Shankar Srinivas at the Department of Physiology, Anatomy, and Genetics (DPAG), University of Oxford. Some of the work in this chapter and Chapter 6 appears in the paper: G. Trichas, A. M. Smith, N. White, V. Wilkins, T. Watanabe, A. Moore, B. Joyce, J. Sugnaseelan, T. A. Rodriguez, D. Kay, R. E. Baker, P. K. Maini & S. Srinivas. Multi-cellular

rosettes in the mouse visceral endoderm facilitate the ordered migration of AVE cells. *PLoS Biology*, 2012. doi: 10.1371/journal.pbio.1001256. A video abstract of the paper can be found at http://www.scivee.tv/node/39309.

We will begin this chapter by discussing the biology behind migration of the anterior visceral endoderm (AVE) in Section 5.1, which takes place in the mouse embryo at five-and-a-half days post-fertilisation. We will describe the structure of the embryo at this time, and explain the crucial role of AVE migration in patterning. We will address some of the key unanswered questions regarding the process, and motivate the need for a computational model.

In Section 5.2 we will describe some preliminary extensions to the 2D model that can be made in order to make it more realistic for this application. These include the implementation of periodic boundary conditions to create a cylindrical model and the addition of a migratory force. A particularly important addition will be the ability of vertices to join together as an alternative to a T1 transition, facilitating the formation of multi-cellular rosettes (described below). A few simulations using the cylinder-based model will be presented, before a discussion of the model's limitations and an explanation of the need for an ellipsoid model.

In Section 5.3 we will describe how initial configurations are created in the ellipsoid model, based on the icosahedron. We will see how vertices are mapped back to the ellipsoid surface after each iteration of a simulation to maintain the integrity of the structure of the embryo. We will verify that the tissue behaves as predicted by our force laws. Growth of the ellipsoid will be implemented during simulations, and we will see how a barrier to migration can also be incorporated.

5.1 AVE migration in the mouse embryo

The VE is a mono-layer of cells surrounding the early post-implantation mouse embryo. At embryonic day 5.5 (E5.5), the arrangement of tissues forms a unique structure known as an egg-cylinder, with an already morphologically defined proximo-distal axis. The proximal region of the egg-cylinder contains the extra-embryonic ectoderm (ExE), while the distal portion is made up of epiblast, with a proamniotic cavity at the centre (Fig. 5.1). At this stage the embryo is around 180μm long (Mesnard et al., 2006).

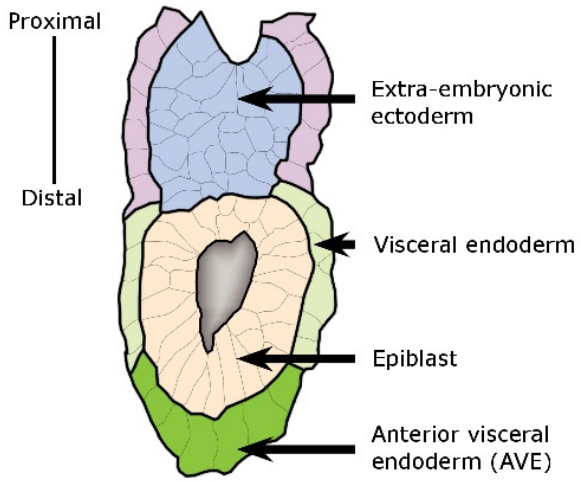


Figure 5.1: *Cross-sectional schematic of a mouse embryo at E5.5. The embryo consists of three tissues; the ExE in the proximal region, the epiblast in the distal region, and the VE, an epithelium surrounding them both. A subset of cells at the distal tip of the VE, known as the AVE, differentiate and migrate towards the barrier between the epiblast and the ExE. Adapted by permission from Srinivas (2006).*

5.1.1 Onset of migration

At roughly E5.5, a subset of around 20 cells from the distal tip of the VE differentiate into morphologically distinct tissue with a more columnar shape (Rivera-Pérez et al., 2003). These cells are referred to as the AVE. As well as their morphology, AVE cells can also be identified by the expression of several marker genes (Belo et al., 1997, Meno et al., 1999, Thomas et al., 1998). It has been shown in labelling experiments

(Rivera-Pérez et al., 2003) and time-lapse microscopy (Srinivas et al., 2004) that the AVE migrates unidirectionally away from its initial position towards the boundary between the epiblast and ExE. Proximal migration ends abruptly at this boundary and the cells begin to move laterally. The exact nature of the barrier is unknown, as no obvious physical barrier can be observed through confocal microscopy. The migration process takes 4-5 hours. The final resting place of the migrating cells is the future anterior, where 'anterior' is defined as the portion of the mouse embryo that, later in development, gives rise to rostral neural tissue (Srinivas, 2006).

The migration of AVE cells is a crucial process in embryogenesis. It is essential for ensuring the correct orientation of the anterior-posterior axis and patterning of the adjacent embryonic tissue. If migration is disrupted, the distal region adopts an anterior character and the proximal region a posterior character (Ding et al., 1998, Kimura et al., 2000). Analogous tissues exist in other species, including the frog (Jones et al., 1999), chick (Foley et al., 2000) and zebrafish (Ho et al., 1999).

Time-lapse movies, in which the AVE is transgenically labelled with green fluorescent protein (GFP), have provided insights into the mechanisms behind AVE migration (Rodriguez et al., 2001, Srinivas et al., 2004). It is an active process, during which the migrating cells change shape and project filopodia in the direction they move. The cells lose their columnar nature to some extent as they migrate, but are still thicker than the surrounding VE at the end of the process (Rivera-Pérez et al., 2003).

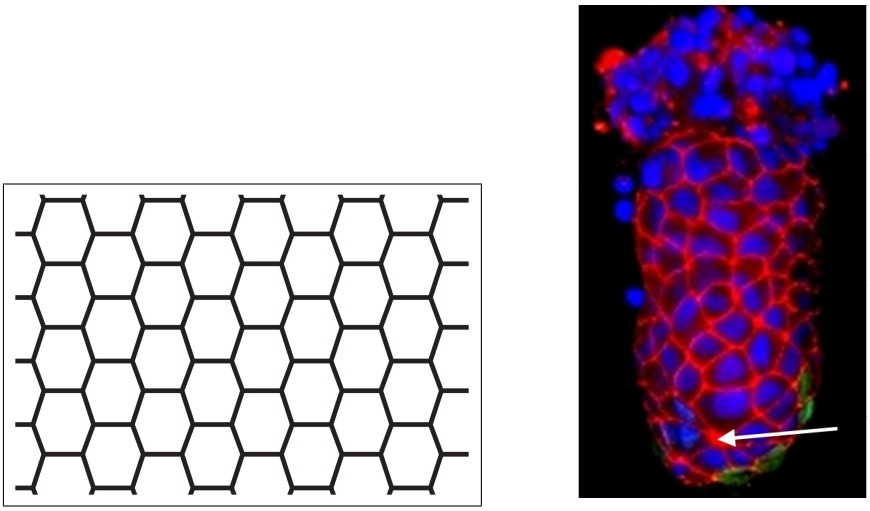
Srinivas (2006) has suggested several possible ways in which the direction of cell migration could be determined. The first possibility is that a faster rate of proliferation in the posterior region forces the AVE cells towards the anterior. The main flaw in this theory is that migration takes place much too quickly to be driven by cell division. It is feasible, however, that increased proliferation at the prospective posterior could be responsible for giving the AVE cells an initial directional clue, sub-

sequent to which they migrate via alternative processes. A second suggestion is that AVE cells respond to an attractive chemical signal present at a pre-defined future anterior. Another possibility is that the direction of migration is determined by the extracellular matrix around the epiblast, and the cells are able to follow this path. The final suggestion is that the locations of the future anterior and posterior are not pre-determined, and the direction of migration is essentially random, with one or two leader cells drawing the others behind them. These various hypotheses are amenable to computational testing, and in Section 5.2 we will describe the rationale and methodology for a computational framework to examine them.

5.1.2 Discovery of rosettes

Recent experiments on the mouse embryo, carried out by Dr. Srinivas, have revealed the presence of multicellular 'rosettes' during AVE migration. Rosettes were first discovered in epithelia by Blankenship et al. (2006) in the *Drosophila* germ-band. Mono-layers of cells can normally be conceptualised as a series of 2D polygons, resembling a honeycomb, with three cells meeting at each vertex (Fig. 5.2(a)).

As we saw in Chapter 2, cells can exchange neighbours via T1 transitions (Section 2.4). During a T1 transition, an intermediate configuration temporarily forms, in which four cells meet at a single vertex. Blankenship et al. (2006) discovered, surprisingly, examples of between five and eleven cells meeting at a common vertex. The authors named these 'rosettes' and concluded that they must be part of a higher-level organisation of cell behaviour. They believe that rosettes in the *Drosophila* germ-band form and split in a directional manner as a novel mechanism of convergent extension; the narrowing of a tissue in one direction and lengthening perpendicularly. Wagstaff et al. (2008) later observed rosettes during cell ingression in the avian primitive streak. They suggest that the formation of higher-order cellular structures such as rosettes may often be crucial in coordinating cell behaviour during morphogenesis. There is



(a) (b)

Figure 5.2: *(a) Honeycomb pattern of hexagonal cells, with three cells meeting at each vertex. Under normal circumstances epithelia approximately resemble this type of pattern. (b) Confocal optical image of mouse embryo with rosette at the distal tip (arrow). Nuclei are in blue, cell borders are in red. Rosettes have been observed during migration of the AVE in the mouse embryo, whereby five or more cells meet at a common vertex. Image courtesy of Dr. Shankar Srinivas.*

no evidence in the mouse embryo that rosettes form in any particular direction, so the role they play must yet be elucidated. Fig. 5.2(b) shows a seven-cell rosette appearing during AVE migration in the mouse embryo.

Over the next few sections we aim to create a computational framework in which AVE migration can be modelled. This will allow hypotheses to be tested via simulation, and further predictions to be made that may then be tested experimentally. It is hoped that simulations will inform suitable experiments, and *vice-versa*. In particular, we aim to test whether rosettes are an integral part of migration, or an unimportant by-product of the process. We would also like to understand the nature of the barrier between the ectoderm and ExE, for instance whether it can be modelled as a step-function in stiffness at the boundary between the two tissues. Other questions to be answered concern which of the mechanisms described in Section 5.1.1 for determining direction are fully consistent with AVE migration. Success in answering these questions will depend on the quality of experimental data available. Over the course of

several iterations between model-driven experimental tests and experimentally-driven model simulations, we believe that much useful information can be elucidated.

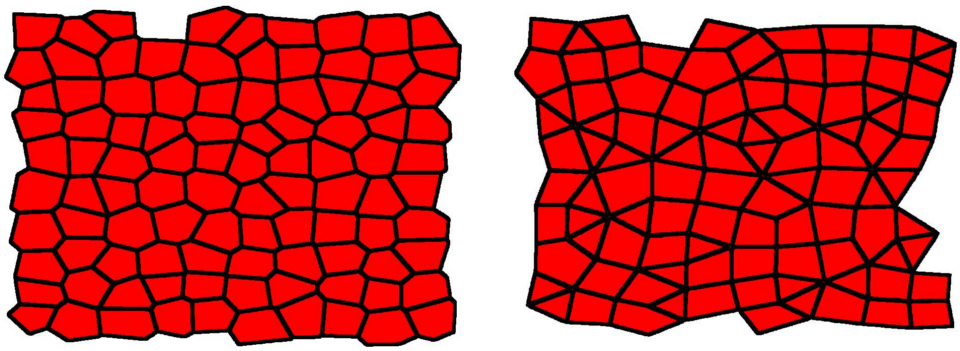
We will use many aspects of the computational model developed in Chapter 2 in order to study AVE migration. Cells will again be modelled as polygons, with forces acting on the vertices. As before, we will include junctional rearrangements, as well as cell growth and proliferation. In Section 5.2 we will explain some preliminary extensions to the 2D model that will allow us to run some migration simulations. In particular, we will describe how rosette formation and splitting have been incorporated into the model, together with a method for implementing periodic boundary conditions to create a cylindrical model. We will then go on to discuss methods for inducing migration within the model, and show simulation results.

5.2 Extensions to the 2D model

5.2.1 Vertex joining and splitting

As an alternative to performing a T1 transition (Section 2.4), we can allow vertices to join together when the distance between them falls below a certain threshold. This permits the formation of rosettes, if a series of neighbouring vertices fall below the threshold distance. Fig. 5.3 shows the joining together of initially close vertices in a cell configuration. Several rosettes of five or more cells are clearly visible.

We would like to allow rosettes to occasionally split apart, as they are thought to be transient rather than permanent features (Blankenship et al., 2006). We therefore define a split probability per unit time, p_s, and assume that, at each iteration, each rosette has a chance $p_s\,\Delta t$ of splitting, where Δt is the time-step between iterations of the solution to the equations of motion (Section 2.8). Rosettes are split using the following algorithm. Two cells within the rosette that do not share any edges



(a) (b)

Figure 5.3: *Joining together of initially close vertices. (a) An initial configuration of cells. (b) The same configuration, with close vertices joined together. Several rosettes of five or more cells can be observed. In this example the threshold for vertex joining has been set artificially high to deliberately create several rosettes.*

are picked at random, and two new vertices are established on the lines connecting the old vertex to the centres of the chosen cells. The remaining cells are then re-connected to whichever of the two new vertices is nearest to them. Two of these cells, however, must be connected to both new vertices, to ensure there are no spaces between the resultant cells. This is demonstrated in Fig. 5.4. Fig. 5.4(a) shows the original rosette. If we simply replace the old vertex with the nearest of the two new vertices in each cell we obtain Fig. 5.4(b), with a space in the middle of the tissue. This is unrealistic in an epithelial sheet, so instead two of the cells are 'stretched' to incorporate both new vertices, thus filling the gap. The positions of the new vertices are chosen so that the distance between them is slightly larger than the threshold for vertex joining, otherwise the rosette would be likely to immediately re-form at the next iteration. Rosettes containing many cells can be completely split by repeating this algorithm several times.

5.2.2 Periodic boundary conditions

In the computational model, cells are currently allowed to roam freely on an infinite domain, with no restriction on their movement. This is clearly unrealistic, as on

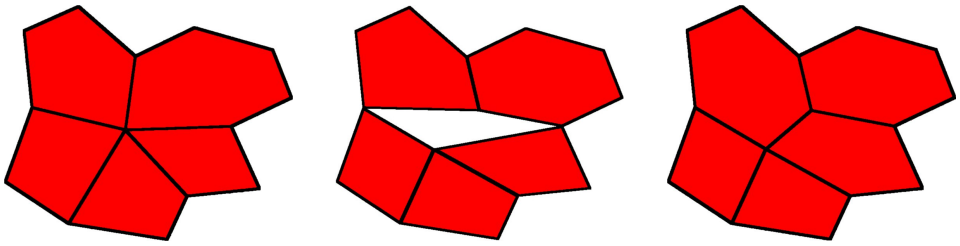


Figure 5.4: *The three stages of rosette splitting. (a) The original rosette. (b) Two new vertices are created within two of the cells that share the rosette, and all cells are re-connected to whichever of these two vertices is closest. This, however, leaves a gap in the tissue which is unrealistic. (c) Two of the cells are stretched to fill the gap. Each of these cells then contains both of the new vertices.*

the surface of a mouse embryo the cells exist in a continuous sheet, and are highly restricted in their potential movements. As a first approximation to the true nature of the embryo we can emulate a cylinder, with cells wrapped around the surface. Ultimately we wish to transfer to a more realistic geometry, but the cylindrical model will provide valuable insights into how this can be achieved, and yield useful results in the meantime.

One way of representing a cylindrical geometry is to implement periodic boundary conditions on the vertical edges of the sheet of cells. For this, we require an initial configuration of cells that is itself periodic. This can be achieved using periodic points as inputs to the Voronoi tessellation. We create an initial array of random points, as in Section 2.1, then juxtapose an identical copy on the left and right sides. When the tessellation is performed, we obtain a repeated array of cells. The remaining challenge is then to strip this extended array of cells down to just a single sheet, where the vertices on the left-hand side match the vertices on the right-hand side. Fig. 5.5 shows a Voronoi tessellation performed on periodic input points. The green cells on the left-hand side are identical to those on the right-hand side. We can therefore keep just one copy of these cells for the purposes of simulation, but keep a record that the 'boundary vertices' on the far left are exactly equivalent to those on the right. Any force that is applied to a boundary vertex must also be applied to its

matching vertex.

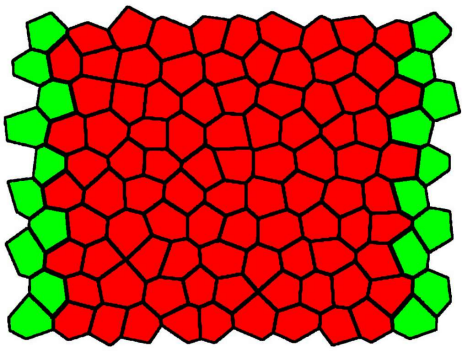


Figure 5.5: *Voronoi tessellation with periodic boundary conditions. Periodic Voronoi points are used to ensure the green cells on either side of the cell configuration are identical. One copy of the green cells can be removed, leaving a single set of points on each side of the domain that are equivalent. Any forces or rearrangements that occur to these points must be reflected on both sides.*

Using periodic boundary conditions in this manner works relatively well for simple simulations, such as allowing an initial random array of cells to relax to a more stable configuration. However, difficulties in this method arise when encoding more complicated junctional rearrangements. As two copies of each boundary vertex are stored, processes such as T1 swaps become much more involved. If they occur on the boundary they must be applied to two separate sets of vertices, and it must be determined whether any newly created vertices are themselves boundary vertices. Cells often must be temporarily transposed to the opposite side of the sheet to calculate new vertex positions, then moved back to the original side afterwards. Therefore a simpler method is desired that does not require more than one copy of any given vertex.

5.2.3 Mapping from the 2D plane to a cylinder

As an alternative to the method described in the previous section, we propose a system where vertices are stored using 3D rather than 2D coordinates. These 3D positions correspond to the location of the vertices on the surface of a cylinder, rather than in the 2D plane. The primary motivation for this description is that only one copy

of each vertex needs to be stored, greatly simplifying the computation required for junctional rearrangements. The initial configuration is set up using a periodic set of random input points to the Voronoi tessellation, as before. However, in this case we ensure that the width of the tissue is equal to 2π, and boundary vertices are exactly 2π apart. These points can then be mapped to the surface of the cylinder of unit radius as follows,

$$\mathbf{c} = \begin{pmatrix} \cos x \\ \sin x \\ y \end{pmatrix}, \tag{5.1}$$

where $\mathbf{c} = [c_1, c_2, c_3]$ is the new 3D coordinate, and x and y are the horizontal and vertical positions, respectively, in the original 2D plane. Due to the fundamental relations $\cos(p) = \cos(p + 2\pi)$ and $\sin(p) = \sin(p + 2\pi)$, the boundary vertices will have the exact same 3D coordinates as their matching vertices, which have been set up exactly 2π apart in the x direction. We therefore discard one copy of this vertex, and ensure that the list of vertices in each cell is updated accordingly.

In order to calculate forces and perform junctional rearrangements, we map back to 2D coordinates. The inverse of the mapping detailed in (5.1) is given by

$$x = \begin{cases} \cos^{-1}(c_1) & \text{if } c_2 > 0 \\ 2\pi - \cos^{-1}(c_1) & \text{if } c_2 < 0 \end{cases}, \tag{5.2}$$

$$y = c_3,$$

where $\cos^{-1}(x)$ is defined for $-1 \leq x \leq 1$ to lie in the range $[0, \pi]$. As the forces on a particular vertex only depend on the cells to which it belongs, and junctional rearrangements only involve cells that are located close to each other, we can map individual cells or groups of cells back to the plane, perform operations on them, then subsequently map back to the cylinder. In other words there is no need to

simultaneously map all vertices back to the 2D plane at the same time, it can be achieved one cell or group of cells at a time. This helps us to eliminate a potential problem when it comes to mapping cells that lie in the region $\{c_1 > 0;\, c_2 \simeq 0\}$. There is a discontinuity in the mapping at $\{c_1 > 0;\, c_2 = 0\}$, as vertices in this region with c_2 just greater than zero are mapped to $x \simeq 0$ in the 2D plane, whereas those with c_2 just smaller than zero are mapped to $x \simeq 2\pi$. This will lead to certain cells having some of their vertices at one edge of the 2D plane and some at the other. Calculations of area, length, and direction will subsequently be incorrect. The problematic region is shown in green in Fig. 5.6.

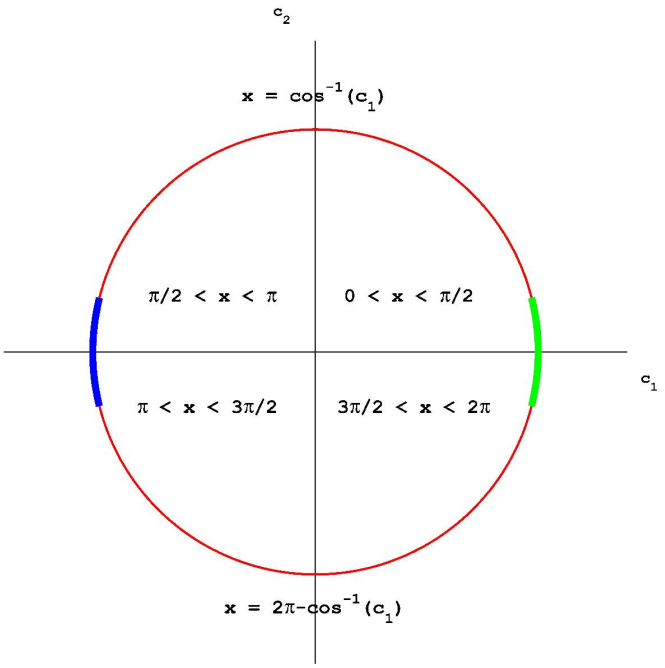


Figure 5.6: *Schematic of mapping from the cylinder to the 2D plane. For $c_2 > 0$, the mapping takes the form $x = cos^{-1}(c_1)$, whereas for $c_2 < 0$ it is $x = 2\pi - cos^{-1}(c_1)$. There is a problematic region shaded in green in which some vertices of a cell can be mapped to the other side of the domain from the rest of the cell. To avoid this problem we take $c_1 = -c_1$ and $c_2 = -c_2$ for vertices in this region before mapping, which is equivalent to moving them into the blue shaded region. In these cases we must add π to the 2D points before mapping back to the cylinder.*

To overcome this problem we perform a preliminary mapping, before the secondary mapping to 2D. The aim of this is to move cells away from this problematic region

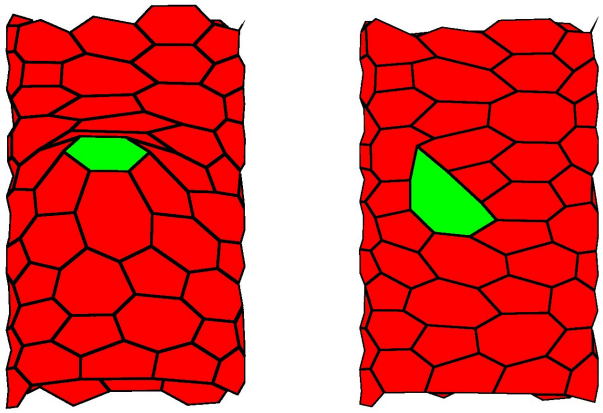
to a position on the cylinder where the secondary mapping is not problematic. The simplest way to achieve this is to move cells around the cylinder by π, to the opposite side (blue region in Fig. 5.6). In practise this is achieved by simply taking $c_1 = -c_1$ and $c_2 = -c_2$. Cells can then be mapped onto the 2D plane, and all the necessary forces applied using the code already developed. Mapping back to 3D can be achieved by simply adding π to the x-values before applying equation (5.1). This ensures vertices are moved back round the cylinder to their original positions. The preliminary mapping only needs to be performed for cells that lie near the green region, with other cells just being mapped straight to the 2D plane using (5.2).

5.2.4 Inducing migration of a single cell

We are now in a position to allow a single cell to migrate up the side of the cylinder and observe effects on surrounding cells. In this section we will not include cell proliferation or apoptosis. Proliferation will be considered in Section 5.3, while cell death will not be included in simulations of AVE migration as it does not play a key role *in vivo* in the process.

There are several possible methods of inducing migration in the vertex model. One potential method is to simply apply an additional force in the positive vertical (z) direction to all the vertices of a chosen migrating cell. This might represent a cell moving towards a uniform chemical source at the top of the cylinder. However, as shown in Fig. 5.7(a), this causes the cells behind the moving cell to quickly become severely stretched, and cells ahead of it to become squashed and deformed. If the applied force is made strong enough, the moving cell will simply move over the top of the cells above it. As we are attempting to model an epithelial sheet, this is not desirable, as cells are not able to pass over or under each other.

Clearly a slightly more subtle force is required to induce migration. In Fig. 5.7(b) the additional force has been applied to just one vertex of the migrating cell. This



(a) (b)

Figure 5.7: *Two methods of inducing migration in the cylindrical model. Migrating cell highlighted in green. (a) We apply a migratory force to all vertices of the migrating cell, and observe that the cells behind it become stretched as it attempts to pass over the cells ahead. (b) The migratory force is applied to a single protruding vertex of the migration cell, which is then able to find its way through the tissue via junctional rearrangements.*

'protruding' vertex is chosen to be the closest to the top of the cylinder, and its pressure force is increased to induce movement. This vertex is able to successfully pass between several cells, by performing junctional rearrangements with nearby vertices. Inducing migration in this way represents the cell's response to a chemotactic signal from the top of the cylinder. The cell integrates signal strength around its periphery and chooses to move in the direction with strongest signal.

We continue with this second method of inducing cell migration, and apply it to a cell initially near the bottom of the cylinder. Fig. 5.8 shows the progression of the cell, highlighted in green. Initially the cell stretches, and its area becomes very large (Fig. 5.8(b)-(d)) compared to that of other cells. Eventually, however, when the cell reaches the top of the cylinder, the rest of the cell begins to 'catch up', and cell size decreases back towards its initial size (Fig. 5.8(e)). The extra migratory force switches off when the cell reaches the top of the cylinder. In reality, migrating cells do change shape as they move, but not in this manner. They instead become more columnar as their height increases in the direction out of the plane. This stretching of the migrating cells may be a result of the particular choice of parameter values

in this simulation, or could more fundamentally be an issue with the model itself. In Owen et al. (2011), the authors model migration of macrophages with a cellular automata framework, and have no problems with distorted cell shapes. Cell shapes during migration in the vertex model will be investigated further in Chapter 6.

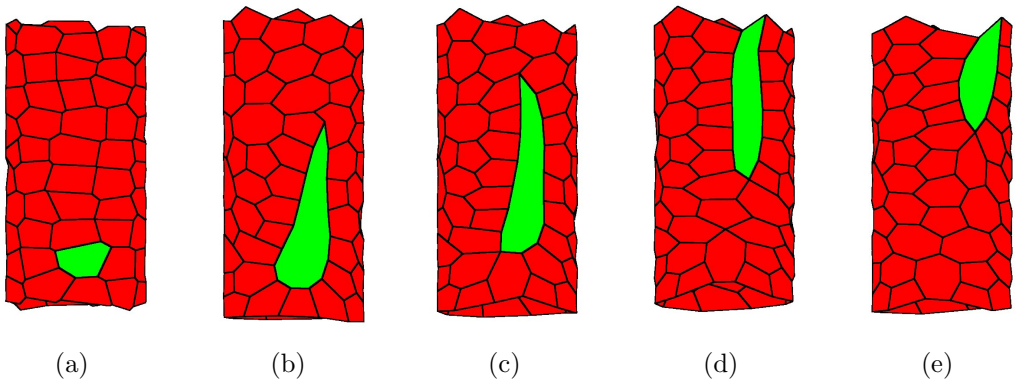


Figure 5.8: *Migration of a single cell (in green) from the bottom of the cylinder (a), to the top (e). The cell area becomes large as the cell extends (b)-(d), and returns towards normal at the top of the cylinder. Along the way junctional rearrangements occur, including T1 transitions and vertex-joining events.*

5.2.5 Summary of the cylindrical model

The main advantage of the cylindrical model is that it enables a simple, efficient implementation of periodic boundary conditions, without the need for any special boundary vertices that must exist in two places at once. This greatly simplifies junctional rearrangements and all other calculations. It utilises the fact that only local interactions are relevant in the model, and there are no long range effects between distant cells, so small groups of cells can be mapped at a time. The cylindrical model is, however, essentially still a 2D model. All forces are calculated in 2D, and the geometry of the cylinder is not accounted for. The domain is also still open-ended in the vertical direction, so cells are not completely restricted to a surface, and the whole sheet can be pulled in either direction. This is unrealistic for the mouse embryo.

In the next section we will address the main flaws of the cylindrical representation

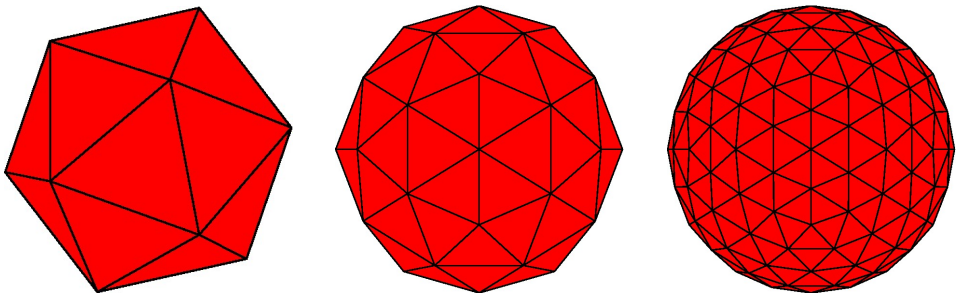
by creating a new model based on the surface of an ellipsoid. The ellipsoid is a more realistic interpretation of the shape we are attempting to simulate, and will ensure the surface geometry is accounted for. This new model will also eliminate boundary considerations, as cells will exist in a continuous sheet. We must also attempt to model the barrier to migration at the boundary between the epiblast and ExE, and ensure that migrating cells are not able to pass between these two distinct sections. The first task is to create an initial configuration of cells on an ellipsoidal surface.

5.3 Ellipsoid model

5.3.1 Creating an initial cellular mesh

The strategy we developed in 2D for creating initial configurations, using a Voronoi tessellation of the plane, does not translate easily to a 3D surface. A new strategy must therefore be devised. The problem can be solved using a three-stage algorithm, initially creating a triangular mesh on a spherical surface, then transforming this to a Voronoi-like cellular mesh, and finally stretching the sphere to create an ellipsoid. To create the initial spherical triangular mesh, we start with an icosahedron. This is a regular polyhedron composed of twenty equilateral triangles, which meet at twelve nodes. Node positions can be chosen to lie on the unit sphere. We can refine this coarse mesh by subdividing each triangle into four smaller triangles (Fig. 3.3(a)). The mid-points between each vertex are found and used as vertices in the new triangles. These new vertices can then be projected back onto the unit sphere. This process can be repeated *ad infinitum* to create as many triangles as required. Fig. 5.9 shows an initial icosahedron, along with the resultant mesh after one and two iterations.

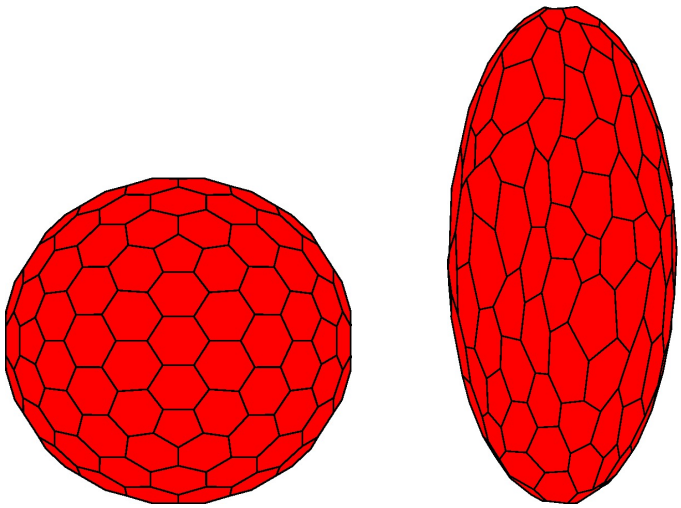
We now turn this triangular mesh into a cellular mesh for our simulations by taking its dual. This uses each vertex of the triangular mesh as the centre of a cell, and the centre of each triangle as a vertex in the cellular mesh. The number of cells



(a) (b) (c)

Figure 5.9: *(a) An icosahedron, with 20 triangular faces meeting at 12 vertices that lie on the unit sphere. (b) The icosahedron is refined so that each triangular face becomes four smaller triangles, leading to 80 faces meeting at 42 vertices. (c) After another level of refinement 320 triangles meet at 162 vertices.*

is, therefore, equal to the number of vertices in the triangular mesh. Fig. 5.10(a) shows the spherical cellular mesh dual of Fig. 5.9(c). It is also possible to add some



(a) (b)

Figure 5.10: *(a) A regular spherical cellular mesh (the dual of Fig. 5.9(c)). (b) A cellular mesh, with random noise added to each point, on an ellipsoidal surface.*

random fluctuations to the vertex positions to give a less regular starting condition. The points are then projected back to the sphere in the same manner as before. We can then finally stretch the resultant sphere along the z-axis, by multiplying all the coordinates in that dimension by an 'elongation' factor. Fig. 5.10(b) shows the final resultant cellular configuration. This type of ellipsoid is a prolate spheroid.

To change the initial number of cells in a simulation, we can run a pre-simulation phase in which the proliferation algorithm is implemented at regular intervals until the number of cells reaches the required number, allowing the cellular configuration to relax to mechanical equilibrium between each proliferation event.

5.3.2 Forces on the ellipsoid surface

The basic force laws on the ellipsoid surface are identical to those described previously in Section 2.2. The key cell quantities including area, perimeter, and height can be worked out, and the equations of motion (2.5) are applied in 3D. The boundary forces described in Section 2.2.3 do not apply as the sheet of cells is now continuous and does not have a boundary.

We must establish the direction in which forces act. This is trivial in 2D (Fig. 1.2), but more complex on the ellipsoid surface. The simplest approximation is a straight line between vertices (Fig. 5.11(a)), however, the component of the force acting into the ellipsoid is balanced *in vivo* by a reaction force from cells inside the VE. This leaves a resultant force in the tangential direction, so ideally we would include this component of the force only.

The appropriate tangential direction for a vertex within a given cell depends on the position of the vertex and the positions of its clockwise and anti-clockwise neighbours. To find the correct direction, we project these neighbouring vertices to the closest point on the plane tangential to the surface at the current vertex (Fig. 5.11(b)). Directions are then calculated on this plane, ensuring that all forces act tangentially. This is achieved in practise by first finding the surface unit normal $\hat{\mathbf{s}}$ at the current vertex, which is perpendicular to the tangential plane. The general equation of the ellipsoid obtained by following the algorithm in Section 5.3.1 is

$$x^2 + y^2 + \frac{z^2}{c^2} = 1,$$

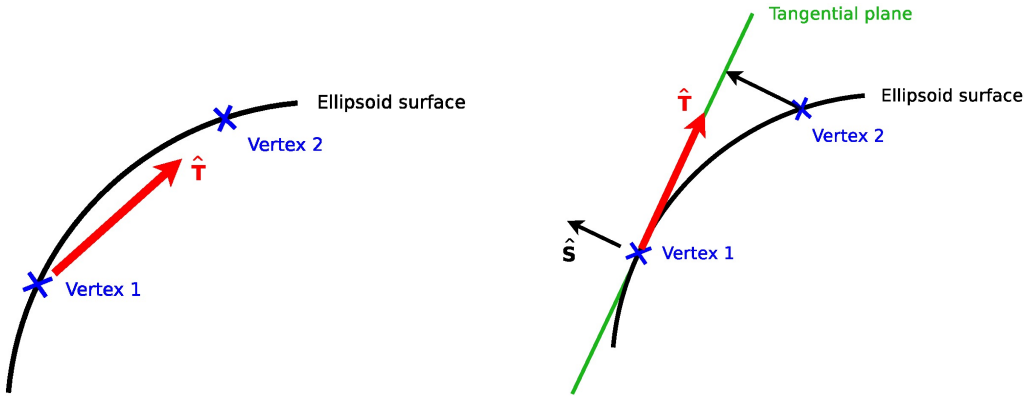


Figure 5.11: *Force directions on the ellipsoid surface. (a) Straight-line force direction. The tension unit vector,* $\hat{\mathbf{T}}$*, acts in a straight line between Vertex 1 and Vertex 2, through the interior of the ellipsoid. (b) Tangential force direction. Vertex 2 is projected onto the tangential plane at Vertex 1 along the unit surface normal,* $\hat{\mathbf{S}}$*, enabling the tangential direction to be calculated.*

where c is the elongation of the ellipsoid, the factor we multiplied by to transform the spherical mesh into an ellipsoid. Setting $\psi = x^2 + y^2 + z^2/c^2$, we find the surface normal by taking

$$\hat{\mathbf{s}} = \frac{\nabla\psi}{||\nabla\psi||},$$

where $\nabla\psi(\mathbf{x}) = [2x, 2y, 2z/c^2]$ and $||\cdot||$ represents the Euclidean norm. As $\hat{\mathbf{s}}$ is perpendicular to the plane, the shortest distance between any point in space below the plane and the plane itself is the distance along the direction specified by $\hat{\mathbf{s}}$. Fig. 5.12 shows, with a 2D schematic, how a neighbouring vertex is projected to the plane. In this case the clockwise vertex with position $\mathbf{x}_c$ is projected to point $\mathbf{x}'_c$ on the plane.

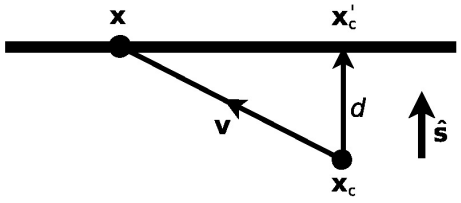


Figure 5.12: *Projecting a vertex to the plane tangential to the ellipsoid surface at a neighbouring vertex. The vertex at position* $\mathbf{x}_c$ *is projected a distance* d *along the vector specified by* $\hat{\mathbf{s}}$ *to the plane at point* $\mathbf{x}'_c$*. The plane is tangential to the surface at the position* $\mathbf{x}$*. The vector from* $\mathbf{x}_c$ *to* $\mathbf{x}$ *is denoted* $\mathbf{v}$*. See text for details.*

The position of the vertex on the plane is given by

$$\mathbf{x}'_c = \mathbf{x}_c + d\hat{\mathbf{s}} = \mathbf{x}_c + (\mathbf{v} \cdot \hat{\mathbf{s}})\hat{\mathbf{s}}.$$

where d is the distance from $\mathbf{x}'_c$ to $\mathbf{x}_c$, and $\mathbf{v}$ is the vector from $\mathbf{x}_c$ to $\mathbf{x}$. In simulations, the distance d will be small relative to the distance between the two vertices.

5.3.3 Mapping vertices to the ellipsoid surface

Applying the force laws along tangential directions, as described in the previous section, vertices move away from the surface of the ellipsoid. *In vivo*, the cells of the VE remain in contact with those of the tissues underneath, due in part to adhesion forces between VE cells and epiblast/ExE cells (S. Srinivas, *pers. comm.*). To simulate these forces, when solving the equations of motion, we apply a mapping back to the surface for each vertex after every iteration. Vertices are mapped to the point at which a straight line from the origin to the vertex meets the ellipsoid surface (Fig. 5.13).

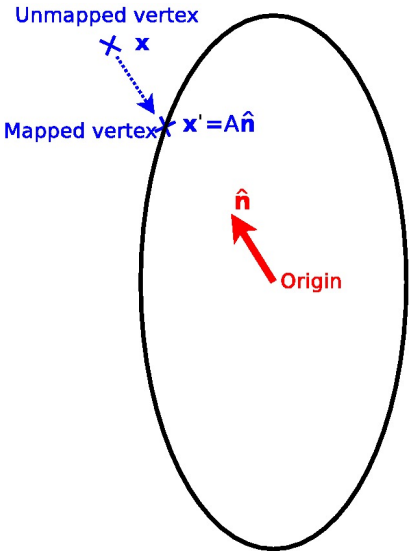


Figure 5.13: *Mapping a vertex to the ellipsoid surface. The unmapped vertex, at* $\mathbf{x}$*, is projected onto the ellipsoid surface at* $\mathbf{x}'$*, on a straight line from the origin to the vertex. The unit vector from the origin to the vertex is denoted* $\hat{\mathbf{n}}$*, and is multiplied by the constant* A *to find* $\mathbf{x}'$*. See text for details.*

For any point with position $\mathbf{x} = (x, y, z)$ in 3D space, we can find the unit vector from the origin at the centre of the ellipsoid via

$$(n_x, n_y, n_z) = \frac{(x, y, z)}{(x^2 + y^2 + z^2)^{\frac{1}{2}}}.$$

We then find the point at which this vector meets the surface of the ellipsoid. In other words, we require the point

$$\mathbf{x}' = (x', y', z') = A(n_x, n_y, n_z), \tag{5.3}$$

such that

$$(x')^2 + (y')^2 + \frac{(z')^2}{c^2} = 1, \tag{5.4}$$

for some constant A. Substituting (5.3) into (5.4) and rearranging for A, we obtain

$$A = \left({n_x}^2 + {n_y}^2 + \frac{{n_z}^2}{c^2} \right)^{-\frac{1}{2}}, \tag{5.5}$$

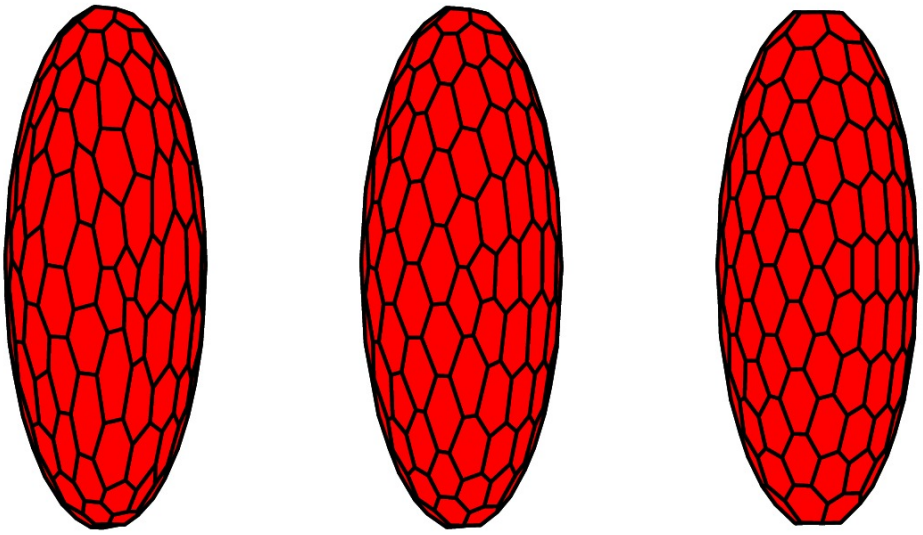
and we can find $\mathbf{x}'$ via (5.3).

Thus we are able to map any point in 3D space back to the surface of the ellipsoid. In reality, Δt will be kept sufficiently small in simulations so that vertices do not stray far from the surface. This ensures that mapping to the ellipsoid does not introduce significant errors into simulations.

5.3.4 Relaxing to mechanical equilibrium

We can now create initial configurations using the icosahedron method, and subsequently apply the force laws and solve equations of motion. Junctional rearrangements and proliferation can be implemented by projecting vertices onto a tangential plane, in a similar manner to finding the force directions (Section 5.3.2).

If we now run a basic simulation, allowing cells to relax from an initial random configuration over time, we can observe the difference between the straight-line approximation and tangential forces. In this simulation we do not consider growth, proliferation, or junctional rearrangements. The simulation is run for $t \in [0, 1]$, with a time-step of 1/10,000, starting with an initial configuration of 162 cells. Parameters used can be found in Table 5.1. Fig. 5.14 shows the evolution of the tissue in the case of tangential forces.



(a) (b) (c)

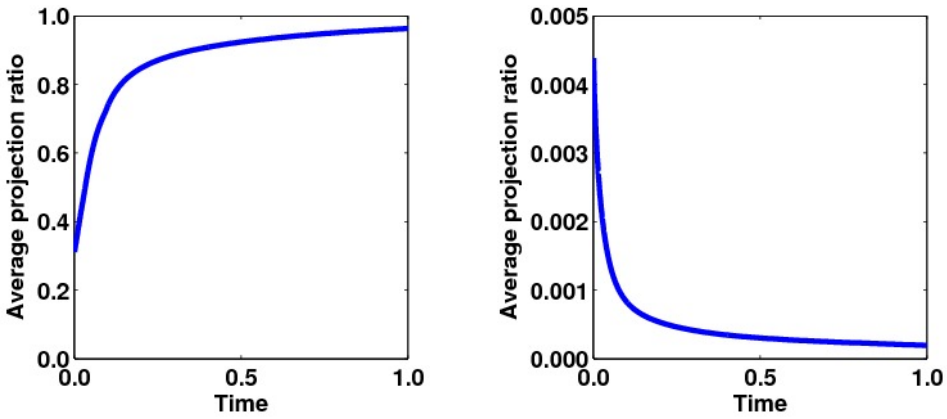
Figure 5.14: *Simulation of cells relaxing to mechanical equilibrium on the ellipsoid surface with tangential forces. Parameter values can be found in Table 5.1. See text for details. (a) t=0, (b) t=0.1, (c) t=1.*

Parameter	C_L	C_P	C_A	C_H	C_D
Value	5×10^{-1}	3×10^{-1}	100	1×10^{-2}	1
Parameter	μ	c	Δt	N_c	$n_1 - n_2$
Value	1	2	1×10^{-4}	162	2

Table 5.1: *Parameter values used in simulation of cells relaxing to mechanical equilibrium on ellipsoid surface.*

Fig. 5.15 compares the average projection ratio at each iteration using the two

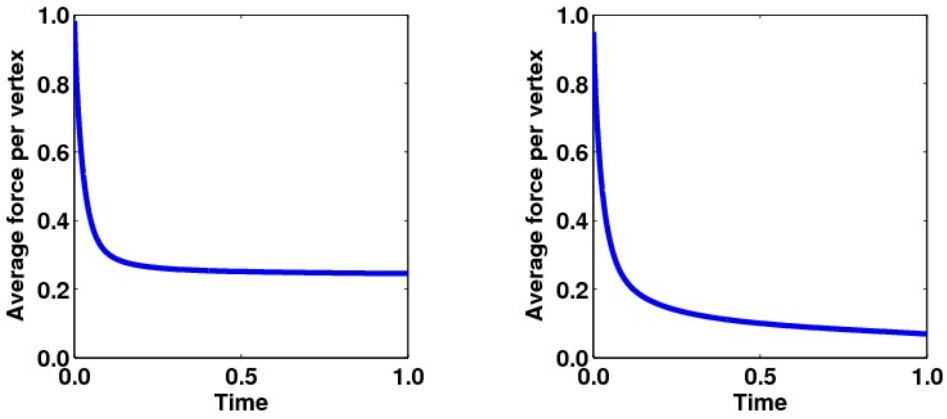
methods of calculating force directions. The projection ratio is calculated for each vertex by dividing the distance by which the vertex is projected upon each iteration by the total distance the vertex moved during that iteration. Under the straight-line approximation for force direction the projection error increases over time. Under the tangential force method, however, the projection ratio is several orders of magnitude smaller, and tends to zero over time. There is also a difference in the average force per



(a) (b)

Figure 5.15: *Average projection error over time for simulation of cells relaxing to mechanical equilibrium on ellipsoid surface. The projection error for each vertex is the distance it is projected back to the ellipsoid surface during each iteration over the total distance moved by the vertex during the iteration. Parameter values can be found in Table 5.1. (a) Straight-line force directions. (b) Tangential force directions.*

vertex over time between the two methods. As Fig. 5.16(a) shows, under the straight-line approximation the average force tends to a non-zero value. In this scenario, vertices move according to the force laws and are then projected back to exactly where they were at the start of the iteration. It is for this reason that the average projection ratio (Fig. 5.15(a)) tends towards one. Using tangential forces, however (Fig. 5.16(b)), the system relaxes towards zero, thus finding mechanical equilibrium.



(a) (b)

Figure 5.16: *Average force per vertex over time for simulation of cells relaxing to mechanical equilibrium on the ellipsoid surface. Parameter values are the same as in Fig. 5.15. (a) Straight-line force directions. (b) Tangential force directions.*

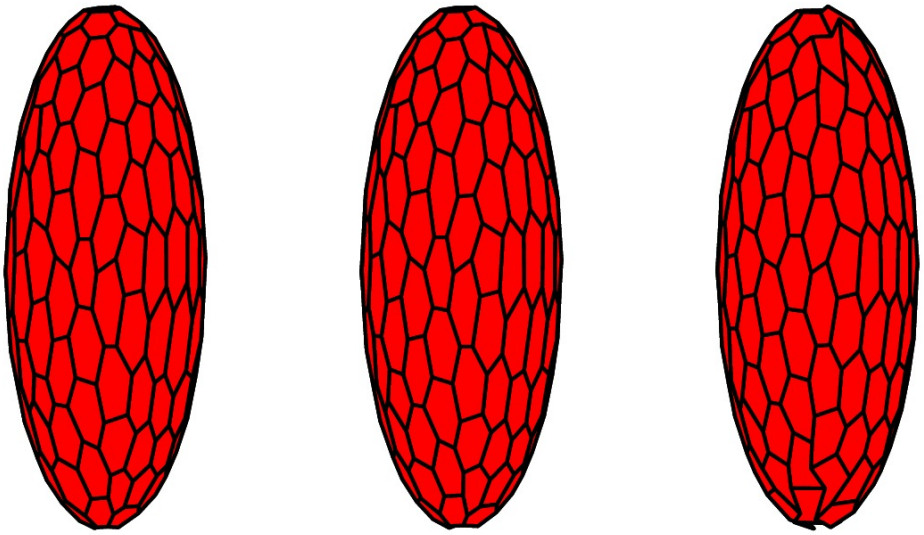
5.3.5 Force validation

In Chapter 2 we tested that the force terms in the 2D model were behaving as expected by running simulations with just one of them active. We can perform a similar analysis in the ellipsoid model. Let us once again consider the area force, given by

$$\mathbf{A} = \left[C_A \frac{|a_t - a|^{n_1+1}}{(a_t - a)} \right] \hat{\mathbf{P}}.$$

Fig. 5.17 shows the evolution of the tissue over $t \in [0, 1]$, for the parameters given in Table 5.2. We observe some unusual cell shapes, including concave cells, arising. As we have set all other constants to zero, there are no forces preventing cells becoming concave, and no restrictions on anything other than cell area, which explains why these shapes can be seen. The other forces ensure that these shapes do not arise naturally in later simulations.

We now check that the force term behaves as expected, by examining how the distribution of cell areas varies over time. Fig. 5.18(a) demonstrates that the mean area stays constant, as the total surface area available to the cells is constant and there is no proliferation or cell death. The standard deviation, however, clearly decreases,



(a) (b) (c)

Figure 5.17: *Simulation of cells relaxing to mechanical equilibrium under influence of area force only in the ellipsoid model. Parameter values can be found in Table 5.2. See text for details. (a) $t = 0$, (b) $t = 0.1$, (c) $t = 1$.*

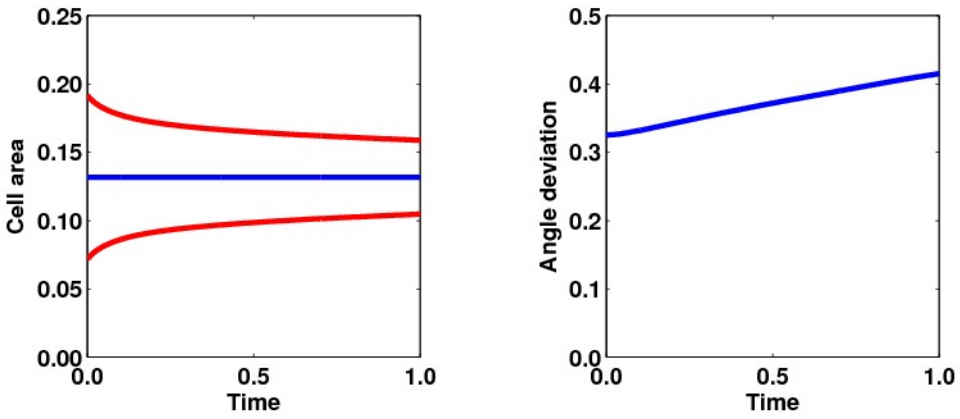
Parameter	C_L	C_P	C_A	C_H	C_D
Value	0	0	200	0	0
Parameter	μ	c	Δt	N_c	n_1
Value	1	2	1×10^{-4}	162	2

Table 5.2: *Parameter values used in simulation of cells relaxing under influence of area force only in the ellipsoid model.*

showing that areas converge as expected towards the target area, a_t. Fig. 5.18(b) shows the mean deviation from internal angle during the simulation. We will use this for comparison purposes with the following simulation, in which we perform the same analysis with the deformation force term given by

$$\mathbf{D} = \left[C_D \frac{|\phi - \theta|^{n_2+1}}{(\phi - \theta)} \right] \hat{\mathbf{P}}.$$

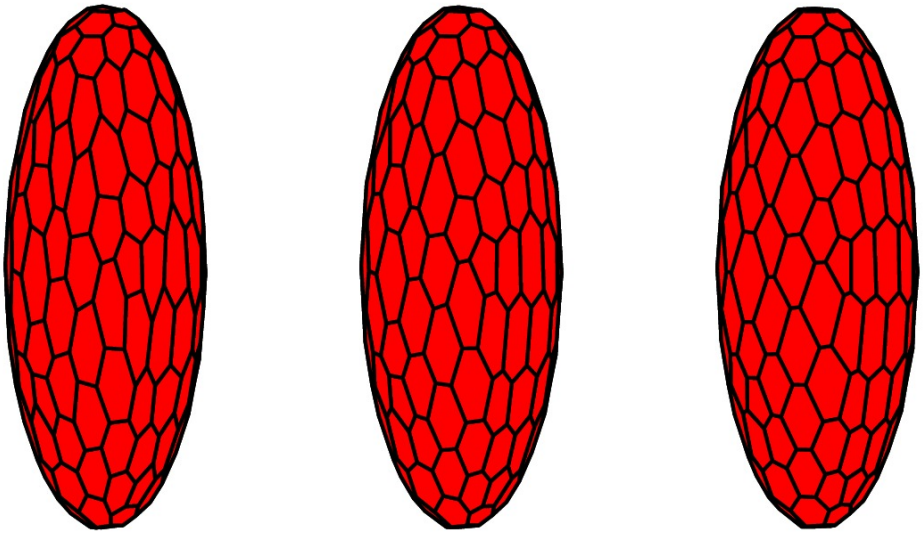
In this case we set the area constant C_A to zero, the deformation constant C_D to one and the constant n_2 to two. All other parameters are the same as in Table 5.2. The



(a) (b)

Figure 5.18: *Cell shape statistics for simulation shown in Fig. 5.17. (a) Mean cell area (blue) and mean +/- 2 standard deviations (red). As the area force is acting, the distribution of cell areas converges towards the mean. (b) Mean deviation from average internal angle. The deformation force is not acting so the mean angle deviation does not decrease, and in fact increases over the course of the simulation.*

evolution of the tissue can be observed in Fig. 5.19.

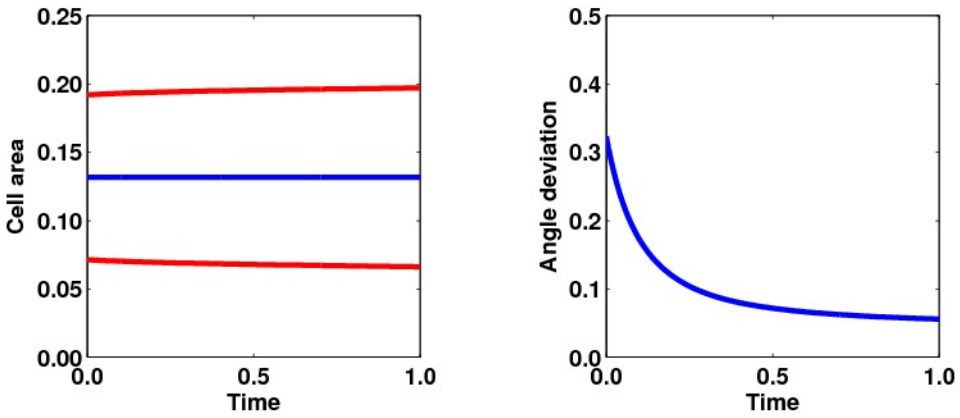


(a) (b) (c)

Figure 5.19: *Simulation of cells relaxing to mechanical equilibrium under influence of deformation force only. See text for parameter values. (a)* $t = 0$*, (b)* $t = 0.1$*, (c)* $t = 1$*.*

As in Chapter 2, we see a marked difference in the behaviour of the deformation

force in contrast to that of the area force. We again observe some very small, as well as large, cells due to the lack of a restriction on cell areas. Fig. 5.20(a) shows the distribution of cell areas for this simulation. We can see that without the presence of the area force, cell areas do not converge over time towards the mean. If we examine deviations from average internal angle, θ, at each vertex, however, we observe that they decrease throughout the simulation (Fig. 5.20(b)).



(a) (b)

Figure 5.20: *Cell shape statistics for simulation shown in Fig. 5.19. (a) Mean cell area (blue) over time and mean +/- 2 standard deviations (red). Without the area force term, the distribution of cell areas does not converge towards the target area. (b) Mean deviation from average internal angle. As the deformation force is acting, the mean angle deviation decreases during the simulation.*

5.3.6 Growth and proliferation

Although it is believed, as stated in Section 5.1, that mitosis is not a driving factor behind AVE migration, it is still important to include it within the computational framework. During the migratory period, it is thought that $\sim 10-20\%$ of cells in the embryo divide, including some of the migrating cells. When cell volumes increase on the ellipsoid surface, as governed by equation (2.7), the average height of cells must also increase, however strong the height-to-area force term is. This is due to the fact that the total surface area available to cells is constant, so the mean cell area cannot

increase. To demonstrate this we run a simulation with cell growth on the ellipsoid surface. Force constants are the same as those in Table 5.1, with $\Delta t = 1/1000$. Cell volumes are drawn from a normal distribution, while cell growth speeds are equal to one. Cell proliferation and cell death do not occur, while T1 transitions are allowed on edges shorter than 5% of the mean. The simulation is run over $t \in [0, 10]$. Other parameter values are as in Table 5.1.

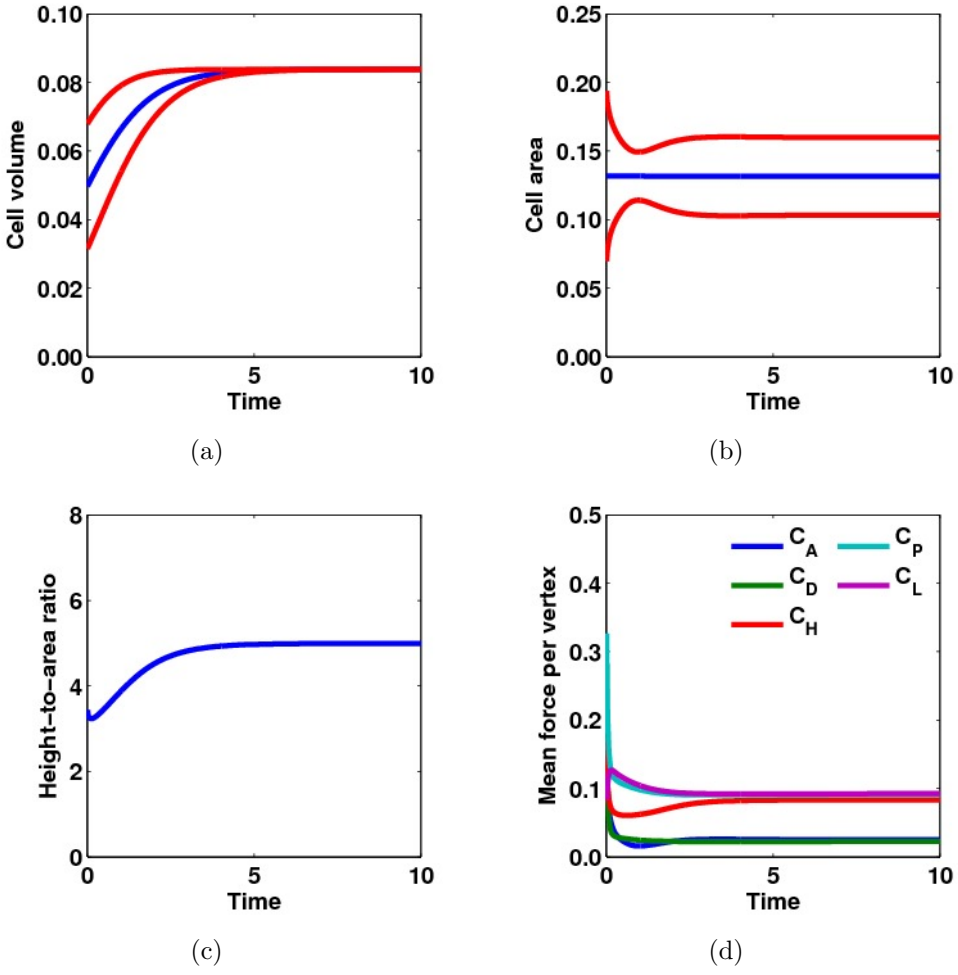


Figure 5.21: *Statistics for simulation of growing cells on ellipsoid surface. See Table 5.1 for parameter values. (a) Mean cell volume over time (blue), and mean +/- 2 standard deviations (red). (b) Mean cell area over time (blue), and mean +/- 2 standard deviations (red). (c) Mean height-to-area ratio over time. (d) Mean force per vertex. The forces in (d) are identified by the constant associated with each. C_A - area force, C_D - deformation force, C_H - height-to-area ratio force, C_P - perimeter force, C_L - line tension force (see Section 2.2.)*

Fig. 5.21 demonstrates that the mean cell volume increases (a), while the mean cell

area stays constant (b). The mean height-to-area ratio constant (c) must therefore increase, regardless of the strength of the constant C_H. Cells, therefore, become elongated in the direction out of the plane of the tissue. Fig. 5.21(d) shows the mean force magnitude of each force term per vertex during this simulation (see simulations in Chapter 2 for explanation).

It is not difficult to allow the ellipsoid radius to increase over time, ensuring that cells do not become as elongated as they grow. This also fits in with the experimental observation that the embryo grows by $\sim 10\%$ during this process (S. Srinivas, *pers. comm.*). Altering the radius means that equation (5.5), for mapping points back to the surface, must also be changed. In our simulations, the radius is generally increased linearly with time.

Fig. 5.22 shows data from a simulation set up in exactly the same way as that in Fig. 5.21, with the only difference being that, on this occasion, the radius of the ellipsoid grows by 10% during the simulation. We observe in (a) that cell volumes change in exactly the same way as before, while the mean cell area (b) increases over the course of the simulation due to the increased ellipsoid radius. The mean height-to-area ratio (c) thus decreases after an initial increase, and ends the simulation at roughly the same value as it started. Obviously, this is dependent on the relative rates of growth of the cells and the ellipsoid. From Fig. 5.21(d) we can observe that the height-to-area force remains lower throughout this simulation than in the previous one.

Since we know roughly the number of cells at the start and end of AVE migration from biological data, proliferation events can be fixed at regular intervals (Section 2.12) such that the desired number of cells is reached at the end of a simulation. Proliferation is implemented at a random angle, in the same manner as it was in 2D.

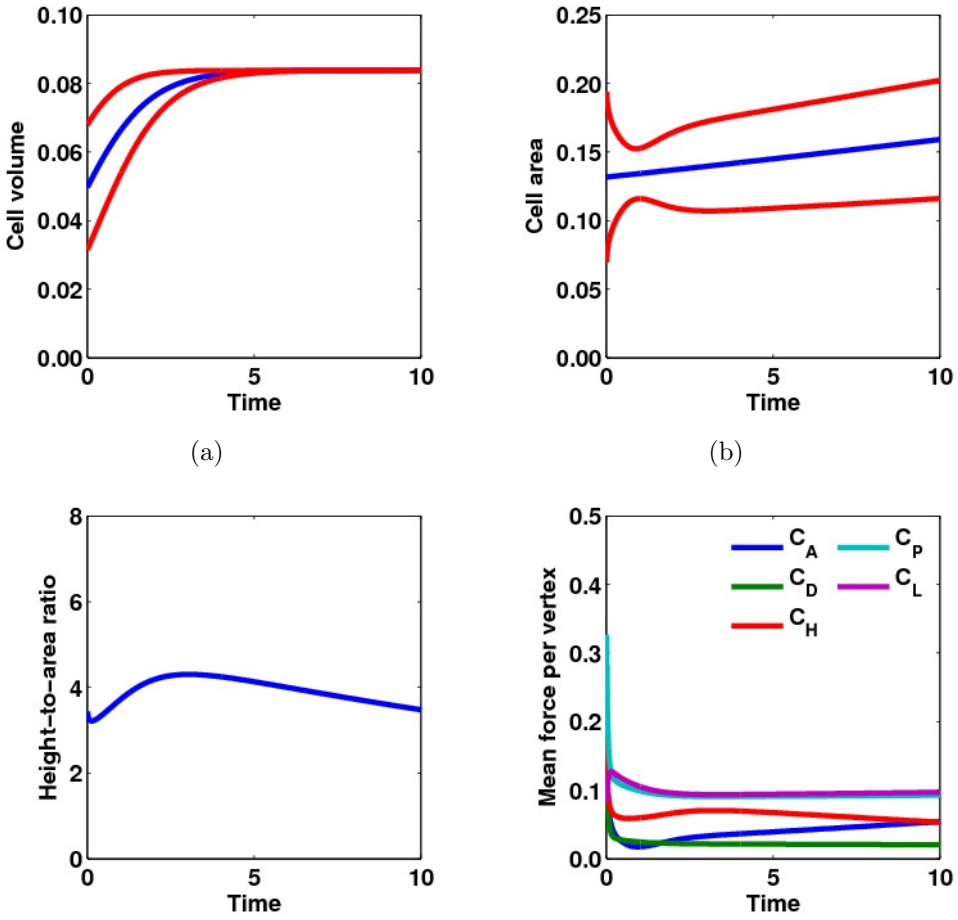


Figure 5.22: *Statistics for simulation of growing cells on ellipsoid surface, with growth of the ellipsoid radius by 10% during simulation. All other parameters as the same as in Fig. 5.21. (a) Mean cell volume (blue) over time, and mean +/- 2 standard deviations (red). (b) Mean cell area (blue) over time, and mean +/- 2 standard deviations (red). (c) Mean height-to-area ratio over time. (d) Mean force per vertex. See Fig. 5.21 for details of force constants.*

5.3.7 Modelling the barrier to migration

It was stated in Section 5.1 that there is a barrier which prevents AVE cells from moving past the boundary between cells overlying the epiblast (Epi-VE) and those overlying the ExE (ExE-VE). The exact nature of this barrier is unknown. Trichas et al. (2011) have shown that the VE cells in these two regions exhibit dramatically different behaviour, with dynamic cell movement and intercalation in the Epi-VE contrasting with a relatively static ExE-VE. It has also been observed that, during

the migration process, actin expression is greater in the proximal region of the embryo, encompassing the complete surface of each cell (Fig. 5.23). This may create a tension force on the whole cell that makes it harder for its vertices to move. In the distal region of the embryo, meanwhile, actin is concentrated on cell edges.

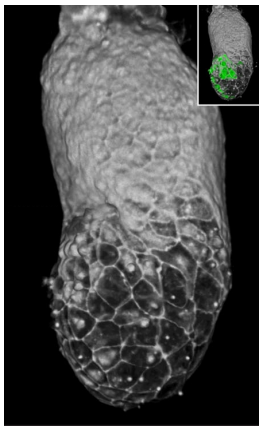


Figure 5.23: *Image of actin staining during cell migration. In the distal region of the embryo, actin staining is concentrated on cell edges, whereas in the proximal portion it encompasses the complete surface of each cell. Inset shows migrating cells labelled with green-fluorescent protein (GFP). Image courtesy of Dr. Shankar Srinivas.*

To incorporate this barrier into the model we could simply fix all the vertices in the proximal region, rendering them completely unable to move. However, this is somewhat unrealistic, as observations show that the proximal region is not completely static, and junctional rearrangements are able to occur in this region. The proximal region appears to simply be less labile than the distal region, so we desire a way to represent this observation. The tension force due to actin on cell edges is already included as part of the model (Section 2.2). There is, however, a possible way to represent the actin shroud in the proximal region. In the equation of motion (2.9), we have a parameter μ that represents the local viscosity. This parameter can be chosen to be equal for all vertices, or can take a different value at each vertex. To simulate the expression of actin in the proximal region of the embryo, we can therefore define separate viscosities, μ_d and μ_p, in the distal and proximal regions of the embryo, respectively.

It could be argued that changing μ does not accurately represent the increased 'stickiness' between cells that we are attempting to model. The viscosity in our case really relates to the adhesion between VE cells and the underlying tissues. The actin shroud might thus be more accurately simulated by altering the tension forces between cells to represent changes in cell-cell adhesion. However, as a simple phenomenological method for inducing the right tissue behaviour, altering μ serves our purpose well. We will implement these separate viscosity parameters in Chapter 6.

5.4 Summary

In this chapter we have adapted our 2D framework, developed primarily in Chapter 2, to model AVE migration in the mouse embryo. We began the chapter by discussing AVE migration. We saw that the AVE is a specialised subset of the VE, an epithelium that surrounds the mouse embryo egg-cylinder at E5.5. The AVE migrates from the distal tip of the embryo to the boundary between the epiblast and ExE. Special configurations of cells known as rosettes have been observed during migration. Unanswered questions about the migration process include: What determines the direction of migration? What is the role of rosettes? Why does migration stop at the boundary between the epiblast and the ExE?

We described some initial extensions to the 2D model, including adding the ability for vertices to join and form rosettes. This is the first time rosettes have been modelled in a vertex framework. We saw that periodic boundary conditions can be implemented, and a cylindrical model established with a mapping from 2D to 3D. However, the cylindrical model has many limitations, and we thus made the jump to a fully 3D ellipsoid model. This novel implementation of the vertex model on an ellipsoid surface includes movement, growth and proliferation of cells. We first detailed how initial configurations are created in this ellipsoid model, then how force direc-

tions are found and how vertices are mapped to the ellipsoid surface. We ran some simulations of cells relaxing to mechanical equilibrium, and showed that the average projection ratio tends to zero when tangential forces are used. We verified that the force terms behave as expected by testing two of them individually, before adding growth and proliferation back in. Finally we discussed the barrier to migration, and saw that it could be represented by an increased viscous coefficient in the proximal region of the embryo.

In the next chapter we will run further simulations of the ellipsoid model. We will induce migration of a single cell, and eventually extend this to a group of AVE cells. We will adjust the threshold at which vertices join together in order to examine the effect of altering the number of rosettes during migration. We will see that rosettes facilitate ordered migration of the AVE, and thus play an important role in development of the mouse embryo.

Chapter 6

Simulations of AVE migration

In Chapter 5, we adapted our 2D vertex model to the surface of an ellipsoid, in order to model AVE migration in the mouse embryo. This takes place at E5.5, when a subset of cells of the VE, known as the AVE, differentiate and migrate from the distal tip to the future anterior. This process is crucial in the patterning of the early mouse embryo.

In this chapter we will display simulation results pertaining to AVE migration, using the model built up in the previous chapter. We will begin in Section 6.1 with migration of a single cell, introducing various methods of applying a migration force and incorporating the barrier to migration into our simulations.

In Section 6.2, we will discuss migration of multiple cells. We will show that cell shapes more closely resemble the biological reality than in the case of a single migrating cell. In this section we will run two types of simulation, one in which rosettes do not form and one in which they do. We will examine polygon number distributions and rosette density to validate our simulations by comparing with experimental data.

In Section 6.3 we will describe a mutant embryo which exhibits fewer rosettes. We will demonstrate that the migration behaviour is similar to that of simulations in which rosettes do not form, leading us to the conclusion that rosettes are crucial

facilitators of ordered migration.

6.1 Migration of a single cell

6.1.1 Migration force

In Chapter 5 we briefly discussed methods for allowing a single cell to migrate in the cylindrical model. To simulate migration, we need to alter the balance of forces acting on migrating cells, in order to represent the dynamic internal changes that occur when a cell migrates. It has been observed that migrating cells often extend protrusions (Aman and Piotrowski, 2009) in the direction of migration. One way of simulating this is to designate a certain vertex to be 'protruding' and apply a migratory force, for example by increasing pressure at the protruding vertex. This was the method employed in Section 5.2.4. In our case, it is known that cells migrate proximally, so we can choose the proximal-most vertex of the migrating cell to be the protruding vertex. The migration force is then given by

$$\mathbf{M} = C_M \hat{\mathbf{P}},$$

where C_M is the migration force constant, and $\hat{\mathbf{P}}$ is the pressure unit vector at the protruding vertex (see Fig. 1.2).

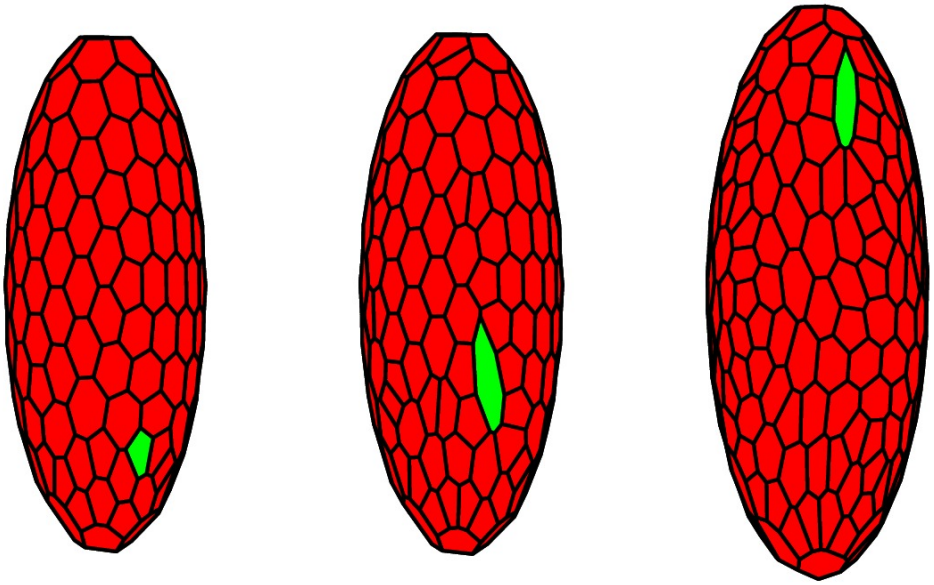
We are now able to put everything together and simulate migration on an ellipsoidal surface. In the first simulation, we choose a cell near the distal tip of the embryo at random, and allow it to migrate proximally. T1 transitions are included, with the T1 threshold set to 5% of the mean edge length ($T_{\mathrm{T1}} = 0.05$). In this simulation, vertices are not permitted to join together. The viscosity is set equal over the whole surface of the ellipsoid ($\mu_p = \mu_d = 1$), so there is no barrier to migration. The simulation is run over $t \in [0, 5]$, with regular proliferation events. The initial number

of cells is 180 and the final number is 260, in line with experimental observations (S. Srinivas, *pers. comm.*). This translates to one proliferation event every 1/16 time-units. Cell volumes are initially equal, so for each cell k, $v_k = mean(cell\ area)^{3/2}$ (see Section 2.8). The ellipsoid radius grows linearly by 10% during a simulation. A summary of key parameters can be found in Table 6.1.

Parameter	C_L	C_P	C_A	C_H	C_D	C_M
Value	5×10^{-1}	3×10^{-1}	100	1×10^{-2}	1	5
Parameter	μ_p, μ_d	$n_1 - n_2$	c	Δt	T_{T1}	g_k
Value	1	2	2	1×10^{-3}	0.05	1

Table 6.1: *Parameter values used in simulation of migration of a single cell.*

Fig. 6.1 shows the cellular configuration at three time-points during the simulation (see also Thesis Movie 4 at http://aaronmsmith.co.uk/movies). We observe that the cell is able to migrate through the tissue, eventually reaching the top of the ellipsoid. During the migratory period the cell becomes stretched slightly in the



(a) (b) (c)

Figure 6.1: *Simulation of migration of a single cell (green) on the ellipsoid surface. Parameter values can be found in Table 6.1. See text for details. (a) $t = 0$, (b) $t = 0.5$, (c) $t = 5$.*

direction of motion, making it flat and reducing the pressure forces acting at other vertices. The large perimeter also creates large tension forces on the edges of the cell, and eventually, once the migratory pressure is removed at the top of the ellipsoid, the cell begins to return to its natural shape. The stretching during migration is not biologically realistic. *In vivo*, the cell becomes more columnar at the start of migration, i.e. its height-to-area ratio increases, and is still above average when migration ends. We will see later that the magnitude of stretching decreases when we allow multiple cells to migrate in our simulations.

6.1.2 Incorporating the barrier to migration

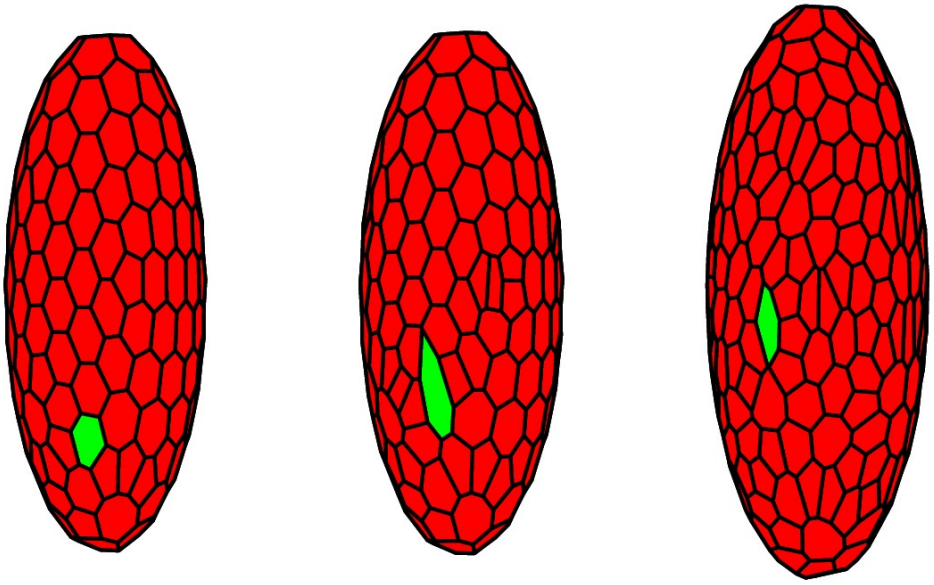
In the following simulation the set-up is identical to the previous section, with one change. We increase μ_p by a factor of 10, thus mimicking the barrier to migration (see Section 5.3.7). The full list of parameters is given in Table 6.2. Fig. 6.2 shows

Parameter	C_L	C_P	C_A	C_H	C_D	C_M	μ_p
Value	5×10^{-1}	3×10^{-1}	100	1×10^{-2}	1	5	10
Parameter	μ_d	$n_1 - n_2$	c	Δt	T_{T1}	g_k	
Value	1	2	2	1×10^{-3}	0.05	1	

Table 6.2: *Parameter values used in simulations of migration with a barrier between the distal and proximal regions.*

that on this occasion the migrating cell comes to a halt at the half-way point round the embryo.

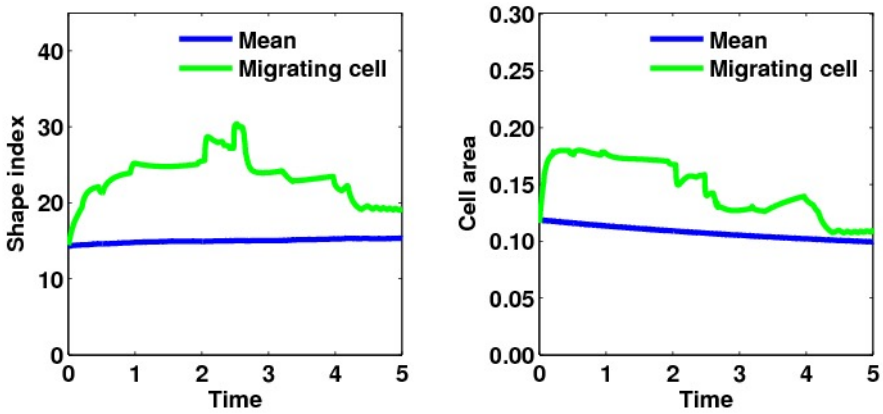
We again observe that the migrating cell becomes stretched along the proximo-distal axis. One way to quantify this stretching is to look at the shape index, which is defined as the perimeter squared over area. The smaller the shape index, the closer to a regular shape the cell is. The smallest shape index possible is that of a circle, which has a shape index of $(2\pi r)^2/(\pi r^2) = 4\pi \approx 12.6$. As a cell stretches non-uniformly, the ratio of its perimeter to area increases, thus leading to a higher shape index. Fig. 6.3(a) shows the shape index of the migrating cell during this simulation, as well as



(a) (b) (c)

Figure 6.2: *Simulation of migration of a single cell (green) with increased viscosity in the proximal region of the embryo to represent the barrier to migration. See text for details. Parameters values are given in Table 6.2. (a) $t = 0$, (b) $t = 0.5$, (c) $t = 5$.*

the mean shape index of all cells in the embryo.



(a) (b)

Figure 6.3: *Cell shape statistics for simulation shown in Fig. 6.2. (a) Mean shape index of all cells and of migrating cells. (b) Mean cell area of all cells and migrating cells.*

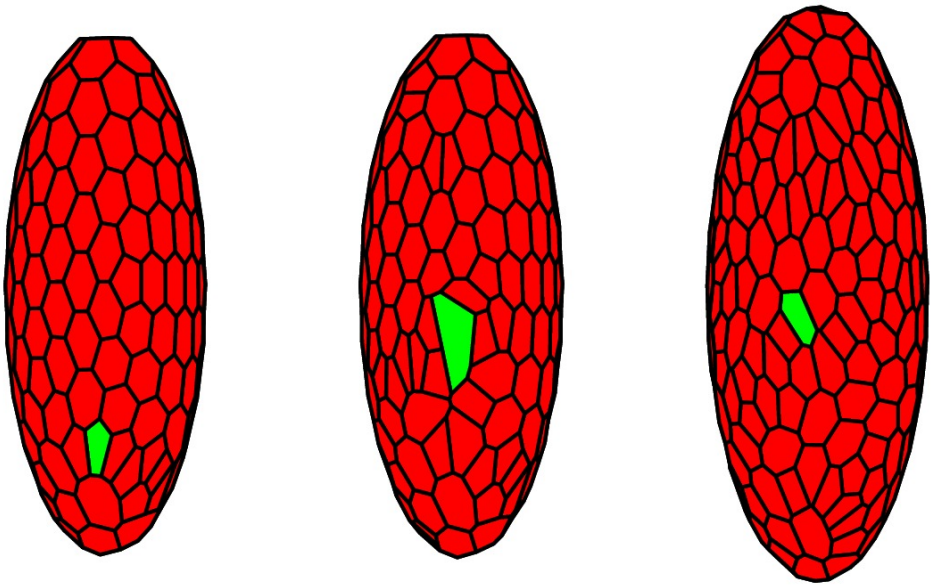
The mean shape index for all cells in the embryo during the simulation ranges from 14.3 to 15.3. The shape index of the migrating cell, meanwhile, increases during

the first half of the simulation, peaking at 30.4, before decreasing back towards the mean by the end. This shows that the cell becomes stretched during migration, but once it reaches the barrier to migration it begins to revert towards its original, more regular shape. Fig. 6.3(b) shows the area of the migrating cell during the simulation, as well as the mean area of all the cells in the embryo. The mean cell area in the embryo ranges from 0.009 to 0.119 over the simulation. We observe an initial increase in the area of the migrating cell to 0.182 at the start of the simulation, followed by reversion towards the mean throughout the rest of the simulation. We will use these data to compare to simulations with more than one protruding vertex in the next section.

6.1.3 More protruding vertices

It may be the case that the migratory force produced by a cell is applied along a section of the perimeter, rather than just at a single point. Although the exact mechanism by which migration occurs is unknown, it is plausible that a force is exerted along a wall of the cell. To represent this in our model we can apply the migration force term to more than one of the vertices of the migrating cells. For example, in Fig. 6.4, we apply the migration force term to the two proximal-most vertices. All parameters are the same as in the previous sections.

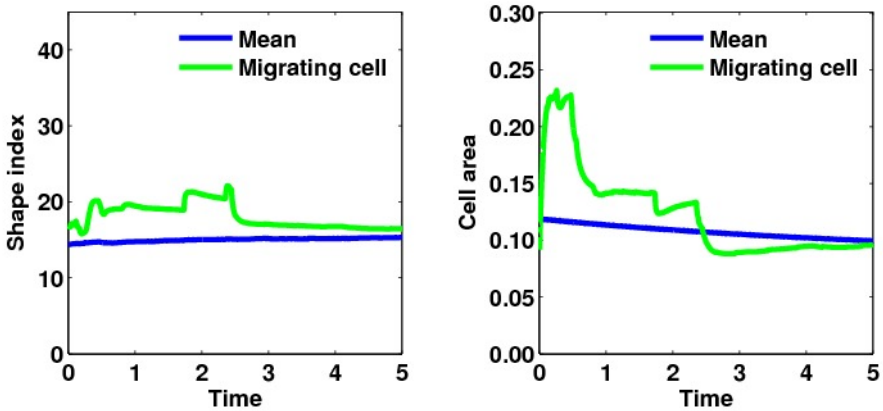
In this case, as before, the cell migrates as far as the barrier. However, migration is faster, as the migrating cell has two vertices pulling it forward rather than just one. The migrating cell seems to become somewhat enlarged due to the extra pressure force at two of its vertices. This can be observed quantitatively in Fig. 6.5(b), which shows the area of the migrating cell during the simulation, as well as the mean cell area of all cells in the embryo. There is a dramatic increase in area at the start of the simulation up to 0.232, followed by a gradual reduction until the migrating cell actually has an area smaller than the mean at the end of the simulation (0.096). This



(a) (b) (c)

Figure 6.4: *Simulation of migration of a single cell (green) with two protruding vertices. The barrier between the distal and proximal regions (bottom half and top half of the ellipsoid, respectively) is in place. Parameters are given in Table 6.2. See text for details. (a) $t = 0$, (b) $t = 0.5$, (c) $t = 5$.*

figure can be contrasted with Fig. 6.3(b). In that simulation, where there was only one protruding vertex, the increase in migrating cell area is not as great.



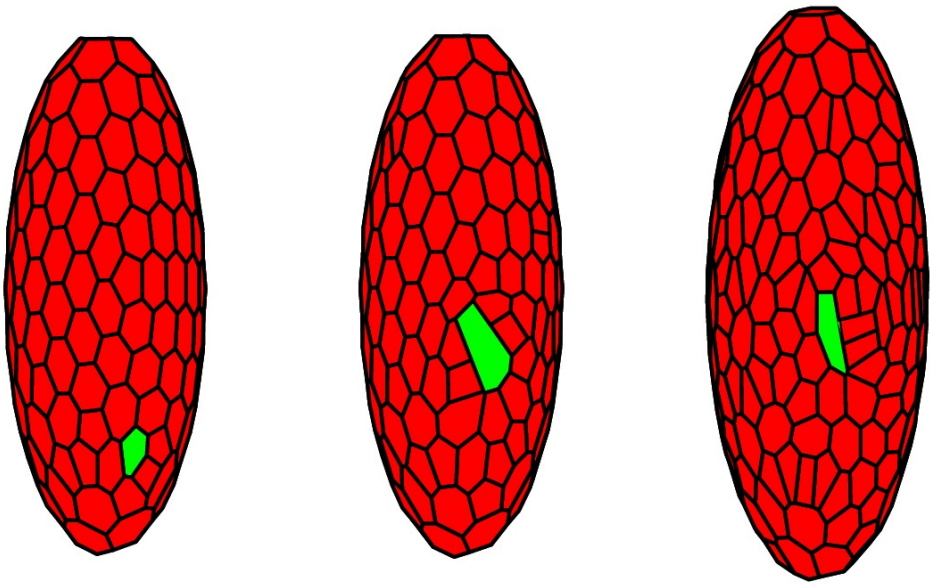
(a) (b)

Figure 6.5: *Cell shape statistics for simulation shown in Fig. 6.4. (a) Mean shape index and shape index of migrating cell. (b) Mean cell area and area of migrating cell.*

The shape index, displayed in Fig. 6.5(a), also exhibits different behaviour in the

case of two protruding vertices. While the shape index of the migrating cell does increase slightly above the mean, with a maximum at 22.1, the effect is not as drastic as in the previous section. In this case we can conclude that having two protruding vertices increases the cell area, but helps keep the shape of the cell more regular.

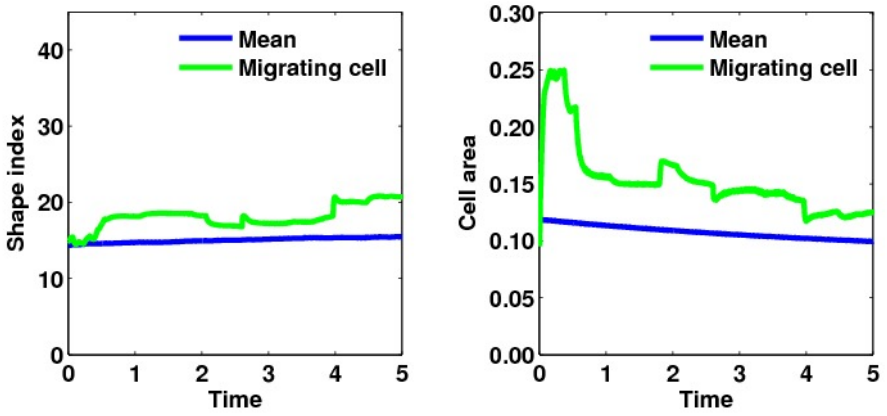
Fig. 6.6 displays the results of a simulation in which three vertices of the migrating cell protrude. Having this extra force at so many vertices makes it more difficult for the cell to move in a single direction as it tends to expand outwards instead. The cell does, however, reach the barrier and subsequently restore itself to the average cell size. In Fig. 6.7, we observe the shape index and area of the migrating cell in



(a) (b) (c)

Figure 6.6: *Simulation of migration of a single cell (green) with three protruding vertices. Parameters are given in Table 6.2. (a) $t = 0$, (b) $t = 0.5$, (c) $t = 5$.*

comparison to the mean values in the embryo. The trends are very similar to those seen in the simulation with two protruding vertices (Fig. 6.5), though the increase in cell area at the start of the simulation is exacerbated, with a maximum of 0.250. In this simulation, the shape index of the migrating cell stays even closer to the mean value, attaining a maximum of 20.85.



(a) (b)

Figure 6.7: *Cell shape statistics for simulation shown in Fig. 6.6. (a) Mean shape index and shape index of migrating cell. (b) Mean cell area and area of migrating cell.*

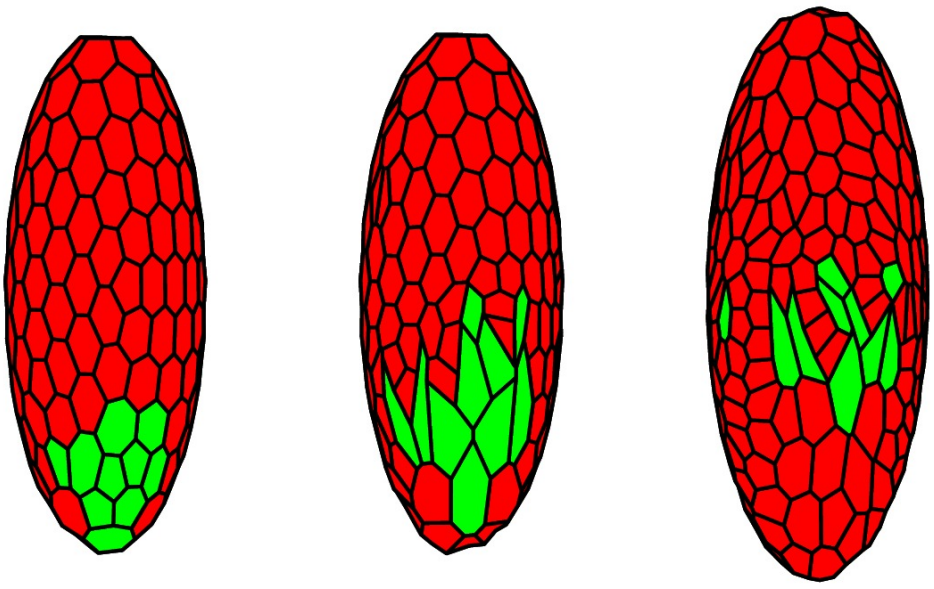
We have seen that when one vertex of the migrating cell protrudes, the shape index of the migrating cell increases significantly, signifying a stretched cell. In the case of two or three protruding vertices, meanwhile, the shape index does not change as dramatically, but the cell area increases significantly. This is biologically unrealistic as the cell area actually decreases slightly for migrating cells, as they become more columnar. For this reason the most realistic way of simulating migration seems to be an extra force at one protruding vertex. We must, however, ensure that further results are not overly sensitive to the exact mechanism chosen for inducing migration, as the exact mechanism acting *in vivo* is unknown. In all further simulations we present results with one protruding vertex, however, in all cases we have run similar simulations with multiple protruding vertices and found the results to be qualitatively the same.

We have so far only considered a single migrating cell. During AVE migration a group of cells migrate from the distal tip to the future anterior, so clearly we need to examine what happens if we induce migration in more than one cell. In the next section we will display simulation results in which several cells of the AVE migrate. We will then introduce some biological data from our experimental collaborators in Dr. Srinivas'

group, and compare our simulations to the experiments. We will examine the effect of rosettes on the system, and show that they facilitate ordered migration.

6.2 Migration of multiple cells

Fig. 6.8 displays a simulation in which ten cells in the distal region of the embryo have been selected to migrate (see also Thesis Movie 5 at http://aaronmsmith.co.uk/movies). The migrating cells are chosen such that they are initially neighbours, in the same quadrant of the distal region of the embryo. Parameters are the same as in Table 6.1, and, as before, we are not yet allowing vertices to join together. Each migrating cell has one protruding vertex, in line with our results from the previous section.

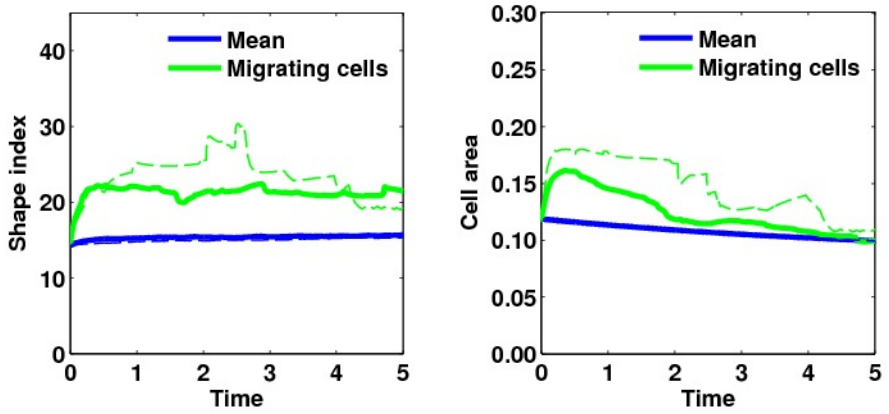


(a) (b) (c)

Figure 6.8: *Simulation of migration of ten cells (green). Parameters are given in Table 6.2. (a)* $t = 0$*, (b)* $t = 0.5$*, (c)* $t = 5$*.*

We observe that the cells are able to migrate from their initial positions to the barrier between the Epi-VE and the ExE-VE. Due to the junctional rearrangements

that occur during migration, the migrating cells are no longer all neighbours at the end of the simulation, and have broken up into several clusters of cells, with non-AVE cells between them. Fig. 6.9 shows the mean shape index and cell area of the migrating cells, as well as the mean over all cells in the embryo. We observe that the increase in mean shape index of the migrating cells is smaller than in the case of a single migrating cell with one protruding vertex, and similarly the increase in mean cell area amongst the migrating cells is not as great. This implies that having a group of cells migrate together goes some way to resolving the problem of cells becoming stretched and enlarged during migration.



(a) (b)

Figure 6.9: *Cell shape statistics for simulation shown in Fig. 6.8. Equivalent statistics for simulation of a single cell migrating are shown with dotted lines. (a) Mean shape index of all cells and of migrating cells. (b) Mean cell area of all cells and of migrating cells.*

6.2.1 Experimental data

Recent measurements by our experimental collaborators in Dr. Srinivas' group have shed insight into the effects of AVE migration on tissue topology, and yielded clues as to mechanisms behind migration (Trichas et al., 2011). Cell shape can be quantified by counting the number of neighbours of each cell to find the so-called *polygon number*. They observed that before AVE migration most cells in the VE are regularly shaped,

and there is no significant difference between the mean polygon number of Epi-VE (5.56) and ExE-VE (5.67) cells. During migration, Epi-VE cells show a greater range of shapes and exhibit irregular packing (mean polygon number = 5.28), whilst there is little change in the ExE-VE (mean polygon number = 5.56). The observed changes in cell packing are thus localised to the region of the embryo in which the AVE is migrating (Trichas et al., 2012).

Dr. Srinivas also examined cell packing in two mutant embryos that display a failure of migration (referred to as $Nodal^{\Delta 600/lacZ}$ and $Cripto^{-/-}$). It was found that, in these mutants, polygon numbers are similar to those in pre-migration wild-type embryos, and differences between the Epi-VE and ExE-VE do not emerge. These results suggest that the changes in polygon number seen in normal embryos, and a shift away from the equilibrium cell packing arrangement, may be directly related to AVE migration. It is not clear, however, whether AVE migration causes the shifts in cell packing, or whether these shifts occur via other mechanisms in order to facilitate migration.

Rosette numbers were also quantified by calculating rosette 'density' at various stages of migration. Rosette density is defined as the number of rosettes divided by the total number of cells in the VE. Using density rather than absolute number ensures that differences in numbers of VE cells are corrected for. It was found that rosette density increases progressively from the 'pre-AVE' to 'distal' to 'migrating' stages, with a slight decrease between 'migrating', the penultimate stage, and 'anterior', the final stage. Rosettes are located almost exclusively in the Epi-VE. To confirm a specific link between rosette number and AVE migration, rosette numbers were quantified in the two types of mutant embryos in which the AVE fails to migrate. Both mutants showed a significant reduction in rosette density compared to wild-type embryos at the same developmental stage. Fig. 6.10 shows the mean rosette density in the four developmental stages, as well as the $Nodal^{\Delta 600/lacZ}$ and $Cripto^{-/-}$

mutant embryos.

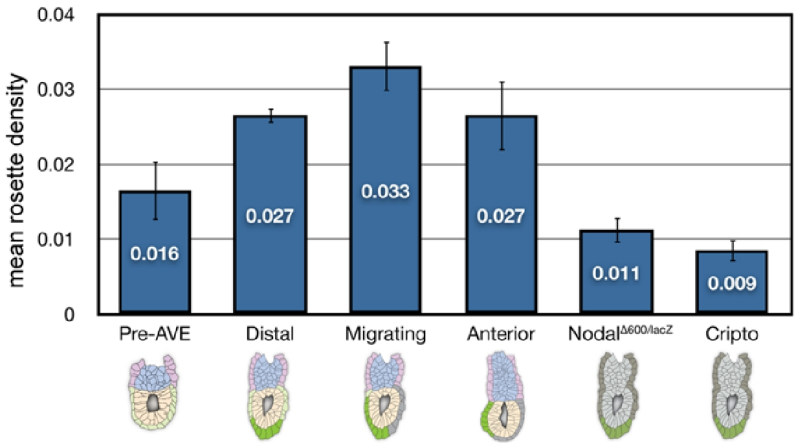
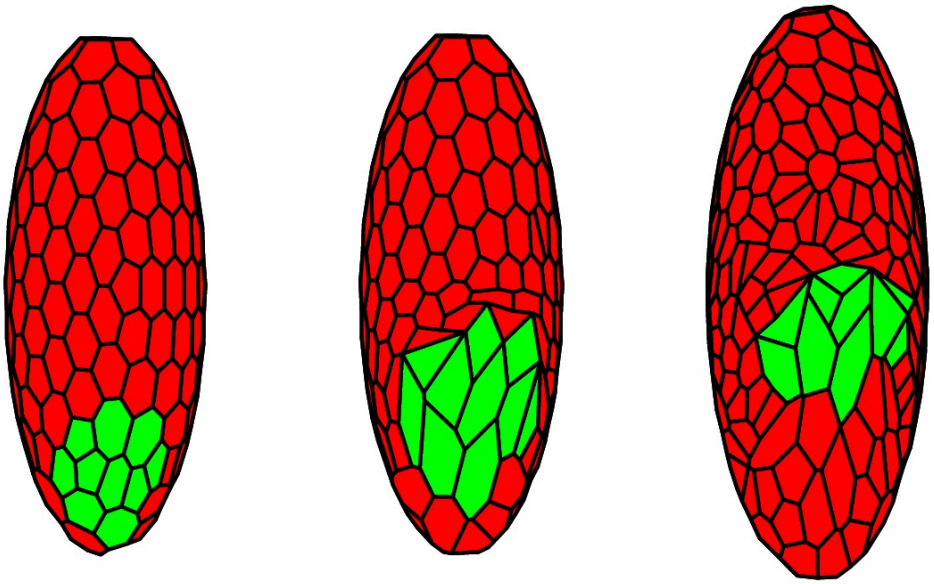


Figure 6.10: *Rosette density (number of rosettes divided by total VE cell number) at different wild-type stages and in the AVE arrest Nodal$^{\Delta 600/lacZ}$ and Cripto$^{-/-}$ mutants. There is a significant increase in rosette density in 'migrating' embryos compared to 'pre-AVE' embryos. The mutants Nodal$^{\Delta 600/lacZ}$ and Cripto$^{-/-}$ mutants show significantly reduced rosette density compared to migrating and anterior embryos, suggesting a direct link between rosettes and AVE migration. Reprinted with permission from Trichas et al. (2012).*

Further experiments by our collaborators were carried out to establish mechanisms behind rosette formation. Time-lapse microscopy was used to confirm that rosettes form by cell intercalation, as opposed to cell division or apoptosis. Cell tracking showed that cells that initially were not in contact with one another became neighbours during rosette formation. Rosettes were not observed to split during AVE migration, suggesting that if they do resolve it is on a longer time-scale than the migration process.

6.2.2 Simulations with rosettes

In Fig. 6.11, we display the results of a simulation in which rosettes form during migration. In this simulation, vertices that fall below the threshold for junctional rearrangements ($T_{T1}\times$ mean edge length), can undergo either a T1 transition or a vertex-joining event, with equal probability. We observe that the AVE tends to stay clumped together in a single patch, in contrast to Fig. 6.8, where it has broken up



(a) (b) (c)

Figure 6.11: *Simulation of migration of ten cells (green), with rosette formation. Parameters are given in Table 6.2. See text for details. (a) $t = 0$, (b) $t = 0.5$, (c) $t = 5$.*

into several clusters. We also see that during migration the cells ahead of the AVE are pushed against the barrier, forming a kind of 'crescent' shape (see also Thesis Movie 6 at http://aaronmsmith.co.uk/movies). This is very similar to what is observed *in vivo* (Fig. 6.12).

We can compare the rosette density during this simulation to the experimental data in order to test the accuracy of our simulations. Fig. 6.13(a) shows the rosette density during the simulation. It increases from zero at the start of the simulation to a maximum of just over 0.20. The graph indicates that the rosette density changes in discrete jumps. There is a discrete increase in rosette density when a new rosette forms, while a cell proliferation event causes the density to decrease.

Comparing Fig. 6.13(a) with Fig. 6.10, we see that rosette density is lower in our simulation than in the experimental data. In the experimental data, the rosette density peaks at 0.033 in the migrating phase. In Fig. 6.13(b) we display the mean rosette density over ten simulations, each with a different initial condition. The

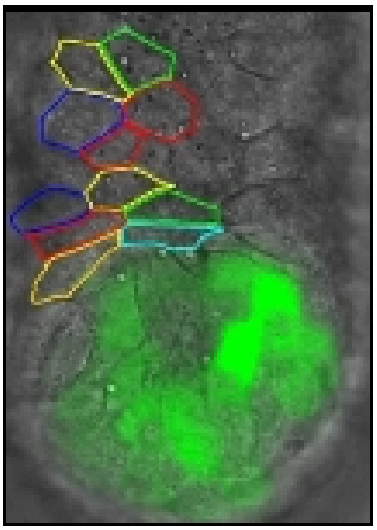
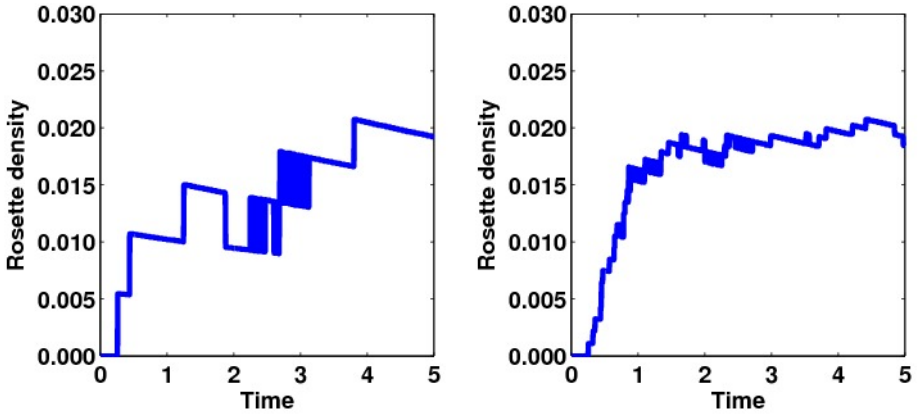


Figure 6.12: *Image of AVE cells (green) near the end of migration. The cells ahead of the AVE are squashed by the migrating cells and form a 'crescent' shape, similar to that observed in simulations with rosette formation. The AVE, labelled using green fluorescent protein, migrates as a single, coherent body as in simulations. Image courtesy of Dr. Shankar Srinivas.*



(a) (b)

Figure 6.13: *Rosette density statistics for simulations of migration of multiple cells with rosette formation. Parameters are given in Table 6.2. (a) Rosette density for simulation shown in Fig. 6.11. The density changes in discrete jumps as new rosettes form or the number of cells in the tissue changes. (b) Mean rosette density taken over ten simulations, each with a different initial condition.*

highest mean density is clearly lower than the experimental mean, showing either that fewer rosettes are forming in our simulations than occur in experiments, or the total cell numbers in the VE are smaller *in vivo*.

This problem could be resolved in several ways: increasing the threshold at which

junctional rearrangements occur (see Fig. 6.14); increasing the probability of vertex-joining for vertices that fall below the rearrangement threshold; or decreasing the total number of cells in the embryo. We are not aiming, however, for an exact quantitative match between the experimental and simulation data, because we do not have access to all the parameters of the system. It is more important that qualitative trends are replicated, and in this sense our simulation data show a similar progression to the experimental data, with a dramatic increase in rosette density between the pre-AVE and migrating stages.

We do not observe the drop-off encountered in the experimental data between migrating and anterior phases. This has been proven to be caused by an increase in the total number of cells in the VE, rather than a decrease in the number of rosettes (Trichas et al., 2012). If we run simulations for a longer time-period, the number of cells continues to increase while the number of rosettes remains unchanged because migration has come to an end. The rosette density therefore decreases in line with the experimental data (results not shown).

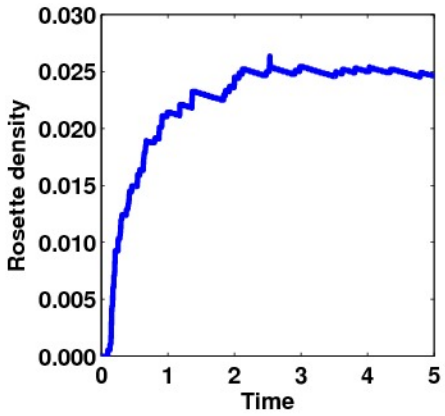
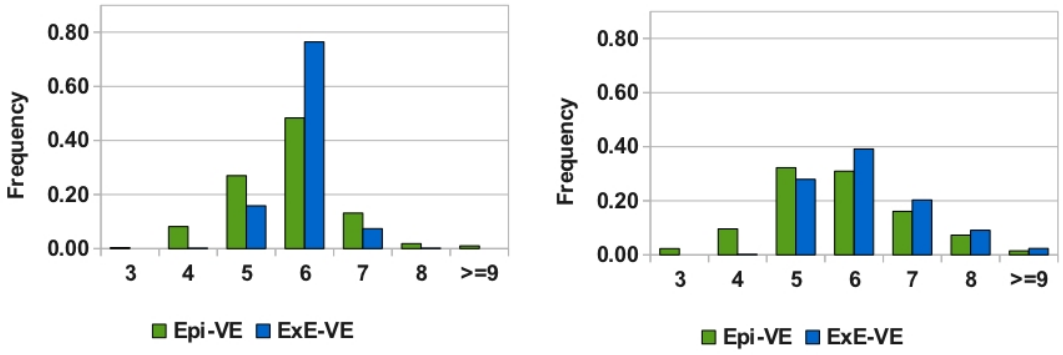


Figure 6.14: *Mean rosette density taken over ten simulations with different initial conditions. A large junctional rearrangement threshold ($T_{T1} = 0.2$) is used in these simulations, encouraging more rosettes to form. All other parameters are as in Table 6.2.*

We can also compare simulations and experimental results by examining the distribution of polygon numbers during migration. Fig. 6.15 shows the mean distribution of polygon numbers in the Epi-VE and ExE-VE over ten simulations at two stages

during migration, $t = 0.5$ and $t = 5$. A cell is defined as being in the Epi-VE if its centre lies below the mid-point of the ellipsoid. The distributions are obtained by finding the number of sides of each cell, which is equal to the number of neighbours.



(a) (b)

Figure 6.15: *Mean distribution of polygon numbers in the Epi-VE and ExE-VE over ten simulations of migration with rosette formation. Parameters are given in Table 6.2. (a)* $t = 0.5$. *(b)* $t = 5$.

We observe that in the early stages of migration 48.3% of cells in the Epi-VE are six-sided (mean polygon number = 5.76), while 76.4% of cells in the ExE-VE have six sides (mean polygon number = 5.92). At the end of the simulation, however, there has been a shift in the peak of the distribution. In the Epi-VE, there are now more five-sided (32.2%) than six-sided (31.0%) cells (mean polygon number = 5.65), while the proportion of six-sided cells in the ExE-VE has shrunk to 39.9% (mean polygon number = 5.86).

Fig. 6.16 shows polygon number distributions in the Epi-VE and ExE-VE from experiments. The two histograms represent embryos in the pre-AVE and migrating stages. Comparison between exact time-points *in vivo* and in simulations is not possible, however, we can still observe general trends in the distributions and validate our computational experiments. We observe that in the pre-AVE stage, the peak in the ExE-VE distribution is at six-sided cells, whereas in the Epi-VE there are slightly more five-sided cells. Although computationally we found the peak in both distribu-

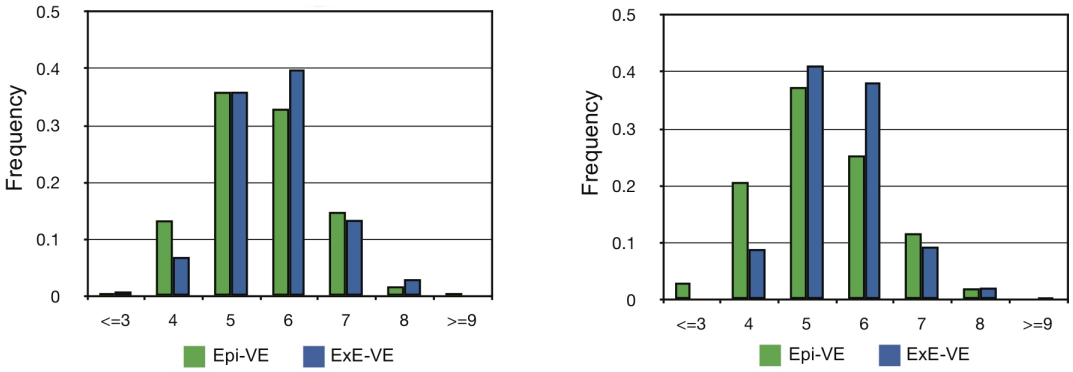


Figure 6.16: *Mean distribution of polygon numbers in vivo in the Epi-VE and ExE-VE. (a) Pre-AVE cells. (b) Migrating cells. Reprinted with permission from Trichas et al. (2012).*

tions at six, there was a clear difference between the Epi-VE and ExE-VE, with a shift towards higher numbers in the ExE-VE, as is found in the experimental data. The increase in five-sided cells *in vivo*, at this early pre-migration phase, suggests a mechanism independent of migration that alters the cell packing in the VE away from standard hexagonal packing. During the migrating phase the experimental data show a peak at five-sided cells in both the Epi-VE and ExE-VE. The shift towards five-sided cells can be seen clearly in both sections of the embryo in our simulations. Although *in vivo* the mean polygon number is lower, both at the pre-AVE and migrating stages, the qualitative trend for a shift towards lower polygon numbers during migration is observed in both the experimental and simulation data.

We have shown in this section that simulations with rosette formation show qualitative agreement with experimental data, both in terms of the polygon number distributions and the nature of migration itself, with cells migrating together and forming a crescent shape at the boundary between the Epi-VE and ExE-VE. In the next section we will look at mutant embryos in which fewer rosettes form, and show that the emergent migration behaviour is similar to that observed earlier when rosettes were not allowed to form in our simulations. This will lead us to the conclusion that rosettes are

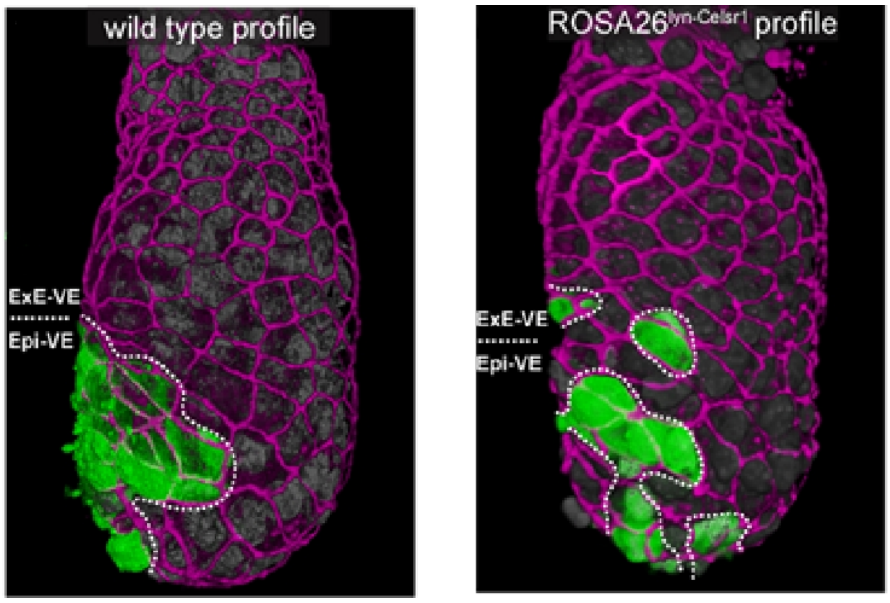
important facilitators of ordered migration.

6.3 PCP-signalling mutants

PCP (Planar Cell Polarity) signalling, which coordinates polarisation and rearrangements across tissues in various contexts, is believed to play a key role in rosette formation *in vivo*. PCP-signalling is disturbed in $ROSA^{Lyn\text{-}Celsr1}$ mutant embryos (Trichas et al., 2011). Our experimental collaborators quantified rosettes in mutant embryos at E5.75 in order to test if rosette formation was affected. They found that rosette density was significantly reduced in comparison to wild-type embryos. They confirmed that this reduction was due to a decrease in the average number of rosettes per embryo, rather than an increase in the number of VE cells.

In most cases the AVE migrates in $ROSA^{Lyn\text{-}Celsr1}$ mutants, however, it does so in a disordered manner similar to simulations in which rosettes do not form (Fig. 6.17). We can compare the images in Fig. 6.17 to those obtained in simulations with and without rosettes (Fig. 6.18).

We observe striking similarities between Fig. 6.17 and Fig. 6.18. In the wild-type cases (Fig. 6.17(a) and Fig. 6.18(a)), the AVE stays clumped together, reaching the barrier between the Epi-VE and the ExE-VE as a single coherent body. In the mutant cases, meanwhile, where rosette formation is disturbed but migration still occurs, the AVE breaks up, both *in vivo* and in simulations, into separated clusters of cells. This suggests that, while rosettes are not essential for the occurrence of migration, they are crucial in ensuring it occurs in an ordered manner. It should be noted that the simulations displayed in Fig. 6.18 were run with exactly the same parameters, the only difference being the ability for vertices to join together in (a). This simple change in the model leads to all the observed differences in migratory behaviour.



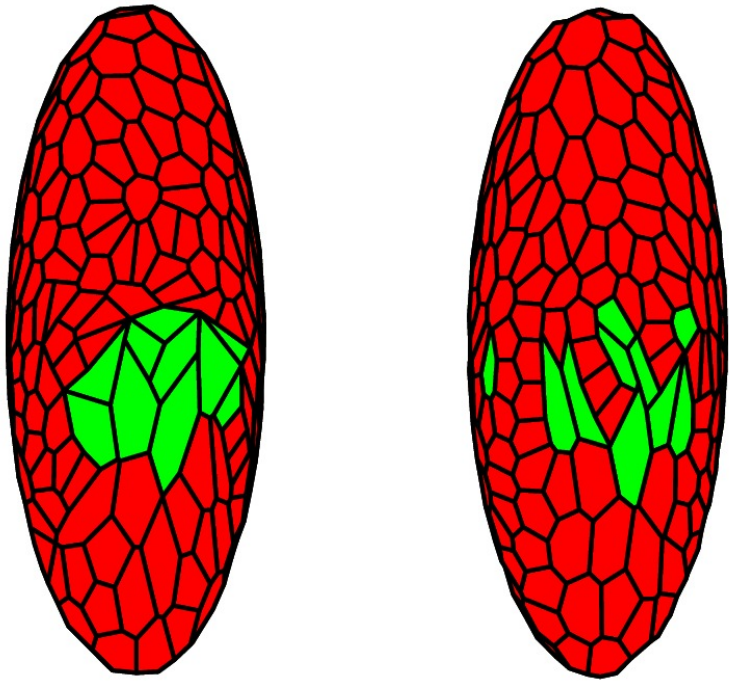
(a) (b)

Figure 6.17: *Profile view of representative 'anterior' phase embryos. (a) Wild-type. (b) $ROSA^{Lyn\text{-}Celsr1}$ mutant AVE migration. The wild-type exhibits ordered migration, while the mutant shows abnormal migration, with AVE cells broken into several groups and spread more broadly through the VE. Cell outlines were visualised by staining for ZO-1 (magenta), and AVE cells by the expression of Hex-GFP (green). Reprinted with permission from Trichas et al. (2012).*

6.4 Summary

In this chapter we presented simulation results concerning AVE migration in the mouse embryo. We began the chapter by choosing a random cell in the distal region of the embryo and applying a migratory force to its proximal-most vertex. We found that the cell migrates through the epithelial VE to the top of the ellipsoid through a series of T1 transitions. However, the cell becomes stretched in the proximo-distal axis, as demonstrated by an increase in its shape index. We introduced a barrier to migration by increasing the viscosity in the proximal region of the embryo, and showed that this causes the cell to stop migrating at the point between the Epi-VE and the ExE-VE.

We then looked at how the system responds if we have two or three protruding vertices in each cell, rather than one. We found that although the shape index of



(a) (b)

Figure 6.18: *(a) Migration with rosettes. See Fig. 6.11 for details. (b) Migration without rosettes. See Fig. 6.8 for details. In (a), the AVE stays clumped together throughout migration, reaching the barrier as a single coherent body. In (b), the AVE breaks up into clusters, separated by non-AVE cells at the barrier.*

the migrating cell remains closer to the mean of all the other cells as the number of protruding vertices increases, there is a concurrent increase in cell area. This is biologically unrealistic, as, *in vivo*, the area of migrating cells actually decreases slightly.

We then began to examine the effects of having multiple migrating cells within the system. This much more closely resembles the biological reality of AVE migration, where up to 20 cells migrate together. We initially continued with the policy of only allowing T1 transitions, and not permitting vertices to join together. We saw that when a group of cells migrates with a single protruding vertex each, the increase in mean shape index is less pronounced than in the case of a single migrating cell.

Next we introduced some experimental data from our colleagues in the laboratory

of Dr. Srinivas, and ran simulations with rosettes forming to compare our model to experiments. It was found biologically that, prior to AVE migration, the distribution of cell polygon number is comparable in the Epi-VE and ExE-VE, with a peak between 5 and 6 sides. During AVE migration stages, mean polygon number decreases in both the Epi-VE and ExE-VE, however, this drop is more significant in the Epi-VE (5.56 to 5.28, compared to 5.67 to 5.56 in the ExE-VE). In simulations, meanwhile, we also observe a more significant drop in mean polygon number in the Epi-VE compared to the ExE-VE during migration. Averaged over ten simulations, the mean polygon number early in the migration process was found to be 5.76 in the Epi-VE and 5.92 in the ExE-VE. At the end of migration the mean polygon numbers were 5.65 and 5.86, respectively. This validates our model, as, even though the numbers are not exactly the same as in experiments, the same broad trends are clearly visible.

A specific link between AVE migration and changes in epithelial topology has been reinforced experimentally by two mutant embryos in which the AVE fails to migrate and in which the mean polygon number in the Epi-VE remains close to that in wild-type embryos in which the AVE has not yet started migrating.

In the *Drosophila* germ-band, rosettes have been shown to play active roles in the coordinated cell movements of convergent extension (Blankenship et al., 2006). These movements do not manifest in the mouse VE and rosettes appear to play a different role in this context. The increase in rosettes during AVE migration in wild-type embryos and the reduction in rosettes in mutants with a failure of AVE migration point to a specific role for rosettes in AVE migration. Rosettes are mainly found in the Epi-VE, the region of the VE in which AVE migration occurs.

Our model predicts that rosettes are essential for ordered migration, in which the AVE cells migrate as a coherent group. When simulations are run without rosettes, AVE migration takes place in an abnormally dispersed manner. This dispersed migration is similar to that found in the PCP-signalling mutant $ROSA^{Lyn\text{-}Celsr1}$, in which

AVE migration occurs despite the presence of significantly fewer rosettes. When rosettes are allowed to form in simulations, AVE migration is much more orderly and closely resembles that seen in actual embryos.

Rosettes have not been observed to break apart in time-lapse experiments. We have the capability in our modelling framework to include rosette splitting, and simulations have been run with this functionality. We find that in simulations in which rosettes are highly transient and split shortly after they form, the AVE behaves similarly to the case of no rosettes, and breaks up into separate clusters. In simulations where rosettes stay together for a long time after forming, the AVE stays as a coherent body, consistent with the results of simulations where rosettes do not split at all. Polygon distributions also follow similar trends to previous simulations (data not shown).

Our collaborators believe that the role of PCP-signalling in the Epi-VE is to coordinate the cell intercalation that must occur for migration to happen. This is achieved partly through the formation of rosettes, which buffer the increased disequilibrium in cell packing that accompanies AVE migration. The fact that mean polygon number is lower in mutants with disrupted PCP-signalling supports this view. One suggestion for how rosette formation reduces disequilibrium in the Epi-VE is that it allows non-AVE cells to group together and behave as a single unit. This makes it easier for AVE cells to migrate through the VE.

The combination of our mathematical model and experimental intervention is an effective tool for the study of cell migration in epithelia. The mouse VE provides an appropriate model for the study of cell movements in epithelia on elongated curved surfaces, such as lung buds, ureteric buds or developing intestinal villi. New experimental techniques, such as light sheet microscopy, allow cell movements to be monitored over extended time-scales and could allow AVE migration to be probed in unprecedented detail (Huisken and Stainier, 2009, Keller and Stelzer, 2008). Our

mathematical model is based upon simple assumptions, from which complex behaviour emerges, accurately recapitulating what is observed *in vivo*.

Chapter 7

Discussion

Simple epithelia, mono-layers of tightly packed cells, play important roles in both animal development and the adult organism. A better understanding of key epithelial processes such as cell migration and tissue size control offers the potential to mediate the debilitating effects of serious abnormalities, by curing problems at their source or by tissue engineering. We saw in this thesis that cell migration is crucial in the patterning of the mouse embryo. It has also been shown to be important in wound healing and has been implicated in many pathologies (Yates, 2011). It is, therefore, essential that we learn as much as possible about these processes using the most effective means at our disposal, and in many cases mathematical and computational modelling are the ideal tools. In this chapter we briefly mention the key results obtained in the thesis, then present possible future research directions and end with a summary.

7.1 Results

In Chapter 2 we developed and tested a 2D vertex model framework that includes force laws, junctional rearrangements, growth, proliferation and death. We built upon previous models, including those of Farhadifar et al. (2007), Nagai and Honda

(2001) and Weliky and Oster (1990) by including new, realistic force terms, such as a force that represents the reaction of a cell to its shape being distorted. A boundary force term was also introduced, ensuring that the tissue boundary remains smooth and circular. The model was then extensively tested computationally, showing that a forward Euler approximation to the equations of motion converges to a more accurate solution as time-step decreases and the force terms behave as expected when they act both individually and together.

In Chapter 3 we showed that, by adopting an ALE formulation of diffusion-like equations, the FEM can be integrated smoothly into the vertex model to simulate the spreading of morphogens. This is the first time an ALE reference frame has been combined with a cell-based model to accurately represent diffusing morphogens. In our formulation, unlike previous studies, chemical diffusion is de-coupled from cell movements and the morphogen is external to the cells. Crucially, our set-up allows the chemical to feed back into the vertex model and influence variables such as the growth rate of cells or the mechanical forces. This enables questions regarding the regulation of growth in epithelial tissues such as the *Drosophila* wing disc to be answered in a fully dynamical model for the first time.

Chapter 4 focused on incorporating more realistic source and ingestion terms into the morphogen model. We defined an internal chemical concentration in each cell and modelled the key process of endocytosis by defining an endocytotic rate. The model was validated computationally before we examined data concerning the *Drosophila* epidermis. It had been shown that compartment size may be regulated by the limited secretion of a growth-factor called Spitz. We showed that domain size differed in two simulations, one with limited and one with constant source, suggesting that limited production of morphogen is a feasible size control mechanism.

The advances in Chapter 3 and Chapter 4 allow us to begin to answer questions on tissue size control, for example growth regulation in the *Drosophila* wing imaginal

disc. We showed an example in which the growth rate of cells was made dependent on the distribution of a chemical representing Dpp in the wing disc and showed that it led to a higher rate of proliferation in areas of the disc where the amount of Dpp was greater.

In Chapter 5 and Chapter 6 we set out to determine the effect of rosettes during AVE migration in the mouse embryo, which were first discovered by our collaborator Dr. Srinivas. In Chapter 5 we initially developed a cylindrical model, before moving on to describe a more realistic representation based on the surface of an ellipsoid. In this model forces are applied tangentially and vertices are mapped back to the ellipsoid surface during each iteration. We were able to model the barrier to migration that appears to exist *in vivo* by increasing the viscous coefficient in the proximal region of the ellipsoid.

In Chapter 6 we simulated migration on the ellipsoid surface and found that when multiple rosettes form, the resultant migration behaviour is similar to that observed *in vivo*. When rosettes are not allowed to form in simulations, meanwhile, the AVE migrates in a disordered fashion and breaks up into separate clusters. Experiments in mutant embryos, in which PCP-signalling is disrupted and fewer rosettes form, confirmed our prediction of a causative link between the presence of rosettes and the ordered fashion in which wild-type migration occurs. Our conclusion from this section of work is that rosettes are crucial facilitators of ordered migration.

7.2 Further work

7.2.1 Theoretical

Although the cells in our 2D framework and the ellipsoid model have volume and height, they are not fully 3D, in the sense that forces act only on apical surfaces, and there is no consideration of the fact that neighbouring cells might be at different

heights. A fully 3D vertex model has been proposed by Honda et al. (2004). The authors examine the deformation and rearrangement of cells when subjected to external forces. In the biological applications we have considered in this thesis, representing the tissue as a 2D sheet has proved sufficient, and it is not clear what further biological questions could be answered using a 3D model. However, as models become more sophisticated and further biological data are obtained, 3D vertex models may become an increasingly useful tool.

In Chapter 3, we implemented refinements of the spatial mesh in order to create an accurate approximation to the solution of the diffusion equation on the moving domain. A further useful extension to the model would be to include an adaptive mesh refinement scheme that can be implemented when necessary during simulations, based on the local deformation of the mesh. This would need to cope with the various rearrangements and could help prevent distorted triangular elements from arising during these processes.

Due to the size of the systems currently considered, `Matlab`'s backslash operator is a relatively fast and efficient solver for the governing equations. In future large-scale problems, iterative solvers may need to be employed. In our simulations, the time-step was chosen to be small due to the explicit nature of cell movement, not due to restrictions imposed by the numerical morphogen solver. This is physically reasonable as the cell movements capture processes such as T1 transitions, which require precise knowledge of when the length of an edge falls below a certain threshold.

Computational speed-up could also be attained by parallelising the formation of the matrix systems. This is currently performed sequentially, by looping over either basis functions or cells. Each of these calculations could, in theory, be sent to a different processor and performed simultaneously, reducing the time taken to create the matrices by at least an order of magnitude.

7.2.2 Applications

There are several ways in which the *Drosophila* epidermis simulations presented in Chapter 4 could be made more realistic. We began our simulations with 100 cells, in order to remain consistent with the simulations presented throughout this thesis. *In vivo*, the number of cells is lower, with an average wild-type compartment consisting of 44 cells (Parker, 2006). When Parker induced excess proliferation in the compartment, about half of the extra cells died off via apoptosis. We also ran simulations with apoptosis dependent on Spi concentration, and found that in the case of limited Spi, more cells die further away from the source, as observed *in vivo*. With constant Spi, however, this effect is dramatically reduced (results not shown).

Further computational experiments could examine the effects of excess proliferation. When cells divide in our simulations, the internal chemical is split between the two daughter cells. These cells, therefore, have a relatively low internal concentration compared to their neighbours, and are likely to be smaller and subsequently to die, particularly in the case of limited morphogen production. We might also allow Spi to be produced ubiquitously across the domain, rather than just at the left-hand edge, replicating an experiment by Parker (2006) in which EGFR activity was altered, changing cell perception of Spi and leading to excess signalling. It was found that in this case the compartment overgrows. We would expect that having chemical produced throughout the domain would cause the tissue to grow larger than normal in simulations, as cells everywhere would be able to ingest chemical and grow at a faster rate, rather than just those at one side of the domain.

Our model of morphogen dynamics could also be used to further probe the role of chemical signalling factors and mechanical feedback in the regulation of growth in the *Drosophila* wing imaginal disc. Our model allows this kind of question to be examined systematically. As we saw in Chapter 3, a recent study by Wartlick et al. (2011) has claimed that temporal changes in signalling levels induce cell division. If

true, this would show how uniform growth can be achieved across the disc despite the presence of a Dpp gradient. Schwank et al. (2011), meanwhile, have claimed that uniform growth is attained via a parallel Fat gradient. Both hypotheses can be made consistent with uniform growth within our framework. To verify which, if either, is likely to be correct, we must compare simulations to experimental mutants in which one or more elements of the supposed growth-control mechanism are absent or altered in some way.

Our model of AVE migration in the mouse embryo could be extended in several ways. Although the ellipsoid shape is more realistic than a flat 2D tissue and the cylindrical model, the embryo itself is less regularly shaped. For example, a slight 'pinching' of the circumference has been observed at the barrier boundary between the epiblast and the ExE. It is unknown whether this is a result of the barrier that exists to stop AVE migration at this point, or indeed a cause. A deformable geometry, in which the shape of the embryo is determined by the forces acting on cells, is required to investigate this phenomenon further.

Mutant embryos have been observed by our collaborators in which cells are able to move slightly beyond the normal barrier. In these mutants a reduction in the number of rosettes has also been observed. It is not clear, however, whether there is a causative link between the movement of the barrier and the reduction in the number of rosettes. We can test whether the number of rosettes decreases in our model if the barrier is moved proximally. Our preliminary results (not shown) indicate that a small movement of the barrier is not sufficient to drive a reduction in the number of rosettes. It appears that the barrier must be moved far from its normal position, or removed completely, in order to see a significant reduction in the number of rosettes that form. This implies that the two phenomena are not directly related, and a third, unknown, mechanism may be causing both the reduction in rosettes and the movement of the barrier.

Another issue that could be examined in more detail is how the direction of migration is determined. We assumed that a migratory force exists at the proximal-most vertex of certain migrating cells. It is unclear whether cells *in vivo* are moving up a chemical gradient, or are given a directional cue by excess proliferation in the posterior region of the embryo, or have another mechanism for determining direction. A chemical gradient could be imposed in the model along the proximal-distal axis, with migrating cells set to respond to the chemical by moving up the gradient. A more complete representation of a chemical gradient might involve solving the diffusion equation on the ellipsoid surface. The work presented in Chapter 3 and Chapter 4 of this thesis lays some of the groundwork for how this might be achieved.

7.3 Summary

Vertex models are just one of a number of cell-based models (Graner and Glazier, 1992, Meineke et al., 2001, Newman, 2005) that can be used to simulate tissues and ask key questions in developmental biology. Computational simulations have several advantages over traditional experiments; they are cheaper, faster, easier to replicate and allow the system inputs to be manipulated precisely. The vertex framework is ideally suited to simple epithelial tissues, where cells can be accurately represented as 2D sheets of polygons (Honda, 1978). The combination of experimental intervention and vertex-based modelling has been shown to yield critical insights in a variety of recent development studies (Canela-Xandri et al., 2011, Farhadifar et al., 2007, Rauzi et al., 2008). Cell-based models also have applications in many other areas, from cancer modelling (Osborne et al., 2010) to slime moulds (Maree et al., 1999).

We began in Chapter 2 by outlining a 2D vertex model of cells in a simple epithelium. Throughout this thesis we have extended this model and applied it in a variety of developmental contexts. We incorporated a model of diffusing chemical growth fac-

tors, with applications in the *Drosophila* wing imaginal disc and an internal chemical model, which can be applied to the *Drosophila* epidermis. We extended the model to the surface of an ellipsoid to simulate AVE migration in the mouse embryo. Accurate parameter values were a limiting factor in simulations, and for this reason we looked for qualitative, rather than quantitative, consistency with experiments. As more accurate experimental data become available our models may be better parametrised and quantitative agreement sought.

By including some of the potential extensions detailed in Section 7.2, we will ensure that our vertex model, when used in conjunction with experimental data, continues to be capable of answering important biological questions.

Bibliography

T. Aegerter-Wilmsen, C. M. Aegerter, E. Hafen, and K. Basler. Model for the regulation of size in the wing imaginal disc of Drosophila. *Mech. Dev.*, 124(4):318–326, 2007.

T. Aegerter-Wilmsen, A. C. Smith, A. J. Christen, C. M. Aegerter, E. Hafen, and K. Basler. Exploring the effects of mechanical feedback on epithelial topology. *Development*, 137(3):499–506, 2010.

M. Affolter and K. Basler. The Decapentaplegic morphogen gradient: from pattern formation to growth regulation. *Nat. Rev. Genet.*, 8(9):663–674, 2007.

B. Aigouy, R. Farhadifar, D. B. Staple, A. Sagner, J.-C. Röper, F. Jülicher, and S. Eaton. Cell Flow Reorients the Axis of Planar Polarity in the Wing Epithelium of Drosophila. *Cell*, 142:773–786, 2010.

A. Aman and T. Piotrowski. Cell migration during morphogenesis. *Dev. Biol.*, 341: 20–33, 2009.

U. M. Ascher and L. R. Petzold. *Computer Methods for Ordinary Differential Equations and Differential-Algebraic Equations*. SIAM, 1998.

J. A. Belo, T. Bouwmeester, L. Leyns, N. Kertesz, M. Gallo, M. Follettie, and E. M. De Robertis. Cerberus-like is a secreted factor with neutralizing activity expressed in the anterior primitive endoderm of the mouse gastrula. *Mech. Dev.*, 68(1-2):45–57, 1997.

T. B. Belytschko and J. M. Kennedy. Computer models for subassembly simulation. *Nucl. Eng. Des.*, 49(1-2):17–38, 1978.

J.-D. Bénazet and R. Zeller. Vertebrate limb development: moving from classical morphogen gradients to an integrated 4-dimensional patterning system. *Cold Spring Harb. Perspect. Biol.*, 1(4):a001339, 2009.

C. Bertet, L. Sulak, and T. Lecuit. Myosin-dependent junction remodelling controls planar cell intercalation and axis elongation. *Nature*, 429(6992):667–671, 2004.

T. Bittig, O. Wartlick, A. Kicheva, M. González-Gaitán, and F. Jülicher. Dynamics of anisotropic tissue growth. *New. J. Phys.*, 10(6):063001, 2008.

J. T. Blankenship, S. T. Backovic, J. S. P. Sanny, O. Weitz, and J. A. Zallen. Multicellular rosette formation links planar cell polarity to tissue morphogenesis. *Dev. Cell*, 11(4):459–470, 2006.

P. J. Bryant and P. Simpson. Intrinsic and extrinsic control of growth in developing organs. *Q. Rev. Biol.*, 59(4):387–415, 1984.

R. Burke and K. Basler. Dpp receptors are autonomously required for cell proliferation in the entire developing Drosophila wing. *Development*, 122(7):2261–2269, 1996.

O. Canela-Xandri, J. Buceta, and M. Milan. Dynamics and mechanical stability of the developing dorsoventral organizer of the wing imaginal disc. *PLoS. Comp. Biol.*, 7(9):e1002153, 2011.

M. A. Chaplain. Mathematical modelling of angiogenesis. *J. Neuro.-Oncol.*, 50(1-2): 37–51, 2000.

I. Conlon and M. Raff. Size control in animal development. *Cell*, 96(2):235–244, 1999.

S. J. Day and P. A. Lawrence. Measuring dimensions: the regulation of size and shape. *Development*, 127(14):2977–2987, 2000.

J. Ding, L. Yang, Y. T. Yan, A. Chen, N. Desai, A. Wynshaw-Boris, and M. M. Shen. Cripto is required for correct orientation of the anterior-posterior axis in the mouse embryo. *Nature*, 395(6703):702–707, 1998.

J. Donea, S. Giuliani, and J.P. Halleux. An arbitrary Lagrangian-Eulerian finite element method for transient dynamic fluid-structure interactions. *Comput. Method. Appl. M.*, 33(1-3):689 – 723, 1982.

D. Drasdo and S. Höhme. A single-cell-based model of tumor growth in vitro: monolayers and spheroids. *Phys. Biol.*, 2(3):133–147, 2005.

R. Farhadifar, J.-C. Röper, B. Aigouy, S. Eaton, and F. Jülicher. The influence of cell mechanics, cell-cell interactions, and proliferation on epithelial packing. *Curr. Biol.*, 17(24):2095–2104, 2007.

K. J. Finney, D. R. Appleton, P. Ince, J. P. Sunter, and A. J. Watson. Proliferative status of colonic mucosa in organ culture: 3H-thymidine-labelling studies and computer modelling. *Virchows. Arch. B.*, 56(6):397–405, 1989.

A. G. Fletcher, C. J. W. Breward, and S. J. Chapman. Mathematical modeling of monoclonal conversion in the colonic crypt. *J. Theor. Biol.*, 300C:118–133, 2012.

A. C. Foley, I. Skromne, and C. D. Stern. Reconciling different models of forebrain induction and patterning: a dual role for the hypoblast. *Development*, 127(17): 3839–3854, 2000.

A. Garcia-Bellido and J. R. Merriam. Parameters of the wing imaginal disc development of Drosophila melanogaster. *Dev. Biol.*, 24(1):61–87, 1971.

M. C. Gibson, A. B. Patel, R. Nagpal, and N. Perrimon. The emergence of geometric order in proliferating metazoan epithelia. *Nature*, 442(7106):1038–1041, 2006.

J. A. Glazier and F. Graner. Simulation of the differential adhesion driven rearrangement of biological cells. *Phys. Rev. E*, 47(3):2128–2154, 1993.

M. E. Gracheva and H. G. Othmer. A continuum model of motility in ameboid cells. *Bull. Math. Biol.*, 66(1):167–193, 2004.

F. Graner and J. A. Glazier. Simulation of biological cell sorting using a two-dimensional extended Potts model. *Phys. Rev. Lett.*, 69(13):2013–2016, 1992.

E. Hairer, S. P. Norsett, and G. Wanner. *Solving Ordinary Differential Equations I: Nonstiff Problems*. Springer, 1993.

C. Y. Ho, C. Houart, S. W. Wilson, and D. Y. Stainier. A role for the extraembryonic yolk syncytial layer in patterning the zebrafish embryo suggested by properties of the hex gene. *Curr. Biol.*, 9(19):1131–1134, 1999.

H. Honda. Description of cellular patterns by Dirichlet domains: the two-dimensional case. *J. Theor. Biol.*, 72(3):523–543, 1978.

H. Honda, M. Tanemura, and T. Nagai. A three-dimensional vertex dynamics cell model of space-filling polyhedra simulating cell behavior in a cell aggregate. *J. Theor. Biol.*, 226(4):439–453, 2004.

L. Hufnagel, A. A. Teleman, H. Rouault, S. M. Cohen, and B. I. Shraiman. On the mechanism of wing size determination in fly development. *Proc. Natl. Acad. Sci. USA*, 104(10):3835–3840, 2007.

T. J. R. Hughes, W. Kam Liu, and T. K. Zimmermann. Lagrangian-Eulerian finite element formulation for incompressible viscous flows. *Comput. Method. Appl. M.*, 29(3):329–349, 1981.

J. Huisken and D. Y. R. Stainier. Selective plane illumination microscopy techniques in developmental biology. *Development*, 136(12):1963–1975, 2009.

C. M. Jones, J. Broadbent, P. Q. Thomas, J. C. Smith, and R. S. Beddington. An anterior signalling centre in Xenopus revealed by the homeobox gene XHex. *Curr. Biol.*, 9(17):946–954, 1999.

P. Kaur and C. S. Potten. Cell migration velocities in the crypts of the small intestine after cytotoxic insult are not dependent on mitotic activity. *Cell. Tissue. Kinet.*, 19(6):601–610, 1986.

E. F. Keller and L. A. Segel. Initiation of slime mold aggregation viewed as an instability. *J. Theor. Biol.*, 26(3):399–415, 1970.

P. J. Keller and E. H. K. Stelzer. Quantitative in vivo imaging of entire embryos with Digital Scanned Laser Light Sheet Fluorescence Microscopy. *Curr. Opin. Neurobiol.*, 18(6):624–632, 2008.

D. Kimelman and M. Kirschner. Synergistic induction of mesoderm by FGF and TGF-beta and the identification of an mRNA coding for FGF in the early Xenopus embryo. *Cell*, 51(5):869–877, 1987.

C. Kimura, K. Yoshinaga, E. Tian, M. Suzuki, S. Aizawa, and I. Matsuo. Visceral endoderm mediates forebrain development by suppressing posteriorizing signals. *Dev. Biol.*, 225(2):304–321, 2000.

K. P. Landsberg, R. Farhadifar, J. Ranft, D. Umetsu, T. J. Widmann, T. Bittig, A. Said, F. Jülicher, and C. Dahmann. Increased cell bond tension governs cell sorting at the Drosophila anteroposterior compartment boundary. *Curr. Biol.*, 19 (22):1950–1955, 2009.

P. A. Lawrence and G. Struhl. Morphogens, compartments, and pattern: lessons from Drosophila? *Cell*, 85(7):951–961, 1996.

M. Loeffler, R. Stein, H. E. Wichmann, C. S. Potten, P. Kaur, and S. Chwalinski. Intestinal cell proliferation. I. A comprehensive model of steady-state proliferation in the crypt. *Cell. Tissue. Kinet.*, 19(6):627–645, 1986.

A. F. M. Maree, A. V. Panfilov, and P. Hogeweg. Migration and thermotaxis of Dictyostelium discoideum slugs, a model study. *J. Theor. Biol.*, 199(3):297–309, 1999.

F. A. Martín and G. Morata. Compartments and the control of growth in the Drosophila wing imaginal disc. *Development*, 133(22):4421–4426, 2006.

F. A. Martín, S. C. Herrera, and G. Morata. Cell competition, growth and size control in the Drosophila wing imaginal disc. *Development*, 136(22):3747–3756, 2009.

F. A. Meineke, C. S. Potten, and M. Loeffler. Cell migration and organization in the intestinal crypt using a lattice-free model. *Cell. Prolif.*, 34(4):253–266, 2001.

C. Meno, K. Gritsman, S. Ohishi, Y. Ohfuji, E. Heckscher, K. Mochida, A. Shimono, H. Kondoh, W. S. Talbot, E. J. Robertson, A. F. Schier, and H. Hamada. Mouse Lefty2 and zebrafish antivin are feedback inhibitors of nodal signaling during vertebrate gastrulation. *Mol. Cell.*, 4(3):287–298, 1999.

R. M. H. Merks and J. A. Glazier. Dynamic mechanisms of blood vessel growth. *Nonlinearity*, 19(1):C1–C10, 2006.

D. Mesnard, M. Guzman-Ayala, and D. B. Constam. Nodal specifies embryonic visceral endoderm and sustains pluripotent cells in the epiblast before overt axial patterning. *Development*, 133(13):2497–2505, 2006.

M. Milàn, S. Campuzano, and A. Garciá-Bellido. Cell cycling and patterned cell proliferation in the wing primordium of Drosophila. *Proc. Natl. Acad. Sci. USA*, 93(2):640–645, 1996.

J. C. M. Mombach and J. A. Glazier. Single cell motion in aggregates of embryonic cells. *Phys. Rev. Lett.*, 76(16):3032–3035, 1996.

T. Nagai and H. Honda. A dynamic cell model for the formation of epithelial tissue. *Philos. Mag. B.*, 81:699–719, 2001.

T. P. Neufeld, A. F. de la Cruz, L. A. Johnston, and B. A. Edgar. Coordination of growth and cell division in the Drosophila wing. *Cell*, 93(7):1183–1193, 1998.

T. J. Newman. Modelling multicellular systems using subcellular elements. *Math. Biosci. Eng.*, 2:613–624, 2005.

F. Nobile. *Numerical approximation of fluid-structure interaction problems with application to haemodynamics*. PhD Thesis, École Polytechnique Fédérale de Lausanne, 2001.

G. M. Odell, G. Oster, P. Alberch, and B. Burnside. The mechanical basis of morphogenesis. I. Epithelial folding and invagination. *Dev. Biol.*, 85(2):446–462, 1981.

J. M. Osborne, A. Walter, S. K. Kershaw, G. R. Mirams, A. G. Fletcher, P. Pathmanathan, D. Gavaghan, O. E. Jensen, P. K. Maini, and H. M. Byrne. A hybrid approach to multi-scale modelling of cancer. *Philos. Transact. A Math. Phys. Eng. Sci.*, 368(1930):5013–5028, 2010.

M. R. Owen, I. J. Stamper, M. Muthana, G. W. Richardson, J. Dobson, C. E. Lewis, and H. M. Byrne. Mathematical modeling predicts synergistic antitumor effects of combining a macrophage-based, hypoxia-targeted gene therapy with chemotherapy. *Cancer. Res.*, 71(8):2826–2837, 2011.

K. J. Painter, P. K. Maini, and H. G. Othmer. A chemotactic model for the advance and retreat of the primitive streak in avian development. *Bull. Math. Biol.*, 62(3): 501–525, 2000.

J. Parker. Control of compartment size by an EGF ligand from neighboring cells. *Curr. Biol.*, 16(20):2058–2065, 2006.

U. Paulus, M. Loeffler, J. Zeidler, G. Owen, and C. S. Potten. The differentiation and lineage development of goblet cells in the murine small intestinal crypt: experimental and modelling studies. *J. Cell. Sci.*, 106:473–483, 1993.

E. M. Purcell. Life at low Reynolds number. *Amer. J. Phys.*, 45(1):3–11, 1977.

M. Rauzi, P. Verant, T. Lecuit, and P.-F Lenne. Nature and anisotropy of cortical forces orienting Drosophila tissue morphogenesis. *Nat. Cell. Biol.*, 10(12):1401–1410, 2008.

J. A. Rivera-Pérez, J. Mager, and T. Magnuson. Dynamic morphogenetic events characterize the mouse visceral endoderm. *Dev. Biol.*, 261(2):470–487, 2003.

T. A. Rodriguez, E. S. Casey, R. M. Harland, J. C. Smith, and R. S. Beddington. Distinct enhancer elements control Hex expression during gastrulation and early organogenesis. *Dev. Biol.*, 234(2):304–316, 2001.

D. Rogulja and K. D. Irvine. Regulation of cell proliferation by a morphogen gradient. *Cell*, 123(3):449–461, 2005.

N. J. Savill and P. Hogeweg. Modelling morphogenesis: from single cells to crawling slugs. *J. Theor. Biol.*, 184(3):229 – 235, 1997.

S. Schilling, M. Willecke, T. Aegerter-Wilmsen, O. A. Cirpka, K. Basler, and C. von Mering. Cell-sorting at the A/P boundary in the Drosophila wing primordium: a computational model to consolidate observed non-local effects of Hh signaling. *PLoS. Comp. Biol.*, 7(4):e1002025, 2011.

G. Schwank and K. Basler. Regulation of organ growth by morphogen gradients. *Cold Spring Harb. Perspect. Biol.*, 2(1):a001669, 2010.

G. Schwank, S. Restrepo, and K. Basler. Growth regulation by Dpp: an essential role for Brinker and a non-essential role for graded signaling levels. *Development*, 135 (24):4003–4013, 2008.

G. Schwank, G. Tauriello, R. Yagi, E. Kranz, P. Koumoutsakos, and K. Basler. Antagonistic growth regulation by Dpp and Fat drives uniform cell proliferation. *Dev. Cell*, 20(1):123–130, 2011.

N. Serrano and P. H. O'Farrell. Limb morphogenesis: connections between patterning and growth. *Curr. Biol.*, 7(3):R186–R195, 1997.

B. I. Shraiman. Mechanical feedback as a possible regulator of tissue growth. *Proc. Natl. Acad. Sci. USA*, 102(9):3318–3323, 2005.

A. M. Smith, R. E. Baker, D. Kay, and P. K. Maini. Incorporating chemical signalling factors into cell-based models of growing epithelial tissues. *J. Math. Biol.*, 2011.

F. A. Spencer, F. M. Hoffmann, and W. M. Gelbart. Decapentaplegic: a gene complex affecting morphogenesis in Drosophila melanogaster. *Cell*, 28(3):451–461, 1982.

S. Srinivas. The anterior visceral endoderm-turning heads. *Genesis*, 44(11):565–572, 2006.

S. Srinivas, T. Rodriguez, M. Clements, J. C. Smith, and R. S. P. Beddington. Active cell migration drives the unilateral movements of the anterior visceral endoderm. *Development*, 131(5):1157–1164, 2004.

S. Tanaka, T. Kunath, A. K. Hadjantonakis, A. Nagy, and J. Rossant. Promotion of trophoblast stem cell proliferation by FGF4. *Science*, 282(5396):2072–2075, 1998.

P. Q. Thomas, A. Brown, and R. S. Beddington. Hex: a homeobox gene revealing peri-implantation asymmetry in the mouse embryo and an early transient marker of endothelial cell precursors. *Development*, 125(1):85–94, 1998.

G. Trichas, B. Joyce, L. A. Crompton, V. Wilkins, M. Clements, M. Tada, T. A. Rodriguez, and S. Srinivas. Nodal dependent differential localisation of dishevelled-2 demarcates regions of differing cell behaviour in the visceral endoderm. *PLoS. Biol.*, 9(2):e1001019, 2011.

G. Trichas, A. M. Smith, N. White, V. Wilkins, T. Watanabe, A. Moore, B. Joyce, J. Sugnaseelan, T. A. Rodriguez, D. Kay, R. E. Baker, P. K. Maini, and S. Srinivas. Multi-cellular rosettes in the mouse visceral endoderm facilitate the ordered migration of anterior visceral endoderm cells. *PLoS Biol*, 10(2):e1001256, 2012.

S. Turner and J. A. Sherratt. Intercellular adhesion and cancer invasion: a discrete simulation using the extended Potts model. *J. Theor. Biol.*, 216(1):85–100, 2002.

I. M M van Leeuwen, G. R. Mirams, A. Walter, A. Fletcher, P. Murray, J. Osborne, S. Varma, S. J. Young, J. Cooper, B. Doyle, J. Pitt-Francis, L. Momtahan, P. Pathmanathan, J. P. Whiteley, S. J. Chapman, D. J. Gavaghan, O. E. Jensen, J. R. King, P. K. Maini, S. L. Waters, and H. M. Byrne. An integrative computational model for intestinal tissue renewal. *Cell Prolif.*, 42(5):617–636, 2009.

J. A. Vernon and J. Butsch. Effect of tetraploidy on learning and retention in the salamander. *Science*, 125(3256):1033–1034, 1957.

L. J. Wagstaff, G. Bellett, M. M. Mogensen, and A. Münsterberg. Multicellular rosette formation during cell ingression in the avian primitive streak. *Dev. Dyn.*, 237(1):91–96, 2008.

V. Walbot and N. Holder. *Developmental Biology*. Random House, 1987.

O. Wartlick, P. Mumcu, A. Kicheva, T. Bittig, C. Seum, F. Jülicher, and M. González-Gaitán. Dynamics of Dpp signaling and proliferation control. *Science*, 331(6021): 1154–1159, 2011.

K. Weigmann, S. M. Cohen, and C. F. Lehner. Cell cycle progression, growth and patterning in imaginal discs despite inhibition of cell division after inactivation of Drosophila Cdc2 kinase. *Development*, 124(18):3555–3563, 1997.

M. Weliky and G. Oster. The mechanical basis of cell rearrangement. I. Epithelial morphogenesis during Fundulus epiboly. *Development*, 109(2):373–386, 1990.

M. Weliky, S. Minsuk, R. Keller, and G. Oster. Notochord morphogenesis in Xenopus laevis: simulation of cell behavior underlying tissue convergence and extension. *Development*, 113(4):1231–1244, 1991.

C. A. Yates. *Comparing stochastic discrete and deterministic continuum models of cell migration*. DPhil thesis, University of Oxford, 2011.